Thermal Modelling of the Ventilation and Cooling inside Axial Flux Permanent Magnet Generators

LIM, CHIN,HONG

Thermal Modelling of the Ventilation and Cooling inside Axial Flux Permanent Magnet Generators

Chin Hong, LIM

A thesis presented for the degree of
Doctor of Philosophy

School of Engineering and Computer Science
Durham University
United Kingdom
April 2010

Thermal Modelling of the Ventilation and Cooling inside the Axial Flux Permanent Magnet Generators

Chin Hong LIM

Submitted for the degree of Doctor of Philosophy
April 2010

Abstract

Axial flux permanent magnet generators are of particular interest for power generation in harsh and confined conditions. Due to their compactness and high power density, the ventilation and cooling inside axial flux permanent magnet generators have becoming increasingly important for further performance improvement. This thesis describes the developments of a lumped parameter, thermal modelling technique for axial flux permanent magnet generators. The main aim of this research is to develop a fast and accurate thermal modelling tool which can be used for rapid machine design and ultimately, to replace complex and time consuming CFD analyses in the machine design process.

The thesis illustrates the construction of a generic thermal equivalent circuit, which comprises of conductive and convective sub-circuits, to model the conduction and convection heat transfers and temperature distributions in the radial and axial directions, within these machines. The conduction heat transfer between the solid components of these electrical machines is modelled by an annulus conductive thermal circuit derived from previous researchers; whereas, for convection heat transfer between the working fluid (air) and solids, the author has developed two convective thermal circuits, which are demonstrated as the Temperature Passing Method (TPM) and Heat Pick-up method in (HPM) in the thesis. Several case studies were designed to investigate the validity and accuracy of these thermal sub-circuits with both steady and transient boundary conditions. Since all the thermal impedances and capacitances used in the thermal circuits are in dimensionless form, the developed generic thermal equivalent circuit is capable of performing thermal simulations for axial flux generators of different sizes and topologies. Furthermore, special correction

factors were introduced into the developed generic thermal equivalent circuit, to take into account the heat transfer in the circumferential direction in axial flux machines.

The thesis also demonstrates how the heat transfer in the stator windings is modelled in the generic thermal equivalent circuit. Two analytical models, which are the Simple Concentric Model (SCM) and Concentric-annulus Layer Model (CLM) were developed, for the evaluation of the thermal resistances of the stator windings. The results evaluated from these analytical models were validated by several numerical models and experimental results of two-phase materials published by previous researchers.

Lastly, experimental validation of the lumped parameter thermal equivalent circuit model and CFD simulations was conducted. Heat transfer coefficient measurements were carried out on two separate test rigs, which were a simplified single-sided axial flux machine test rig and a large-scale low speed axial flux machine. The experimental results were compared with the numerical results obtained from both the lumped parameter and CFD models. Good agreement between the experimental, lumped parameter model and CFD results were found. These indicate that the developed generic thermal circuit is potentially capable of replacing CFD analyses in the axial flux machines design process.

Declaration

This work in this thesis is based on research carried out in the School of Engineering and Computing Sciences at Durham University. No part of this thesis has been submitted elsewhere for any other degree or qualification and it is all my own work unless referenced to the contrary in the text.

Chin Hong LIM
PhD Thesis 2010
School of Engineering and Computer Science

Acknowledgements

Firstly, I am heartily grateful to my academic supervisors Dr. Robert Dominy and Dr. Grant Ingram whose encouragement, guidance and support from the initial to the final level enabled me to complete my 3 year Ph.D. research. I also want to give a big thanks to Dr. Khamid Mahkamov, who was my research project main coordinator, for giving me full financial and emotional supports upon the completion of the Ph.D studies and the construction of the project test rig. A special thanks goes to Dr. Jim Bumby and Professor Li He, who gave insightful comments and shared their technical knowledge about axial flux machines in the early stage of the project.

This research project was fully funded by Cummins Generator Technologies, Stamford. Without the constructive and industrial supports from Cummins Generator Technologies, the findings from the research couldn't be validated (with the experimental results) and hence to be publicised in several conferences and renown academic journals. All these have to thank to Dr. Neil Brown, Dr. Salem Mebarki and Dr. Martin Shanel.

For the construction of the Perspex test rig, I would like to thank to Durham School of Engineering chief mechanical technician- Mr Colin Wintrip, mechanical technician- Mr Roger Little, and research technician- Mr David Jones. Extra credits go to Mr Roger Little for rescuing me out from "Epoxy-Resin" tragedy, helping me in dissolving the "clearance" crisis and polishing the Perspex with "Wet and Dry".

At the end, I would like express my deepest gratitude to Dr. Giovanni Airoldi who was my colleague, officemate, and housemate. We worked together in the same research group and he has offered me assistance in every single minor thing in the project. Most of the ideas developed in the research were inspired by him. Without him, my research life in Durham is going to be very bored and uneventful.

Contents

List of Figures

Chapter 1: Induction

Chapter 2: Literature Review

Chapter 3: 2-D Lumped Parameter Model

Chapter 4: Stator Winding Thermal Modelling

Chapter 5: The Construction of 2-D Generic Lumped Parameter model of Axial Flux Permanent Magnet Generators

Chapter 6: Experimental Validation of the Lumped Parameter thermal modelling technique: Single-sided Slotted Axial Flux Permanent Magnet Generator

Chapter 7: Experimental Validation of CFD Modelling Method: Large Scale Low Speed Test Rig

Nomenclatures

Symbol	Description
A	Cross-sectional/ Surface area, m^2
A_d	Conductive surface area, m^2 or winding packing ratio
α	Temperature constant, $°C^{-1}$
b	Width, m
B_{max}	Peak magnetic flux density
c	Air clearance, m
CLM	Concentric Annular Layer Model
C_p	Specific heat capacity, J/kgK
CV	Control volume
θ	Angle, °
d	Diameter, m
dm	Magnet Groove depth, m
f	Rotational frequency, Hz
g	Heat generated per unit volume, W/m^3
G_{ratio}	Gap ratio
$[G']$	Thermal network admittance matrix
h	Heat transfer coefficient, W/m^2K
$h_{convection}$	Convection heat transfer coefficient, W/m^2K
$h_{contact,\ gas}$	Gas gap contact coefficient, W/m^2K
$h_{contact,\ solid}$	Solid spot contact coefficient, W/m^2K
$\overline{h}_f$	Average heat transfer coefficient of free rotating plate, W/m^2K
$\overline{h}_p$	Average peripheral edge heat transfer coefficient, W/m^2K
$\overline{h}_{rs}$	Average heat transfer coefficient of rotor surface in rotor-stator system, W/m^2K
$h_{w\text{-}c}$	Winding and stator core contact coefficient, W/m^2K
H	Fluid flow pressure, Pa
HPM	Heat Pick-up Method
H_s	Heat storage, J

H_{se}	Element heat storage, J
k_a	Axial thermal conductivity, W/mK
$k_{c,}$	Cable filling thermal conductivity, W/K
k_d	Copper conductor thermal conductivity, W/K
k_{eq}	Equivalent thermal conductivity, W/K
k_{eq_sc}	Equivalent thermal conductivity, W/mK
k_r	Radial thermal conductivity, W/mK
k_g	Gas thermal conductivity, W/mK
K	Thermal conductivity, W/mK
$K_{calibration}$	Calibration Factor, μV/W/m^2
K_n	Heat fraction
L	Length or thickness, m
L_w	Winding length, m
m	Mass, kg
$\dot{m}$	Mass flow rate, kg/s
n	Power coefficient
n_{sc}	Number of continuous particles at the outer layer of the mixture
N	Numberth of annular layer
Nu	Nusselt number
Nu_{forced}	Forced convection Nusselt number
$Nu_{mixed\text{-}assisting}$	Assisting flow mixed convection Nusselt number
$Nu_{mixed\text{-}opposing}$	Opposing flow mixed convection Nusselt number
$Nu_{natural}$	Natural convection Nusselt number
$\overline{Nu}_f$	Average Nusselt number of free rotating plate
$\overline{Nu}_p$	Average peripheral edge Nusselt number
$\overline{Nu}_{rs}$	Average Nusselt number of rotor surface in rotor-stator system
ρ	Density, kg/m^3
ρ_0	Resistivity, Ωm
P	Contact pressure, Pa
P_{25}	Resistivity at 25°C, Ωm
P_d	Winding packing ratio
P_{eddy}	Eddy current power loss, W

Pr	Prandtl number
Pwr_{cc}	Joule loss of centre winding conductor, W
$Pwr1$	1st annular layer joule loss, W
q	Heat flux, W/m^2
$q_{convection}$	Convection heat flux, W/m^2
$[Q]$	Power source matrix
r_c	Conductor radius, m
r_c	Radius at transition occurs from laminar to turbulent flow, m
r_c	Winding slot diameter, m
r_d	Discontinuous particle, m
r_{eq}	Equivalent radius, m
r_{eq_0}	Equivalent centre circle radius, m
r_{eq_k}	Equivalent kth annulus outer radius, m
r_{in}	Inner radius, m
r_{in_k}	kth annulus inner radius, m
r_m	Mixture particle, m
r_{mid_k}	kth annulus middle radius, m
r_{out}	Outer radius, m
r_{out_k}	kth annulus outer radius, m
r_{sc}	Winding radius, m
R, r	Radius, m
R_a	Axial conductive thermal resistance, K/W
R_c, R_{conv}	Convective thermal resistance, K/W
R_{c1_k}	kth annulus inner cable filling thermal resistance, K/W, Fig. 4-9
R_{c2_k}	kth annulus outer cable filling thermal resistance, K/W, Fig. 4-9
$R_{cc\text{-}c}$	Centre winding filling resistance, K/W
$R_{cc\text{-}d}$	Centre conductor resistance, K/W
R_d, R_{cond}	Conductive thermal resistance, K/W
R_{d1_k}	kth annulus inner conductor thermal resistance, K/W, Fig. 4-9
R_{d2_k}	kth annulus outer conductor thermal resistance, K/W, Fig. 4-9
R_{d3_k}	kth annulus interconnecting thermal resistances, K/W, Fig. 4-9
R_{eq_sc}	Equivalent radial thermal resistance, K/W

R_m	Mass flow resistance, $J^{-1}Ks$
R_r, R_{radial}	Radial conductive thermal resistance, K/W
$R_{thermal}$	Thermal resistance, K/W
Re	Reynolds number
Re_d	Rotor disk Reynolds number
Re_ω	Rotational Reynolds number
Sc	Schmidt number
SCM	Simple Concentric Model
Sh	Sherwood number
t	Time, s
t_n	Thickness at n node, m
$tan\ \theta$	Surface profile slope
T_0, $T_{initial}$	Initial temperature, K
T_∞	Steady state temperature, K
ΔT	Temperature difference/ Temperature increased, K
T_{amb}	Ambient temperature, K
T_{aw}	Adiabatic wall temperature, K
T_c	Temperature of the cable filling, K
T_{CFD}	Temperature predicted by CFD, K
T_d	Temperature of copper conductor, K
T_{in}	Inlet temperature, K
T_l	Axial temperature profile, K
T_{LPM}	Temperature predicted by lumped parameter model, K
T_m	Mean temperature, K
T_{out}	Outlet temperature, K
TPM	Temperature Passing Method
T_r	Radial temperature profile, K
T_s, T_{surf}	Surface temperature, K
T_{total}	Total temperature, K
v	Fluid kinematic viscosity, m^2/s
$v_{X\text{-}axis}$	Velocity profile on X-axis, m/s
$v_{Y\text{-}axis}$	Velocity profile on Y-axis, m/s

V	Volume, m^3
V_{HFS}	Voltage output from Heat Flux Sensor, μV
ω	Rotational speed, rad/s
WM_{th}	Convection heat flow, W
WM_{cv}	Heat flow to control volume, W
$[\theta]$	Temperature vector
δ	Surface profile height, m
δ_{eff}	Effective mean thickness, m

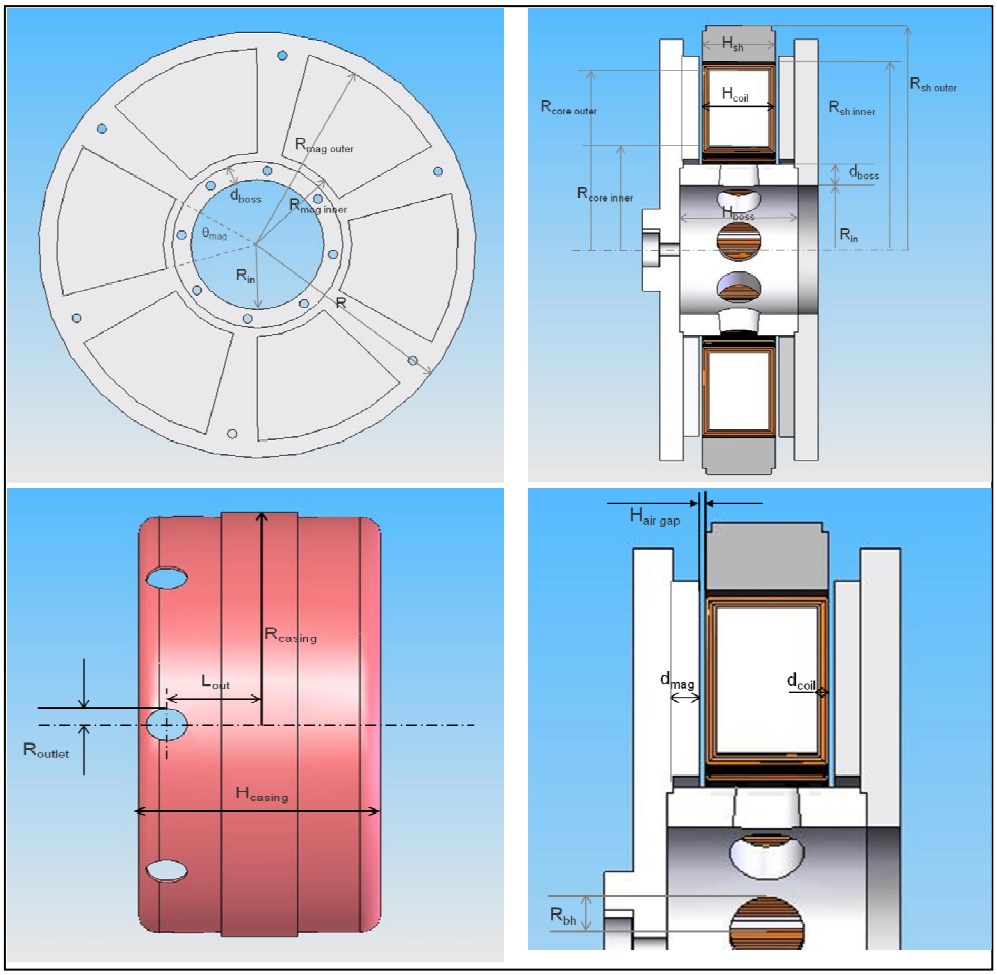

Chapter 1

Introduction

1.1. Axial Flux Permanent Magnet Generator

The axial flux permanent magnet (AFPM) generator is defined as an electrical generator in which the magnetic fluxes are parallel to the rotating axes. In general, AFPM generators have cylindrical rotors with permanent magnets attached to them, and annular stators, which include the generator windings. The history of electrical machines shows that the first electrical machine was realised in the form of an axial flux machine, in 1831 by Faraday. Shortly afterwards, Davenport patented the design of the radial flux permanent magnet machine in 1837, which has been widely accepted as the mainstream configuration for electrical machines since then.

Despite the success of radial flux permanent magnet machines, axial flux permanent magnet machines continue to be of interest, particularly for power generation applications in harsh and confined working environments. Unlike the radial flux machines, axial flux generators have high flexibility operating at a variety of rotational speeds. By changing the number of magnets on the rotating disks and varying its diameter, the AFPM is capable of accommodating different rotational speeds applications. The large diameter axial flux machines with a high number of poles are ideal for low rotational speed, high torque applications, such as, electromechanical traction drives, hoists, and horizontal axis wind turbines.

Conversely, small diameter axial flux machines with fewer poles are suitable for high speed low torque applications, such as vertical axis wind turbines, and Kaplan turbines.

Another advantage of the AFPM generator is the compactness of the machine. Since AFPM generators are generally less bulky (it has shorter axial length) than convectional radial flux machines, it makes the axial flux machines very attractive for power generation applications, where space is confined. The slim and light-weight AFPM generators have higher power density compared with the conventional radial flux generators. Therefore, AFPM generators are suitable for electrical vehicles (e.g. solar cars), wind turbines, robot arms, and other industrial applications, which require light weight generators for power generation.

Due to several significant improvements of the properties of the permanent magnets themselves and of the power electronic devices in these past few decades, most AFPM machines have high electrical efficiency and good starting torque. The use of rare earth permanent magnet material, such as Samarium Cobalt (SmCo5) and recently introduced Neodymium-Iron-Boron (NdFeb) further improved the power generation capability at higher ambient temperature. Several axial flux machine configurations have been proposed, regarding the stator(s) position with respect to the rotor(s) position and also regarding the winding arrangements, giving freedom to select the most suitable machine structure for particular applications. From the construction point of view, AFPM machines can be designed as single-sided or double sided, with or without armature slots or armature cores, with surface mounted permanent magnets or surface embedded permanent magnets, and as single or multi-stage machines. Fig. 1-1 shows some of the diverse topologies of AFPM machines.

The single-rotor-single-stator structure, shown in Fig. 1-1(a) is the simplest AFPM machine configuration. However, this structure suffers from an unbalanced axial force between the rotor and the stator as a consequence of which more complex bearing arrangements and a thicker rotor disk are needed. The machine demonstrated in Fig. 1-1(b) is the single-stator-two-rotors design, also known as the TORUS design. The TORUS AFPM machines can adapt to either slotted stator (Fig. 1(b)) or coreless

stator (Fig. 1-1(c)) configurations. The toroidal wound phase winding is the most common and preferable AFPM machine design because it has short end-windings, higher machine efficiency and power density. Fig. 1-1(d) shows a more complex arrangement of AFPM machine, in which several machines are lined up on the same shaft forming a multistage AFPM machine. Such a configuration is designed for high torque applications such as ship propulsion.

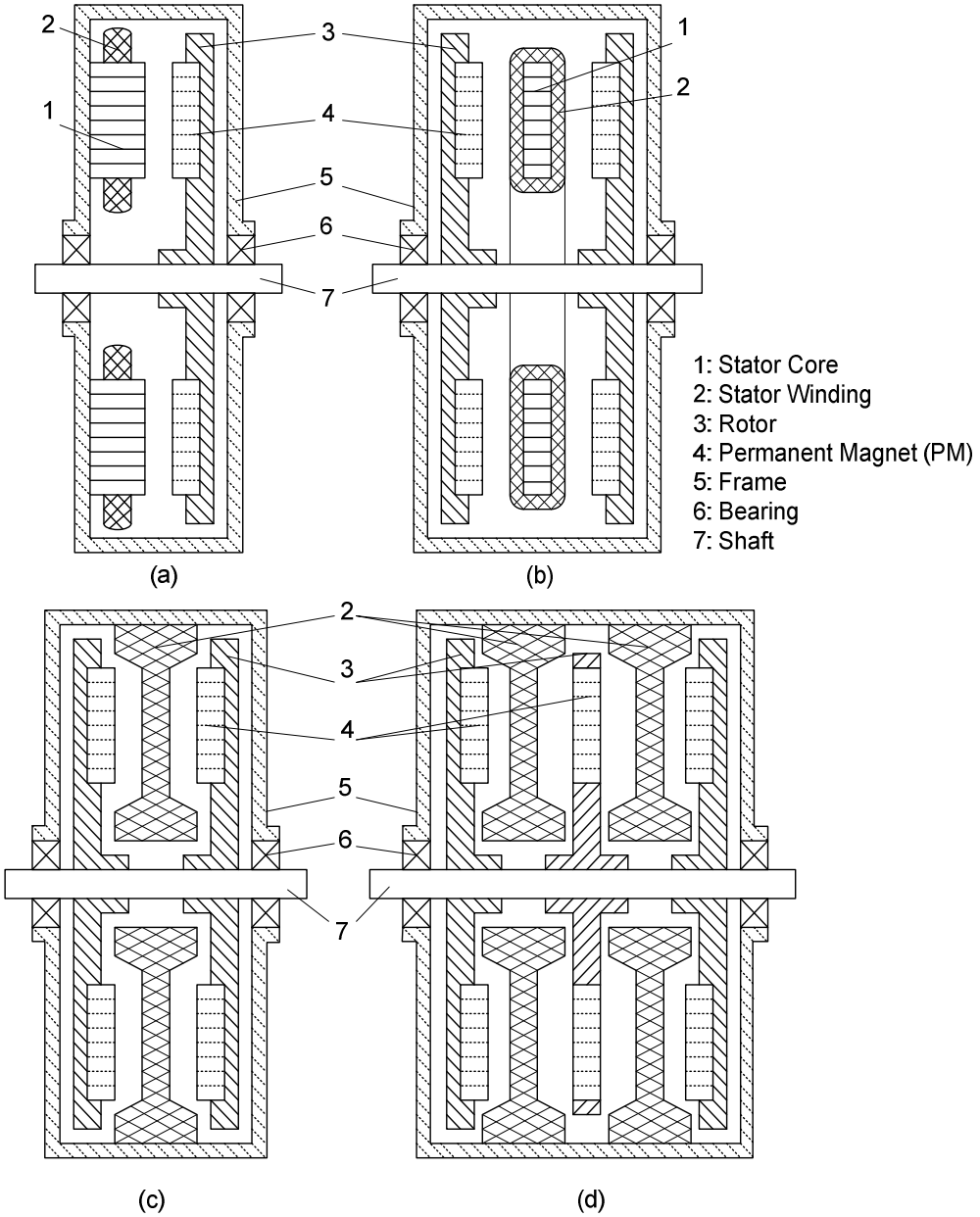

Fig. 1-1. Axial flux permanent magnet generators: (a) single-sided slotted machine, (b) double-sided slotless machines with internal stator, (c) double-sided coreless machine, (d) Multistage axial flux permanent magnet generators.

Recently, extensive research has been conducted on the electromagnetic design to obtain the optimum power yield configuration for axial flux machines. Bobbin stator design [1], multiple stage air gap configurations etc, have pushed the AFPM design towards a bottle neck, where the thermal properties of the generator components start to play an important role in the generator design consideration. Recently, commercial axial flux generator configurations, which have small air gap size, low rotational speed and high power density, have lead to machines operating at the temperatures, which are near to the ferromagnetic material limits. For example, the remanence flux density of Neodymium-Iron-Boron (Nd-Fe-B) permanent magnet material depends on the operating temperature. At high temperature, normally around 120°C, Nd-Fe-B permanent magnets start to demagnetise and this affects the amplitude of the induced back-EMF in the stator windings.

Furthermore, mechanical hazards are possible if the permanent magnets are glued to the rotor surfaces or if the stator windings are wound with epoxy resin. When the rotor or stator temperature exceeds the glue or epoxy resin critical limits, the magnets and winding start loosening and eventually detach from the rotors and stators. This can be catastrophic, especially at high speed applications.

1.2. Thermal Modelling

Extensive research has been devoted to thermal studies of conventional radial flux electrical machines, but AFPM machines have received very little attention. Depending on the sizes of the machine and the types of enclosure, different cooling mechanism arrangements have been introduced for AFPM machines. Generally, they can be classified into two configuration categories, which are self-ventilated and externally ventilated configurations. For self-ventilated configurations, the disk type AFPM generators use their inherently advantageous feature of the rotor disks (with attached magnets), which act like pump impellers, drawing the ambient air flow through the inlet and subsequently into the gaps between the stator and rotor disks, to cool the stator core and windings. Most self-ventilated machines are air-cooled. For medium to high power rated AFPM generators, the heat loss ratios are high and self

ventilated air-cooled mechanisms are not sufficient to bring down the machine temperature to the safe operating temperature limits. Therefore, forced cooling with the aid of external devices, such as, water pumps or external fans is necessary. Some of the available commercial external ventilated machines embed a water-cooling system into the stator core, to lower the temperature of the stator core and windings. These configurations are known as external ventilation cooling systems.

Quantitative studies of the heat dissipation potential of AFPM machines with vastly different topologies are clearly needed. Although there are several general purpose advanced computational fluid dynamic (CFD) codes (e.g. FLUENT, Ansys CFX, OpenFoam) which are commercially available that can be used for 2D and 3D thermal modelling of AFPM machines, these modelling methods usually require high performance multiprocessor computers and considerable computing time to obtain accurate numerical solutions. Furthermore, CFD numerical results are significantly influenced by the mesh/grid qualities. By refining the mesh quality, the CFD numerical results improve, but at the same time, it requires higher computer memory and longer computational time. This makes it difficult to use advanced CFD techniques to perform rapid-design and optimisation analyses for APFM machines.

The feasible alternative to CFD modelling of the thermal state of electrical machines is the application of the advanced lumped parameter model (LPM) technique. In such an approach, firstly the electrical machines are subdivided into a number of lumped components and each lumped component is represented by a collection of thermal impedances and capacitances. By knowing the thermal and physical properties of the machine components, these thermal impedances and capacitances of each component can be evaluated by well-known analogies. Subsequently, by connecting these collections of thermal impedances and capacitances, based on the heat flow paths in the electrical machine, the thermal equivalent circuit is constructed. Hereby, the temperature and surface heat flux can be predicted by solving the thermal equivalent circuit.

Fundamentally, the thermal equivalent circuit is analogous to an electrical circuit. The heat flowing in each path of the thermal circuit is analogous to the current in the

electrical circuit. The heat flow is driven and determined by the temperature differences, in which it is analogous to the voltage difference in the electrical circuit and the thermal resistances and capacitances in the machine thermal equivalent circuits are analogous to the resistances and capacitances in the electrical circuit. Thermal predictions from the equivalent thermal circuit obtained from previous research demonstrate good agreements with both experimental and CFD results. In addition, the LPM demonstrates the advantage of using the corresponding thermal resistances and capacitances in the dimensionless form, to perform thermal analysis for a wide range of machine dimensions and topologies. 2-D thermal equivalent circuits are developed and discussed in this thesis, to model the conduction and convection heat transfers, in the radial, axial and circumferential directions, within AFPM generators.

1.3. CFD validations

Unlike the water-cooled machines, the machine temperatures predicted by the thermal equivalent circuit of air-cooled electrical machines have a strong influence on the surface convection heat transfer coefficients that are applied, especially for self-ventilated axial flux machines, where the heat generated in the machine during the machine operation is mainly dissipated to the cold air drawn from the surroundings. The surface convection heat transfer coefficients have a direct impact on the accuracy of the thermal equivalent circuits, yet there are neither analytical nor empirical formulae that directly correlate the surface convection heat transfer coefficients with the AFPM machines dimensions. Therefore, parametric studies of local surface convection heat transfer coefficients of AFPM machines are essential.

The surface convection heat transfer coefficient parametric studies investigate the effect of surface convection heat transfer coefficient on different machine sizes, topologies and operating conditions. These include stator disk radius, magnet groove depth, number of magnets, rotational speed etc. Since it is costly, time consuming and complex to design and construct a test rig which allows investigations on different

machine parameters, the parametric investigations were conducted numerically using the CFD modelling technique. However, the numerical solutions predicted by the commercially available CFD solvers are strongly influenced by the mesh quality, the solver equations, turbulence models and the boundary conditions applied. Furthermore, these influences vary with different modelling applications. Therefore, before applying empirical formulae derived from the parametric studies derived from CFD, it is paramount to validate the CFD models with the results obtained from the experiments, to determine the compatibility of the mesh quality, solvers equations, turbulence models and boundary conditions of the CFD models.

A large scale low speed AFPM test rig was designed and constructed to perform surface convection heat transfer coefficient measurements for CFD validation. The AFPM test rig is scaled up four times from the original Durham 1.5kW Torus AFPM generator, to allow higher resolution heat flux and temperature measurements inside the air gaps. Additionally, the test rig was made in Perspex, reducing both the weight and cost of the test rig. The experimental results obtained from the large scale, low speed test rig were compared with the numerical results obtained from both the lumped parameter and CFD models. The discrepancies were identified and investigated.

1.4. Thesis Overview

The primary motivation of this research is to develop a fast and high accuracy thermal modelling tool, specifically for axial flux permanent magnet generators. Ideally, this thermal modelling tool would replace CFD analysis, in the product rapid design process. The developed thermal modelling tool merges the principles of the lumped parameter model and thermal equivalent circuit, to construct a generic thermal model, which can be used to perform thermal analysis, for a wide range of AFPM generator topologies and sizes. Both CFD modelling and experiments were conducted to validate the temperatures and heat fluxes predicted by the new thermal modelling tool.

This thesis consists of seven chapters, and a summary of each chapter is shown as below:

1.4.1. Chapter 1: Introduction

The thesis begins with an introductory chapter, which provides background information for axial flux electrical machines, thermal modelling tools and experimental techniques for CFD validation. Firstly, this chapter gives a brief history of the developments of axial and radial flux machines and discusses the major distinctions and advantages of the axial flux permanent magnet generators over the conventional radial flux machines. Several axial flux machines designs are introduced and the machine configurations were demonstrated. This chapter also highlights the necessity of performing thermal modelling in the electrical machine design process. Several numerical modelling methods are discussed and the basic principles of the lumped parameter thermal equivalent circuit are illustrated. CFD validation experiments are discussed at the end of the first chapter and descriptions of the large scale low speed Perspex test rig are provided.

1.4.2. Chapter 2: Literature Review

The second chapter reviews the literature which is relevant to the numerical thermal modelling tools, stator winding thermal resistance modelling and the heat transfer coefficient measuring techniques. The first section describes previous research relevant to using the CFD modelling tool to simulate the physical and thermal processes in the systems of interest and the CFD verifications and validations. CFD modelling guidelines and recommendations for turbomachinery applications are quoted in this section. This section also illustrates the research which has been conducted for the development of lumped parameter thermal equivalent circuits for electrical machines and highlights the necessity of developing convective thermal circuits for modelling of convection heat transfer in axial flux machines.

The second section illustrates the development of thermal resistances of two-phase mixtures. Both experimental and analytical researches identifying the thermal resistance of two-phase mixtures found are discussed in details. Subsequently, these works are compared with the empirical equations of stator winding based on experimentation and concludes that the development of a new analytical model of stator winding thermal resistance modelling is necessary.

Finally, this chapter summarises the commonly used (popular) convection heat transfer coefficient measurement techniques, including direct (steady state) measuring methods, indirect (transient) measuring methods and the Naphthalene sublimation mass transfer measuring method. The basic principle, accuracy, experimental uncertainty and calibration method of each measuring method are discussed and consequently the most suitable heat transfer measuring method is suggested.

1.4.3. Chapter 3: 2D Lumped Parameter Model

This chapter begins by illustrating the basic theory behind the one-dimensional lumped parameter thermal equivalent circuit for electrical machines and stating the definitions of the thermal resistances and capacitances used in the thermal equivalent circuits. The chapter then describes the construction of a two-dimensional conductive thermal circuit of the AFPM machines, which is capable of modelling the conduction heat transfer in the radial and axial directions. To further improve the accuracy of the lumped parameter model, the implementation of the 2D convective thermal circuit into the existing 2D conduction circuit is demonstrated. Two distinctive convective thermal circuit algorithms are developed, compared and validated using CFD models.

Two case studies are designed to verify the accuracy and compatibility of the proposed 2D lumped parameter thermal circuit. The first case study is conducted on a flow in a heated pipe. It is designed to investigate the accuracy of the 2D lumped parameter thermal circuit at different flow conditions and to obtain the optimal discretisation level for the simple pipe flow system. The second case study describes the construction of the 2D lumped parameter thermal circuit of the simplified

axisymmetric AFPM machines. The primary motivation of this case study is to compare the temperatures predicted from the 2D lumped parameter thermal circuit with the CFD models. Finally, the temperature discrepancies between the two modelling methods are identified and discussed.

1.4.4. Chapter 4: Stator Winding Thermal Modelling

Two stator winding radial thermal resistance analytical modelling methods are discussed in chapter 4, which are the simple concentric model (SCM) and the concentric circle layer model (CLM). SCM simplifies the stator winding by lumping all the copper conductors into a solid cylinder and the remaining winding filling into an annulus surrounding the conductor solid cylinder. By applying the one-dimensional Fouriers heat conduction differential equation in the radial direction and taking the integral of it in the circumferential direction, the stator winding radial thermal resistance is deduced.

When current passes through the stator winding, the copper conductors inside the stator winding are heated due to joule heating. Subsequently, these copper conductors become independent heat sources and dissipate heat to the stator winding. To take into account the distributions and positions of these independent heat sources inside the stator winding, the CLM is developed. CLM lumps the copper conductors and the winding filling of the stator winding and divides them into layers of alternative concentric annuli. Each of the concentric annulus is represented by the annulus conductive thermal circuit. The total equivalent thermal resistance of the stator winding is calculated by summing the total the temperature difference across all the annulus conductive thermal circuits in the stator winding, and dividing it with the total heat generated from the conductors.

Both of these stator winding radial resistance analytical methods (SCM and CLM) are validated by numerical and experimental results published by previous researchers. Finally, a 2D CFD model of the stator winding is constructed and simulated using

FLUENT, to verify the temperature variations in the radial direction of the stator winding predicted from the CLM analytical method.

1.4.5. Chapter 5: The Construction of a 2D Generic Lumped Parameter model of Axial Flux Permanent Magnet Generators

This chapter begins by identifying the distinctions between specific lumped parameter models and generic lumped parameter models. An introduction to the generic lumped parameter model is given and it highlights the importance of developing the generic lumped parameter in electrical machine thermal modelling. Subsequently, the derivations of the dimensionless thermal resistances, capacitances and heat sources used in the generic lumped parameter model are illustrated. The second section of chapter 5 demonstrates the construction of a 2D generic lumped parameter model for axial flux permanent magnet generators, by using the developed dimensionless thermal impedances and capacitances. A sophisticated user interface for the 2D generic lumped parameter model is developed by incorporating two independent pieces of software, Microsoft Excel and Portunus, to simplify the thermal modelling process of the axial flux machines. A Visual Basic macro script is written to control the information exchange between the two independent programs. The details and definition of the geometric parameters and model variables used in the interface and generic model are defined in the third section of chapter 5.

The 2D generic lumped parameter model for AFPM generators is validated in the forth section. This case study validates the solid and fluid temperatures predicted by the generic lumped parameter model with the numerical results simulated by CFD. Furthermore, the transient boundary conditions are specified for both modelling methods and the discrepancies are identified and discussed. Finally, the generic thermal model of water-cooled totally enclosed axial machines is proposed. Since the cooling in water-cooled machines is dominated by the water jacket inside the stator core, the air convection heat transfer modelling is neglected. The proposed model is examined with transient boundary conditions, such as temperature dependent resistive

heat losses, time dependent electrical loading and water pump loading. No validation is conducted for the water-cool machines generic lumped parameter model.

1.4.6. Chapter 6: Experimental Validation of the Lumped Parameter Thermal Modelling Technique: Single-sided Slotted Axial Flux Permanent Magnet Generator.

This chapter illustrates the experimental validation of the developed 2D lumped parameter thermal equivalent circuit of a single-side, slotted axial flux permanent magnet generator. Firstly, the construction of the thermal circuit of the single-sided slotted AFPM generator is demonstrated, followed by the construction of 2D axisymmetric CFD models of the corresponding machine. The convection heat transfer empirical models of the simple flat rotating disk system developed by past researchers are used in the construction of 2D lumped parameter thermal circuit.

To validate the numerical results predicted from both lumped parameter and CFD models, a test rig of the simplified single-sided slotted axial flux machine is designed and constructed. The details of the test rig design are illustrated in the fourth section of Chapter 6. The experimental measuring technique for the apparatus and its temperature, heat flux and air mass flow rate measuring techniques are discussed, including the equipment uncertainty, calibration techniques, procedures and correction factors. The results obtained from the experiments are compared with the lumped parameter and CFD numerical solutions.

Finally, additional experimental investigations are conducted to examine the compatibility of the 2D LPM thermal circuit for performing thermal modelling on the 3D models. Six additional Perspex sectors are attached on the rotor disk of the test rig and heat transfer experiments are carried out. The experimental results obtained from the modified test rig are compared with the numerical results obtained from the 3D CFD model and the 2D generic LPM thermal circuits. Modifications are suggested to the original 2-D LPM thermal circuit model to simulate 3-D heat flow system.

1.4.7. Chapter 7: Experimental Validation of the CFD Modelling Method: Large Scale Low Speed Test Rig

The last major chapter of the thesis describes the experimental validation of the lumped parameter thermal model of the large scale low speed test rig. Firstly, the topology of the large scale low speed test rig for the heat transfer coefficient measurement is illustrated, followed by the dimensional analysis of the test rig conducted prior to its construction. The rig schematic plan and corresponding experimental equipment configurations are also shown.

Before conducting the heat transfer coefficient measurements, all the measuring equipment is examined and re-calibrated. The experimental procedures are described in section 4 and section 5. Section 6 discloses the convective heat transfer coefficients measured from the large scale low speed test rig. The experimental results are compared with the numerical results predicted from the 3D CFD model. The discrepancies between the experimental and 3D CFD numerical results are identified and discussed. Extra experiments are conducted to verify the effect of natural convection on the machines cooling.

The final section describes the modification of the totally enclosed axial flux machine, by embracing a Perspex cylinder casing around it. The stator surface heat transfer coefficients are measured and compared with the measurements taken from the open channel axial flux machine. The differences are identified and the results are discussed.

Chapter 2

Literature Review

This chapter describes the literature relevant to this study. This chapter consists of two major sections. The first section discovers and discusses the various thermal modelling methods which have been developed and published, including computational fluid dynamics techniques, lumped parameter thermal modelling techniques and winding bundle thermal resistance modelling. The second part of the chapter investigates experimental measuring techniques for surface temperature, heat transfer coefficient, surface heat flux and air mass flow rate. Each of the experimental measuring techniques is discussed and evaluated, to identify the most suitable experimental method, to give the most accurate experimental results, within the provided time and research budget.

2.1. Thermal Modelling Methods

During the last three decades, computer simulations of physical and thermal flow processes have been used widely in scientific research, analysis, and design of engineered systems. There are several general purpose advanced computational fluid dynamic (CFD) codes, e.g. ANSYS CFX and FLUENT, that are commercially available. These CFD packages use the most up to date solution technology and extremely efficient parallelization algorithms to perform 2D and 3D mass transfer and thermal modeling of internal and external flow systems.

As compared with experimental investigation, CFD based research is more robust, economical, less time consuming and safer. Therefore, this new trend towards modelling, and simulation-based design methodologies is increasingly driven by manufacturing industries, for example: aerospace [2]-[5], automobile [6]-[8], power generation systems [9]-[11], and consumer products such as vacuum cleaners [12] and baking ovens [13], which require intensive research and high cost testing to improve their products competitiveness in the market. Furthermore, CFD is a good option to provide preliminary predictions for several high-risk and hazardous systems that cannot ever be tested experimentally, such as the catastrophic failure of a nuclear power [14]-[15], global weather prediction [16]-[17], and explosions [18]-[19]. CFD simulations are also used for environmental predictions e.g. upland urban river modeling [20], pollution [21] and nuclear-waste disposal [22] for the development of public policies, safety procedures and legal liabilities.

However, the numerical results predicted by CFD are highly dependent on the mesh/grid quality, the flow and turbulence models, and the applied boundary conditions. Several publications [23]-[25] provide guidelines for CFD modelling of turbomachinery applications, for which a rotating machine may be regarded as a simple turbomachinery system. It is suggested that hexahedral structure mesh, which has superior accuracy, is the most appropriate meshing scheme for stator-rotor internal flow systems [23]. Also, the hexahedral meshing scheme has better control over the boundary layer mesh at the near-wall region. The model near wall mesh quality is justified by two governing quantities: the dimensional wall distance Y^+ value and the aspect ratio. The Y^+ can be defined as:

$$Y^+ = \frac{u^* y}{\nu} \tag{2.1}$$

$$u^* = \sqrt{\frac{\tau_w}{\rho}} \tag{2.2}$$

where, u^* is the friction velocity at the nearest wall, y is the distance between the wall and first grid point, ν is the local kinematic viscosity of the fluid and τ_w is the shear stress on the wall. Y^+ is also used in the boundary layer theory in defining the law of wall. Y^+ is particularly crucial in modeling large gradient region. Y^+ of 30-200 is

suitable for high Reynolds flow with standard wall functions; where as for a low Reynolds flow condition, enhanced wall treatment is recommended. For enhanced wall treatment, Y^+ should not be more than 5 [24]. The aspect ratio is defined as the ratio of the length of the mesh element edges. The aspect ratio of the mesh element is suggested to keep below 4 by general rules of thumb.

The irregular, randomly fluctuating velocity fields in the fluid flow system are governed by time and ensemble average equation sets, which are known as turbulence models [25]. Examples are the Spalart-Allmaras model, *k-ε* models, k-*ω* models, Reynolds stress model (RSM) and Large eddy simulation model (LES). These turbulence models were developed individually to model different kinds of flow pattern and physics encompassed in the fluid flow systems. The Spalart-Allmaras model is a relatively simple one-equation turbulence model, which was designed specifically for aerospace and turbomachinery applications involving wall-bounded flows with adverse pressure gradients. However, the Spalart-Allmaras model is still relatively new and no claim is made regarding its suitability to all types of complex engineering flow. For instance, it failed to predict the decay of homogeneous, isotropic turbulence and is unable to rapidly accommodate changes in length scale.

In LES, large eddies in the turbulent flows are resolved directly with filtered Navier-Stokes equations, while small eddies are modelled by a subgrid-scale turbulence model. Eddy modelling is time-dependent and resolving the large eddies requires long flow time to obtain stable statistics of the flow. Therefore, the computational cost involved with LES is normally orders of magnitudes higher than that for other turbulence models, in terms of memory (RAM) and CPU time. High-performance computing is a necessity for LES and only suitable for industrial applications.

The RSM resolves the turbulent effects in the flow by solving transport equations for the Reynolds stresses, together with an equation for the dissipation rate, which requires seven equations for in 2D flows and nine equations are required for 3D flows. RSM takes into account most of the effect of different flow types, such as the effects of streamline curvature, swirl, rotation and rapid changes in strain rate in the flows. It is also useful for flow features of anisotropy in Reynolds stresses. Examples are

cyclone flows, highly swirling flows in combustors, rotating flow passages and stress-induced secondary flows in ducts.

The standard k-ε and k-ω models are the most commonly used turbulence models due to their robustness, economy and reasonable accuracy for a wide range of turbulent flows. Two equations are solved in these models to allow turbulent velocity and length scales to be determined independently. The standard k-ε model is a semi-empirical model based on model transport equations for turbulence kinetic energy (k) and its dissipation rate (ε). The model transport equation for k is derived from the exact equation while the model transport equation for ε is obtained using physical reasoning and bears little resemblance to its mathematically exact counterpart. The standard k-ε model is only valid only for fully turbulent flows.

The standard k-ω model is an empirical model based on model transport equations for the turbulence kinetic energy (k) and the specific dissipation rate (ω). The model incorporates for low-Reynolds number effects, compressibility and shear flow spreading in the flow modelling. As the k-ω model has been modified over the years, several production terms have been added to both the existing k and ω equations, which have improved the accuracy of the model for predicting free shear turbulent flows.

However, no single turbulence model is universally accepted as being the superior for all classes of problems. The choice of turbulence model depends on the fluid flow physics, established practices for specific classes of fluid flow, the level of accuracy and available computational resources and time constraint. In this research, three turbulence models, which are k-ε, k-ω and RSM models were used and compared with the experimental results. The results show that k-ε turbulence model is the most suitable one for 3-D axial flux machines modelling.

The computational simulation results are strongly influenced by the mesh sizes, the turbulence flow models and the boundary conditions applied. The primary means to assess the accuracy and reliability of the computational simulations is by verification and validation against other trusted models or experimentation. The process of

assessing the magnitude of the numerical errors, and the uncertainty in those error estimations is defined as CFD verification. In CFD verification, the accuracy of a computational solution is primarily measured relative to two types of highly accurate solutions: analytical solutions and highly accurate numerical solutions. It is assessed by conducting iterative and parametric convergence studies by using multiple solutions with systematic parameter refinement, to estimate the numerical errors and uncertainties [26-28]. On the other hand, the fundamental strategy of CFD validation is to assess the accuracy of the computational results by using benchmark experimental data, with quantified error and uncertainty estimates for both. A set of guidelines was proposed by William et al. [26] for designing and conducting validation experiments. New experimental procedures were suggested [26] for estimating experimental uncertainty, which have been proven more effective at estimating random and correlated bias errors than traditional experimental methods. Extensive research on validating self-developed and commercially available CFD codes has been conducted, e.g. [26-32] and most researchers claimed that the CFD numerical results show good agreement with experimental data, except for Casey [29], who claimed that, the most recent advanced turbulence models were not yet satisfactory for predicting the detail of unsteady turbulent flows that occur in extremely complex turbomachinery flows.

The CFD modelling technique has been used extensively by electrical machine manufacturers to perform the thermal analyses of electrical machines [30], cooling and air ventilation modelling [31], and the thermal managements of AC electrical motors [32]. However, this sophisticated CFD modelling involves complicated and time consuming processes, including geometrical meshing and iterative calculation processes. Depending on the application, some of the complex models may take up to several months, to obtain accurate numerical solutions. This makes it very difficult to use the CFD techniques to perform machine rapid optimisation analyses and parametric studies.

A feasible alternative to CFD modelling of the thermal state of electrical machines is the application of the advanced lumped parameter model (LPM) method. Instead of solving the heat conduction (Fourier) and convective heat transfer (Newton) equations

analytically to simulate the fluid temperature distribution inside the generators [33], the LPM approach described in [34-35], splits the electrical machines into a number of lumped components (or control volumes), which are connected to each other in the calculation scheme through thermal impedances to form thermal equivalent circuits. The temperature distributions inside the generators can be predicted by solving these thermal equivalent circuits. Several researchers have constructed and tested the thermal equivalent circuits of induction motors [36], radial flux generators [37-38] and stationary axial flux generators [39]. They concluded that the results of lumped parameter thermal equivalent circuit modelling are in good agreement with experimental data. Similar researches were conducted on radial flux electrical machines [40-43] but using a commercially available LPM thermal modelling tool, namely Motor-CAD [44].

However, one of the shortcomings of the LPM method employed in the previous work [34-43] & [45] is that the variation of the fluid temperature was neglected. For axial flux permanent magnet (AFPM) machines, which typically have narrow and long flow passages and relatively high air mass flow rate, the fluid temperature variation in the air gap has a substantial influence on the thermal state of the solid components. Lim et al. [46][1] proposed another technique of constructing the generic equivalent thermal circuit of AFPM generators, which takes into account the temperature change in the air flow. The proposed generic equivalent thermal circuit is able to model the heat flow paths in the axial and radial directions in the electrical machines. The heat flow path in the circumferential direction is relatively small as compared to the other two directions, and hence it was usually neglected [47]. Mellor [47] implemented the cylindrical conductive thermal circuit to model the conduction heat transfer in the solid components of electrical machines in both radial and axial directions.

For convective heat transfer modelling in electrical machines, convective thermal circuits were proposed [46]. Lim et al. [46] also suggested that that the accurate determination of the convective heat transfer coefficients at the machine surfaces is essential for obtaining reliable simulation results from the 2D lumped parameter thermal equivalent circuit. Convection heat transfer in several complex flow regimes

[1] Reference [45] is prepared by the thesis author

was investigated [48-53], however no suitable correlation was found for the application of 2D LPM thermal circuits of AFPM machines. Furthermore, all the surface heat transfer correlations examined in [48-53] use the ambient temperature as the reference temperature. In order to be applicable in the convective thermal circuit, correlations of surface heat transfer coefficient which are based on the local bulk air temperature are needed. Parametric studies of the convective heat transfer coefficients for AFPM generators were conducted by Airoldi [54]. The author applied a factorial design method [55-56], by performing CFD simulations on various sizes and geometries of AFPM generator, to develop empirical formulae that relate the local convective heat transfer coefficients with the machine geometrical parameters. The research presented in this thesis was performed interactively with Airoldi to obtain the convective heat transfer empirical formulae, which can be applied to the developed LPM thermal equivalent circuit. Experimental rigs were constructed and heat transfer coefficient measurements were carried out to validate the developed heat transfer coefficient empirical formulae.

2.2. Stator winding thermal resistance modelling

Hot spots in electrical machines usually take place in the stator windings, due to the resistive joule losses generated in the copper conductors and the low thermal conductivity of the winding filling and insulation. Therefore, to construct a complete 2-D equivalent LPM thermal circuit for AFPM machines, it is paramount to understand the thermal properties of the stator winding, and to represent the stator windings with appropriate thermal resistances and capacitances. The stator winding, which consists of a bundle of copper wire conductors and winding filler, has similar thermal properties to a two-phase mixture. A two-phase mixture is defined as two different substances, which consist of the continuous phase and discontinuous phase, which are mixed together but are not combined chemically, for example. reinforced concrete (mixture of cement and steel bars), epoxy fibre glass etc. Maxwell57], who pioneered the study of material thermal conductivity, derived an equation to predict the thermal conductivity of two-phase mixtures on the basis of potential theory. Since

then, a number of studies, for example [58]-[67] were conducted to develop analytical and numerical techniques for predicting the thermal conductivity of heterogeneous systems for specific materials and products. For example, Nieberlein [68] proposed a model based on particle to particle heat transfer to evaluate the thermal conductivity for epoxy-aluminum powder mixture. However, no general equation for calculating the thermal conductivity of two-phase materials was derived, until Tsao [69]. Tsao implemented the mean and standard deviation to model the distributions of the discontinuous phase in the continuous phase mixture and hence derived a semi-empirical equation for thermal conductivity prediction of two-phase mixtures. Cheng and Vachon [70] further improved Tsaos equation, by assuming parabolic distribution correlations of the discontinuous phase in the continuous phase mixtures, to circumvent the necessity of experimentally determining mean and standard deviation in the semi empirical equations.

Nevertheless, all of these studies [57-70] assumed that the two-phase mixtures are thermally isotropic and the heat only travels in one direction. The equivalent thermal conductivity of the stator winding, which has significant different thermal conductivities in the axial and radial directions, can not be calculated with those derived equations. Bousbane [71] and Mellor [47] separated the heat flow in the stator windings into two directions, which are the axial and radial directions, and modelled them individually. In the axial direction, since the thermal conductivity of the conductor is a lot higher than the thermal conductivity of the winding filler, the equivalent thermal conductivity in the axial direction of the stator winding was assumed to be equal to the thermal conductivity of the copper conductor, where the effect of the winding filler was neglected; In the radial direction, the stator winding was assumed as a homogenous solid which has a thermal conductivity of F_{kx} times that of the winding filling alone. F_{kx} is determined from experimental curves produced by Generic Electric [72], by estimating the percentage of conductor by volume in the stator excluding any winding filler regions.

This study extends Mellor's model [47] and circumvents the necessity of experimentally determining the stator winding radial thermal resistances. An analytical equation, which is a function of the conductor diameter, packing ratio,

conductor length and thermal conductivities of the conductor and winding filling, was derived to estimate the radial thermal resistance of the stator windings. Furthermore, the radial thermal resistance equation was improved, to take into account the resistive Joule loss in the stator winding conductors. When electric current passes through the conductor, the conductor transforms into an individual heat source distributing heat in the stator winding. Since the distribution of heat sources in the stator winding has a significant effect on the thermal state of the stator winding, another analytical model was developed, incorporating the radial distance of each heat source, to evaluate the equivalent radial thermal resistance of the stator windings. The radial thermal resistances calculated from the improved algorithm were verified with the results obtained from CFD models.

2.3. Reviews of Convection Heat Transfer Measurements

A convection heat transfer measuring experiment is required to obtain the local surface heat transfer coefficients in AFPM machines, to validate the numerical solutions predicted by CFD models. However, there is no instant device that can be used to measure energy and hence heat or heat flux directly. All of the heat flux experiments conducted by previous researchers [e.g. 73-128] were measuring the effect of heat transferred via a medium, or by spectral emissions. Childs et al. [73] and Rohsenow et al. [74] reviewed the available experimental techniques for heat transfer measurement, including: direct (or steady state) measuring methods, indirect (or transient) measuring methods and heat-mass analogy measuring methods. The authors concluded that there is no one method is suitable to all applications because of the differing consideration of accuracy, sensitivity, size, cost and robustness. All the available heat transfer measuring methods were reviewed, and the feasibility of each measuring method was evaluated for the AFPM machine heat transfer measurements.

2.3.1. Direct Heat Transfer Measuring Method: Heat Flux Sensor

Direct heat transfer measuring methods involve the measurement of the local surface heat transfer in the steady state system. One of the most commonly used devices for direct heat transfer measurement is the thin film heat flux sensor. Thin film heat flux sensors measure the temperature differences between two or several location within a thermal insulation material with known thermal properties, to determine the local heat flux via Fourier's one dimensional law of conduction equation. The temperature difference between the top and bottom of the insulation layer can be measured by thermopiles formed by a number of thermocouple junctions. This method was first reported by Martinelli et al. [75] and more advanced thermopile design was presented by Hartwig et al. [76].

The calibration of the heat flux sensor is essential in order to acquire accurate heat flux measurements. When the heat flux sensor is affixed to a solid surface, the presence of the sensor disrupts the geometric surface profile and the thermal conditions due to the mismatch of thermal properties. Flanders [77] suggested that the overall error due to surface profile disruption is the order of 10 per cent. The modifications of thermal boundary conditions due to the presence of heat flux sensor were also described by Dunn et al. [78]. He highlighted the necessity to re-calibrate the entire heat flux sensor with the similar boundary conditions. The heat flux sensor calibration can be carried out by mounting the sensor on a good thermal insulator medium, with a known heat source at the other end. However, the calibration factor is strongly influenced by the wind or moving fluid above the sensors. Danielsson [79] found out that the influence of wind on the calibration value is greatly reduced when the sensor is attached to a surface with lower thermal conductivity. Alternatively, the sensors can be calibrated against a well-defined convection correlation, such as for jet impingement [80-81]. In this technique, the sensor is mounted on the surface, which is exposed to a fluid jet of known geometry and flow conditions. Subsequently, the electrical signal generated in the sensor is calibrated by using the jet impingement convection correlations developed.

2.3.2. Direct Heat Transfer Measuring Method: Gardon Gauge

Another device that can be used to measure the steady state heat transfer is the Gardon gauge [82-83]. The Gardon gauge comprises of a thin disk, connecting to a heat sink at its periphery edge (Fig. 2-1). As the surface is heated (or cooled) by the flow above it, the heat is conducted from disk radially to the heat sink at the edge of the disk. The Gardon gauge implements the principle, that the instantaneous heat flux is proportional to the electrical voltage between the centre of the plate and the copper heat sink, as shown in equation (2.3), to measure the surface heat fluxes.

$$q = \frac{4Lk\Delta T}{R^2} \tag{2.3}$$

Where L = thickness of the thin-foil constantan disk, m,

k = Thermal conductivity, W/mK,

R = radius of the thin-foil constantan disk

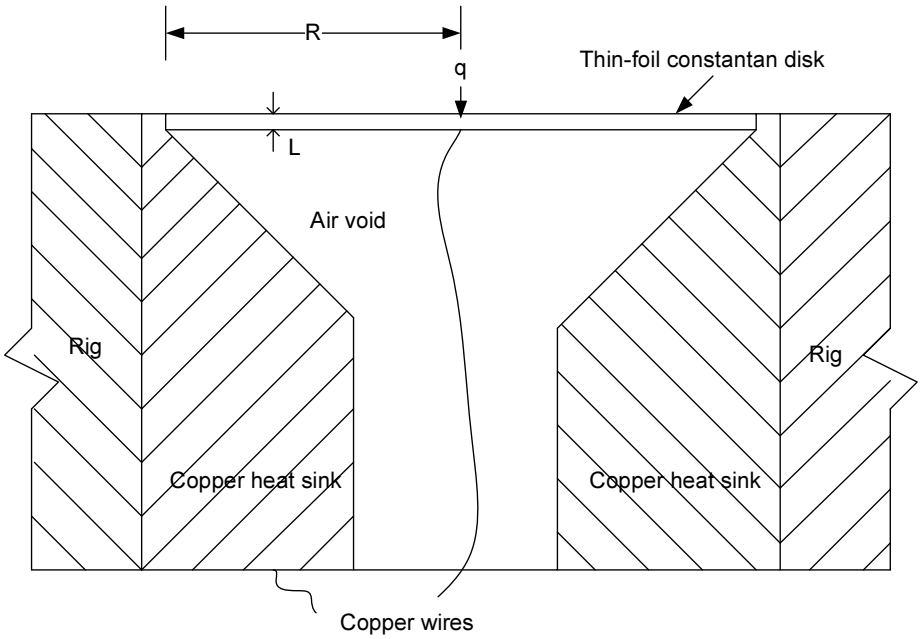

Fig. 2-1. Gardon gauge geometry

However, Gardon gauges are only suitable for radiation heat transfer measurements. Kuo et al. [84] confirmed that for systems, where convection heat transfer is significant, large errors were found, due to the non-uniformities in the foil temperature. Hence, correction ratios were introduced by Kuo et al. [84] to off-set these experimental errors. Water-cooled Gardon gauges were introduced by the Vatell Corporation to provide accurate heat flux readings for conduction and convection heat

transfer measurements. However, the cost of these water-cooled Gardon gauges is extremely high, and they are complex to use. Also, they are not suitable for rotating surface measurements because of the complex water pumping and circulation systems that are required for the water-cooled Gardon gauges.

2.3.3. Direct heat transfer measuring method: Energy supply technique

This technique measures surface convective heat transfer coefficients by measuring the temperature on one side of the solid surface, while actively providing heat on the other side of the solid. Heat transfer coefficient is defined by heat flux per unit temperature increase. Hence, by controlling the electric power supply of the heating devices, and by measuring the surface temperature, the surface heat transfer can be evaluated. Controlled heating of the solid surface can be achieved by means of electric heater strips, silicon heater mats or printed circuit boards [87], with the integration of the feedback control circuits to the power supply. For most of the applications, the front side of the heater device is attached on the solid surface by high temperature resistance industrial glue or epoxy resin, whereas the back side of the heater is thermally insulated by low thermal conductivity materials, such as clear plastic, or fibre glass.

The surface temperature on the other side of the solid can be measured by commercially available thin film thermocouples, resistance temperature devices (RTD), or thermal liquid crystal. However, due to the low response time of the heater and the thermal capacity of the solid subjects, this method is only suitable for steady state heat transfer coefficient measurements [73]. High errors may incur for transient heat transfer measurements.

The energy supply heat transfer convection measurement technique has been used by Rule et al. [85], Radhakrishnan et al. [86] and Howey et al. [87]. Rule constructed a microscale heater array comprising of 96 platinum array heater elements having a dimension of 2.7mm x 2.7mm, deposited on a quartz substrate to measure time and space-resolved heat transfer in a boiling process. The heaters were each controlled by

a Wheatstone bridge circuit with op-amp feedback and digital potentiometer, allowing heater temperature to be controlled. On the other hand, Howey combined heat flux measurement and temperature sensing into one single device, which is a printed circuit board (PCB) with 14 concentric spiral shaped copper heater elements. Since the copper resistance varies with temperature, the surface temperature was measured directly by measuring the copper resistances on the PCB. The PCB copper heater elements were affixed to the stator surface of a rotor-stator disk system, to measure the stator surface heat transfer coefficients and temperature profiles.

2.3.4. Direct Heat Transfer Measuring Method: Refractive Index Method

The local refractive index of transparent materials, such as Acrylic, varies with the temperature gradient across the material. Hence by measuring the refractive index of the transparent material with the use of optical techniques, such as schlieren, shadowgraph and interferometry, the heat flux across the solid surface can be evaluated. This method was reviewed by Goldstein [88] in detail. Owing to the complexity of the optical measurement techniques, it is not applicable for measuring surface heat transfer in narrow gaps and complex geometries.

2.3.5. Transient (or indirect) heat transfer measurement techniques

Transient heat transfer techniques involve the measurement of the rate of change of temperature with time at a location near to or on the surface of interest. The surface heat flux is quantified by applying the appropriate forms of heat conduction and heat balance equations with accurate knowledge of the material properties. Several temperature measuring devices, such as capacitance calorimeters, thin film sensors, thermal liquid crystal, and infra red camera, have been used to measure the transient heat transfer coefficient based on this principle.

Capacitance calorimeters measure the instantaneous heat transfer rate into a surface, by measuring the rate of change in thermal energy of an element embedded inside the

solid surface. A typical capacitance calorimeter comprises of a cylindrical slab which is thermally insulated from its surroundings (Fig. 2-2). The cylindrical slab in the middle of the capacitance calorimeter is usually manufactured from high conductivity, chemically stable metal, such as copper, aluminum nitride or titanium insulation. Thermocouples are attached to the bottom of the cylindrical slab material and the heat flux into the calorimeter is determined by the electric signals obtained from the thermocouples. When the capacitance calorimeter is directly exposed to a convective flow, the heat transfer coefficient can be determined by equation (2.4), provided the thermal properties of the surface are known.

$$\frac{T - T_\infty}{T_0 - T_\infty} = e^{-\frac{t(hA)}{mc_p}} \tag{2.4}$$

Where T_∞ = Cylindrical slab temperature at steady state, K

T_0 = Cylindrical slab temperature at initial state, K

t = Time, s

A = Surface area, m^2

m = Mass of the cylindrical slab, kg

C_p = Specific heat capacity, $J/(kg.K)$

h = Heat transfer coefficient, W/m^2K

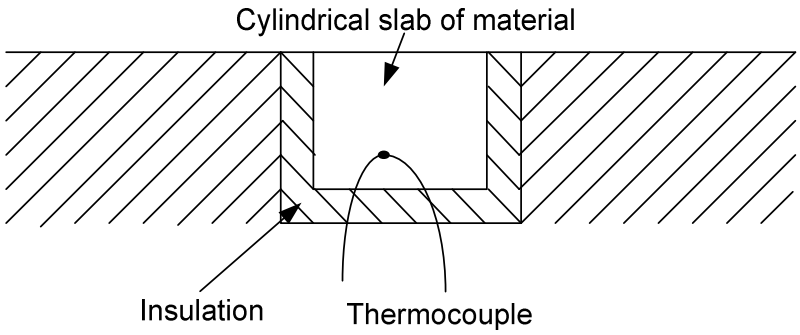

Fig. 2-2. Thermal capacitance calorimeter

Capacitance calorimeters are normally used for constant energy input to the surface and they are only applicable for short exposure measurements: the duration is limited by the time when the temperature of the cylinder slab reaches its steady state. The standard method for operating the capacitance calorimeters, their design parameters and their limitations are documented at ASTM E457-96 [89]. Owen [90] applied the capacitance calorimeter method to determine the heat transfer for a copper sphere

experiencing condensation and evaporation. The main disadvantage of this form of device, particularly when measuring with large heat fluxes, is the disruption to the thermal boundary layer, due to the thermal discontinuities introduced by the sensor material boundaries. Also, it is impossible to evaluate the heat losses through the insulation layers.

Another transient heat transfer measurement is achieved by measuring the one dimensional thermal pulse penetration into the surface of interest. Typically, the applications of this form of heat flux measurement are in short duration hypersonic facilities [91] and blow down turbomachinery experiments [92]. In this transient state experiment, only one parameter is measured, which is the surface temperature history, to evaluate the experimental convection heat transfer coefficient, see equation (2.5)

$$\frac{\left(T_s(t)-T_{initial}\right)}{\left(T_{aw}-T_{initial}\right)}=1-\exp^{\beta^2}\cdot erfc(\beta), \tag{2.5}$$

where $\beta=\dfrac{h\sqrt{t}}{\sqrt{\rho c_p k}}$

T_s = Surface temperature, K

T_{aw} = Adiabatic wall temperature, K

ρ = Density of the solid surface, kg/m^3

k = Thermal conductivity of the solid surface, W/K

However, it is difficult to determine the wall surface heat transfer coefficient by equation (2.5), since the local adiabatic wall temperatures, T_{aw}, in most of the experiments are unknown. A new method of temperature data processing was introduced by Wang [93] to evaluate both the transient heat transfer coefficient and the local adiabatic wall temperatures in the experiments. In equation (2.5), the heat transfer coefficient, h, and wall adiabatic temperature, T_{aw}, are related to the surface temperature history, $T_s(t)$. Hence, theoretically if the correct combination surface heat transfer coefficient and wall adiabatic temperature are applied into equation (2.5), the surface temperature history predicted by equation (2.5) would be the same as the surface temperature history recorded from the experiments. Wang applied this principle and introduced the minimal root mean square regression method to obtain

the combination values of these two parameters accurately, by ultilising the full surface temperature measured from the experiments.

Transient heat transfer experiments on a flat plate using a propane air burner were conducted by Talib [94], by using the regression analysis method introduced by Wang [93]. Furthermore, Talib investigated accuracy of the regression method with multiple steps change in gas temperature. The experimental results showed that, by increasing the gas temperature step from one to four, the maximum experimental uncertainty has reduced from 27% to 9%. This demonstrates that by applying the multiple temperature steps technique in the regression analysis method, it has potential to reduce in the experimental uncertainties in measurement of surface heat transfer coefficient and adiabatic wall temperature.

There are several techniques available to measure the temperature history on the surface of interest. One of the most popular ways is by using the thin-film thermocouple. The thin-film thermocouple is physically small, of the order of one micrometer thick, and it has minimal disruption to the surface thermal boundary and flow condition on top of the surface of interest. In addition, the thin-film thermocouple has swift response to thermal condition due to its low thermal capacitance. Nevertheless, to evaluate the surface heat transfer coefficients accurately by the principles outlined in equation (2.5), material properties in terms of the product of $\rho c_p k$ of the solid surface and thin-film thermocouple are required for the sensor calibration process. Procedures for obtaining the product of $\rho c_p k$ values of the thin-film sensor were demonstrated by Doorly [95]. The possible experimental errors associated with the effect of thin film thermocouple in the transient heat transfer coefficient measurement and its corresponding correction ratios were documented by Schultz et al. [96].

Alternatively, thermal liquid crystals (TLC) have become increasingly popular for surface temperature measuring experiments in the last decade. Liquid crystal molecular structure is intermediate between a crystalline solid and an isotropic liquid. It possesses some of the mechanical properties of a liquid and the optical properties of crystalline solids. The cholesteric (or nematic) structure of liquid crystal is optically

active and reacts to changes in temperature. The details of the cholesteric structure of liquid crystal can be found in [97]. Davenport [98] and Ireland et al. [99] are those pioneers who started using thermal liquid crystal for surface heat transfer measurements on turbomachinery and aerodynamic applications. The fundamentals of liquid crystal measurements of heat transfer were reviewed by Jones et al. [97] and Ireland et al. [100].

Transient heat transfer tests by using TLC offer full coverage data from a single test and can produce high resolution data by using multiple narrow-band TLCs [101]. In transient heat transfer experiments, the solid surface coated with TLC is typically illuminated from a diffuse source and the reflected light is monitored and recorded by a colour CCD camera. It was shown by Camci et al. [102] and Akino et al. [103] that hue component of the colour video signal from the TLCs recorded during heat transfer experiment can be accurately calibrated to the surface temperature. Most importantly, hue-temperature calibration is independent of the strength of illumination from the TLC. Wang [93] demonstrated a sophisticated video recoding system to enable the complete continuous hue history recording during heat transfer experiments for transient surface heat transfer coefficients evaluation. Later, Ling et al. [104] claimed that hue-temperature calibration was problematic due the camera viewing angle, lighting and internal reflections. Therefore, Ling concluded that the temperature calibration by mean of colour intensity is better for transient experiments. Due to the robustness of TLC, it also was applied in several steady-state heat transfer experiments by numerous researches, for example Ouden et al. [105], Cooper et al. [106], Baughn et al.[107], Lucas et al.[108] and Sargison et al. [109].

Harmand et al. [110] and Mori [111] introduced the use of the infrared camera to measure the surface temperature on a matt coated rotating disc, to evaluate the convective heat transfer coefficients on the corresponding surface of interest. All materials continuously absorb and emit electromagnetic waves by raising and lowering their molecular energy levels (by heating or cooling the substance). Therefore, the infrared camera which measures the intensity and wavelengths of emission from the surface of interest can be applied to determine the surface temperatures. The merit of using the infrared camera is its capability to cover the

complete surface, allowing global temperature distributions to be found. Yet, the optical access is essential. Special anti-reflective coated windows would be required for taking infrared images inside the generator. This would be become an issue as the maximum diameter of the anti-reflective coated window that can be manufactured is limited to 300mm (quoted from Hawk IR International Ltd.).

Baugh et al. [112] conducted convective heat transfer coefficient measuring experiments on a pin fin in a duct by using both the steady and transient state methods. They concluded that both the measuring methods compared well at stagnation regimes. On the other hand, Critoph [113] used the radiant heating method with liquid crystal thermography to measure the local heat transfer coefficient on the plate fins used in the plate fin tube heat exchangers. He claimed that either steady state or transient tests may be used to derive heat transfer coefficients, but they were not comparable if the heat transfer coefficients calculated were based on the inlet air temperatures as the reference temperatures. Butler [114] investigated the effect of thermal boundary conditions on the transient heat transfer measurements on a flat plate. He found that the transient method produced heat transfer coefficients that were lower in uniform temperature boundary conditions, and higher in the uniform heat flux boundary conditions then the steady state measuring methods, in the same flow condition. These results indicated the importance of thermal boundary conditions in the transient heat transfer coefficient measuring method.

2.3.6. Heat and Mass Transfers Measurements: Naphthalene Sublimation Methods (NSM)

In many heat transfer experiments, it is often difficult to measure high resolution local heat transfer coefficients, especially when the temperature changes rapidly over small regions resulting in large wall conduction errors, and on rotating or moving surfaces, where bulky remote sensors are used. On the surface of highly volatile materials, such as Naphthalene, the surface heat transfer coefficient can be determined with good confidence by measuring the mass transfer, via a well developed heat-mass analogy [115-116]. The Naphthalene sublimation method (NSM) works by measuring the

naphthalene surface profile coated on the specimens by using a high precision linear variation differential transformer (LVDT), before and after conducting the experiments, to deduce the local heat transfer coefficients. Also, the NSM has been used, by several researchers [117-122] to measure local surface heat transfer coefficients on moving parts such as rotating disks, cylinders, cavities and annular fins, to circumvent the inherent problems of maintaining electrical connections between fixed and rotating parts.

NSM is able to produce good experimental measurements, provided accurate values of the Naphthalene properties are available to be applied into the heat and mass analogy. The basic properties, such as the density of the solid, saturated vaporized pressure, mass diffusion coefficient in air etc, were carefully measured and quantified by Kudchadker et al. [123] and Dean [124]. The accuracy of the heat transfer coefficient evaluated from NSM is governed by the heat and mass transfer analogy, and the corresponding thermal boundary conditions. The basic heat and mass transfer analogy is the Colburn $(Sc/Pr)^n$ analogy (equation (2.6)) and its fundamental principles were described in detail by Eckert [115] and Eckert et al. [116]. However, Lewis [125] showed that the mass and heat transfer coefficient can be related more accurately using a stricter treatment rather than the simple Colburn $(Sc/Pr)^n$ analogy. Lewis demonstrated a new analogy expression derived from universal velocity profiles in a turbulent boundary layer. For flow over a flat plate, von Karman [126] has given the analytical correlation of equation (2.7) and Petukhov [127] has presented a theoretically based correlation, equation (2.8), for a smooth tube wall. Nevertheless, these analogies were derived for only for isothermal and adiabatic wall boundary conditions.

Colburn $(Sc/Pr)^n$ heat and mass transfer analogy,

$$\frac{Nu}{Sh} = \left(\frac{\mathrm{Pr}}{Sc}\right)^n \tag{2.6}$$

For Flow over a flat plate by von Karman [126],

$$St = \frac{1.6(\ln \mathrm{Re})^{-2.584}}{1+1.265(\ln \mathrm{Re})^{-1.29}\left[5\,\mathrm{Pr}+5\ln(5\,\mathrm{Pr}+1)-14\right]} \tag{2.7}$$

For Flow over a smooth tube wall by Petukhov [127],

$$St = \frac{\left[2.236\ln(\mathrm{Re})-4.639\right]^{-2}}{1+27.2\left[2.236\ln(\mathrm{Re})-4.639\right]^{-2}+\dfrac{\left(11.7+\dfrac{1.8}{\sqrt[3]{\mathrm{Pr}}}\right)\left(\mathrm{Pr}^{\frac{2}{3}}-1\right)}{2.236\ln(\mathrm{Re})-4.639}} \tag{2.8}$$

The heat transfer coefficients obtained from NSM are time-averaged values. The heat transfer measured includes the transient effect, for example, before the experiment reaches its steady state. Therefore, NSM results in high experimental errors for low-velocity flow, for which the run times exceed two hours [128]. Also, due to the saturated naphthalene vapor pressure, the technique is highly sensitive to fluid temperature variations and the aerodynamic and viscous heating effect in high velocity flows. Therefore, NSM is not recommended for use for flow velocity higher than 30m/s [128]. NSM was reviewed in detail by Goldstein [128]. The author claimed that the NSM experimental uncertainty within a 95% confidence interval was 7% and it was mainly due to the use of inaccurate Naphthalene properties.

2.3.7. Conclusions

Three distinct types of heat transfer coefficient measuring method were reviewed in this section, which are the direct steady state method, the indirect transient method and the heat-mass transfer analogy method. Due to experimental and financial limitations, the heat transfer measurement technique which was implemented for this research was the thin-film heat flux sensor direct steady state method. Through-bore slip rings were used to obtain temperature and heat flux measurements on rotating surfaces. To eliminate the high frequency noise caused by the slip rings, signal amplification circuits were implemented (see section 7.3).

Chapter 3

2-D lumped parameter model

3.1. Introduction

Extensive computational fluid dynamics (CFD) codes have been developed in the past few decades to estimate velocity field, temperature and heat transfer in both external and internal flows. However, those CFD codes consume a great deal of computational resources and time to obtain reasonably accurate solutions. In this chapter, an advanced lumped parameter model is developed for axial flux permanent magnet (AFPM) generators, which is capable of reducing the numerical calculation effort necessary for CFD in machine design from days into minutes. Ideally, the developed lumped parameter model will replace the general CFD code in the AFPM machine design process.

The lumped parameter technique models the process of heat transfer in an electrical machine by constructing an equivalent thermal circuit. Electrical machines are subdivided into basic elements and each basic element is identified by a node in the equivalent thermal circuit. By knowing the thermal properties of the materials used in the electrical machine, the corresponding thermal impedances, thermal capacitances and heat sources of each machine component can be calculated and applied into the equivalent thermal circuit, to predict the air and surface temperature rises in the real

electrical machine. Additionally, those thermal impedances are derived from entirely dimensional information of the electrical machine. Hence, the same thermal equivalent thermal network can be easily adapted to a range of machine sizes, boundary conditions and configurations.

3.2. Theory

The lumped parameter model works by transforming the heat flow paths in the real electrical machine into a thermal equivalent circuit. The thermal equivalent circuit is fundamentally an analogy of an electrical circuit, in which Heat, *q (W)*, is analogous to Current, *I (Amps)*; Temperature difference, *ΔT (K)*, is analogous to voltage difference, *ΔV (v)*; and thermal resistance, R_t *(K/W)*, is analogous to electrical resistance, *R (Ohm)*. Those thermal resistances are defined differently for conduction, convection and radiation.

For conduction, the thermal resistance depends on the thermal conductivity of the material, *k*, the length, *l*, and cross-sectional area, A_d, of the heat flow path and may be expressed as:

$$R_d = \frac{l}{A_d k} \tag{3.1}$$

The thermal conductivity resistance calculated from equation (3.1) is derived from the one dimensional heat flow equation. It assumes that the heat flow is uni-directional and the thermal conductivity *k*, is constant all along the length *l*.

For convection, thermal resistances for forced convection are defined as:

$$R_c = \frac{1}{A_v h} \tag{3.2}$$

Where A_v is the surface area of convective heat transfer between two regions and *h* is the convective heat transfer coefficient. The convection heat transfer coefficient is a function of the flow condition and geometries. Hence, it may change for different

flow channels inside the machine. In particular, the heat transfer coefficient for flow across a flat plate can be expressed as:

$$Nu_x \equiv \frac{h_x X}{k_f} = 0.332\,\mathrm{Re}_x^{1/2}\,\mathrm{Pr}^{1/3} \tag{3.3}$$

Where X is the distance from the leading edge and X=0 at the leading edge, k_f is the fluid thermal conductivity, Re_x is the flow Reynolds number at position X, and Pr is the flow's Prandtl's number.

The thermal circuit for the steady state simulation consists of thermal resistances and heat sources connected between motor component nodes. For transient analysis, the thermal capacitances are used in the thermal circuit, to account for the change of internal energy in the various parts of the machine with time. The heat capacitance is defined as:

$$C = \rho V c_p = m c_p \tag{3.4}$$

Where c_p is the specific heat capacity of the material, ρ is the density, and V and m are the volume and mass of the material respectively.

Radiation heat transfer in the generator is generally small and hence it is neglected in this model.

Fig. 3-1(a) and 3-1(b) show a sectional view of an axial flux permanent magnet generator (with slot-less stator) and its equivalent 1-D thermal circuit, respectively. In Fig. 3-1(a) the machine is subdivided into five lumped components, which consists of the stator, the winding, the air gap, the permanent magnet and the rotor disks. These five lumped components are interconnected with corresponding thermal conductive resistances ($R_{d1\text{-}d4}$), convective resistances ($R_{c1\text{-}c9}$) and capacitances (C). The heat source terms, P_{eddy}, $P_{winding}$ and P_m in Fig. 3-1(b), stand for eddy current losses in the stator, winding losses and losses in the magnet, respectively. By applying Kirchoff's first law to the 5-node thermal network shown in Fig. 3-1(b), the steady state results can be represented in a matrix equation form as shown below:

$$[G']\times[\theta]=[Q] \tag{3.5}$$

Where $[Q]$ is the power source vector, $[\theta]$ is the temperature vector and $[G']$ the network admittance matrix which is formed by the thermal resistances and capacitances.

Hence, the temperature at each of the node can be obtained by inverting equation (3.5), that is,

$$[\theta]=[G']^{-1}[Q] \tag{3.6}$$

Equation (3.6) is solved automatically by using a commercially available system circuit solver, *Portunus*[2]. By constructing the thermal equivalent circuit of the electrical machine and specifying the corresponding magnitude of each thermal resistance in *Portunus*, the network admittance matrix, [G'], of the machine is constructed automatically and hence the temperature at each node is calculated. All of the thermal circuits shown in this thesis were solved by using *Portunus*.

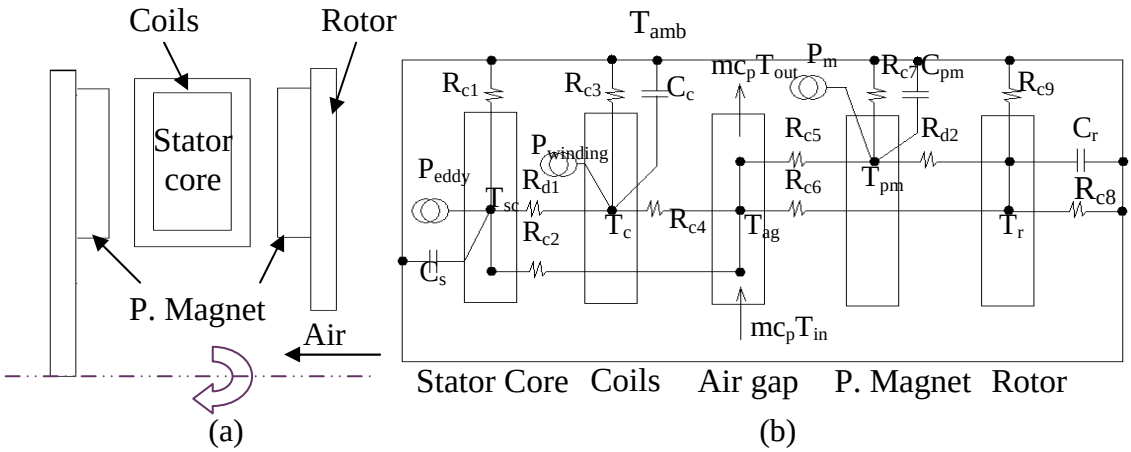

Fig. 3-1: Thermal resistance circuit of an AFPM with slot-less stator.

This chapter describes and discusses the construction of the 2-D conductive thermal network for the AFPM generator and how it is coupled with the convective thermal circuits. The "2-D" in this study refers to the heat flow in two directions, which are in

[2]http://www.cedrat.com/en/software-solutions/portunus.html

the radial and axial directions. The heat flow in circumferential direction is ignored. The effects of different levels of node discretisation are also investigated, to find the best compromise between the simplicity of the model and the accuracy required of the simulations. Finally, several example cases are tested, to validate the accuracy of these lumped parameter models compared with experimental and conventional CFD results.

3.3. 2-D Thermal Equivalent Circuit of AFPM Generator

The thermal circuit shown in Fig. 3-1 indicates a 1-D thermal network of the AFPM generator [35-37]. In the 1-D thermal circuit, the heat fluxes in the generator are assumed to travel in one direction only, i.e. heat fluxes (in both the axial and radial directions) generated from the stator are summed and represented by one total heat flux. Consequently, one mean temperature is used to represent the whole stator. However, problems occur when predicting the highest surface temperature for laminated stators, which have different thermal conductivities in the axial and radial directions. The mean temperature predicted in the 1-D circuit is far below the highest temperature of the stator. Hence, it is necessary to look for a more sophisticated 2-D thermal network to replace the existing 1-D thermal network.

To generate a 2-D thermal equivalent circuit, the electrical machine is subdivided into a number of annuli, as shown in Fig. 3-2. Both the generator's windings and magnets are simplified into annuli (instead of separated circular arc sections). As a result, the AFPM generators are axisymmetric and can be modelled with a 2-D thermal network. Several assumptions are made for modelling the AFPM generators with the 2-D thermal network. These assumptions are:

- Slotted stator winding.
- The inter-magnet and inter-winding grooves are relatively small compared with the magnet and stator circumferential widths.
- The magnet and winding thickness are small relative to size of the air gap.

For electrical machines with large inter-magnet and inter-winding grooves, additional cooling effects occur in the circumferential direction. Since the 2-D thermal circuit neglects the heat flow in circumferential direction, the temperatures predicted on the magnet and stator surfaces may have significant errors. However, the model can be improved by using the angle-weighted heat transfer coefficients on the magnet and stator surfaces in the thermal equivalent circuit. When the generator rotates, the heat transfers on the magnet's and stator's surfaces fluctuate continuously and periodically, like a Sinus wave. Therefore, by using the angle-weighted heat transfer coefficient average as a representation of the fluctuating heat transfer coefficient on the magnet and stator surfaces, the discrepancy due to the additional cooling effects on the inter-magnet and inter-winding grooves can be minimised.

In general, the 2-D equivalent thermal circuit of AFPM generators consists of two sub-circuits, which are the conductive thermal circuit and the convective thermal circuit. Both sub-circuits are interconnected with each other and work iteratively to predict the air and solid surface temperatures in the machines.

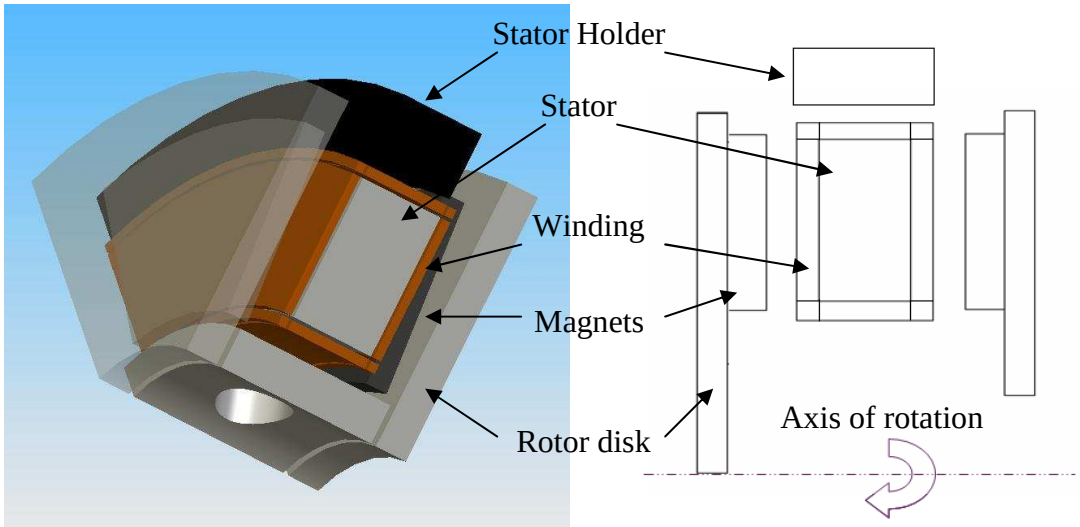

Fig. 3-2. 3D (a) and 2D (b) views of an axisymmetric axial flux permanent magnet generator.

3.3.1. 2-D Conductive Thermal Circuit

In the 2-D conductive thermal network of an AFPM generator, conductive heat in the machine is assumed to travel in the axial and radial directions only. The heat flow in the circumferential direction is small and can be neglected. To obtain simple, but physically significant expressions of the thermal resistances that describe the heat conduction across the generator components, the following assumptions are made.

- Heat flows in the radial and axial directions are independent.
- A single mean temperature defines the heat flow both in the radial and axial directions in the control volume.
- The thermal capacities and heat generations in the control volumes are uniformly distributed.

The 2-D conductive thermal network of the AFPM generator is built based on the general annulus/ring component as shown in Fig. 3-3(a). For an annulus of length L, with inner and outer radii, r_1 and r_2, axial and radial thermal conductivities k_a and k_r respectively and internal heat generation/loss q per unit volume, it can be represented by two separated, three terminal networks, which are the axial terminal network (left hand side of Fig. 3-3(b)) and the radial terminal network (right hand side of Fig. 3-3(b)).

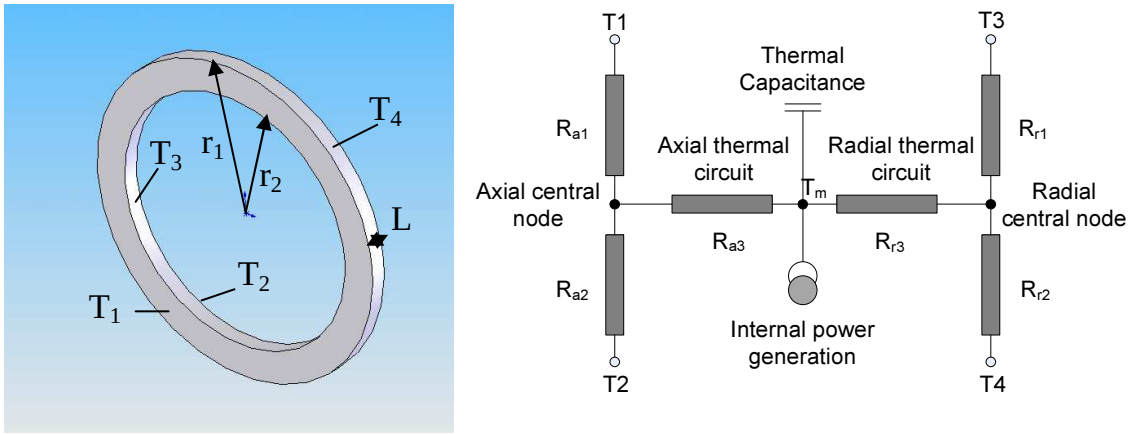

(a) (b)

Fig. 3-3. 2-D Thermal circuit of annulus solid.

In each network, two of the terminals represent the surface temperatures of the annulus (for e.g. T1 is the temperature on the annulus front surface; *T2* is the annulus back surface temperature etc), whereas the third represents the central node (Fig. 3-3).

The central node of each network would give the mean temperature of the component if there were no internal heat generation or thermal storage. The superposition of the two circuits at node T_m, with the internal heat generation and thermal capacitance requires the additional thermal resistance R_{a3} and R_{r3}. Details of the derivation of R_{a3} and R_{r3} can be referred to Sectopm 5.2.1 or [35]. It can be noticed that both R_{a3} and R_{r3} are negative resistance. Hence is shows that the mean temperature of annulus is lower than the temperature at the centre nodes of the separated radial and axial thermal circuit alone, see equation (3.9) and (3.12). These values of the thermal resistances in each network are derived directly from the independent solutions of the heat conduction equation in the axial and radial directions [35, 129]. These are given in terms of the dimensions of the annulus and its axial and radial thermal conductivities k_a, k_r, by the following expressions:

$$R_{a1} = \frac{L}{2\pi k_a \left(r_1^2 - r_2^2\right)} \tag{3.7}$$

$$R_{a2} = \frac{L}{2\pi k_a \left(r_1^2 - r_2^2\right)} \tag{3.8}$$

$$R_{a3} = \frac{-L}{6\pi k_a \left(r_1^2 - r_2^2\right)} \tag{3.9}$$

$$R_{r1} = \frac{1}{4\pi k_r L}\left[1 - \frac{2r_2^2 \ln\left(\frac{r_1}{r_2}\right)}{\left(r_1^2 - r_2^2\right)}\right] \tag{3.10}$$

$$R_{r2} = \frac{1}{4\pi k_r L}\left[\frac{2r_1^2 \ln\left(\frac{r_1}{r_2}\right)}{\left(r_1^2 - r_2^2\right)} - 1\right] \tag{3.11}$$

$$R_{r3} = \frac{-1}{8\pi\left(r_1^2 - r_2^2\right)k_r L}\left[r_1^2 + r_2^2 - \frac{4r_1^2 r_2^2 \ln\left(\frac{r_1}{r_2}\right)}{\left(r_1^2 - r_2^2\right)}\right] \tag{3.12}$$

By applying the annulus thermal circuit as the basic circuit, with the corresponding thermal resistances, the conductive circuit of the full generator was constructed, as

illustrated in Fig. 3-4. Each generator component is represented with an annulus conductive circuit, and is connected in such way that it is physically connected in the real machine. Thermal contact resistance, which is defined in equation (3.13), is introduced in between the two temperature terminals of each contact component, to take into account the temperature drop on each contact interface.

$$R_c = \frac{1}{A_c h_c} \tag{3.13}$$

Where A_c is the surface area of contact between two solid and h_c is the thermal contact conductance coefficient.

The heat transfer between the air and the generators components is usually dominated by the convective heat transfer when the generator is rotating. To complete the 2-D thermal circuit of the AFPM generator, a fluid flow circuit is introduced to take into account of the convective heat transfer between the air and the solid components of the generator. It is further discussed in the following section.

3.3.2. 2-D Convective Thermal Circuit

Convective heat transfer describes the energy transfer between the solid surface and the fluid moving over the surface. Normally, for working fluid such as air, the convective heat transfer dominates the heat transfer in the electrical machine. Hence it is important to develop a 2-D convective thermal circuit that works interactively with the conductive circuit, to provide accurate temperature prediction for rotating electrical machines.

The 2-D convective thermal circuit works by transforming the energy balance equation into the thermal network, to determine how the fluid temperature varies with the distance travelled and to relate the total convective heat transfer with the change of fluid temperature. Two distinctive convection heat transfer modelling methods are discussed, which are the Temperature passing method (TPM) and Heat pick-up method (HPM). TPM is developed by the author based on the energy conservation

equation whereas HPM is the convection heat transfer modelling method introduced by previous researchers [130]. The nature and accuracy of these two modelling methods are investigated and tested with case studies.

3.3.2.1. Temperature Passing Method (TPM)

The TPM convective thermal circuit works by splitting the air domain inside the AFPM generator into a number of control volumes. By considering the energy balance equation, each of the air control volumes can be represented as a separate thermal circuit. Fig. 3-4 shows an example of an internal fluid flow in a pipe.

Assume that the air moves at constant flow rate, $\dot{m}$, from the inlet (at left hand side), and is heated from T_{in} to T_{out} by the inner pipe wall.

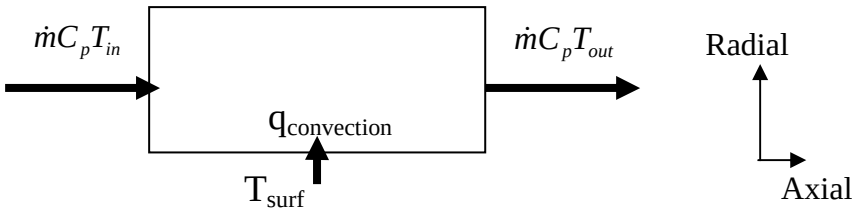

Fig. 3-4. Control volume of an internal fluid flow in a pipe.

By neglecting the heat transfer by conduction in the axial direction, the heat transfer from the inner pipe wall by convection, heats the fluid from T_{in} to T_{out}, and can be expressed as:

$$q_{convection} = hA\left(T_{surf} - \left(\frac{T_{in} + T_{out}}{2}\right)\right) = \dot{m}C_p\left(T_{out} - T_{in}\right) \tag{3.14}$$

Assume that the temperature change across the pipe flow is small, hence equation (3.14) can be simplified to:

$$q_{convection} = hA\left(T_{surf} - T_{in}\right) = \dot{m}C_p\left(T_{out} - T_{in}\right) \tag{3.15}$$

Arranging equation (3.15), the fluid temperature at the outlet, T_{out}, can be written in terms of $q_{convection}$, with known boundary conditions of T_{in}, $\dot{m}$ and c_p, at the inlet.

$$T_{out} = \frac{q_{convection}}{\dot{m}C_p} + T_{in} \tag{3.16}$$

From equation (3.16), in order to calculate the outlet temperature, T_{out}, the exact amount of convective heat transferred into the fluid, $q_{convection}$ is required. Equation (3.15) is rearranged as illustrated in equation (3.17), so that the air control volume convection heat transfer can be represented as a simple thermal circuit, as shown in Fig. 3-5, where *1/hA* is the convective thermal resistance. Hence, the $q_{convection}$ can be evaluated from the simple thermal circuit. By substituting the $q_{convection}$ obtained from the thermal circuit into equation (3.16), T_{out} can be predicted if both inlet temperature, T_{in} and air specific heat capacity, *Cp*, are known.

$$q_{convection} = \frac{\left(T_{surf} - T_{in}\right)}{\frac{1}{hA}} \tag{3.17}$$

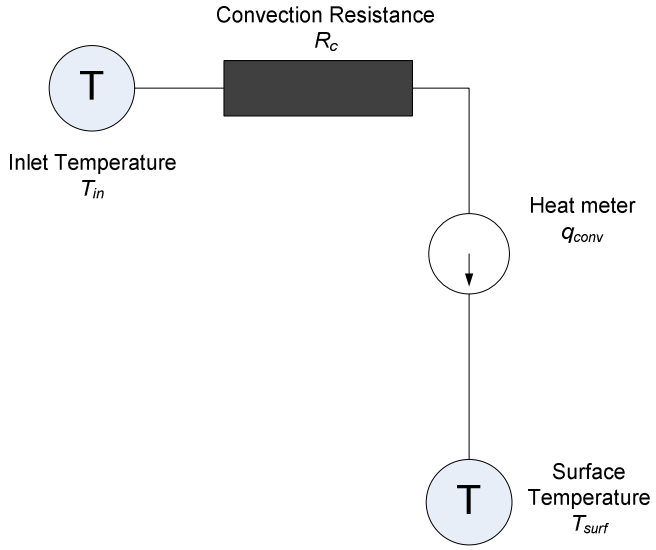

Fig. 3-5. Air control volume thermal circuit.

Once computed, the predicted T_{out} of the air control volume is passed to the neighbouring air control volume. Similarly, the outlet temperature in the second air

control volume is predicted using its corresponding equivalent convective thermal circuit and equation (3.16). By using this process, all the air control volume temperatures from the system inlet to the outlet are determined. The calculation is run iteratively until the solution reaches convergence.

The accuracy of the convective equivalent thermal circuit depends on the assumption made to derive equation (3.15), i.e. that the temperature change between the inlet and outlet is small. To improve the accuracy of the fluid flow circuit, it is necessary to discretise the air domain into finer control volumes to minimise the temperature change across each one. Fig. 3-6(a) shows the pipe flow example which is subdivided into 3 control volumes and its corresponding equivalent convective circuit. Although these control volumes are not physically connected in the equivalent convective circuit, as illustrated in Fig. 3-6(b), they are programmed in such way that the outlet temperature of one control volume is carried forward to the control volume next to it as the inlet temperature for the next time step. The calculation is run for each time step until the system reaches steady state.

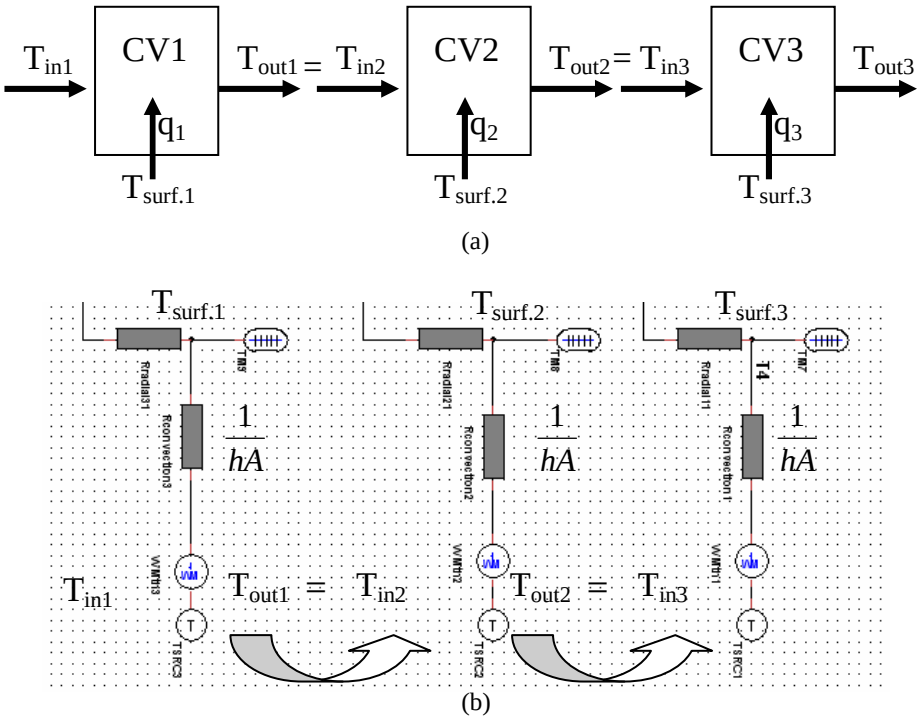

Fig. 3-6. Convection thermal circuit for pipe flow with three control volumes.

The equivalent convective circuit calculation steps for multiple control volumes are (See Fig. 3-7):

I. Initially the inlet temperatures of all the control volumes are set to the ambient temperature.

II. The convection thermal circuit is executed and the $q_{convection}$ and outlet temperature of each control volume is evaluated, by using the initial inlet temperatures as the initial condition.

III. For the second time step, the inlet temperature of CV2 is set equal to the outlet temperature of CV1, and similarly, the inlet temperature of CV3 is set equal to the outlet temperature of CV2, from the first time step.

IV. The fluid flow circuit is re-run with the new inlet temperatures and new $q_{convection}$ of each control volumes is calculated again.

V. Steps III and IV are repeated until a steady state solution is obtained.

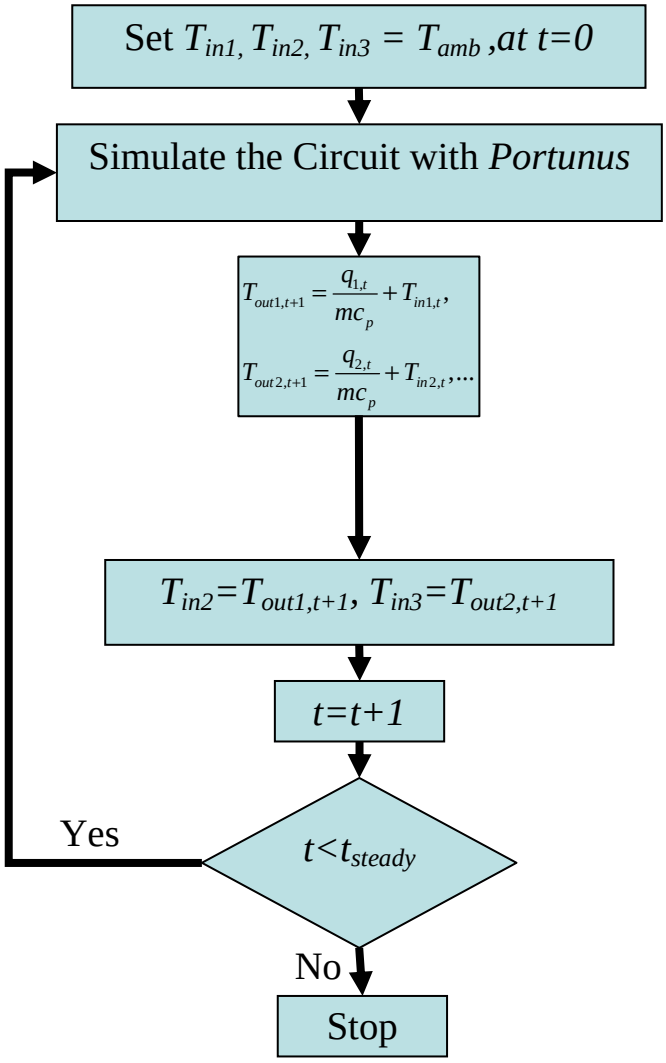

Fig. 3-7. Temperature Passing method algorithm.

3.3.2.2. Heat Pick-up Method (HPM)

Similar to the Temperature passing method, the heat pick-up method (HPM) models the convection heat transfer by using the circuit analogy. In HPM, the working fluid in the machines is discretised into a number of control volumes, and represented as a number of nodes in the thermal circuit. Fig. 3-8(b) shows the corresponding convection thermal circuit of the fluid control volume in Fig. 3-8(a) by using HPM. The HPM convection thermal circuit consists of two sub-circuits, which are the convection heat circuit and the flow circuit, as shown in Fig. 3-8(b). The flow circuit, which is situated at the top of the circuit, models the energy transfer across the fluid

flow, whereas the convection heat circuit, which is located at the bottom part of Fig. 3-8(b), models the convection heat transfer from the surface to the fluid. Both of the circuits are connected at node T_{out}.

By applying the conservation energy equation into the fluid control volume shown in Fig. 3-8(a), the heat transfer by convection, $q_{convection}$ from the bottom surface with constant temperature T_{surf} is equal to the energy used to heat up the fluid from the inlet temperature, T_{in} to the outlet temperature T_{out}.

$$q_{convection} = \dot{m}C_p\left(T_{out} - T_{in}\right) \tag{3.18}$$

The heat transfer by convection, $q_{convection}$, can also be written as:

$$q_{convection} = hA\left(T_{surf} - T_{out}\right) \tag{3.19}$$

Hence, by rearranging equations (3.18) and (3.19),

$$q_{convection} = \frac{\left(T_{out} - T_{in}\right)}{\frac{1}{\dot{m}C_p}} = \frac{\left(T_{surf} - T_{out}\right)}{\frac{1}{hA}} \tag{3.20}$$

Equation (3.20) can be represented as the convection thermal circuit shown in Fig. 3-8(b), by assuming:

$$R_m = \frac{1}{\dot{m}C_p};\ \ R_{conv} = \frac{1}{hA} \tag{3.21}$$

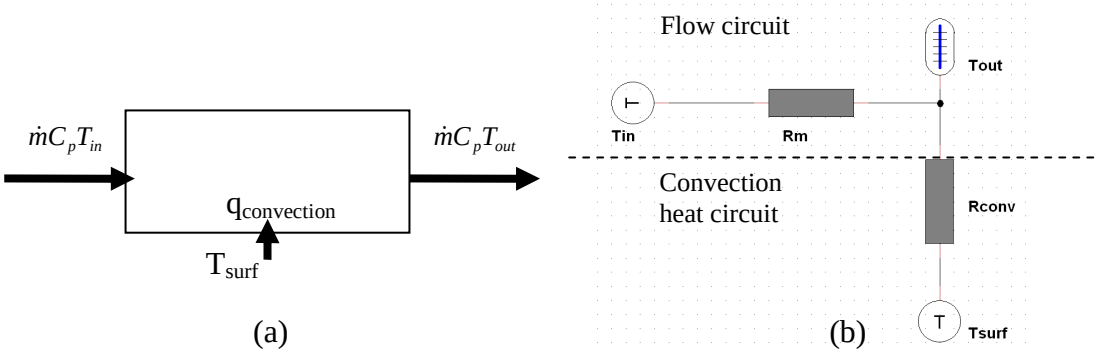

Fig. 3-8(a)&(b). Convection heat transfer modeling with Heat Pick-up method

Equation (3.19) assumes the temperature of the fluid is equal to the outlet temperature, T_{out}. However, this is only valid if the temperature increase across the control volume

is small. For cases where the temperature increase is big, a higher level of discretisation is required in order to maintain the accuracy of HPM convection heat transfer modelling. Fig. 3-9(a) and 3-9(b) show the fluid flow partitioned into three control volumes and the corresponding HPM thermal circuit, respectively.

The flow resistance derived from equation (3.21) is not appropriate for a flow configuration that consists of more than one control volume. Fig. 3-9(b) shows the flow configuration is divided into three control volumes and represented by HPM thermal circuit. The heat generated from the heat source Pth1, flows to the ambient, Tamb, via three different paths, which are CV1, CV2 and CV3, and the three flow resistances, R_{m1}, R_{m2} and R_{m3} respectively. From the heat flow path shown in Fig. 3-9(a), the total heat flows into CV3 is the heat flows from the wall of CV3 (WM_{th3}); the total heat flows into CV2 is the sum of the heat flows from the wall of CV2 (WM_{th2}) and CV3 (WM_{th3}); the heat flow into CV1 is the sum of the heat flows from the wall of CV1 (WM_{th1}), CV2 (WM_{th2}) and CV3 (WM_{th3}). This can be represented as equations:

$$WM_{cv3} = WM_{th3} \tag{3.22}$$

$$WM_{cv2} = WM_{th2} + WM_{th3} \tag{3.23}$$

$$WM_{cv1} = WM_{th2} + WM_{th3} + WM_{th1} \tag{3.24}$$

Where WM_{cv1} is the heat flow into CV1

WM_{cv2} is the heat flow into CV2

WM_{cv3} is the heat flows into CV3

WM_{th1} is the convection heat flow at CV1

WM_{th2} is the convection heat flow at CV2

WM_{th3} is the convection heat flow at CV3

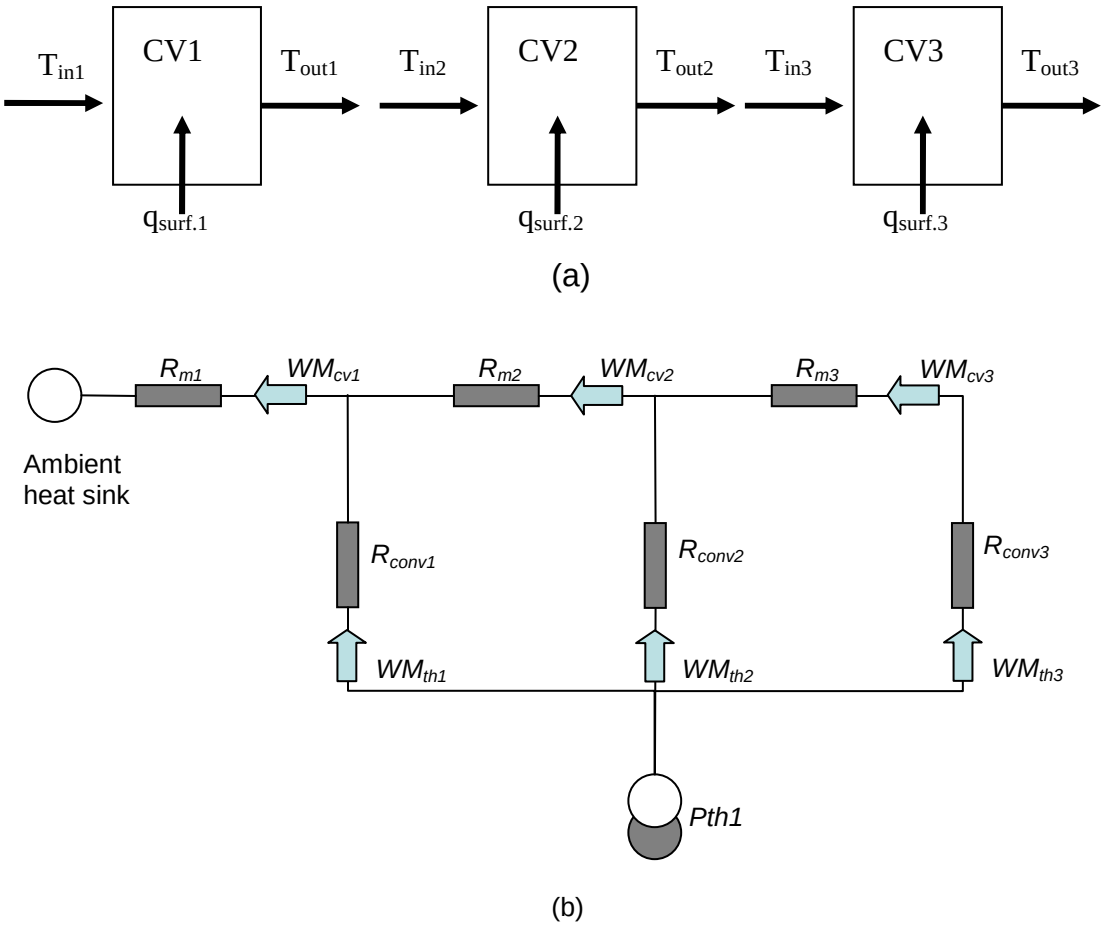

Fig. 3-9 (a)&(b). HPM thermal circuit for multiple control volumes modelling.

The circuit works fine in predicting the temperature of CV3, but it over-predicts the temperatures of CV2 and CV1. From the circuit shown in Fig. 3-9(b), the heat flow (WM_{cv2}) across the thermal resistance R_{m2} is the sum of WM_{th2} and WM_{th3}; however, from the physical model, shown in equation (3.20), the heat flow across the mass flow resistance R_{m2} is only equal to the heat flow from the wall of CV2 (WM_{th2}). The extra heat flow from CV3 (WM_{th3}) flow in the mass flow resistance R_{m2} deviates the temperature predicted for CV2. It is similar for CV1, where connecting CV2 and CV3 at the back of CV1 flow circuit increases the heat flow in the mass flow resistance R_{m1}, hence over-predicts the temperature of CV1. These results show that HPM thermal circuit is not capable of predicting temperature for more than one control volume.

Correction factors are introduced into HPM thermal circuit so that it is apply to multiple control volume flow modeling. In the multiple control volume HPM models,

the flow resistances R_{m1}, R_{m2} and R_{m3}, are divided by fractions, K_n, as shown in equation (3.25) to offset the over-predicted temperatures as discussed as above. The fraction, K_n, is defined as the ratio between the heat across the convection and flow circuits, equation (3.26).

$$R_{m1} = \frac{1}{K_1 \dot{m} C_p}; \quad R_{m2} = \frac{1}{K_2 \dot{m} C_p}; \quad R_{m3} = \frac{1}{K_3 \dot{m} C_p} \tag{3.25}$$

$$K_1 = \frac{WM_{th1}}{WM_{cv1}}; \qquad K_2 = \frac{WM_{th2}}{WM_{cv2}}; \qquad K_3 = \frac{WM_{th3}}{WM_{cv3}} \tag{3.26}$$

However, these heat fractions, K_n are unknown and they vary with different flow conditions, for example laminar and turbulent flows, curved and parallel flows etc. Each of these different flows incurs a different set of heat transfer coefficients and hence it changes the heat fractions across each control volume. Therefore, an iterative method is used to find the exact heat fractions for different flow conditions. Fig. 3-10 shows the flow chart of the HPM iterative algorithm that is used to find the heat fractions in a multiple control volume flow system.

Initially, all the heat fractions, K_n, are set to 1. The HPM thermal circuit is run in *Portunus* with the corresponding original flow resistances. The temperature and the corresponding heat ratio of each control volume are obtained by applying equation (3.26). On the second time step, the heat fractions obtained from the first time step are used. The thermal circuit is re-run and hence another set of heat fraction and temperature are evaluated. The iterative process is repeated until the solutions are converged, i.e. the temperature differences in each control volume predict from the last two iterations is less than 0.001 °C.

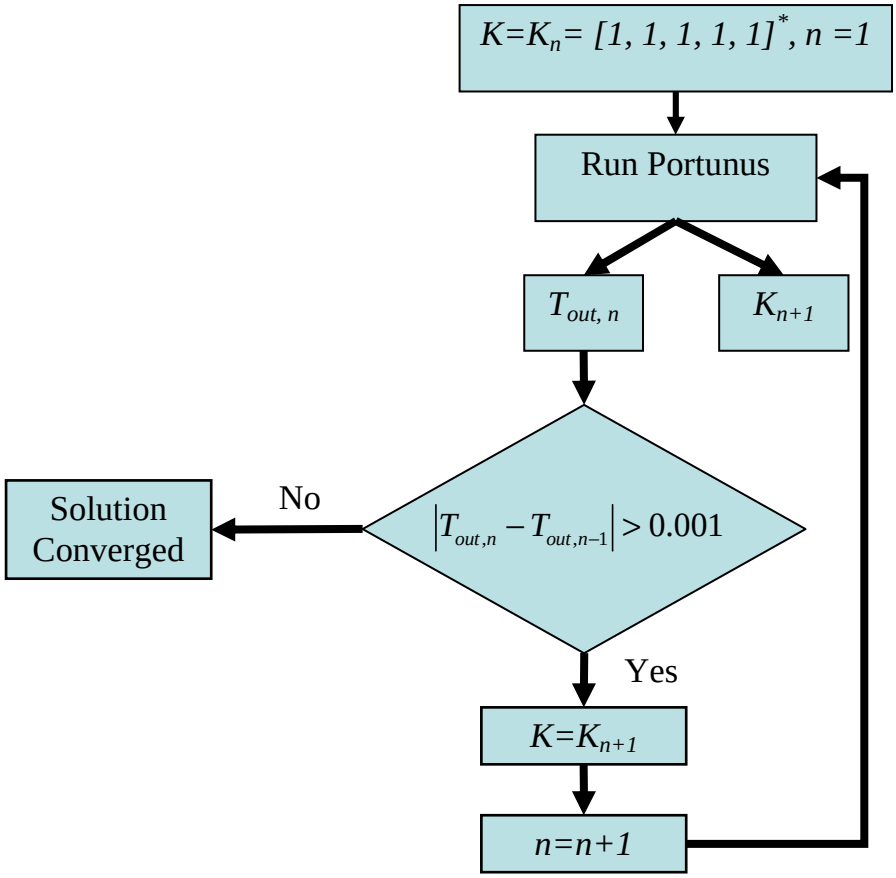

**Each column in the matrix represents the heat function of each control volume in the multiple control volume model.*

Fig. 3-10. Heat pick-up method iterative algorithm.

Two case studies are conducted to validate the accuracy of the TPM and the HPM compared with the CFD results. However, the accuracy of the temperature prediction of these methods is closely related to the accuracy of the convective heat transfer coefficient used in the equivalent convective circuit. Therefore, in order to make a valid comparison with the CFD results, the convective heat transfer coefficients applied for these two convection heat modelling methods were directly obtained from the CFD simulations. In the future, parametric studies of the convective heat transfer coefficient of the AFPM generator will be conducted to develop empirical formulae that directly relate the convective heat transfer coefficient with different flow conditions, mass flow rates and geometrical parameters. With these parametric data, the lumped parameter model is potentially capable of working independently from CFD, to provide accurate temperature predictions.

3.3.2.3. Comparisons of Temperature Passing Method (TPM) and Heat Pick-up method (HPM)

The aim of this section is to investigate the accuracy and practicability of TPM and HPM convection heat modeling methods compared with the existing CFD modelling technique. Three different test cases were designed to monitor the accuracies of these two modelling methods with different boundary conditions, including both steady and unsteady boundary conditions. The CFD models of these test cases were built to provide benchmarks for these two modelling methods. At the same time, the heat transfer coefficients of these three different boundary conditions for these two LPM models were extracted from the solutions of the CFD models. A flow system in a heated pipe of 250mm length and 50mm radius is demonstrated in Fig. 3-11. Fig. 3-12(a) & (b) show the five control volume thermal circuits of the temperature passing method (TPM) and the heat pick-up method (HPM), respectively.

The CFD model was constructed using the Gambit meshing software. The model was meshed with structural Quad mesh and very fine mesh was applied at the area near to the wall to capture the velocity boundary layers effect. An asymmetric boundary condition was used to reduce the size of model to half: Only half of the pipe was modeled. In total, the 2-D CFD model of the flow system in the heated pipe consists of 10486 cells. Uniform axial velocity, 1m/s, was specified at the inlet of the pipe, and the corresponding pipe flow Reynolds number was 5.76×10^6. The realisable k-ω turbulence model was used to attain the turbulent effect in the model. The 2-D CFD model of flow in the heated pipe is simulated in FLUENT 6.3. The calculations took an hour on a 1gigabyte RAM, 1.73GHz Core DUO PC, to reach both residual and absolute convergences.

The thermal circuits with both convection heat transfer modelling methods (TPM and HPM) of the heated pipe flow system consist of five control volumes (CVs) (Fig. 3.12). TPM used the pipe inlet temperature to predict the outlet temperature of the first fluid control volume. Subsequently, the outlet temperature calculated from the first CV based on the inlet temperature of the system and the boundary condition of the first bottom wall surface was passed to the second CV as the inlet temperature.

Similarly, the outlet temperature calculated from the second CV, was based on the outlet temperature of the first CV1, and the boundary condition on the second wall surface. Similarly, the outlet temperature of CV2 was passed to CV3. The temperature information was hence propagated from the inlet to the outlet of the pipe flow system.

For HPM, the convection thermal circuits of each control volume were connected to each other with flow resistances. Heat fractions, K_n, were used to amplify the flow resistances, which were used to counterbalance the heat accumulated at each temperature node in the multiple control volume model, in order to accurately predict the temperature rise in each control volume. Initially, the heat fractions were unknown for different flow conditions, but they can be found by using the iterative method mentioned in section 3.3.2.2.

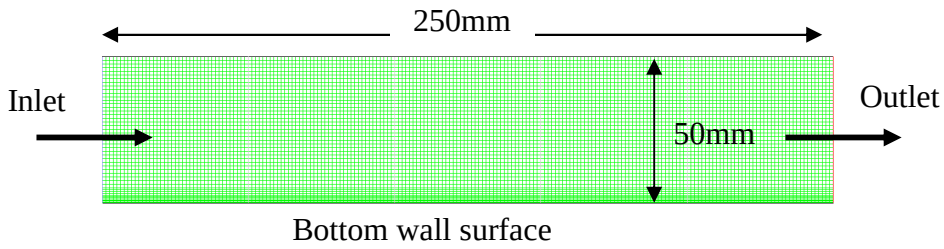

Fig. 3-11. CFD model of the flow through the heated pipe test case.

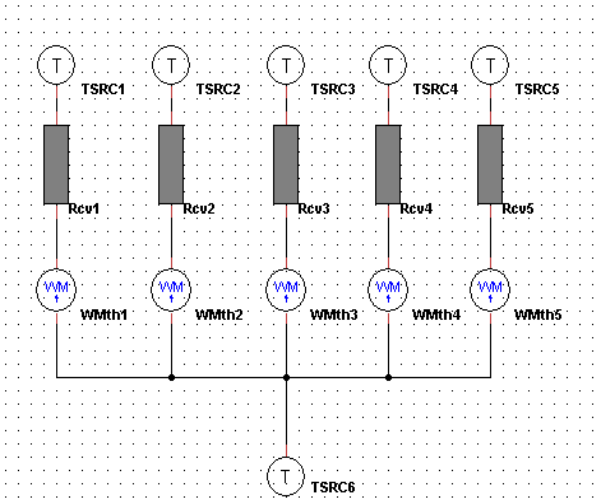

(a)

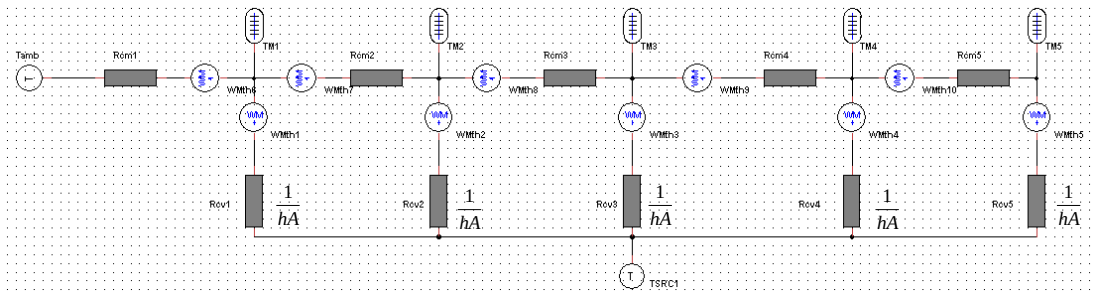

(b)

Fig. 3-12(a) &(b). Temperature Passing (a) and Heat Pick-up (b) method thermal circuits.

Three different boundary conditions were used to investigate the accuracy of these two modelling methods, which were constant temperature, constant heat and temperature dependent heat source boundary conditions. Both the constant temperature and heat source are steady state boundary conditions. They were used to model the constant temperature or heat flux on the wall boundary of the pipe. Alternatively, the temperature dependent heat source is an unsteady state boundary condition. The heat flux flowing into the system (or the thermal circuit) with this boundary condition varies as the temperature on the wall changes, which is similar to the resistive heating element boundary condition.

The fluid temperatures of each control volume predicted from HPM and TPM were compared with the results obtained from the CFD model. Fig. 3-13, 3-14 and 3-15 show the fluid temperature and the relative fluid temperature errors of each control

volume of HPM and TPM for constant temperature source, constant heat source and temperature dependent heat source, respectively. The relative fluid temperature discrepancy is defined as in equation (3.27):

$$\text{Relative fluid temperature discrepancy} = \frac{(T_{LPM} - T_{in}) - (T_{CFD} - T_{in})}{(T_{CFD} - T_{in})} \times 100\% \quad (3.27)$$

Where, T_{LPM} and T_{CFD} are the temperatures predicted in the lumped parameter model and CFD model, respectively. T_{in} is the inlet temperature.

By specifying the constant temperature boundary condition onto the wall of the pipe flow model, TPM predicted higher fluid temperatures than the CFD; whereas HPM under-predicted the fluid temperatures. Yet, overall, the results show that both the modelling circuits work well in predicting temperatures for flow inside the heated pipe, having a constant temperature boundary condition, where the maximum relative discrepancy was slightly above 1%, (see Fig. 3-13).

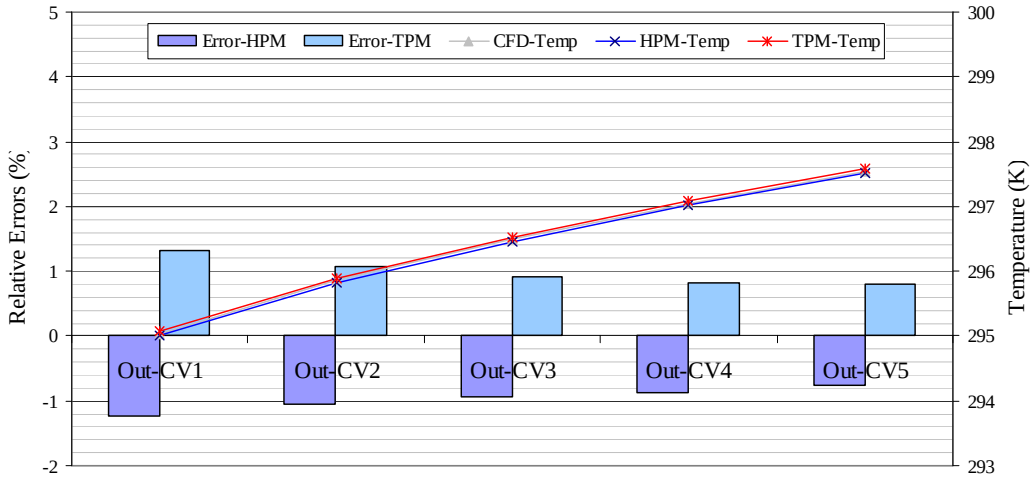

Fig. 3-13. Temperature and relative temperature error of the pipe flow model by specifying the constant temperature boundary condition.

Subsequently, constant heat flux boundary conditions were applied to these models and the results are indicated in Fig. 3-14. The relative discrepancies are generally higher when a constant heat flux was specified in the pipe flow model. The maximum relative discrepancy of the thermal circuits (by applying both HPM and TPM) is about 5% (Fig. 3-14), as compared with the thermal circuits when constant

temperature source is applied, the maximum relative discrepancy is only 3%. The decline in accuracy of convective circuits when a constant heat flux boundary condition is specified on the thermal circuits is because of the abrupt pipe wall temperature changes in the flow direction. As mentioned in the previous section, the convective resistances (or heat transfer coefficients) used in both of the convective circuit algorithms were obtained from the CFD models. For each control volume, the heat transfer across the pipe wall, q, and area-weighted average wall temperature, T_{surf}, can be evaluated from the CFD solution. Hence, by applying this information into equation (3.28), an area-weighted average heat transfer coefficient of each control volume can be calculated and is used in the convective thermal circuits.

Average heat transfer coefficient:

$$h_{convection} = \frac{q}{A\left(T_{surf} - T_{in}\right)} \tag{3.28}$$

Where q represents the total heat transfer in *Watt*, A represents the wall surface area and T_{in} represents the fluid inlet temperature.

For constant heat flux wall boundary conditions, the pipe wall temperature increased steeply in the flow direction and the local heat transfer coefficient of each cell changes accordingly. Therefore, it is not sufficient to model the fluid temperature by applying only the area-weighted average heat transfer coefficient calculated from equation (3.28) of each control volume in the convective thermal circuits. Further partition was required, especially in the first control volume where the temperature gradient is the steepest, to improve the results obtained from the convective thermal circuits. However, it can be observed that HPM algorithm provides a slightly better accurate result than TPM algorithm, with the constant heat flux wall boundary pipe flow model.

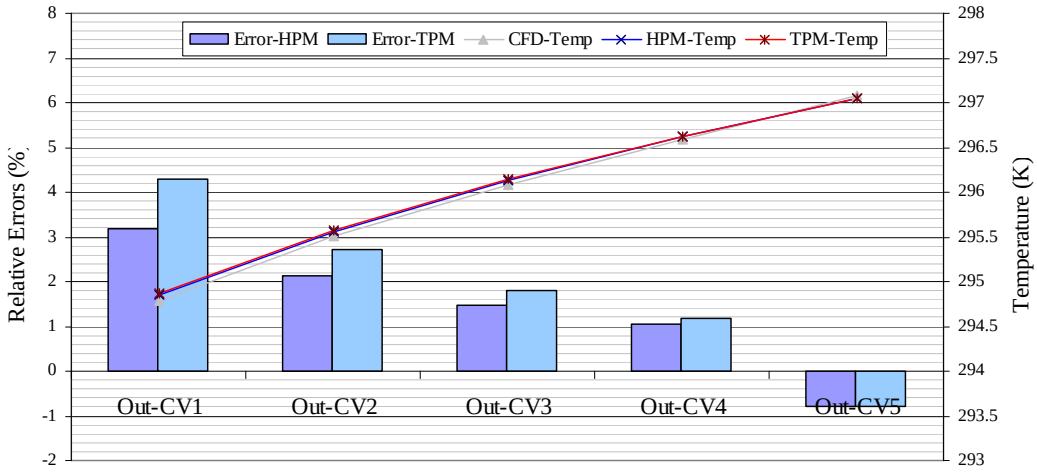

Fig. 3-14. Temperature and the relative temperature errors for constant heat source.

Fig. 3-16 shows the fluid temperature and corresponding relative errors of the pipe flow model with the application of temperature dependent heat sources. A reverse trend is observed. The temperature predicted by using the TPM algorithm is more accurate than the HPM algorithm. This is mainly due to the fact that the TPM algorithm iterates the fluid temperature against the time step whereas the HPM algorithm iterates in response to the heat fraction. The TPM algorithm is more capable of capturing the transient effect for the temperature dependent heat sources and hence the fluid temperatures predicted are more accurate.

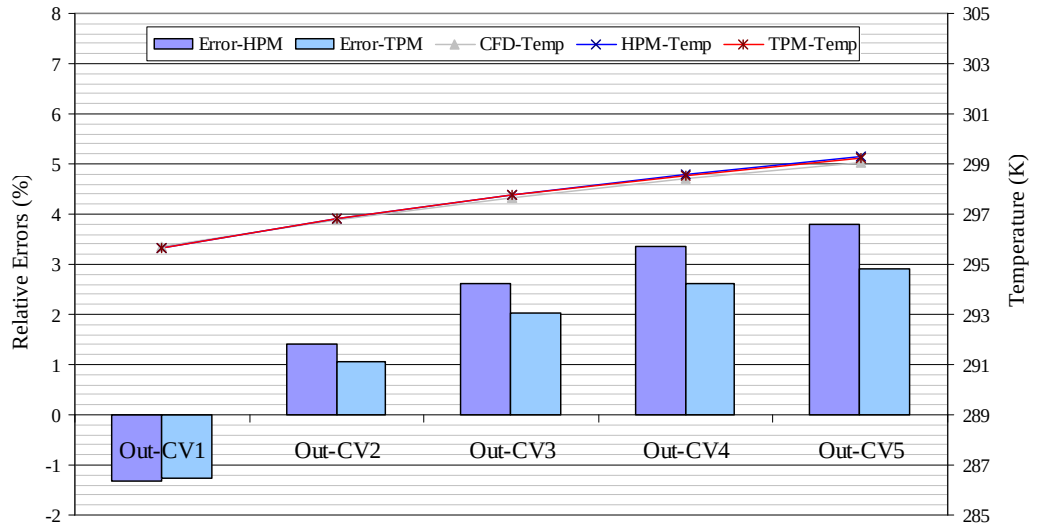

Fig. 3-15. Temperature and relative temperature errors for temperature dependent heat source.

In conclusion, both convection heat transfer modelling methods were tested with three different boundary conditions, which were the constant temperature, constant heat flux and temperature dependent heat flux. The investigation indicates that these two modelling methods were in good agreement with the CFD model and the relative errors were less than 5%. However, due to the fundamental difference in the calculation algorithms, the HPM algorithm gives better results for steady state boundary conditions; whereas the TPM algorithm is better in modelling the transient state boundary conditions. In the next section, two more case studies are presented, to validate the accuracy of the lumped parameter thermal circuit compared with the CFD results. Because the TPM algorithm has been proved to be the better option for transient state modelling, all of the convective circuits in the following sections were built based on TPM algorithm.

3.4. Case Study I: Flow in the Heated Pipe

This case study investigates the fluid temperature distribution in the heated pipe for different flow conditions, e.g. Laminar and turbulent flows. Both CFD and lumped parameter techniques were used to model the fluid temperature increase in the heated pipe. The objectives of this case study are:

- To compare the accuracy of the lumped parameter thermal circuit with the CFD model.
- To investigate the optimal discretisation level for the construction of the lumped parameter thermal circuit.

3.4.1. Descriptions

In this case study, air, with mass flow rate of $\dot{m}$, flows through a heated steel pipe, having an inner radius 10mm, outer radius 20mm, and length 45mm (Fig. 3-16). The pipe is subdivided into three annuli where $5W/m^3$ volumetric heat generation is specified at the middle annulus. The air inlet temperature is specified as

19.85°C/293K and it is assumed that there is no heat loss in the pipe outer surface. Two different flow conditions were investigated in this case study, which are laminar flow with Reynolds number less than 700 and turbulent flow with Reynolds number greater than 4000. (For pipe flow, Re<2300 is laminar, 2300<Re<4000 is transition, Re>4000 is turbulent).

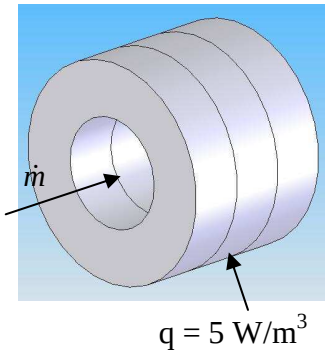

Fig. 3-16. Case study I: Pipe flow.

3.4.2. CFD model of the Pipe Flow

The CFD modelling of the pipe flow was conducted to provide benchmarks for the temperatures predicted from the lumped parameter thermal circuit. The pipe flow system was modelled with the commercially available CFD code, Fluent. The pipe flow model was built in the Fluent's pre-process software, Gambit with Quad meshing schemes. The mesh of the model is shown in Fig. 3-18. Extremely fine mesh was applied in the area near to the wall to model the velocity boundary layers. In this case study, the model was tested with two different flow conditions. For laminar flow modelling (Reynolds number ≈ 700), the *laminar viscous model* [131] was used; while for turbulent flow modeling (Reynolds number ≈ 3500), the *realization k-epsilon viscous model* [131] with enhanced wall function was specified.

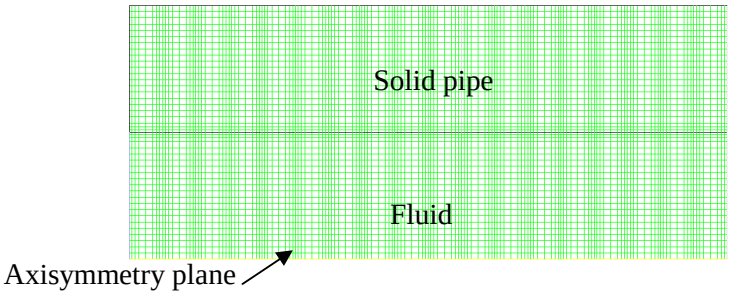

Fig. 3-17. Grid of the 2D-axisymmetric model of pipe flow case study.

3.4.3. Lumped Parameter Thermal Circuit of the Pipe Flow

The pipe flow system lumped parameter thermal equivalent circuit shown in Fig. 3-18 consists of two major parts, which are solid conductive circuit (above the dash line in Fig. 3-18) and convective circuit (below the dash line in Fig. 3-18). The solid pipe and the fluid inside the pipe were sub-divided into three annuli and three cylinder disks, respectively. Each solid annulus was represented as the annulus conductive circuit, whereas each fluid cylinder disk was modeled as separate control volume in the equivalent thermal network.

Each annulus conductive circuit consists of four temperature terminals, two in the axial direction, (the front and back surfaces temperature terminals) and two in the radial direction, (the outer and inner surfaces temperature terminals). Three annulus conductive circuits were connected one after another, where the back surface temperature terminal of the front annulus was connected to the front temperature terminal of the back annulus, shown in Fig. 3-18. The inner surface temperature terminals of the solid pipe were connected with the convective circuit for fluid temperature prediction in each control volume. Due to the fact that the pipe was assumed to be fully insulated, the heat flow paths to the pipe surfaces were neglected.

The convective heat transfer coefficients on the pipe inner surface used in the lumped parameter model are extracted from the solution pre-simulated by the CFD model. Equation (3.28) shows the pipe inner surface heat transfer coefficient, $h_{convection}$, is calculated based on the heat flux, q, and area-weighted surface temperature, $T_{surf,}$ obtained from the CFD model.

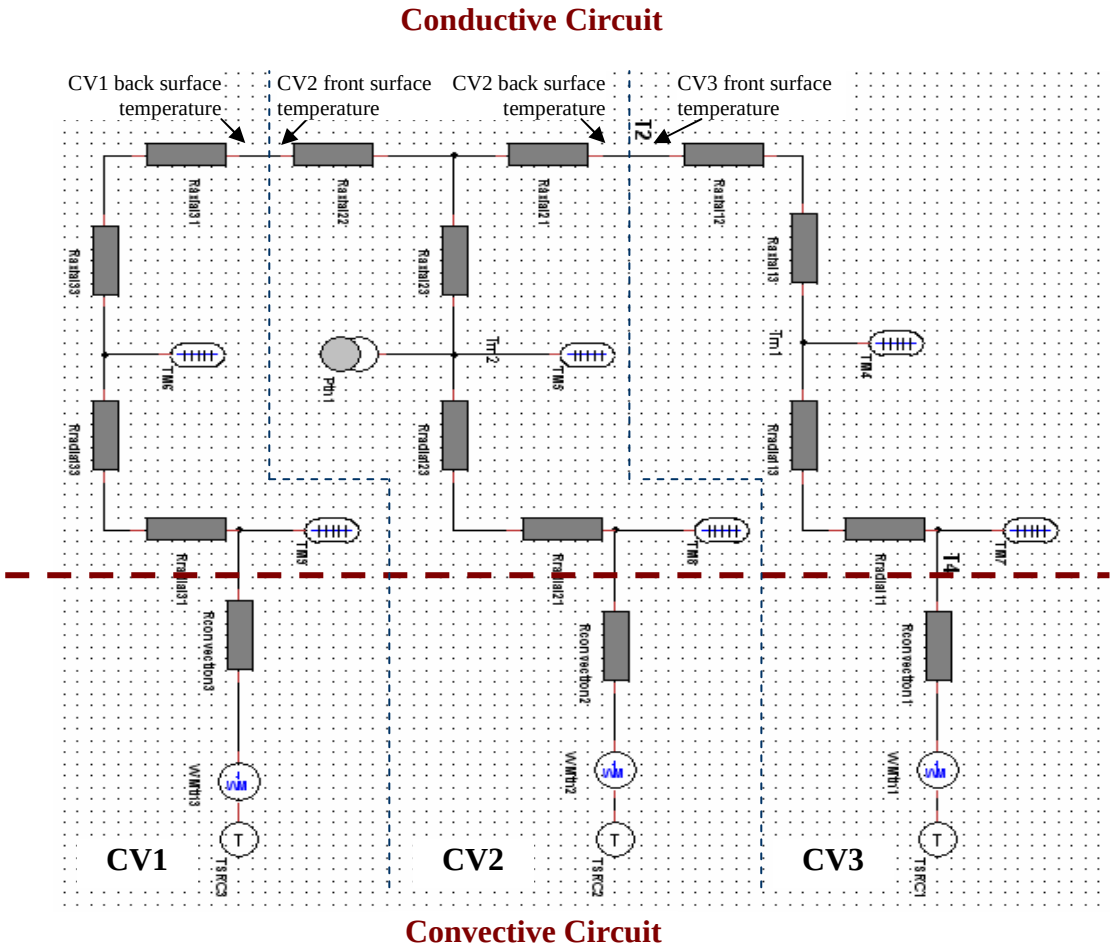

Fig. 3-18. Thermal network for the pipe flow.

3.4.4. Results and comparisons

Fig. 3-19 shows the solid pipe volumetric average temperature and fluid mass-weight average temperature at the exit from each control volume, predicted from both the lumped parameter thermal model (LPM) and the CFD model, for laminar flow. The results show that the temperatures predicted by LPM are slightly higher than the CFD models, whereas the maximum discrepancy of approximately 1.5%, occurs in the CV1 fluid temperature. The discrepancy is due to the assumption made in equation (3.15), where the fluid average temperature was assumed to be equal to the fluid inlet temperature. Consequently, the convective heat flow was over-predicted, causing the temperatures predicted to be slightly higher. Hence, it shows that the assumption made in equation (3.15) is valid if the change of fluid temperature across the control

volume is small. By dividing the air control volume into smaller control volume, the errors arisen from LPM thermal equivalent circuit can be minimised.

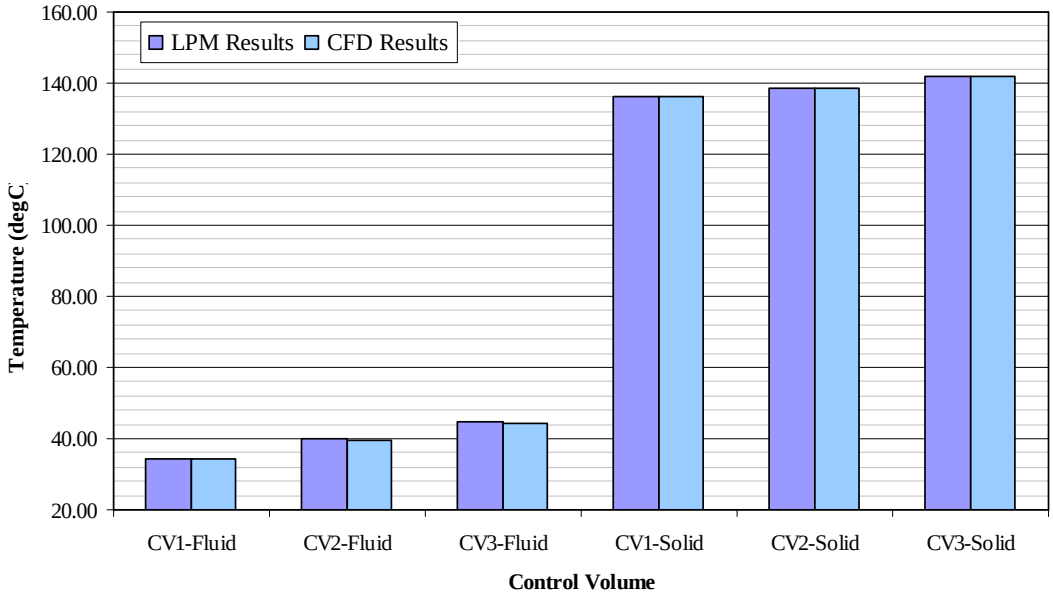

Fig. 3-19. Temperatures predicted of flow in the heated pipe (Laminar flow, *Re* = 700).

The accuracy of the temperature predicted by LPM depends on the fluid regime discretisation level. The discretisation dependency study was assessed by further sub-dividing the pipe into 3, 9 and 18 nodes respectively. Because the absolute errors were small and insignificant, in order to identify the cell discretisation effect, the discrepancies between the LPM and CFD models were amplified by introducing the relative discrepancy, which is defined as:

$$\text{Relative discrepancy} = \frac{(T_{LPM} - T_{in}) - (T_{CFD} - T_{in})}{(T_{CFD} - T_{in})} \times 100\% \tag{3.29}$$

Where, T_{LPM} and T_{CFD} are the temperatures predicted in lumped parameter model and CFD model respectively, and T_{in} is the inlet temperature.

The comparison of relative discrepancy of different levels of discretisation for low Reynolds flow is shown in Fig. 3-20. The first three sets of bar charts indicate the

relative errors for solid pipe temperature predictions and the remaining three sets of bar charts indicate the relative errors for the fluid.

The results shown in Fig. 3-20 indicate that as the discretisation level increases, the relative error for fluid temperature at the first control volume decreases from 3.2% to 2.85%. However, the decreases of the fluid relative errors of the second and third control volumes are less significant, being 0.08% for the second control volume, and insignificant decrease of error for the third control volume. The accuracy of the convective circuit used in this case study depends on the magnitude of temperature change of the fluid control volume. High temperature change across the inlet and outlet temperature of the fluid control volume incurs high discrepancy for fluid temperature prediction in LPM. (refer to Temperature Passing Method in section 3.3.2). Therefore, the steep temperature gradient at the first fluid control volume of the laminar pipe flow induces the highest fluid temperature relative error. However, when the first fluid control volume was further divided into smaller sub-control volumes, the change of temperature across each sub-control volume decreases, and hence the accuracy was improved. In contrast, the temperature changes at second and third fluid control volume were gradual. Therefore, it shows that further reducing the size of the control volume doesn't play an essential role in improving the accuracy.

The solid pipe temperatures prediction of the thermal circuit shows a reverse trend. When the number of cells increases, the relative errors of the solid temperature predicted by the thermal circuit increase simultaneously. This is due to the fact that the annulus conductive circuit implemented in the lumped parameter circuit presumes the axial and radial heat flows are independent from each other. As the pipe is further divided into a thinner annulus, the interference of heat flows in the axial and radial directions becomes significant. Hence the accuracy degenerated as level of discretisation increased.

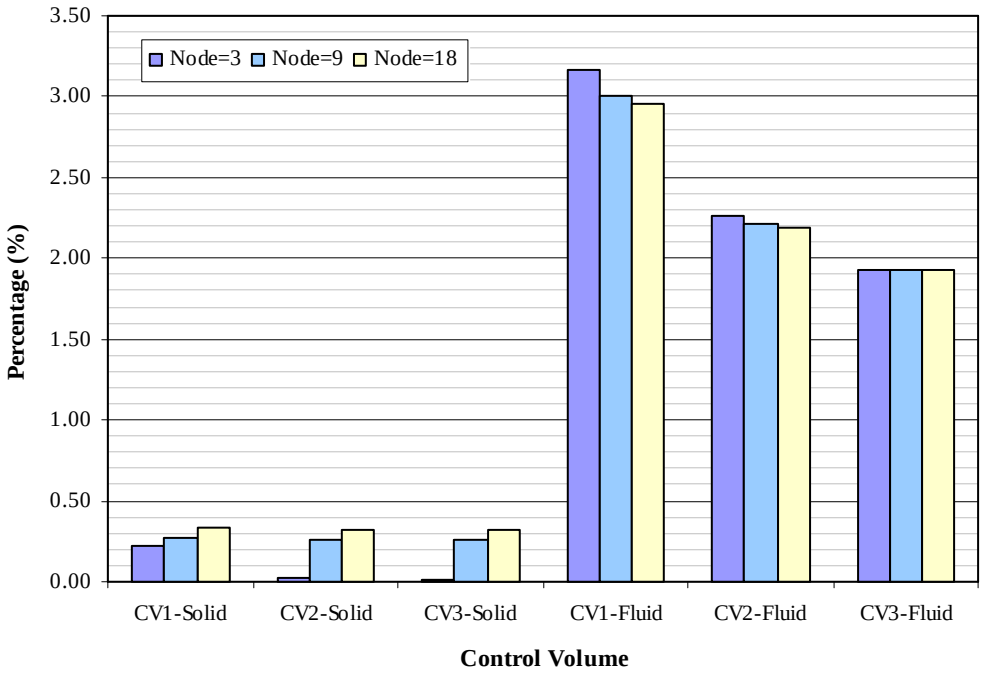

Fig. 3-20. LPM relative discrepancy of different discretisation level for low Reynolds' flow in the heated pipe.

Fig. 3-21 shows the fluid and pipe temperatures predicted from LPM and CFD for turbulent flow in the heated pipe. Because the temperature increases in the fluid and the pipe wall of each control volume in the turbulent pipe flow case are comparably smaller than for laminar flow case, the temperatures predicted from LPM were closer to the temperatures predicted from the CFD techniques. Errors between the lumped parameter models and CFD models were insignificant for high Reynolds number flow as compared with low Reynolds number.

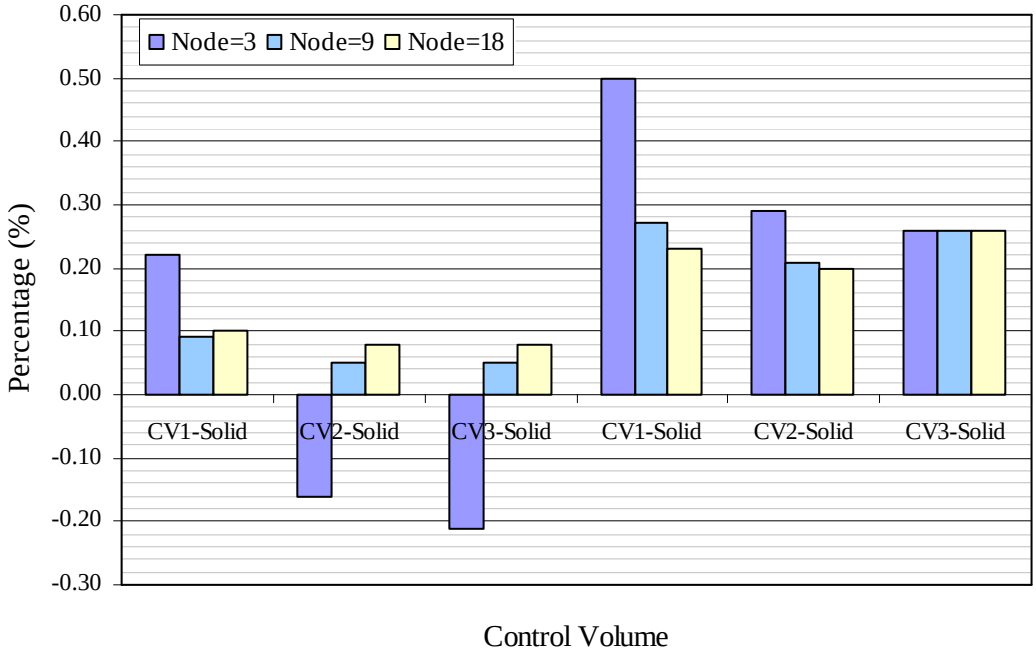

Fig. 3-21. LPM relative discrepancy of different discretisation level for High Reynolds' flow in the heated pipe.

3.4.5. Conclusions

In this case study, the lumped parameter thermal equivalent circuit of the pipe flow was built and it was compared with the results obtained from the CFD models. The results show a good agreement between the lumped parameter thermal network model and CFD model for both low and high Reynolds flow. The effect of the accuracy of the lumped parameter network with different dicretisation levels was investigated. Higher discretisation levels show positive effects on the fluid temperature prediction, but exhibit a negative influence on the solid temperature. Fig. 3-22 illustrates the maximum discrepancy incurred for 3-, 9- and 18-nodes discretisation level models, for low and high Reynolds number flows. In conclusion, a 3-node discretisation level is sufficient to obtain reasonably accurate results. Further discretisating the model into 9- and 18-nodes is not necessary. Discretisation level does not play as significant part as heat transfer coefficient in lumped parameter thermal network models.

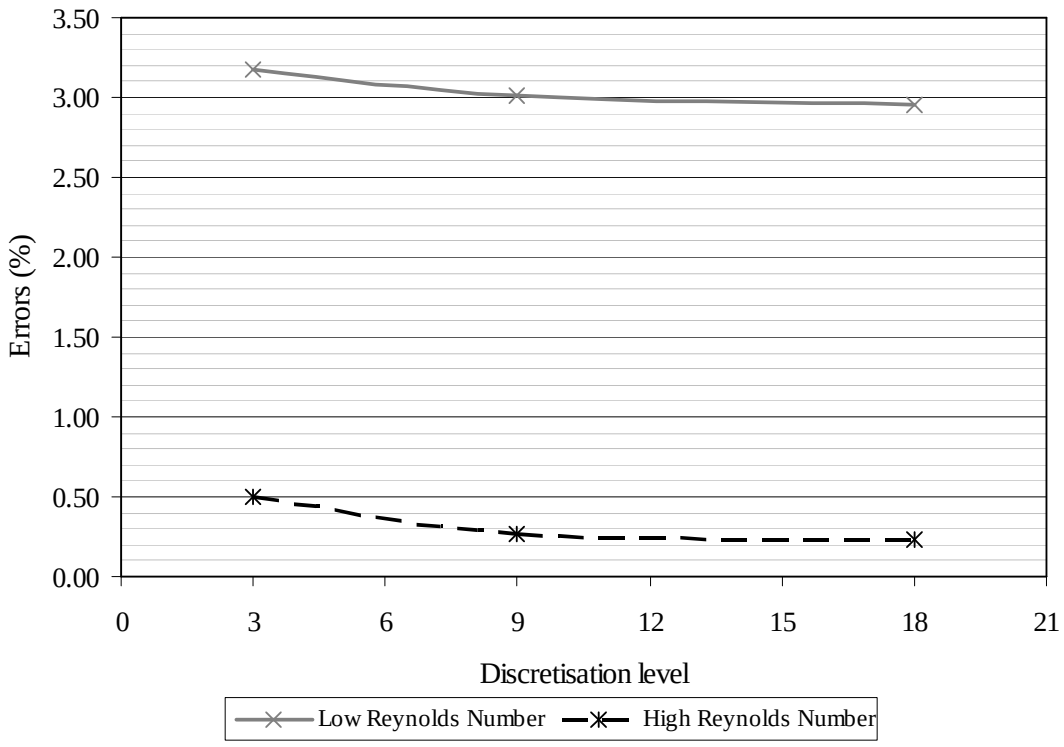

Fig. 3-22. Maximum discrepancy incurred for 3-, 9- and 18-nodes thermal network for low and high Reynolds flows.

3.5. Case Study II: Simplified Axial Flux Permanent Magnet (AFPM) Generator

This case study describes the construction of a 2D axisymmetric lumped parameter thermal equivalent circuit of an AFPM generator by using the annulus conductive circuit and the convective thermal circuit with the TPM algorithm. Similarly, convection heat transfer coefficients and mass flow inlet acquired from the pre-simulated CFD model are applied into the lumped parameter thermal circuit to predict the temperature increase in the generator. Finally, the results calculated from the lumped parameter thermal circuit are compared with the result predicted by CFD models.

3.5.1. Case Descriptions

Fig. 3-23(a) and (b) show the configuration of the 2D axisymmetric AFPM generator and its corresponding lumped parameter network. Comparing with the full generator, the stator holder and stator boss were omitted and the windings were simplified to surface heat generaters. To further simplify the analysis, symmetry about the axial plane at the centre of the stator was assumed, hence only half of the generator thermal circuit was built.

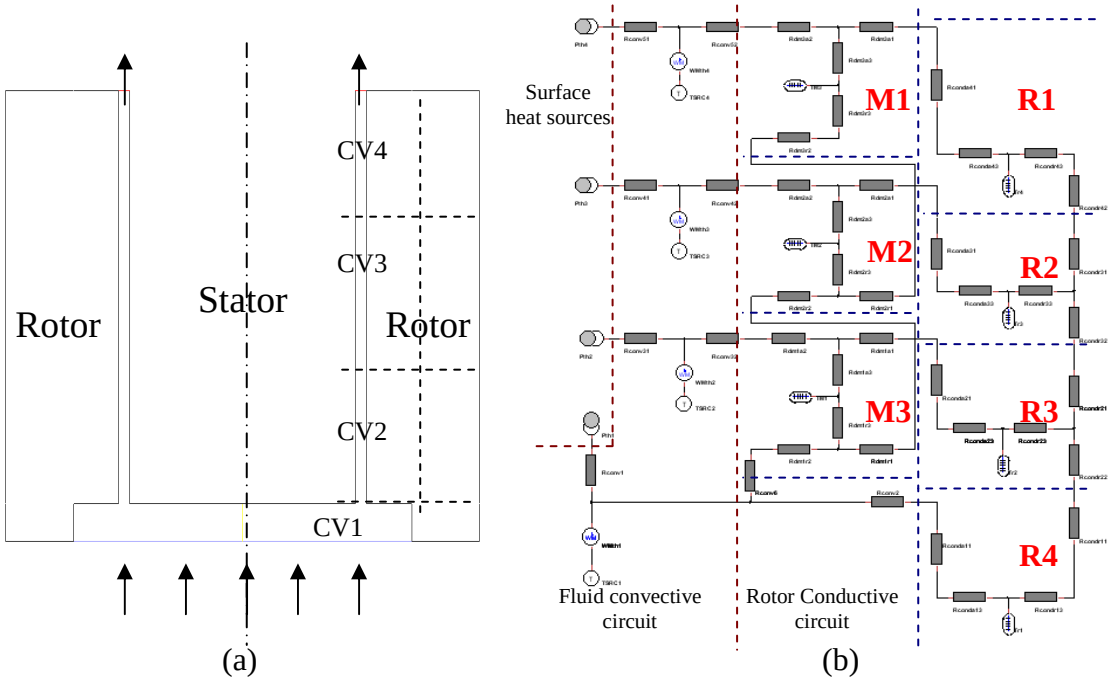

Fig. 3-23. Simplified AFPM generator's lumped parameter thermal network.

3.5.2. Lumped Parameter Thermal Equivalent Circuit of A Simplified Axial Flux Permanent Magnet Generator

The thermal equivalent circuit of a simplified AFPM generator consists of three major parts, which are the rotor conductive circuit, the fluid convective circuit and the stator heat source circuit, see Fig. 3-23(b). The rotor is divided into seven annuli (M1 M2, M3, R1, R2, R3 and R4), as shown in Fig. 3-23(a) where three of the annuli on the left hand side represent the magnets and four of the annuli on the right hand side represent the rotor disk. Each annulus of the rotor part is represented as the annulus

conductive circuit in the thermal circuit and they are inter-connected at the axial and radial temperature terminals. For the stator part, the stator winding is simplified into four surface heat sources in the thermal network to eliminate the uncertainty of the effective thermal resistance of the stator windings. Each of those heat sources is connected to the flow circuit next to it through a convective resistance. The working fluid inside the generator is sub-divided into four fluid flow control volumes, CV1, CV2, CV3 & CV4, and each control volume is represented as a fluid convective circuit shown as below:

3.5.2.1. Control Volume 1 (CV1):

CV1 indicates the first air nodes at the entrance of the simplified AFPM generator (Fig. 3.24(a)). Heat is transferred into/out from CV1 from three surfaces, which are the stator surface (T_{surf}), the magnet bottom surface ($T_{magsurf}$) and the rotor surface ($T_{rotorsurf}$). By summing all the convective heat transfers to the fluid, and substituting as q_1 into equation (3.30), the temperature at the exit of CV1 can be calculated. Hence, the convective circuit of CV1 was constructed in such way that they were linked up to individual heat source from the stator, magnet and rotor surfaces to the inlet temperature with its corresponding convective heat coefficient, to evaluate the total heat transfer, q_1, (Fig. 3-24(b)). Since CV2 is connected after CV1, the outlet temperature of CV1 was passed CV2, as the inlet temperature of CV2.

$$T_{cv1\_out} = \frac{q_1}{\dot{m}C_p} + T_{in} = T_{in\_CV2} \tag{3.30}$$

Where, T_{cv1_out} is the temperature at the exit of CV1, q_1 is the total heat transfer, and T_{in_cv2} is the inlet temperature of CV2.

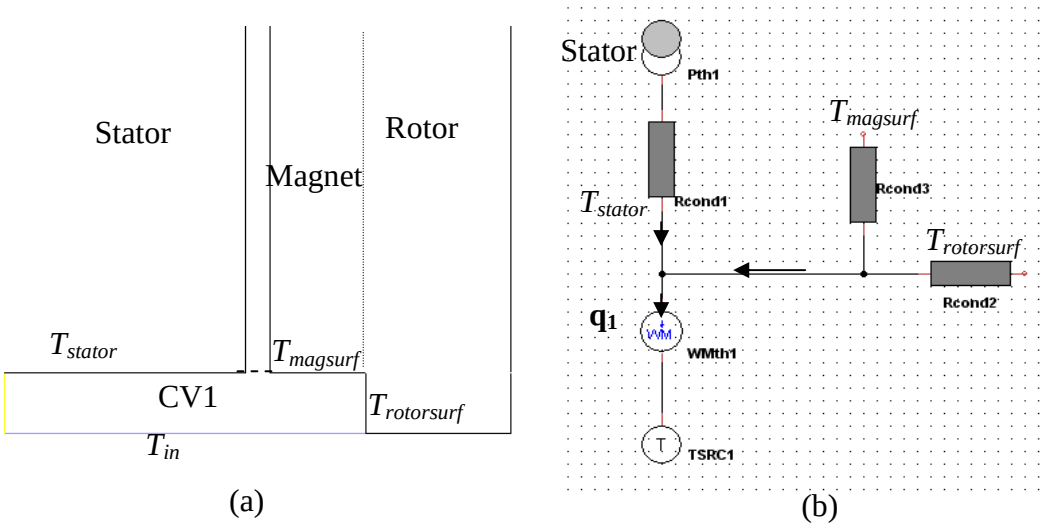

Fig. 3-24. Fluid convective circuit for control volume 1 (CV1).

3.5.2.2. Control Volume 2 (CV2):

CV2 indicates the air control volume directly above the CV1, see Fig. 3-25(a). For CV2, convective heat transfer on two surfaces were involved, where one was from the stator winding on the left hand side, and the other one was from the rotating magnet surface. Like CV1, by summing the heat transfer from these two surfaces by using the fluid convective circuit, as shown in Fig. 3-25(b), and substituting the calculated total heat transfer as q_2 into equation (3.31), the temperature at the exit of CV2 can be calculated. Similarly, the CV2 outlet temperature was passed to CV3 as the inlet temperature of CV3.

$$T_{cv2\_out} = \frac{q_2}{\dot{m}C_p} + T_{in\_cv2} = T_{in\_CV3} \tag{3.31}$$

Where, T_{cv3_out} is the temperature at the exit of CV2, q_2 is the total heat transfer in CV2, and T_{in_cv2} is the inlet temperature of CV2.

Since CV3 and CV4 both shared the same boundary conditions as CV2, the fluid convective circuit of CV3 and CV4 were identical to CV2's, except the inlet temperatures of CV3 and CV4 were equal to exit temperature of CV2, and CV3 respectively.

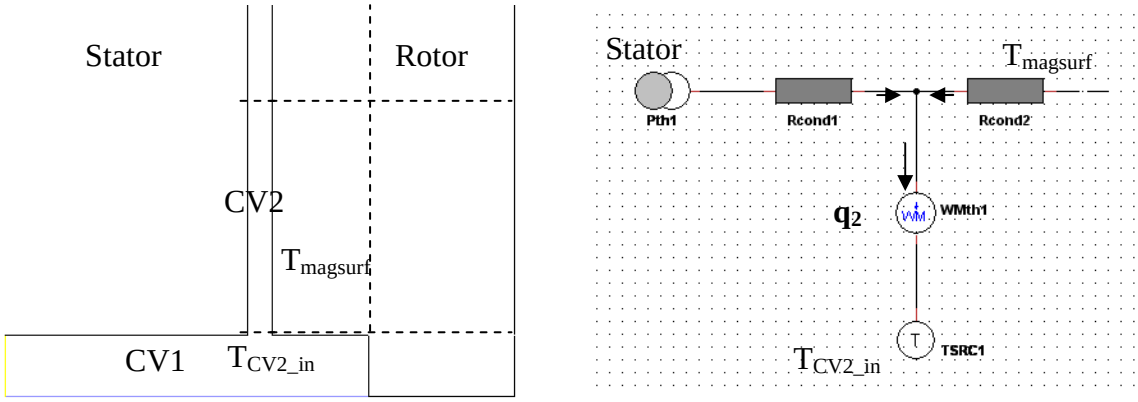

Fig. 3-25. Fluid flow circuit for control volume 2 (CV2).

3.5.3. CFD model of A Simplified Axial Flux Permanent Magnet Generator

Similar to case study I, the CFD of a 2D axisymmetric AFPM generator was constructed and run in Fluent to provide the convective heat transfer coefficient and mass flow rate that, is required for the lumped parameter thermal equivalent circuit. The temperatures obtained from the thermal network circuit were then compared with the CFD results.

The 2D axisymmetric model of the simplified AFPM generator, as shown in Fig. 3-26, was constructed in Gambit and meshed with Quad meshing schemes. Details of the model are:

I. Finer mesh was applied in the area near to the wall so that Y^+ value is lower than 5.
II. *Realizable k-epsilon* turbulent model with enhanced wall function was used to model the turbulence in the machine.
III. The rotor disk and magnet annuli were specified to rotate at 1500rpm (157rad/s) with rotating reference plane boundary condition.
IV. Zero total pressure and zero static pressure were specified at the inlet and outlet of the simplified AFPM generator model.

Temperatures obtained from both CFD and the thermal network circuit are compared and discussed in the following section.

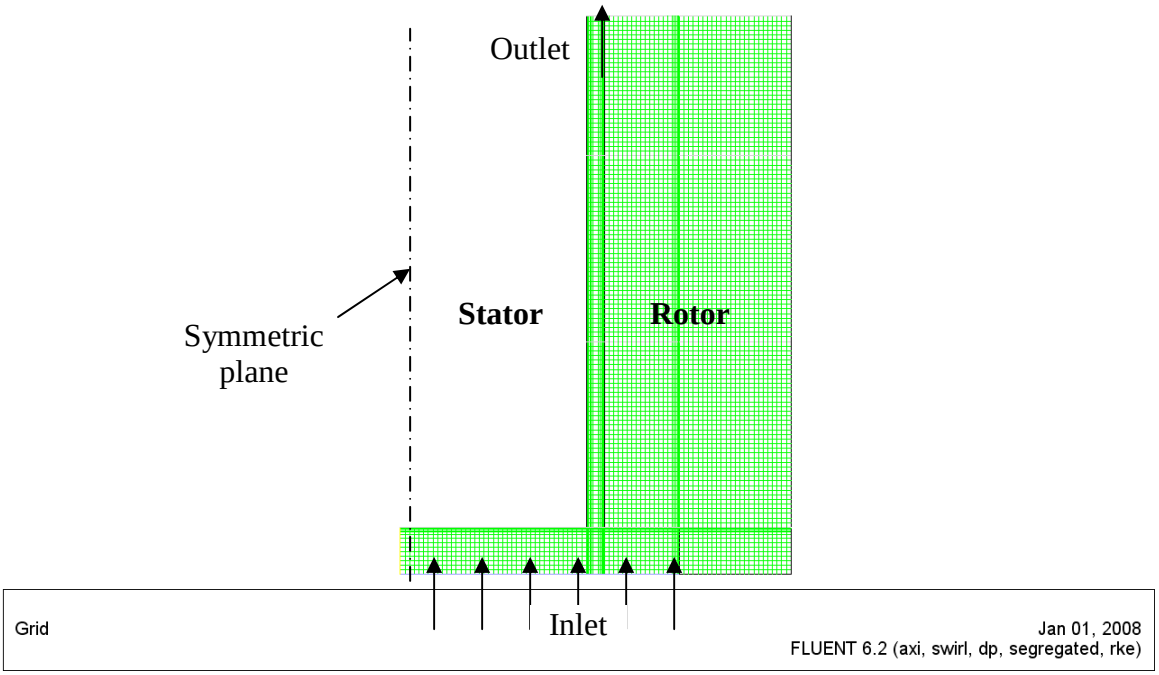

Fig. 3-26. The meshing grid of simplified axial flux permanent magnet generator.

3.5.4. Results and Discussions

The air temperatures predicted at the exit of each control volume of the AFPM generator from both the CFD and the thermal network circuit are plotted in Fig. 3-27(a). The Y- and X- axes of Fig. 3-27(a) represent the radial coordinate of the exit of each control volume and its corresponding air temperature, respectively. For example, a radial distance of 55mm represents the exit of CV1; a radial distance of 60mm represents the exit of CV2 etc. Large discrepancies were evident in the results obtained between the CFD and LPM techniques, as shown in Fig. 3-27(a). The temperatures predicted from the LPM technique are approximately 1 degree higher than the CFD predicted temperatures. The two temperature curves begin to deviate at the exit from CV1 (at radial distance 55mm), and remain almost parallel after the first control volume. These results reflect that the major error was inherent in CV1 and the error developed in CV1 was carried forward to the following control volumes. This is further illustrated in Fig. 3-28, where the relative error of each control volume is

plotted. The relative error of the exit of CV1 was about 32% and it was by far the highest compared with other control volumes.

Fig. 3-27(b) illustrates the temperature contours (in Kelvin) inside the AFPM generator obtained from CFD. Because the temperature at the bottom of the stator was a lot higher than the temperature inside the air gap, the temperature contour scale was adjusted so that the temperature increase in the radial direction in the air gap is visible. Consequently, the black contour located at the bottom of the stator winding represents that the air temperature was greater than 350K (77 degC).

The air temperature at the entrance of the air gap (radial distance of 55mm) was lower than the rotor disk temperature, (Fig. 3-27(b)). Hence, the heat travelled from the rotor disk to the air. As the air was slowly heated by the windings on the left hand side, the air temperature increased gradually in the radial direction. Around the middle point of the rotor disk, the air reached the same temperature as the rotor disk. After the middle point, the air was further heated by the stator, and its temperature was higher than the rotor solid temperature. Hence, the heat travelled from the air to the rotor disk. Table 3-1 shows the heat transfer calculated for each air control volume in the convective circuit. It indicates that the thermal equilibrium circuit is capable of taking account of heat flows in both directions, i.e. from air to solid and from solid to air, to predict the thermal state of the machine accurately.

Fig. 3-27(b) shows that the highest temperature occurred at the bottom of the stator winding, where the air velocity was the lowest. However, these results may change significantly if the generator boss is included into the model, where significant air flow impinges from the holes of the boss, to cool down the bottom of the stator winding.

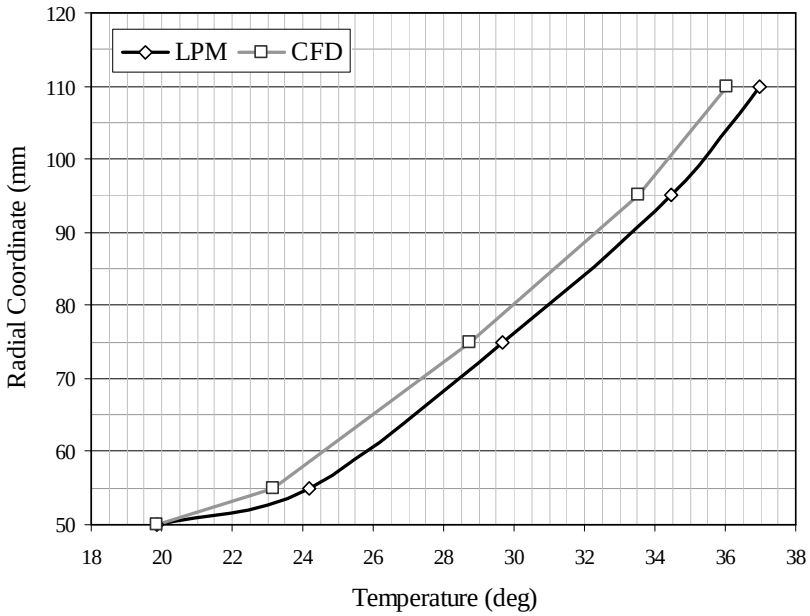

(a)

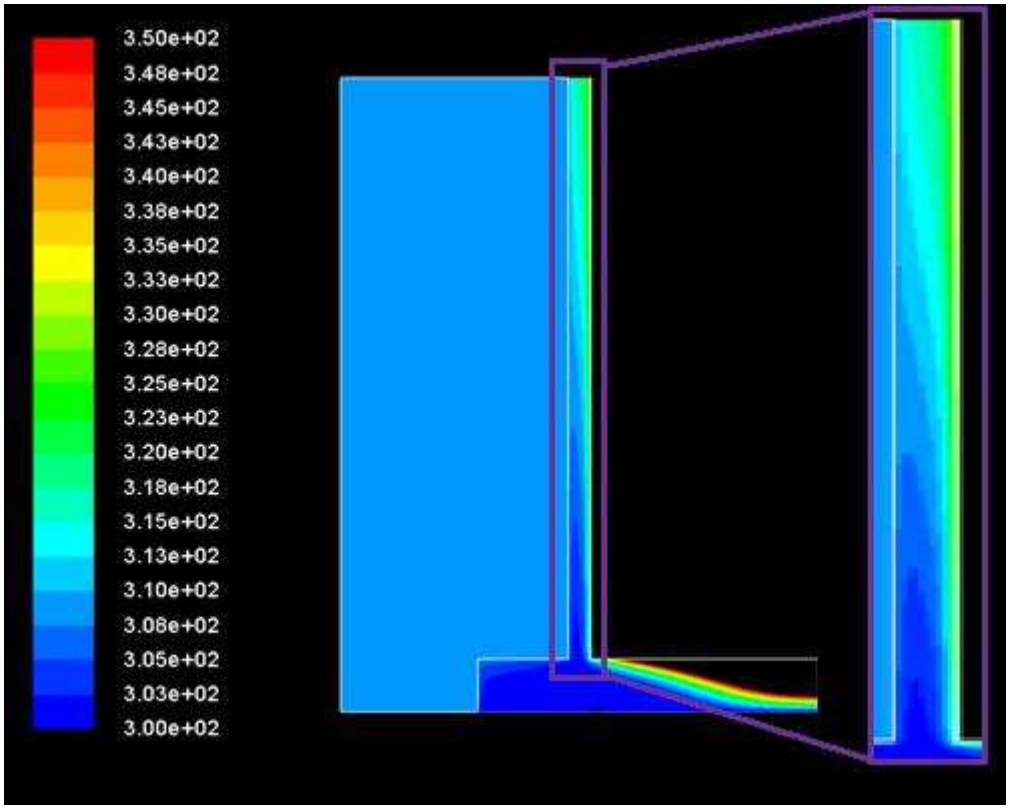

(b)

Fig. 3-27. Air temperature inside the simplified AFPM generator predicted from CFD models and lumped parameter thermal circuit.

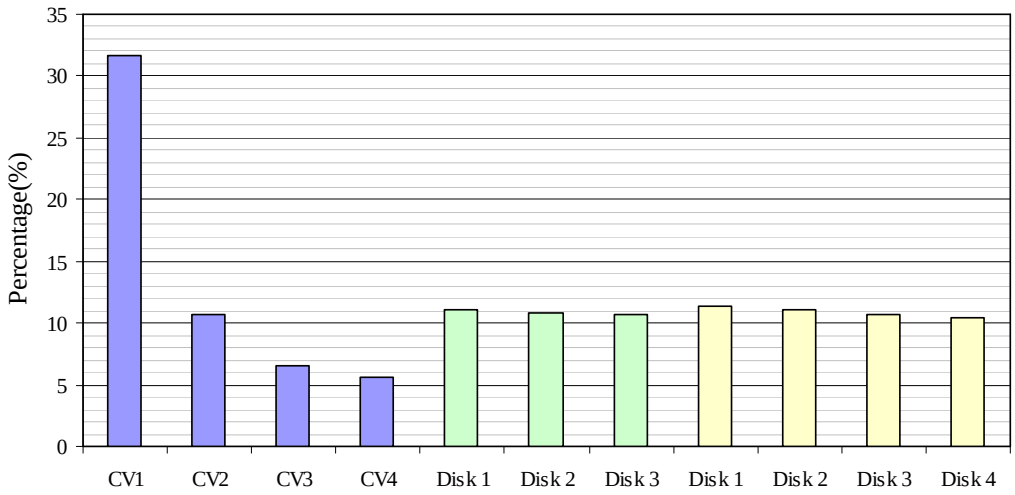

Fig. 3-28. Relative errors for components of the AFPM generator.

	Heat transfer (W)
CV1	-1.210
CV2	-3.156
CV3	0.800
CV4	4.426

Table 3-1: Convective heat transfer calculated from the thermal network circuit for each control volume.

The accuracy of the thermal network technique was further investigated by sub-dividing CV1 in the simplified AFPM model into three smaller control volumes, which were CV1-1, CV1-2 and CV1-3, (Fig. 3-29(a)). Hence, the original equivalent thermal circuit shown in Fig. 3-23(b) was modified to Fig. 3-29(b).

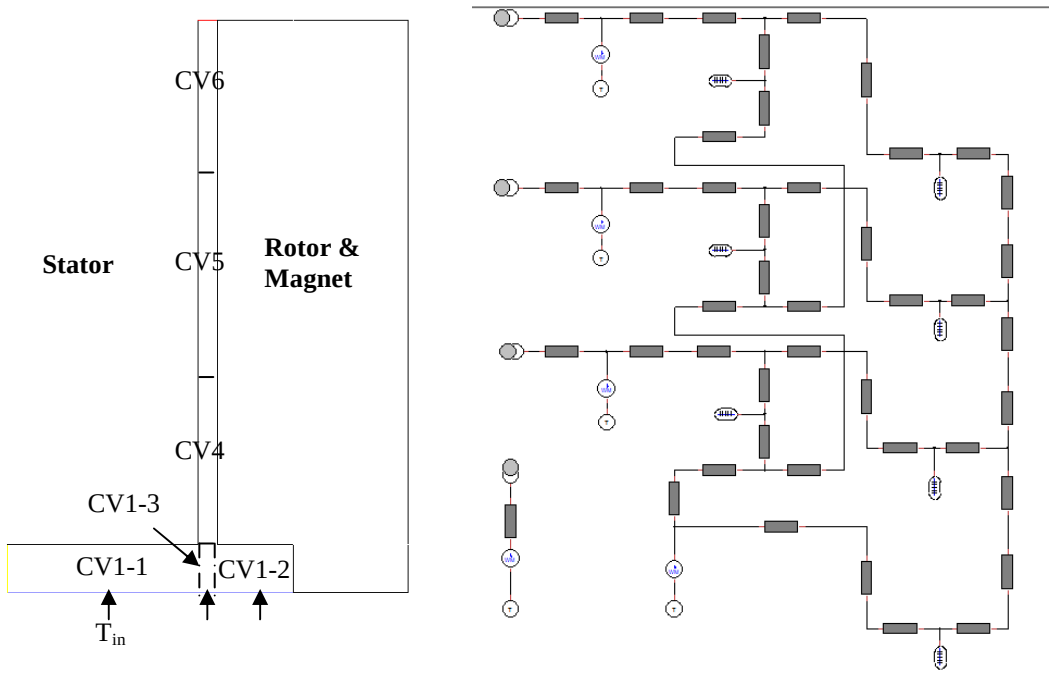

(a) (b)

Fig. 3-29. Improved simplified axial flux generator lumped parameter thermal network: Higher discretisation level.

The new thermal equivalent circuit was similar to the original circuit except the CV1 fluid flow circuit was modified into three separate circuits. Each of the separated fluid control volume convective circuit is shown as follows:

3.5.4.1. Control Volume 1-1 (CV1-1)

CV1-1 indicates the air node on the left hand side of original CV1, (Fig. 3-30(a)). In CV1-1, the heat generated from the stator is transferred by convection, to the fluid via the inner peripheral surface of the stator. With the convective resistance calculated from heat transfer coefficient obtained from the CFD model and the fluid mass flow rate, the outlet temperature of CV1-1, $T_{out1\text{-}1}$, can be calculated by equation (3.32). The equivalent thermal circuit of CV1-1 is shown in Fig. 3-30(b).

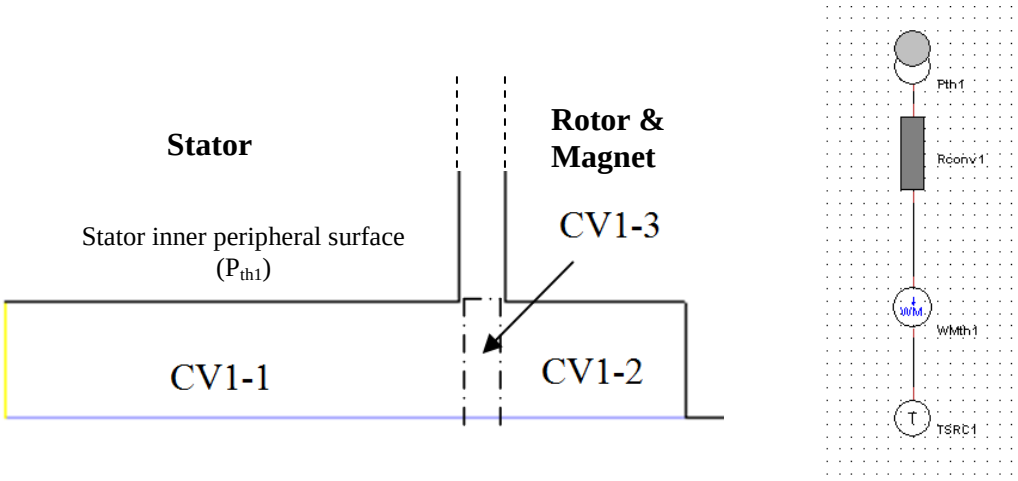

(a) (b)

Fig. 3-30. Fluid flow circuit of control volume 1-1 (CV1-1).

$$T_{out1-1} = \frac{q_{1-1}}{\dot{m}_{1-1} C_p} + T_{in1-1} = T_{in2-1} \tag{3.32}$$

Where q_{1-1} is the total transfer in CV1-1, T_{in1-1} is CV1-1 inlet temperature, T_{in1-2} is CV1-2 inlet temperature and $\dot{m}_{1-1}$ is the fluid mass flow rate.

3.5.4.2. Control Volume 1-2 (CV1-2)

Control volume 1-2 (CV1-2) and its corresponding thermal circuit are shown in Fig. 3-31(a) and (b) respectively. When the machine rotates, air is dragged from the surroundings by centrifugal force into CV1-2, to cool the magnets and rotor disk. The temperature at the outlet of CV1-2 can be estimated by equation (3.33), where q_{1-2} is the total heat transfer to CV1-2 via the two contact surfaces, $T_{mag\ surf}$ and $T_{rotor\ surf}$, and $\dot{m}_{1-2}$ is the air mass flow rate of CV1-2.

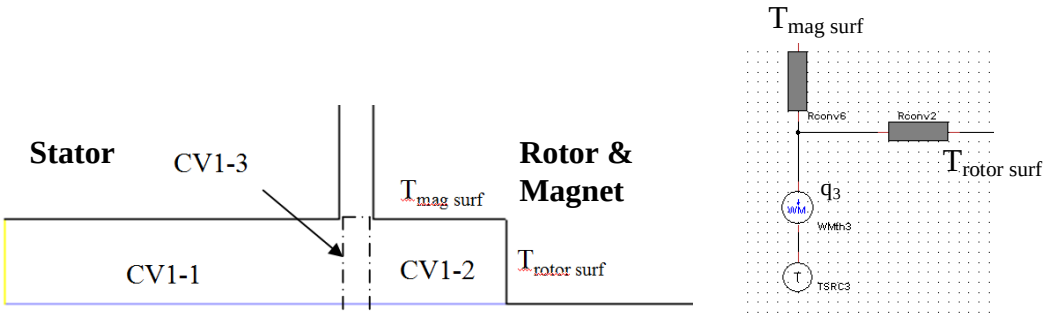

(a) (b)

Fig. 3-31. Fluid flow circuit of control volume 1-2 (CV1-2)

$$T_{out1-2} = \frac{q_{1-2}}{\dot{m}_{1-2} C_p} + T_{in} = T_{in2-2} \tag{3.33}$$

3.5.4.3. Control Volume 1-3 (CV1-3)

Unlike CV1-1 and CV1-2, CV1-3 is not directly in contact with any solid surface in the generator. Therefore, the governing thermal circuit of CV1-3, as shown in Fig. 3-32, was constructed only based on the energy conservation equation. No convective heat transfer/resistance exists in the CV1-3 thermal circuit model. The temperature at the outlet of CV1-3 is calculated directly by summing the total enthalpy of CV1-1, CV1-2 and inlet of CV1-3, see equations (3.34) and (3.35), $\dot{m}_{1-1}$, $\dot{m}_{1-2}$, $\dot{m}_{1-3}$ are the air mass flow rate in CV1-1, CV1-2 and CV1-3 respectively.

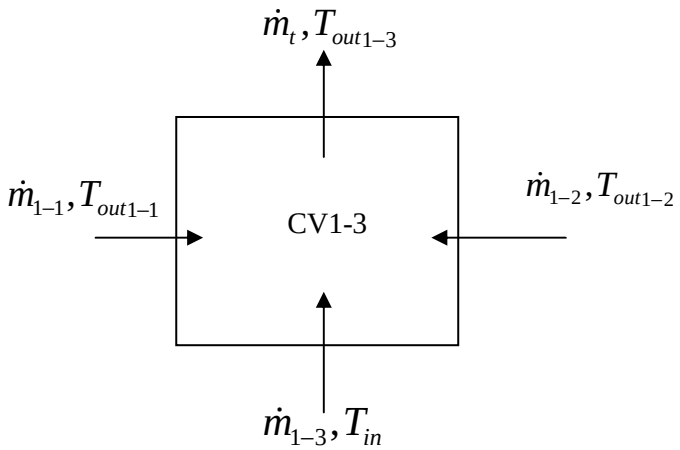

Fig. 3-32. Fluid flow circuit of control volume 1-3, (CV1-3)

$$T_{out1-3} = \frac{\dot{m}_{1-1}}{\dot{m}_t} T_{out1-1} + \frac{\dot{m}_{1-2}}{\dot{m}_t} T_{out1-2} + \frac{\dot{m}_{1-3}}{\dot{m}_t} T_{in} \quad (3.34)$$

$$\dot{m}_t = \dot{m}_{1-1} + \dot{m}_{1-2} + \dot{m}_{1-3} \quad (3.35)$$

Similarly, by using the mass flow rate and convective heat transfer coefficient extracted from the new CFD model into the modified lumped parameter thermal network circuit, new temperatures were predicted as illustrated in Fig. 3-33. By further discretising CV1 into three smaller control volumes, the accuracy of the lumped parameter thermal circuit has improved significantly. The temperatures predicted by the lumped parameter thermal circuit matched closely with the temperatures obtained for the CFD models. The maximum relative error is as low as 0.6%. This reflects that by splitting the complex fluid control volume into smaller and simpler control volumes has a very significant influence on the discrepancy of the lumped parameter technique and should be of great concern.

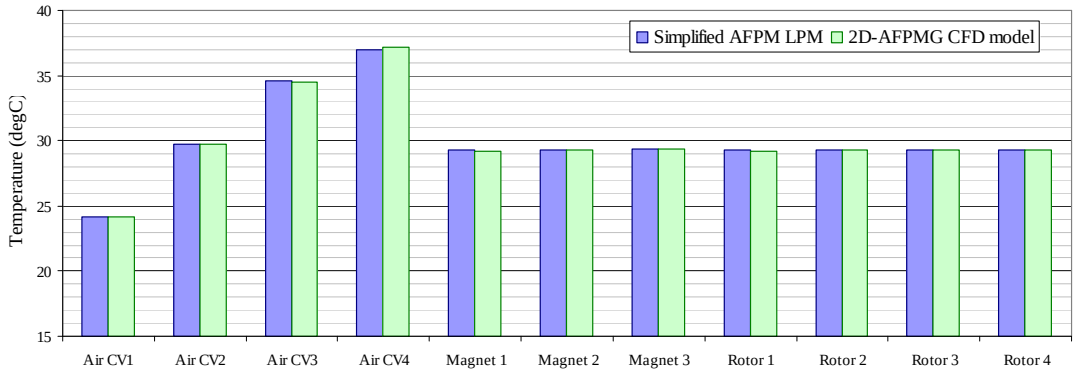

Fig. 3-33. Temperatures of the simplified axial flux generator predicted from lumped parameter thermal network model and CFD model.

3.5.5. Conclusions

The thermal network of the simplified AFPM generator was constructed and compared with the conventional CFD modeling technique. The results show a significant discrepancy at the first air control volume at the generator entrance. The error may due to the hydraulic resistance at the entrance of the narrow air gap.

However, further partitioning of the complex air control volume significantly improved the accuracy of the thermal network circuit.

3.6. Conclusions

A preliminary lumped parameter thermal equivalent circuit of an axial flux permanent magnet generator has been developed. The proposed thermal network circuit consists of two main circuits, which are the conductive and convective thermal circuits, to model both conduction and convection heat transfer inside the generator, respectively. The conductive thermal circuit was constructed based on the annulus ring conductive circuit; whereas, the Heat Pick-up Method (HPM) and the Temperature Passing Method (TPM) were investigated for the construction the convective thermal circuit.

Two case studies were conducted to verify the accuracy and compatibility of the proposed lumped parameter thermal equivalent circuit when compared with the solutions obtained from CFD models. The results show that by dividing the air inside the axial flux machine into simple fluid control volumes, the proposed lumped parameter thermal network was capable of predicting accurate solutions for the 2-D simplified axial flux permanent magnet generator. In the future, the same technique will be applied to construct the thermal equivalent circuit of 3D axial flux machines. The results obtained from the thermal equivalent circuit were compared with the temperatures measured from the experiments to further verify the modelling method.

Chapter 4

Stator Winding Thermal Modelling

4.1. Introduction

Resistive loss in the stator windings is known as the major heat source in most electrical machines. During the normal machine daily operation cycle, the temperature hot spots normally occur in the machine windings. This is due to Joule losses in the winding conductors and low thermal conductivity of the winding filling/insulation. Under extremely high temperature conditions, the insulation on the stator winding breaks down and the performance of the electrical machine deteriorates. Hence, it is paramount to model the thermal properties of the stator winding of electrical machines accurately, to identify the temperature distribution and to improve its cooling.

4.2. Stator Winding Radial Thermal Resistance- Simple Concentric Model (SCM)

Fig. 4-1 shows the cross-sectional view of a single stator cable of radius *r*. The shaded circles indicate the copper conductor (discontinuous phase) and the white area indicates the winding filling or insulation (continuous phase).

Consider an arc sector of angle $d\theta$, at an angle θ from the horizontal centre line in the stator cable, where t_1, t_2, t_3, …, t_n are the perpendicular distances travelled by heat through the arc sector in the radial direction. For a small angle, $d\theta$, it is reasonable to assume that the arc sector of angle $d\theta$, as a triangle, where the base width of the triangle is equal to the arc length, $r\,d\theta$, (Fig. 4-2 (a)).

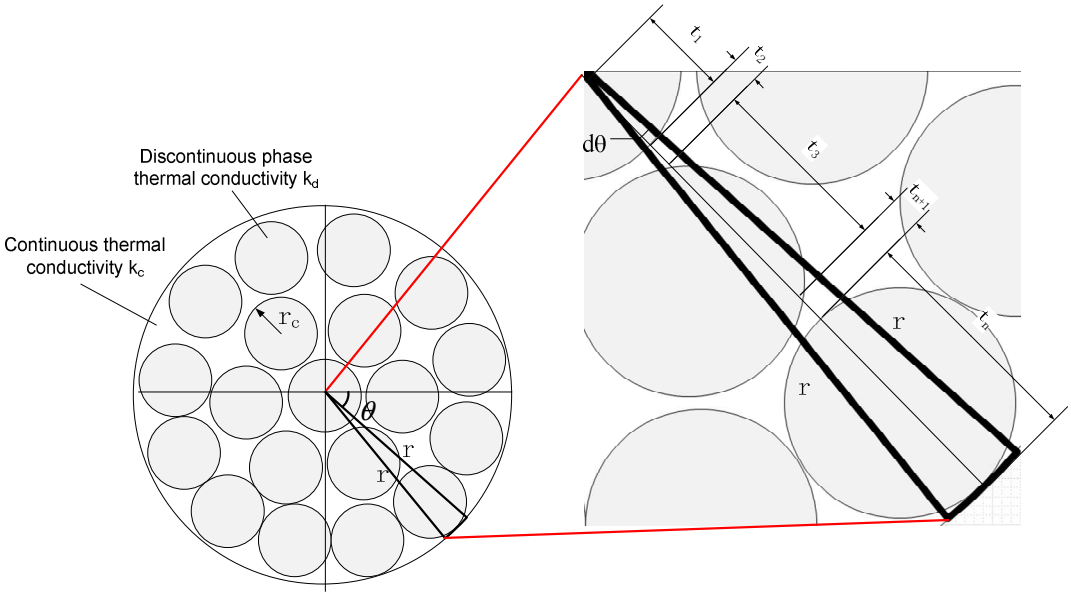

Fig. 4-1: Cross-section view of a stator winding

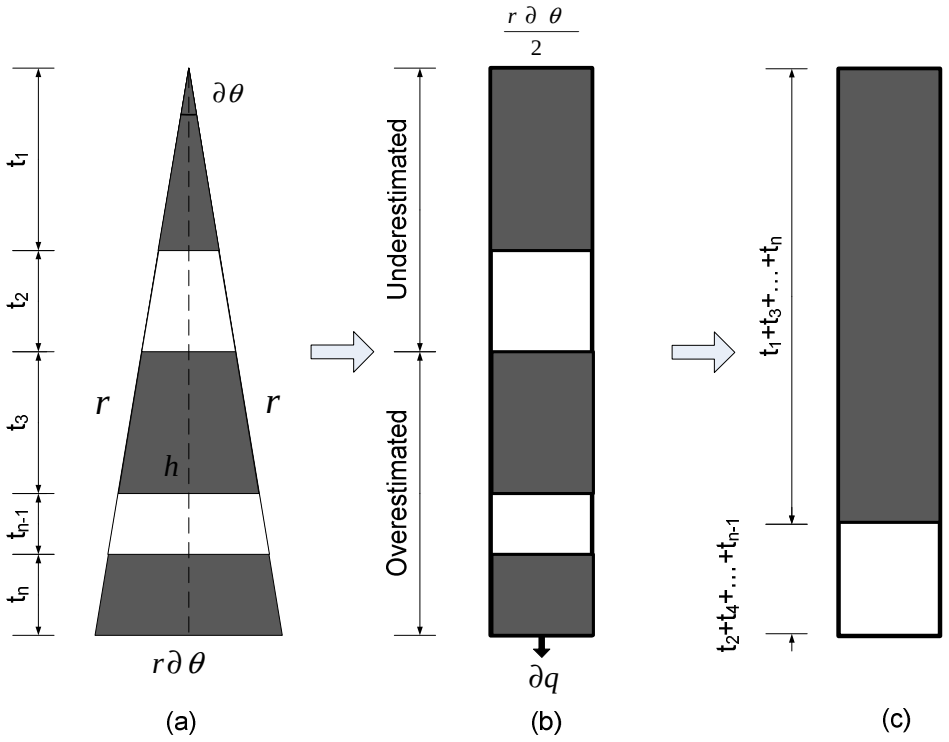

Fig. 4-2: Stator wiring triangle sector

It is impossible to calculate the thermal resistance of the triangle section unless the height of the triangle and trapeziums, t_1, t_2, t_3,…, t_{n-1}, t_n are known for specific θ. These heights vary at different angular position around the stator wire. Hence, to obtain a simple but physically significant analytical solution for the radial thermal resistance in the stator wire, the triangle section is transformed into a rectangle, where the height and width of the rectangle are h and $r\partial\theta/2$ respectively, (Fig. 4-2(b)). In this study, only the heat flux in the radial direction is considered. It is also assumed that the radial heat flux is independent of the heat fluxes in circumferential and axial directions.

Thermal resistance is inversely proportional to the cross sectional area of the medium, A, perpendicular to the heat flux direction. This can be noted from equation (4.1).

$$R_{thermal} = \frac{L}{kA} \tag{4.1}$$

For a triangle section, the cross sectional area (or base) increases as radius increases. For example, at t_1, the cross sectional area is t_1 x $d\theta$ x L ; at (t_1+t_2), the cross sectional area is $(t_1+ t_2)$ x $d\theta$ x L, etc. But for the rectangle section, the cross section is constant in the radial direction, which is equal to r x L x $d\theta/2$. As noted from Fig. 4-2(a) and (b), the cross sectional area of the triangle section is smaller than the rectangle section at the upper half section; but larger at the bottom half. Therefore, the thermal resistances of the rectangle section are lower in the upper half and higher in the lower part, than the actual thermal resistances of the triangle section. In consequence, the sum of thermal resistances of the upper and bottom half of the triangle calculated from the rectangle model is approximately equal to the total thermal resistance calculated from the triangle section. However, this approximation is only valid for small radius, r.

Also, since the rectangles have uniform width at all radii, it is acceptable to lump all the discontinuous (conductor) phase portions (shaded in grey in Fig. 4-2(b)) and the remaining continuous (winding filling) phase portions (indicated in white in Fig. 4-

2(b)) together into two separated rectangles stacking one above another, see Fig. 4-2(c).

By applying the one dimensional Fourier's law to the rectangle blocks, the heat flow across the rectangle block is:

For heat across the continuous phase (cable filling) volumes,

$$\partial q = \frac{r\partial\theta}{2} L\left(k_c \frac{\Delta T_c}{t_c} \right) \tag{4.2}$$

For heat across the discontinuous phase (copper conductors) volumes,

$$\partial q = \frac{r\partial\theta}{2} L\left(k_d \frac{\Delta T_d}{t_d} \right) \tag{4.3}$$

And for heat across the mixture (both cable filling and copper conductors)

$$\partial q = \frac{r\partial\theta}{2} L\left(\frac{k_{eq}\Delta T_{total}}{r} \right) \tag{4.4}$$

Where as:

$$\begin{aligned}
\Delta T_c &= \Delta T_2 + \Delta T_4 ... + \Delta T_{n-1} \\
\Delta T_d &= \Delta T_1 + \Delta T_3 ... + \Delta T_n \\
\Delta T_{total} &= \Delta T_1 + \Delta T_2 + \Delta T_3 + \Delta T_4 ... + \Delta T_{n-1} + \Delta T_n \\
t_c &= t_2 + t_4 ... + t_{n-1} \\
t_d &= t_1 + t_3 + ... + t_n \\
r &= t_c + t_d
\end{aligned}$$

And, since $\Delta T_{total} = \Delta T_d + \Delta T_c$, equation (4.3) can be represented as:

$$\partial q = \frac{r}{2} L\left(k_d \frac{\Delta T_{total} - \Delta T_c}{t_d} \right) \partial\theta \tag{4.5}$$

$$\partial q = \frac{r}{2} L\left(k_d \frac{\Delta T_{total}}{t_d} \right) \partial\theta - \frac{r}{2} L\left(k_d \frac{\Delta T_c}{t_d} \right) \partial\theta \tag{4.6}$$

By arranging equation (4.2), ΔT_c can be represented as:

$$\Delta T_c = \frac{2\partial q t_c}{L k_c r \partial\theta} \tag{4.7}$$

Substitute (7) to (6),

$$\partial q = \frac{r}{2} L\left(k_d \frac{\Delta T_{total}}{t_d}\right)\partial\theta - \frac{r}{2} L\left(k_d \frac{2\partial q t_c}{t_d L k_c r \partial\theta}\right)\partial\theta \tag{4.8}$$

$$\partial q = \frac{r}{2} L\left(k_d \frac{\Delta T_{total}}{t_d}\right)\partial\theta - \left(\frac{k_d t_c}{t_d k_c}\right)\partial q \tag{4.9}$$

$$\left(1 + \frac{k_d t_c}{t_d k_c}\right)\partial q = \frac{L r \Delta T_{total} k_d}{2 t_d}\partial\theta \tag{4.10}$$

$$\partial q = \frac{L r \Delta T_{total} k_d}{2 t_d} x \frac{t_d k_c}{t_d k_c + t_c k_d}\partial\theta \tag{4.11}$$

$$\partial q = \frac{L r \Delta T_{total} k_c k_d}{2\left(t_d k_c + t_c k_d\right)}\partial\theta \tag{4.12}$$

Substitute $t_c = r - t_d$ to equation (4.12)

$$\partial q = \frac{L r \Delta T_{total} k_c k_d}{2\left(t_d k_c + (r - t_d) k_d\right)}\partial\theta \tag{4.13}$$

By taking integration in equation (4.13),

$$\int \partial q = \int_0^{2\pi} \frac{L r \Delta T_{total} k_c k_d}{2\left(t_d k_c + (r - t_d) k d\right)}\partial\theta \tag{4.14}$$

To simplify equation (4.14), it is reasonable to assume that there is no circumferential heat flux in the stator cable, hence ΔT_{total} is constant in the circumferential direction.

Hence equation (4.14) can be simplified as:

$$Q = \frac{k_d k_c L r \Delta T_{total}}{2} \int_0^{2\pi} \frac{1}{\left(t_d k_c + (r - t_d) k_d\right)}\partial\theta \tag{4.15}$$

And

$$R_{thermal} = \frac{\Delta T_{total}}{Q} = \frac{2}{L k_d k_c r \int_0^{2\pi} \frac{1}{\left(t_d k_c + (r - t_d) k_d\right)}\partial\theta} \tag{4.16}$$

To obtain the total equivalent thermal resistance, $R_{thermal}$, of the sector section (shown in Fig. 4-2(a)) from equation (4.16), it is necessary to know the wiring conductor thickness profile, t_d, and cable filling thickness profile, t_c, in the function of θ of the specific cable. But, t_d and t_c vary with the composition of the conductor and winding filling along the radial coordinate. In addition, such information is not easily available. Fig. 4-3 and Fig. 4-4 show examples of t_d and t_c at different radial coordinates of a 5mm diameter stator wire in a histogram and polar diagram respectively.

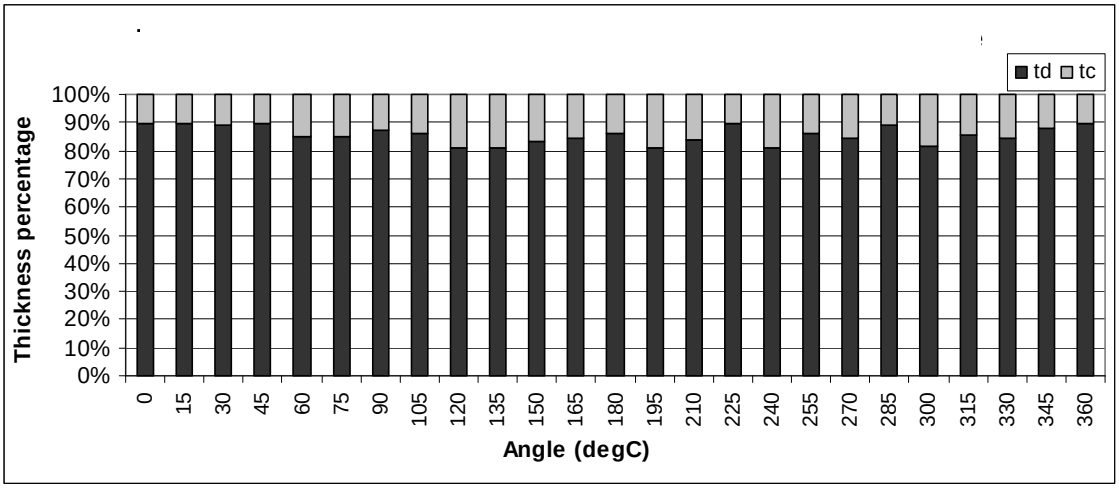

Fig. 4-3. Histogram of thickness percentage of conductor and winding filling at different angle

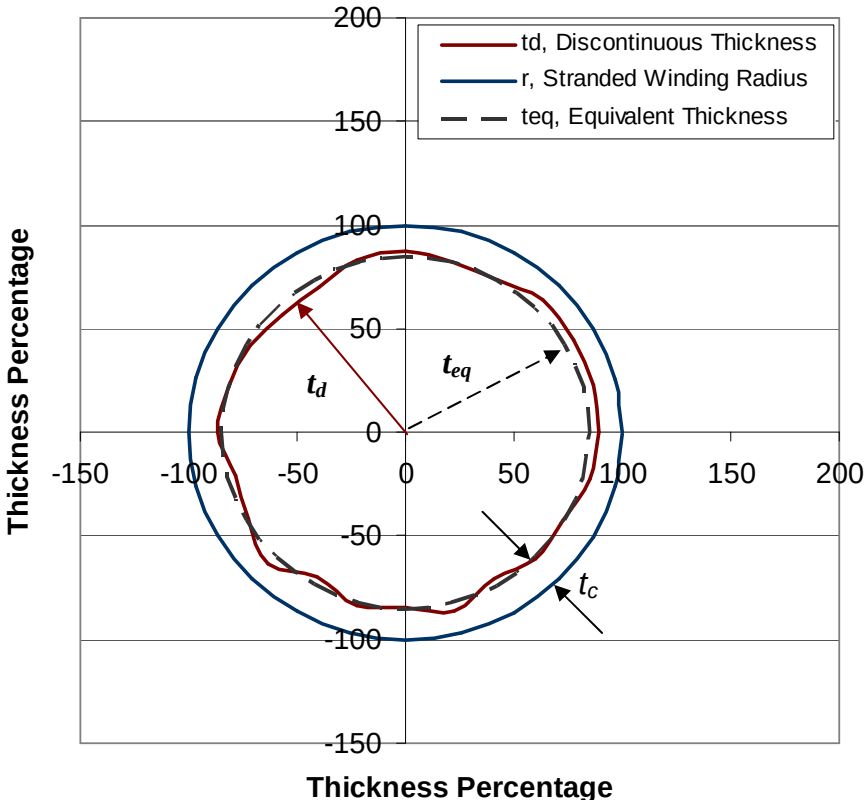

Fig. 4-4. Polar diagram of thickness percentage of the discontinuous phase (copper conductor) and the continuous phase (winding filling).

It is to be noted that the variation of t_c in the stator wire is small and it is acceptable to be represented as a constant equivalent radius, r_{eq}. If the winding packing ratio, A_d is known, the equivalent radius can be calculated as:

$$A_d = \frac{\pi r_{eq}^{\ 2}}{\pi r^{\ 2}} \tag{4.17}$$

$$r_{eq} = r \times \sqrt{A_d} \tag{4.18}$$

Where,

r_{eq} is the equivalent radius

r is the winding radius

Hence equation (4.16) can be written as:

$$R_{thermal} = \frac{2\left((r - r_{eq})k_d + r_{eq}k_c\right)}{Lk_d k_c r \int_0^{2\pi} \partial\theta} \tag{4.19}$$

$$= \frac{rk_d - r\sqrt{A_d}k_d + r\sqrt{A_d}k_c}{\pi Lk_d k_c r} \tag{4.20}$$

$$= \frac{k_d\left(1-\sqrt{A_d}\right)+\sqrt{A_d}k_c}{\pi Lk_d k_c} \tag{4.21}$$

And hence, the equivalent thermal conductivity can be obtained by:

$$k_{eq} = \frac{1}{\pi R_{thermal} L} \tag{4.22}$$

$$k_{eq} = \frac{k_d k_c}{k_d\left(1-\sqrt{A_d}\right)+\sqrt{A_d}k_c} \tag{4.23}$$

For high k_d , where $k_d >> k_c$,

$$k_{eq} = \frac{k_d k_c}{k_d\left(1-\sqrt{A_d}\right)} \tag{4.24}$$

$$= \frac{k_c}{\left(1-\sqrt{A_d}\right)} \tag{4.25}$$

4.3. Improved model: Concentric Annular layer model (CLM)

Unlike the two-phase materials, the conductors inside the stator winding act as the independent heat sources when current passes through. The position and composition of these heat sources in the stator winding affect the equivalent thermal resistance of the stator winding significantly. In order to take into account the distributed heat sources inside the stator winding, the stator winding thermal resistance model is improved by further dividing the winding into a centre circle and *N* layers of concentric annuli, (Fig. 4-5(a)). Each split control volume's conductor-to-winding area ratio is kept the same as the winding packing ratio.

Thermal resistances of the centre circle and each annular layer are calculated from known theories. By adding each individual calculated thermal resistance of the centre

circle and the concentric annuli, the equivalent radial thermal resistance of the stator winding can be evaluated. Fig. 4-5(a) shows the stator winding is separated into one centre circle and two annuli control volumes. In general, the number of annular layers can be predicted based on the radii of the copper conductor, r_c, and the winding, r_{sc}, from equation (4.27), (Fig. 4-5(b)).

$$N \times 2r_c + r_c \approx r_{sc} \tag{4.26}$$

$$N \approx \frac{1}{2}\left(\frac{r_{sc}}{r_c} - 1\right) \tag{4.27}$$

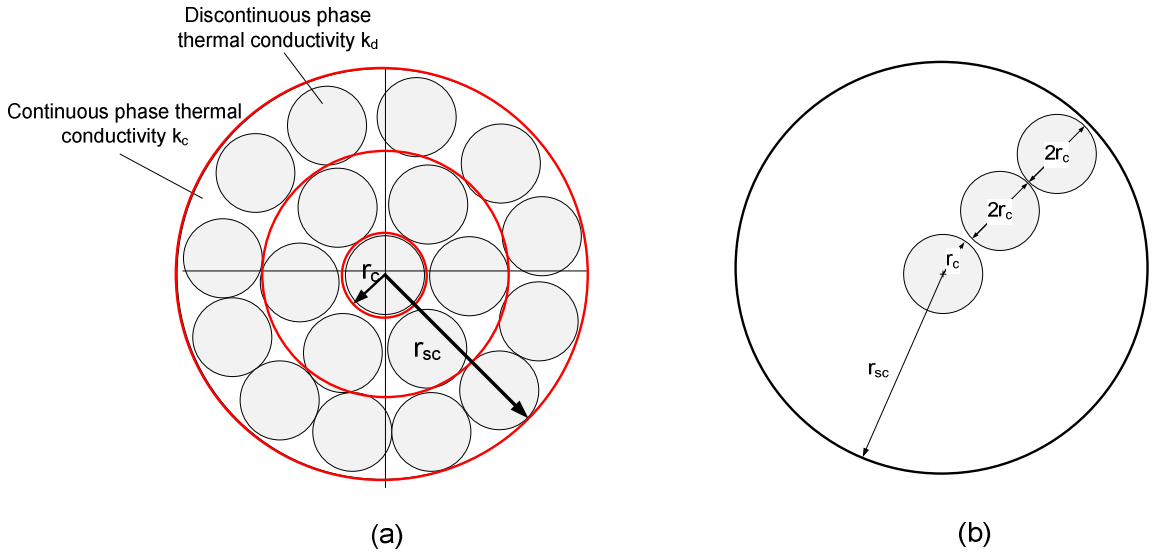

Fig. 4-5(a) and (b). Stator winding divided into 3 concentric circles.

4.3.1. Thermal Resistance of the Centre Circle

Fig. 4-6 shows the centre circle split from the stator winding model. The centre circle consists of two components, which are the conductor (discontinuous phase shaded in grey) and the winding filling (continuous phase shaded in white). r_c is the radius of the single conductor and the radius of the center circle, r_{eq_0}, is determined by the winding packing ratio, A_d, of the winding, see equation (4.29).

$$A_d = \frac{\pi r_c^{\,2}}{\pi r_{eq\_0}^{\,2}} \tag{4.28}$$

$$r_{eq\_0} = \frac{r_c}{\sqrt{A_d}} \tag{4.29}$$

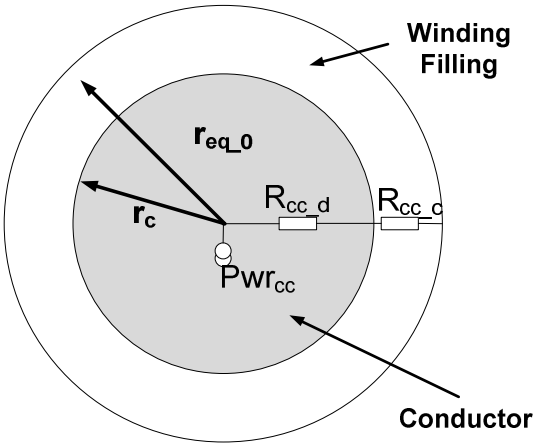

Fig. 4-6. Thermal circuit of centre circle of the stator cable

Fig. 4-6 illustrates that the thermal circuit of the centre circle corresponds to the two thermal resistances, which are the centre conductor (discontinuous phase) resistance, $R_{cc\text{-}d,}$ and the winding filling (continuous phase) resistance, $R_{cc\text{-}c}$, respectively. The thermal resistances are derived theoretically from the heat conduction equation in the radial direction. These are given in terms of the dimension of the centre circle and corresponding thermal conductivities, by the equations (4.30) to (4.32).

The radial thermal resistance of the centre circle control volume, $R_{cc\text{-}d}$, is calculated by the annulus radial thermal resistance equation shown in equation (4.30):

$$R_{radial} = \frac{1}{4\pi k_r L}\left[1 - \frac{2r_{in}^{\,2}\ln\left(\frac{r_{out}}{r_{in}}\right)}{\left(r_{out}^{\,2} - r_{in}^{\,2}\right)}\right] \tag{4.30}$$

Since R_{cc_d} is the radial thermal resistance of a solid cylinder, equation (4.30) can be used to calculate R_{cc_d} by substituting $r_{in} = 0$:

$$R_{cc\_d} = \frac{1}{4\pi k_d L} \tag{4.31}$$

The winding filling annulus thermal resistance, $R_{cc\text{-}c}$, is obtained by applying the standard hollow cylinder conduction equation [33], as shown in equation (4.32).

$$R_{cc\_c} = \frac{\ln\left(\frac{r_{eq\_0}}{r_c}\right)}{2\pi k_c L} \tag{4.32}$$

The joule loss of the winding conductor is taken into account as Pwr_{cc} in the centre circle thermal circuit and it is defined as:

$$Pwr_{cc} = I^2 \times \left(\rho_o \frac{\pi r_c^{\,2}}{L}\right) \times \left(1 + \alpha\left(T - 293\ K\right)\right) \tag{4.33}$$

Where α is the temperature constant of the conductor

ρ_o is the resistivity of the conductor at 293K

T is the temperature of the conductor

4.3.2. Thermal Resistance of the Winding Annulus

To analyse the thermal resistance of the annulus shown in Fig. 4-7(a), the heat flow path through the annulus was investigated. Fig. 4-7(a) indicates a winding annulus, where the annulus' inner and outer radii are r_{eq_0} and r_{eq_1}. The heat generated from the centre circle control volume, Pwr_{cc}, flows into the annulus through a layer of continuous phase material (winding filling), see Fig. 4-7(b). Subsequently, together with the heat generated from the annular copper conductor, the heat flows to the outer radius of the annulus via another layer of continuous phase material. The circumferential heat transfer in the stator winding was assumed to be negligible.

The heat flow paths in the annulus were simplified schematically and shown in Fig. 4-7(c). It can be noted there are three main heat flow paths in the system, which are the q_{top}, q_{middle} and q_{bottom}. In general, the cross sectional areas of the top and bottom heat flow paths are relatively smaller than the mid flow path. In addition, the thermal conductivities of the windings' conductor are very high as compared with the winding filling. The heat passing through the top and bottom continuous phases is usually small and can be neglected. Thus, only the middle heat flow path was considered.

The winding annulus was further simplified to four sub-annuli, as shown in Fig. 4-7(d). The total equivalent thermal resistance of the winding annulus was calculated by applying the standard hollow cylinder conduction equation (4.32) into each of the annuli with its corresponding dimension (inner and outer radii) and thermal conductivities. The following equations show how the radii of the four annuli were derived.

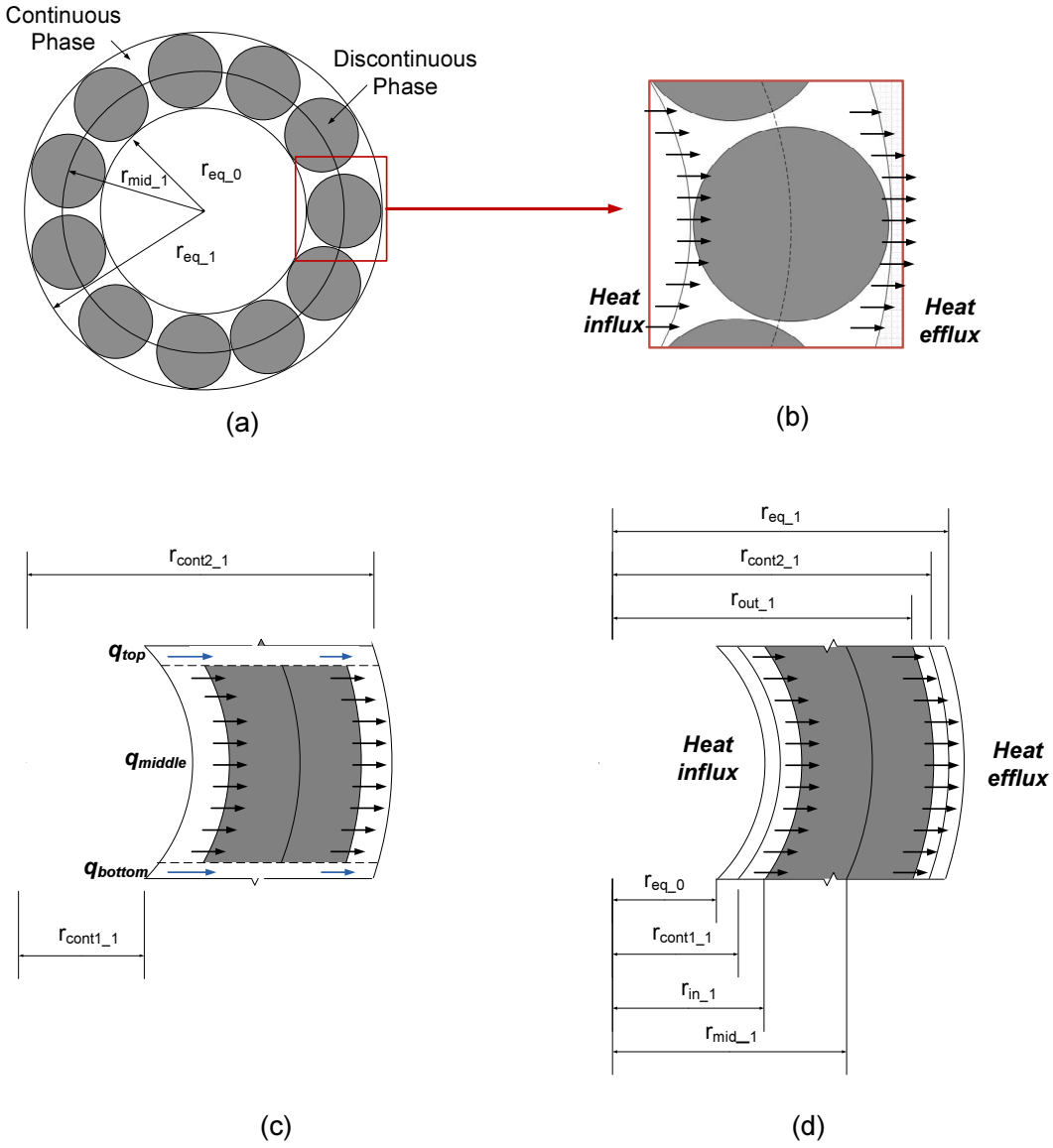

Fig. 4-7. First stator winding annulus after the center circle.

r_{eq_0} was obtained by equation (4.29). If the stator winding is separated into N layers of annuli, r_{eq_1} can be deduced from:

$$r_{eq\_1} - r_{eq\_0} = \frac{r_{sc} - r_c}{N} \tag{4.34}$$

$$r_{eq\_1} = r_{eq\_0} + \frac{r_{sc} - r_c}{N} \tag{4.35}$$

The middle radius, r_{mid_1}, as indicated in Fig. 4-7(a) separates the annulus into two equal area annuli. Therefore, r_{mid_1} is derived as:

$$\frac{\pi\left(r_{mid\_1}^{\ 2} - r_{eq\_0}^{\ 2}\right)}{\pi\left(r_{eq\_1}^{\ 2} - r_{eq\_0}^{\ 2}\right)} = \frac{1}{2} \tag{4.36}$$

$$r_{mid\_1} = \sqrt{\frac{r_{eq\_1}^{\ 2} + r_{eq\_0}^{\ 2}}{2}} \tag{4.37}$$

r_{in_1} and r_{out_1} can be calculated from equation (4.42) and equation (4.43) respectively, based on the winding packing ratio, A_d, r_{eq_0} and r_{eq_1}.

For the inner half annulus,

$$A_d = \frac{\pi r_{mid\_1}^{\ 2} - \pi r_{in\_1}^{\ 2}}{\pi r_{mid\_1}^{\ 2} - \pi r_{eq1}^{\ 2}} \tag{4.38}$$

$$r_{in\_1} = \sqrt{(1 - A_d) r_{mid\_1}^{\ 2} + A_d r_{eq\_0}^{\ 2}} \tag{4.39}$$

For the outer half annulus,

$$A_d = \frac{\pi r_{out\_1}^{\ 2} - \pi r_{mid\_1}^{\ 2}}{\pi r_{eq2}^{\ 2} - \pi r_{mid\_1}^{\ 2}} \tag{4.40}$$

$$r_{out\_1} = \sqrt{(1 - A_d) r_{mid\_1}^{\ 2} + A_d r_{eq\_1}^{\ 2}} \tag{4.41}$$

By substituting equation (4.37) to equation (4.39) and equation (4.41),

$$r_{in\_1} = \sqrt{\frac{(1 - A_d)}{2} r_{eq\_1}^{\ 2} + \frac{(1 + A_d)}{2} r_{eq\_0}^{\ 2}} \tag{4.42}$$

$$r_{out\_1} = \sqrt{\frac{(1+A_d)}{2} r_{eq\_1}{}^2 + \frac{(1-A_d)}{2} r_{eq\_0}{}^2} \tag{4.43}$$

To simplify the model shown in Fig. 4.7(c) to the four annuli model the shown in Fig. 4.7(d), the gaps in between two discontinuous particles (or conductors) are important, to evaluate the inner and outer radii of the middle continuous phase annuli, r_{cont1_1} and r_{cont2_1} respectively. The gap ratio, which is defined as the ratio of total circumferential angle occupied by the winding filling with the total stator winding, vary around 10-20%, depending on the configuration and size of the discontinuous particles (copper conductor), i.e. closely packed, small discontinuous particles have a lower the gap ratio compared with loosely packed, large discontinuous particles. However, it is difficult to obtain the exact continuous-discontinuous phase gap ratio due to the complexity and unpredictability in the mixture. A simple way to approximate the gap ratio using the radii of the discontinuous particle, r_d, and the mixture, r_m is illustrated in Fig. 4-8. Considering the outer layer of discontinuous particles in the mixture, the equivalent gap ratio can be estimated by dividing the total arc angle occupied by the gap, by 360 degrees, equation (4.44).

$$G_{ratio} = \frac{360 - (n_{sc} \times \theta)}{360} \tag{4.44}$$

Where,

$$\theta = 2 \times \cos^{-1}\left(\frac{2(r_m - r_d)^2 - r_d{}^2}{(r_m - r_d)^2}\right) \tag{4.45}$$

n_{sc} = number of continuous particles at the outer layer of the mixture

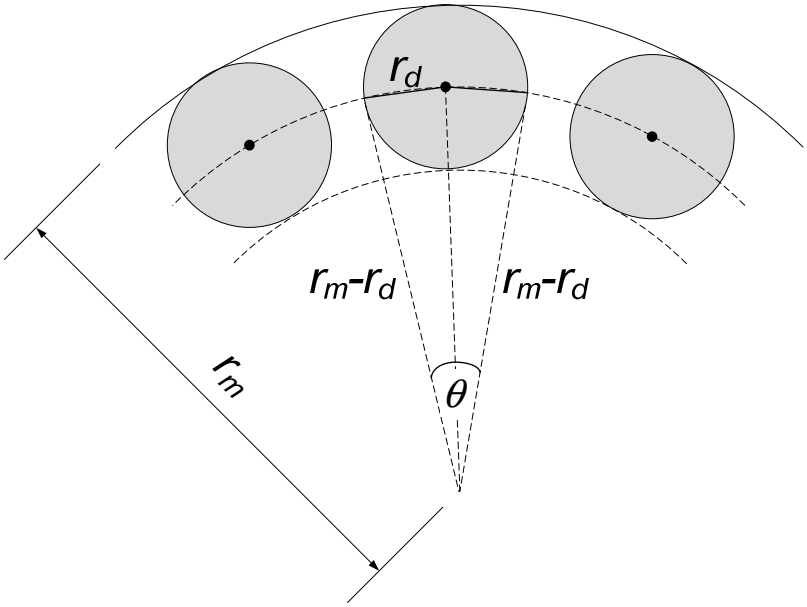

Fig. 4-8. The outer annular layer of the mixture with discontinuous particles.

With the gap ratio approximated by equation (4.45), the middle annuli inner and outer radii, r_{cont_1} and r_{cont_2} can be evaluated as follow:

$$\frac{\pi\left(r_{in\_1}^{\ 2} - r_{cont\ 1\_1}^{\ 2}\right)}{\pi\left(r_{mid\ \_1}^{\ 2} - r_{cont\ \_1}^{\ 2}\right)} = \left(1 - G_{ratio}\ \right)\times A_d \tag{4.46}$$

$$r_{cont\ \_1} = \sqrt{\frac{r_{in\_1}^{\ 2} - \left(1 - G_{ratio}\ \right)\times\left(1 - A_d\right)r_{mid\ \_1}^{\ 2}}{1 - \left(1 - G_{ratio}\ \right)\times\left(1 - A_d\right)}} \tag{4.47}$$

$$\frac{\pi\left(r_{cont\ 2\_1}^{\ 2} - r_{out\ \_1}^{\ 2}\right)}{\pi\left(r_{cont\ 2\_1}^{\ 2} - r_{mid\ \_1}^{\ 2}\right)} = \left(1 - G_{ratio}\ \right)\times A_d \tag{4.48}$$

$$r_{cont\ 2\_1} = \sqrt{\frac{r_{out\ \_1}^{\ 2} - \left(1 - G_{ratio}\ \right)\times\left(1 - A_d\right)r_{mid\ \_1}^{\ 2}}{1 - \left(1 - G_{ratio}\ \right)\times\left(1 - A_d\right)}} \tag{4.49}$$

Fig. 4-9 shows the thermal circuit of the stator winding annulus. $R_{c1\text{-}1}$ and $R_{c2\text{-}1}$ indicate the thermal resistances of the continuous phase (winding filler) layers, which can be calculated from the standard hollow cylinder conduction equations as follows:

$$R_{c1\text{–}1} = \frac{\ln\left(\frac{r_{in\_1}}{r_{cont1\_1}}\right)}{2\pi k_c L} \tag{4.50}$$

$$R_{c\,2-1} = \frac{\ln\left(\frac{r_{cont\_2\_1}}{r_{rout\_1}}\right)}{2\pi k_c L} \tag{4.51}$$

The two discontinuous (copper conductor) phase annuli in between the two continuous (winding filler) layers are lumped into one annulus, and the thermal resistances, $R_{d1\text{-}1}$, $R_{d2\text{-}1}$ and $R_{d3\text{-}1}$ can be deduced from T-equivalent circuits, seen as follows:

$$R_{d\,1-1} = \frac{1}{4\pi k_d L}\left[1 - \frac{2r_{in\_1}{}^2 \ln\left(\frac{r_{out\_1}}{r_{in\_1}}\right)}{\left(r_{out\_1}{}^2 - r_{in\_1}{}^2\right)}\right] \tag{4.52}$$

$$R_{d\,2-1} = \frac{1}{4\pi k_d L}\left[\frac{2r_{out\_1}{}^2 \ln\left(\frac{r_{out\_1}}{r_{in\_1}}\right)}{\left(r_{out\_1}{}^2 - r_{in\_1}{}^2\right)} - 1\right]$$

$$R_{d\,3-1} = -\frac{1}{8\pi k_d L\left(r_{out\_1}{}^2 - r_{in\_1}{}^2\right)}\left[r_{in\_1}{}^2 + r_{out\_1}{}^2 - \frac{4r_{out\_1}{}^2 r_{in\_1}{}^2 \ln\left(\frac{r_{out\_1}}{r_{in\_1}}\right)}{\left(r_{out\_1}{}^2 - r_{in\_1}{}^2\right)}\right] \tag{4.53}$$

(4.54)

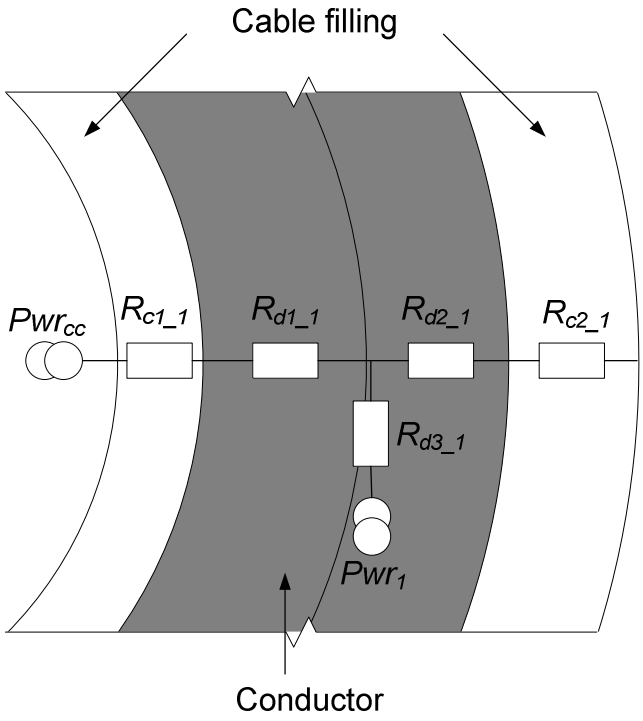

Fig. 4-9. Thermal circuit of the stator winding annulus

Since the copper conductors are distributed randomly inside the stator winding, the heat generated from each of the copper conductors travels to the winding outer periphery via different paths and distances. For example the heat generated by the conductors near to the outer surface of the winding travels a shorter path as compared with heat generated by the conductors at the stator winding centre. As a result, each heat source has a different local thermal resistance corresponding to its travelled distance and medium. In general, these local thermal resistances reduce as the radius increases in the stator winding.

In evaluating the equivalent thermal resistance for the stator winding, it is necessary to take into account of the heat generated due to Joule loss in the each individual conductor in the stator cable. The conductors in the stator winding annulus shown in Fig. 4-7(a) are transformed into an equivalent annulus, shown in Fig. 4-7(d), with inner and outer radii r_{in_1} and r_{out_1} respectively. Hence, the equivalent heat generated due to joule loss, $Pwr_{1,}$ by these conductors can be expressed by equation (55),

$$Pwr_1 = I^2 \times \left(\rho_o \frac{\pi r_{out\_1}^2 - \pi r_{in\_1}^2}{L} \right) \times \left(1 + \alpha \left(T - 293\ K\right)\right) \tag{4.55}$$

4.3.3. Equivalent Radial Thermal Resistance of the Stator Winding

Fig. 4-10(a) shows the thermal circuit of the stator winding by using the concentric annular layers modelling method. The overall thermal circuit consists of two major sub-circuits, which are the centre circle and *k* layers of stator winding annulus sub-circuits. The thermal resistances of these two sub-circuits were derived and elucidated in equations (4.31-4.32) for the centre circle circuit and equations (4.56-4.60) for the winding annulus thermal circuits. A Virtual Basic code was constructed to calculate the thermal resistances and the temperature increase of the overall thermal circuit. (Appendix A).

$$R_{c1\_k} = \frac{\ln\left(\frac{r_{in\_k}}{r_{cont\ 1\_k}}\right)}{2\pi k_c L} \tag{4.56}$$

$$R_{c2\_k} = \frac{\ln\left(\frac{r_{cont\ 2\_k}}{r_{rout\ \_k}}\right)}{2\pi k_c L} \tag{4.57}$$

$$R_{d1\_k} = \frac{1}{4\pi k_d L}\left[1 - \frac{2r_{in\_k}^2 \ln\left(\frac{r_{out\_k}}{r_{in\_k}}\right)}{\left(r_{out\_k}^2 - r_{in\_k}^2\right)}\right] \tag{4.58}$$

$$R_{d2\_k} = \frac{1}{4\pi k_d L}\left[\frac{2r_{out\_k}^2 \ln\left(\frac{r_{out\_k}}{r_{in\_n}}\right)}{\left(r_{out\_k}^2 - r_{in\_k}^2\right)} - 1\right] \tag{4.59}$$

$$R_{d3\_k} = -\frac{1}{8\pi k_d L\left(r_{out\_k}{}^2 - r_{in\_k}{}^2\right)}\left[r_{in\_k}{}^2 + r_{out\_k}{}^2 - \frac{4r_{out\_k}{}^2 r_{in\_k}{}^2 \ln\left(\frac{r_{out\_k}}{r_{in\_k}}\right)}{\left(r_{out\_k}{}^2 - r_{in\_k}{}^2\right)}\right] \tag{4.60}$$

$$r_{out\_k} = \sqrt{\frac{(1+A_d)}{2} r_{eq\_k+1}{}^2 + \frac{(1-A_d)}{2} r_{eq\_k}{}^2} \tag{4.61}$$

$$r_{in\_k} = \sqrt{\frac{(1-A_d)}{2} r_{eq\_k+1}{}^2 + \frac{(1+A_d)}{2} r_{eq\_k}{}^2} \tag{4.62}$$

$$r_{eq\_0} = \frac{r_c}{\sqrt{A_d}} \tag{4.63}$$

$$r_{eq\_k} = r_{eq\_k-1} + \frac{r_{sc} - r_c}{N} \tag{4.64}$$

$$r_{cont1\_k} = \sqrt{\frac{r_{in\_k}{}^2 - (1-G_{ratio})\times(1-A_d) r_{mid\_k}{}^2}{1-(1-G_{ratio})\times(1-A_d)}} \tag{4.65}$$

$$r_{cont2\_k} = \sqrt{\frac{r_{out\_k}{}^2 - (1-G_{ratio})\times(1-A_d) r_{mid\_k}{}^2}{1-(1-G_{ratio})\times(1-A_d)}} \tag{4.66}$$

$$r_{mid\_k} = \sqrt{\frac{r_{eq\_k}{}^2 + r_{eq\_k-1}{}^2}{2}} \tag{4.67}$$

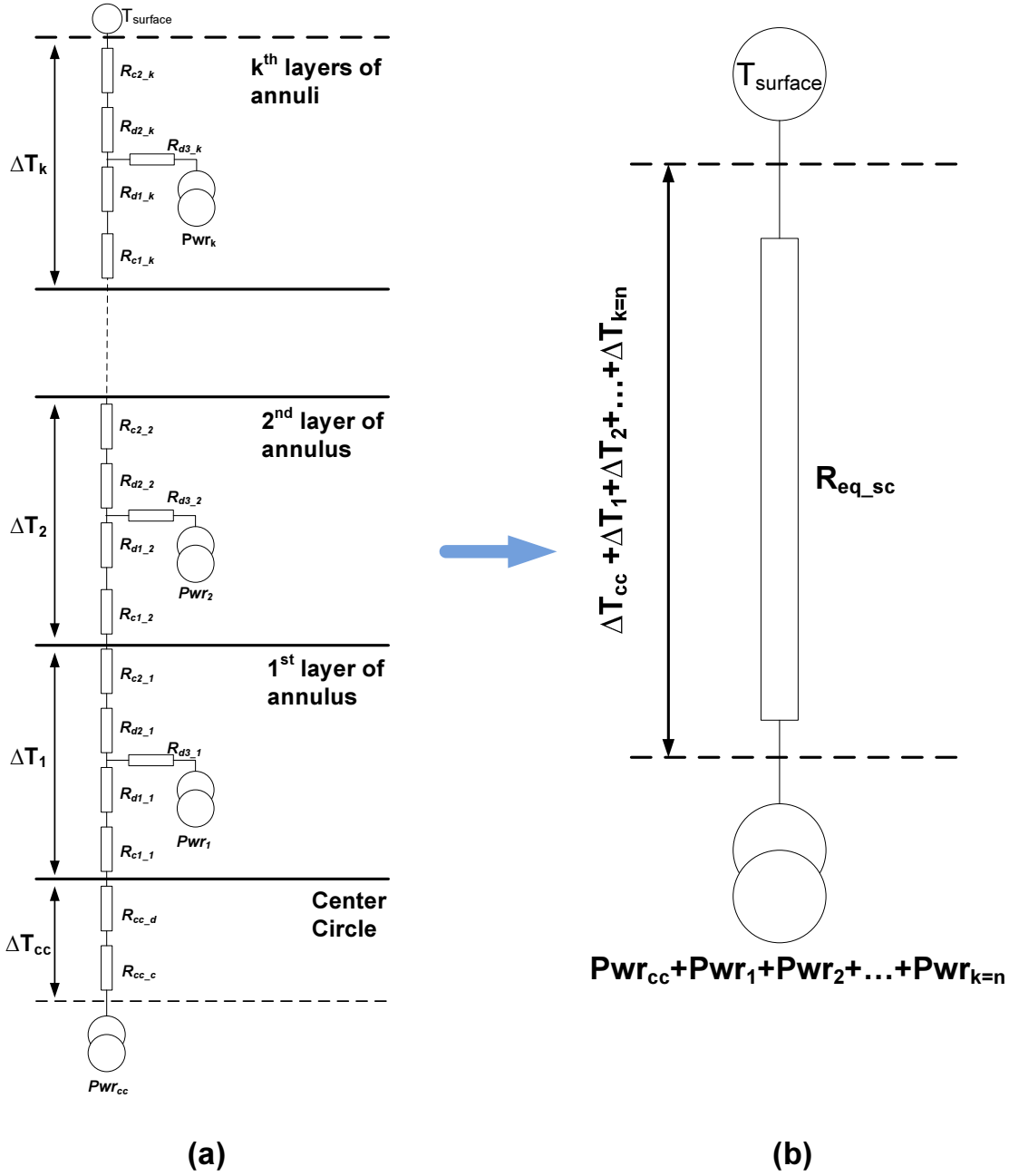

Fig. 4-10. (a) The overall thermal circuit of the stator winding and (b) its corresponding simplified one resistance thermal equivalent circuit.

To alleviate the complexity in calculating the temperature increase across the stator wire in the radial direction by using the overall thermal circuit shown in Fig. 4-10(a), the overall thermal circuit was simplified and represented by a single resistance model shown in Fig. 4-10(b). Furthermore, the simplification of the overall thermal circuit also provides a suitable comparison with the experimental results, as well as other computational fluid dynamic models.

In the single resistance thermal model, the equivalent radial thermal resistance, R_{eq_sc}, was calculated by considering the total temperature increase across the stator cable ($\Delta T_{cc}+\Delta T_1+\Delta T_2+\ldots+\Delta T_k$) and the total heat generated due to joule loss in the cable conductors ($Pwr_c+Pwr_1+Pwr_2+\ldots+Pwr_k$) obtained from the overall thermal circuit, equation (4.68).

$$R_{eq\_SC} = \frac{\Delta T_{cc} + \sum_{1}^{n} \Delta T_k}{Pwr_{cc} + \sum_{1}^{n} Pwr_k} \tag{4.68}$$

Where,

$$\Delta T_{cc} = Pwr_{cc} \times \left(R_{cc\_d} + R_{cc\_c} \right) \tag{4.69}$$

$$= I^2 \times \left(\rho_o \frac{\pi r_c^{\,2}}{L} \right) \times \left(1 + \alpha \left(T - 293\right)\right) \times \left(\frac{1}{4\pi k_c L} + \frac{\ln\left(\frac{r_{eq\_0}}{r_c}\right)}{2\pi k_{cf} L} \right) \tag{4.70}$$

And

$$\Delta T_n = \sum_{1}^{k=n} \left(Pwr_{cc} + Pwr_{k-1}\right) \times \left(R_{c1\_k} + R_{d1\_k}\right) + \sum_{1}^{k=n} \left(Pwr_{cc} + Pwr_k\right) \times \left(R_{d2\_k} + R_{c2\_k}\right) \tag{4.71}$$

Thus, R_{eq_sc} calculated from equation (4.68) can easily be adapted into the thermal circuit of any of the machine designs with negligible computational effort. However, the drawback of this simplification is that the single resistance model is only capable of predicting the temperature at the centre of the stator wind. Information on the temperature profile of the stator cable in the radial direction is lost in the simplification. Hence, the equivalent radial thermal resistance is only suitable to identify the hot spots in the machines.

4.4. Comparison of Analytical and Experimental Results

Several analytical equations have been developed to predict the thermal conductivities of different types of two-phase solid-to-solid mixtures. The most commonly used analytical equations, which are Maxwell [57], Powers [132] and Cheng & Vachon [70], were used to compare with the thermal resistance predicted from the simple concentric model (SCM). Also, experimental data of the thermal conductivities of heterogeneous two-phase mixtures obtained by previous researchers [133-137] were used for comparison with this analysis.

To be comparable with the analytical and experimental data obtained from previous researchers, the analytical thermal resistance of the two-phase material derived from SCM was converted to thermal conductivity form (see equation (4.23)). Similarly, thermal resistances calculated from CLM were converted to thermal conductivity form by equation (4.72).

$$k_{eq\_SC} = \frac{\ln\left(\frac{r_{sc}}{r_c}\right)}{2\pi L R_{eq\_sc}} \tag{4.72}$$

The equations resulting from Maxwell [57], Powers [132] and Cheng & Vachon [70] are shown in equations (4.73), (4.74), (4.75) respectively. These equations were examined and used in comparison with the thermal conductivities obtained from SCM, as well as from the experiments. Table 4-1 to Table 4-5 show the thermal conductivities obtained from the analytical models compared with the experimental results. Five experiments of different two phase mixtures were chosen. Table 4-1 and 4-2 demonstrate the thermal conductivities of silicon rubber with aluminum spheres and cylinder particle mixtures, respectively. Thermal conductivities of the mixture, where its substances have similar thermal properties (Zinc Sulphate in Lard mixture) are examined in Table 4-3. In Table 4-4, thermal conductivities of an emulsion

mixture, copper in water solution, are illustrated. Lastly, fibre glass two-phase mixtures were investigated and the results are shown in Table 4-5

Maxwell [57]- Thermal conductivity of two-phase mixtures

$$k_{eq} = \frac{k_c\left[k_d + 2k_c - 2*\%A_d\left(k_c - k_d\right)\right]}{k_d + 2k_c + P_d\left(k_c - k_d\right)} \tag{4.73}$$

Powers [132]- Thermal conductivity of two-phase mixtures

$$k_{eq} = \frac{k_c k_d}{P_d k_c + (1 - P_d)k_c} \tag{4.74}$$

Cheng & Vachon [70]- Thermal conductivity of two-phase mixtures

$$k_{eq} = \frac{1}{\dfrac{1}{\sqrt{C\left(k_c - k_d\right)\left[k_c + B\left(k_d - k_c\right)\right]}}\ln\left(\dfrac{\sqrt{\left[kc + B(kd - kc)\right]} + \dfrac{B}{2}\sqrt{C\left(k_c - k_d\right)}}{\sqrt{\left[kc + B(kd - kc)\right]} - \dfrac{B}{2}\sqrt{C\left(k_c - k_d\right)}}\right)} + \frac{1 - B}{k_c} \tag{4.75}$$

Where,

$$B = \sqrt{\frac{3x\%A_d}{2}},\ C = -4\sqrt{\frac{2}{3x\%A_d}}$$

Table 4-1: Test 1- Comparison of predicted thermal conductivities of Aluminum spheres in silicone rubber mixture. k_c = 0.216 W/m^{2}K; k_d = 204.2 W/m^{2}K; A_d =16%

Source of k_{eq}	k_{eq} (W/m^{2}K)	Deviation of experimental data (%)
Maxwell	0.3406	3.58
Powers	0.2575	-21.68
SCM	0.3602	-19.96
Cheng & Vachon	0.4207	27.95
Experiment [132-133]	0.3288	n/a

Table 4-2: Test 2- Comparison of predicted thermal conductivities of Aluminum cylinders in silicone rubber mixture. k_c = 0.216 W/m^{2}K; k_d = 204.2 W/m^{2}K; A_d =16%

Source of k_{eq}	k_{eq} (W/m^2)	Deviation of experimental data (%)
Maxwell	0.3406	-24.31
Powers	0.2575	-42.77
SCM	0.3602	9.53
Cheng & Vachon	0.4207	-6.51
Experiment [132-133]	0.45	N/A

Table 4-3: Test 3- Comparison of predicted thermal conductivities of Zinc Sulphate (sphere) in lard mixture. k_c = 0.1973 W/m^{2}K; k_d = 0.6127 W/m^{2}K; A_d =55.5%

Source of k_{eq}	k_{eq} (W/m^2)	Deviation of experimental data (%)
Maxwell	0.3730	6.1576
Powers	0.3055	-13.05
SCM	0.3986	13.45
Cheng & Vachon	0.3775	7.44
Experiment [134]	0.3513	N/A

Table 4-4: Test 4- Comparison of predicted thermal conductivities of Copper (sphere) in water liquid. k_c = 0.6577 W/m^{2}K; k_d =382.5 W/m^{2}K; A_d =29.5%

Source of k_{eq}	k_{eq} (W/m^2)	Deviation of experimental data (%)
Maxwell	1.4773	-18.70
Powers	0.9322	-48.70
SCM	1.4364	-20.95
Cheng & Vachon	1.9280	6.10
Experiment [135]	1.8172	N/A

Table 4-5: Test 5- Comparison of predicted thermal conductivities of Selenium (sphere) in PPG glass fibre. k_c = 0.1402 W/m^{2}K; k_d =5.1921 W/m^{2}K; A_d =50%

Source of k_{eq}	k_{eq} (W/m^2)	Deviation of experimental data (%)
Maxwell	0.5	2.95
Powers	0.2729	-43.88
SCM	0.4494	-7.62
Cheng & Vachon	0.7	44.06
Experiment [136]	0.4863	N/A

4.5. Discussions

The experimental deviations of four analytical solutions for five different tests are summarised in Fig. 4-11. Among all the five analytical models, Maxwell [57] shows the most compatible solution for all ranges of two-phase mixtures; In contrast, Powers [132] demonstrates the worst among the other three solutions, especially at low packing ratio, (Test 5). In comparison with Cheng & Vachon [70], SCM gives slightly more acceptable results.

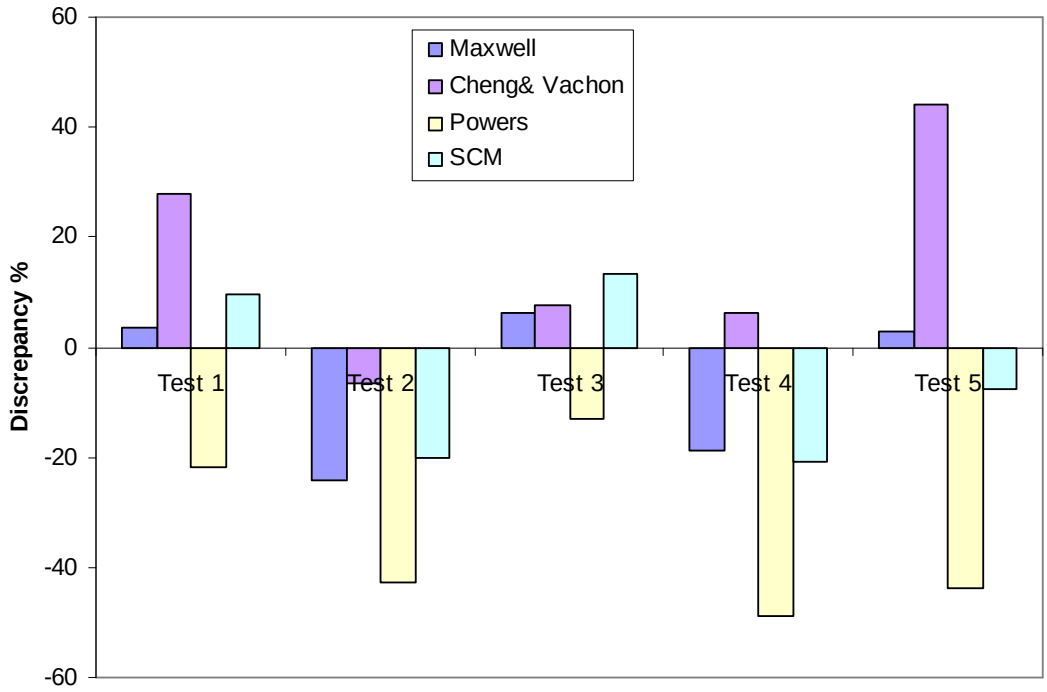

Fig. 4-11. Experiment deviations of five analytical solutions for five different two-phase mixtures.

In most of the test cases, Maxwell [56] predicts more accurate thermal conductivities then SCM, except for Test 2, (Table 4-2). In Test 2, a heterogeneous two-phase mixture was investigated: Aluminum cylinder-silicon rubber mixture (Fig. 4-12(a)). In the derivation of SCM, the higher thermal conductivity material in the two-phrase mixture is simplified to cylindrical discontinuous particles (which is similar to Aluminum cylinder-silicon mixture), whereas for Maxwell, the thermal resistance was derived for homogeneous two-phase mixtures with spherical discontinuous particles

(which is shown in Fig. 4-12(b)). Therefore, the equivalent thermal conductivity predicted from SCM for Aluminum cylinder-silicon rubber mixture is better than the Maxwell method when compared with experimental results. This investigation demonstrates that the accuracies of thermal resistance predictions for two-phrase mixture are dependent on its structure, i.e. SCM is better for cylindrical discontinuous particles, Maxwell predicts better thermal conductivities for spherical discontinuous particles etc. Since the stator windings in the axial flux generator have a similar particle structure to the Aluminum cylinder-silicon mixture, SCM demonstrates a better approximation for thermal resistance prediction of stator winding than the other analytical models.

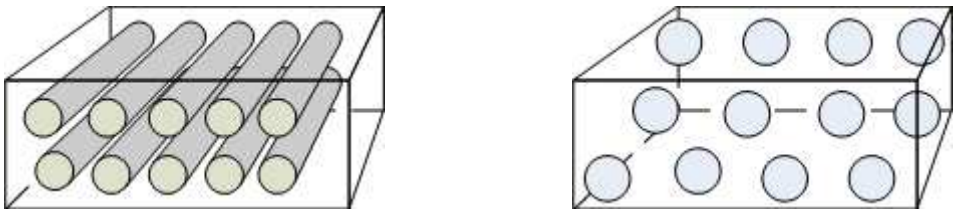

(a) (b)

Fig. 4-12. (a) Aluminum cylinder-silicon rubber mixture and (b) Aluminum sphere-silicon rubber mixture.

CLM is derived for the two-phase mixture with cylindrical discontinuous particles. Nevertheless, CLM predicts higher thermal conductivities for all of the two-phase mixtures measured in Test 1 to Test 5 compared with SCM (Fig. 4-13). Since thermal resistance is the reciprocal of thermal conductivity, this implies that the equivalent thermal resistances predicted from CLM are lower than the equivalent thermal resistances predicted from SCM. These are due to CLM being derived to model the thermal resistance the windings of the electrical machines. On the other hand, CLM takes into account the resistive heat generated in the copper cylindrical particles when the electric current passes through. The heat sources in the CLM are evenly distributed inside the winding (Fig. 4-14(a)). Hence, the resistive heat generated at the copper conductors near to the edge of the winding travels a shorter distance in comparison with the heat generated from the heat sources at the centre of the winding. Therefore, the local thermal resistances of the winding at the edge are lower and

higher at the centre. On the other hand, SCM assumes that all the heat is generated from the concentrated point at the centre of the winding (Fig. 4-14 (b)). As a result, the local thermal resistances of the winding are uniform for a concentrated heat source. Since the heat generated from the centre of the winding travels a longer distance in total than the heat generated from the distributed heat source, the equivalent thermal resistance for the SCM is higher.

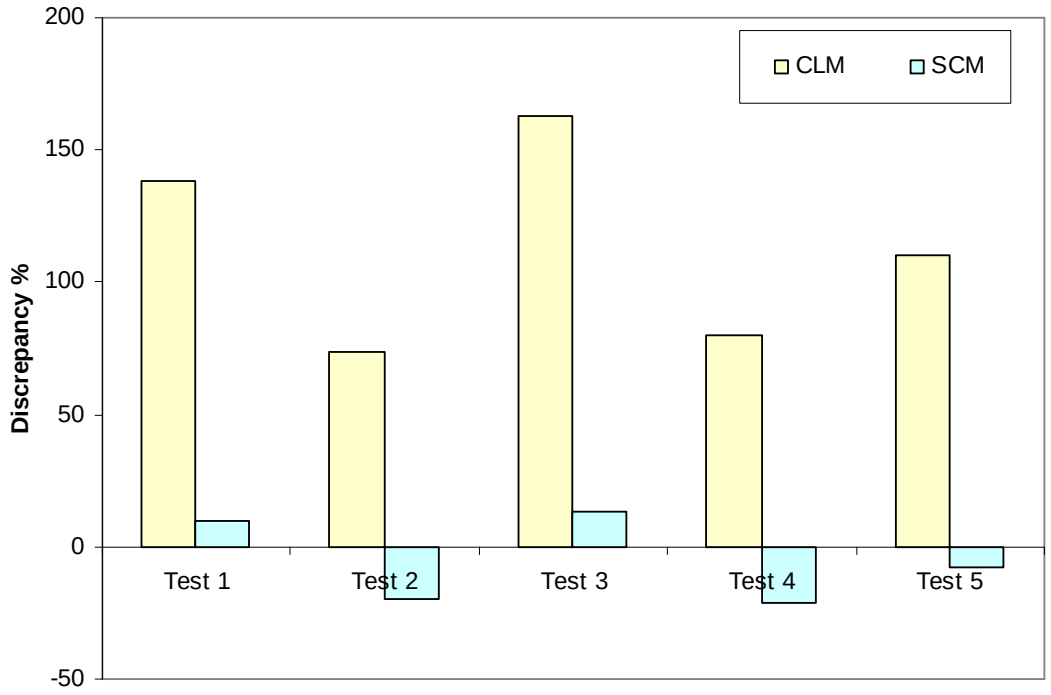

Fig. 4-13. Discrepancies of CLM and SCM analytical solutions as compared with experimental results for five different two-phase mixtures.

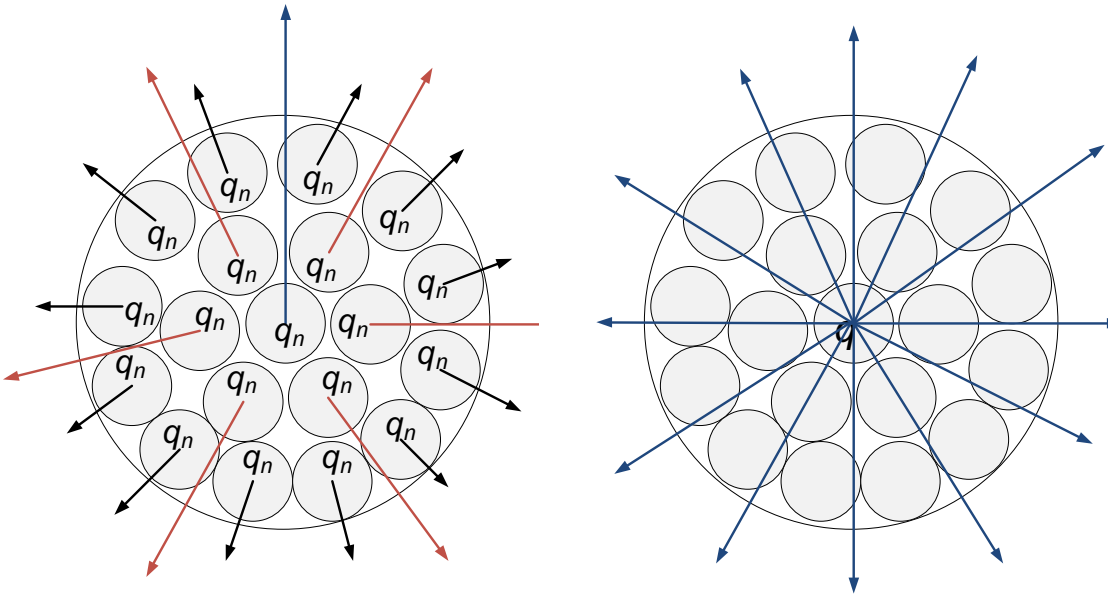

(a) (b)

Fig. 4-14. (a) Distributed heat sources inside the winding of the electrical machines and (b) concentrated heat source winding model

The thermal conductivity predicted by CLM is verified by the 2D-CFD model of the stator winding, (Fig. 4-15(a)). The 2D model of a 5cm diameter winding, with 5mm epoxy-resin encapsulated copper wires, is built using the Gambit meshing software and simulated by FLUENT. The model consists of 5743 cells and only energy equations are considered. The thermal conductivities of copper wire and epoxy resin are 387W/m^{2}K and 0.22W/m^{2}K respectively, and the packing ratio, $\%A_c$, is 0.61. Thermal conductivities predicted by CLM and the other analytical equations are summarized in Fig. 4-15(b).

The results indicate that all the analytical models investigated under-predict the equivalent thermal conductivity of the stator winding with distributed heat sources in these electrical machines. Nevertheless, the thermal conductivity predicted by CLM is closest to the result obtained from the CFD model. Maxwell, Power and SCM all show a huge deviation from CFD data, and this is due to mainly to these models being developed for no distributed heat source two-phase mixtures. Fig. 4-16 plots the temperature across the two perpendicular axes of the winding, which are the lines x = 0 and y = 0, predicted from the CFD model. Since the peripheral edge of the winding

is closest to ambient, the temperatures at the two ends of the curve are the lowest. Moving radially inward to the centre of the winding, the winding temperature rises and reaches a maximum of 52.5 °C at the centre. The winding temperature increases in steps in the stator winding and reaches a plateau at the copper phase due to high thermal conductivity. The winding temperature increases steeply at the epoxy-resin phase due to significantly lower thermal conductivity. These demonstrate that the temperature increase in the stator winding is governed by the thermal conductivity of the epoxy-resin.

It can be noted that the magnitude of the temperature drop increases when moving radially outwards from the centre, for example the temperature drop in the first layer winding filler is 1 deg C, but 5 °C occurs at the second layer (Fig. 4-16). This is due to the effect of the individual heat generated by the copper joule losses scattered around the winding. As the heat travels radially outward from the centre, extra heat is accumulated from each of these individual joule loss generated in the conductors. Since the temperature drop is directly proportional to the heat flow, it increases exponentially when moving from the centre to the periphery along the radial lines.

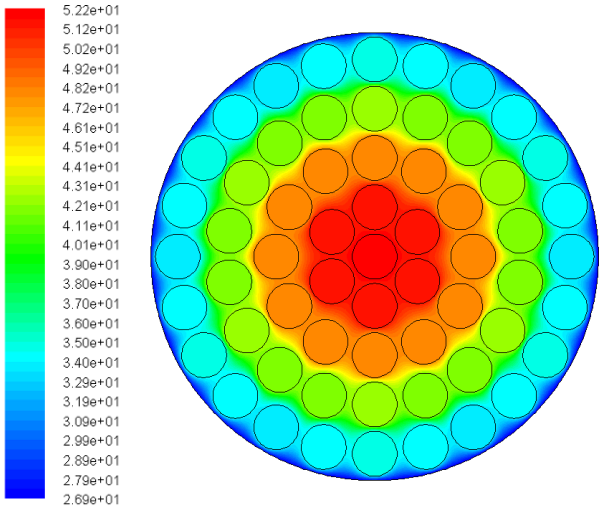

(a)

Source of k_{eq}	k_{eq} (w/m^2)	Deviation from CFD results (%)
Maxwell [56]	1.2478	-69.82
Power [131]	0.5636	-86.37
SCM	1.0026	-75.75
CLM	3.736777	-9.63
Cheng & Vachon [69]	3.5152	-15.78
2-D CFD model	4.1352	N/A

(b)

Fig. 4-15. (a)The temperature contour of the cross section of the stator winding in °C, (b) the comparison of thermal conductivities predicted by the analytical equations and the 2D-CFD model.

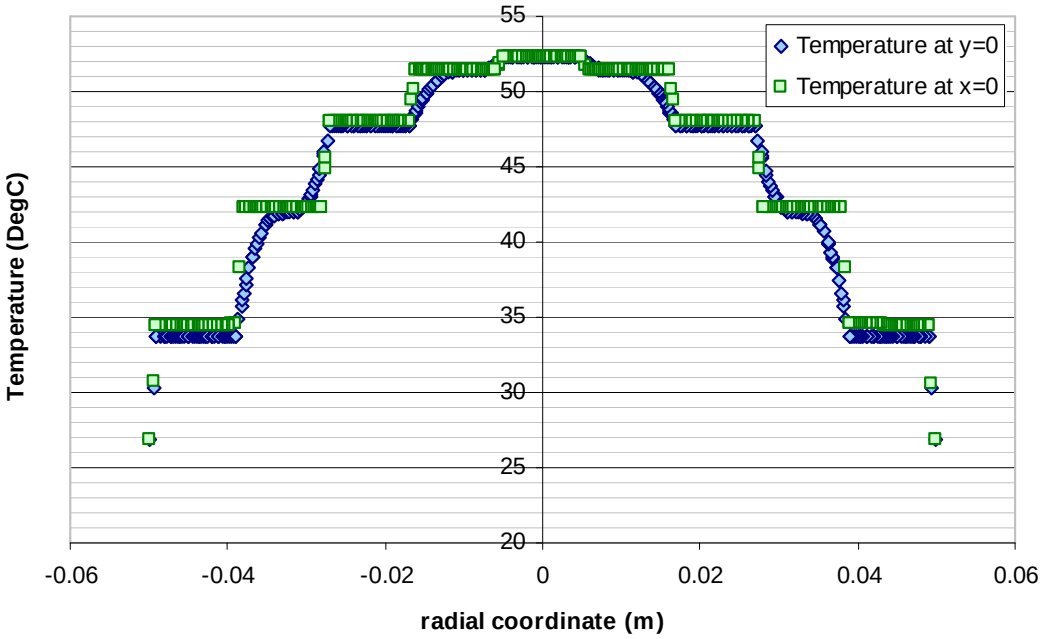

Fig. 4-16. Temperature vs radial coordinate of the winding.

4.6. Conclusions

In conclusion, two techniques of predicting the radial thermal resistance of the electrical machine stator winding are presented in this chapter, which are the simplified concentric model (SCM) and the concentric annular layers model (CLM). These two analytical models are applied into the pre-built electrical machine thermal circuits, to provide better temperature predictions.

These two analytical models circumvent the necessity of conducting experiments, to obtain the radial thermal conductivity of stator winding based on the several easily available winding parameters, such as the thermal conductivities of the conductors and winding filler, packing ratio of the conductors, conductor and winding radii etc. The thermal conductivities obtained from these two techniques were compared with the thermal models published by past researches for two-phase mixtures. These thermal conductivities were also verified by experimental results found in several past publications.

Overall, SCM exhibits a better prediction of the thermal conductivities of stator windings as compared to the other analytical models. SCM was derived from cylindrical discontinuous particle heterogeneous two-phase mixtures whereas the other analytical models were derived based on spherical discontinuous particle homogeneous two-phase mixtures. However, if heat generation due to joule losses in the winding is taken into consideration in the thermal model, CLM is more capable of predicting accurate thermal resistances of the stator winding.

Chapter 5

The Construction of 2-D Generic Lumped Parameter model of Axial Flux Permanent Magnet Generators

5.1. Introduction

The lumped parameter method has been widely used for thermal modelling, especially in electrical machines, including radial machines [e.g. 37-38] and axial flux machines [e.g. 33, 39]. This is because LPM is relatively faster and simpler to use in comparison with the general purpose, advanced computational fluid dynamic (CFD) packages. In chapter 3, the author has shown in his test cases, which by incorporating the convective circuit into the thermal circuit, with an appropriate discretisation level, the results obtained from lumped parameter circuits were in good agreement with both CFD and experimental testing.

However, constructing the lumped parameter thermal equivalent circuit of the electrical machines requires a high level of thermodynamic background and knowledge. Prior to the construction of the thermal network of the electrical machine, it is necessary to identify the (conduction and convection) heat flow paths, heat sources and heat sinks in the electrical machines and to evaluate the thermal resistances of each corresponding lumped component, depending on the machine

specification and machine configuration. Subsequently, the thermal circuit is constructed based upon all this information, and solved either with a self-developed circuit solver or a commercially available thermal circuit solver, for example *Portunus*. The results obtained from the solver are transferred to a dedicated program for data post-processing. A sequential diagram of the construction of a specific lumped parameter thermal circuit is shown in Fig. 5-1(a).

The specific lumped parameter thermal circuit can be used to perform thermal simulation for one specific electrical machine. A slight change on the machine geometry specification, for example the size of the air clearance or the rotor disk radius, or an alteration of the machine operating condition, such as the generator rotational speed and the ambient air temperature requires a new specific lumped parameter thermal circuit. Therefore, it is tedious and time consuming to re-construct the specific lumped parameter thermal circuits for different machine designs, especially when performing a rapid machine design process. Furthermore, some of the thermal circuit model users might have very little experience in constructing thermal network circuits. Hence, in this chapter, a new improved generic lumped parameter thermal modelling framework is introduced.

The new modelling framework, shown in Fig. 5-1(b), has a user friendly interface that makes for easy data input and interpretation of results. The thermal model in the new improved lumped parameter thermal modelling framework is based upon a generic analytical lumped-circuit, making it applicable to a range of different sizes and topologies of axial flux machine. This allows the user to perform “what-if” calculations for a rapid design process. All the thermal resistances and capacitances in the new modelling framework are calculated automatically based on the geometric dimensions and material properties of the machines specified by the user. Hence, the users are not required to be familiar with complex heat transfer phenomena, such as dimensionless analysis of conduction, convection etc. The user interface is fully automated; it is programmed to receive the machine geometric dimensions and material properties from the user and to feed in the thermal resistances and capacitances to a thermal circuit solver to perform the thermal modelling. The results obtained from the thermal modelling are exported back to the Excel spreadsheet

automatically. Therefore, the new modelling framework is designed for the non heat transfer specialist to carry out thermal analysis of electric machines during the design process in a quicker and more straightforward way. No specialised thermodynamic and heat transfer background knowledge is required.

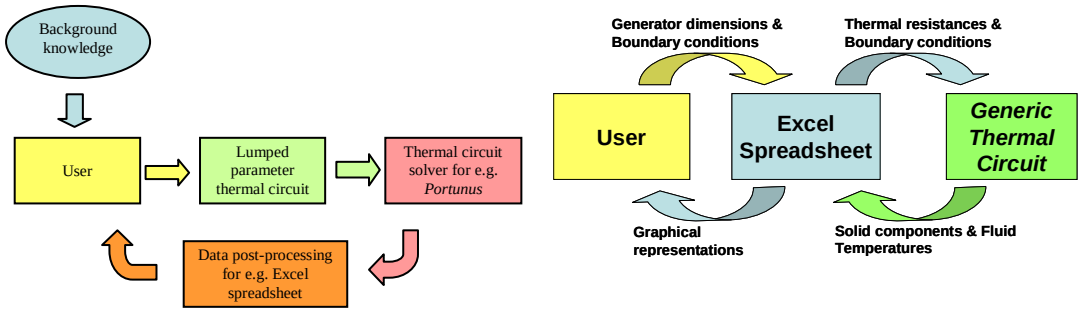

(a) (b)

Fig. 5-1. Lumped parameter modelling schemes (a) with specific thermal network and (b) with generic thermal network.

5.2. The Construction of a 2-D generic lumped parameter thermal circuit

The generic thermal network circuit is a standardised thermal circuit for similar architecture of electrical machines. Unlike the specific thermal circuits that have been developed by previous researchers, for example [35-43], which are specifically constructed for a certain type and size of electrical machine, the generic thermal network circuit is able to perform thermal modelling of a range of different sizes and topologies of axial flux machines.

Like the specific thermal circuit, the generic thermal circuit consists of conductive and convective thermal resistances, thermal capacitance and temperature dependant heat sources. However, these thermal resistances and capacitances in the generic thermal circuit are non-dimensionalised with the machine's geometry and material properties, so that the thermal circuit is applicable to different sizes and types of machines. Fig. 5-2 shows a generic thermal circuit of slotted axial flux machines. The red boxes indicate the stator conductive circuits; the grey boxes indicate the rotor

conductive circuits and the convective thermal circuits (fluid flow circuits) are represented in the blue boxes.

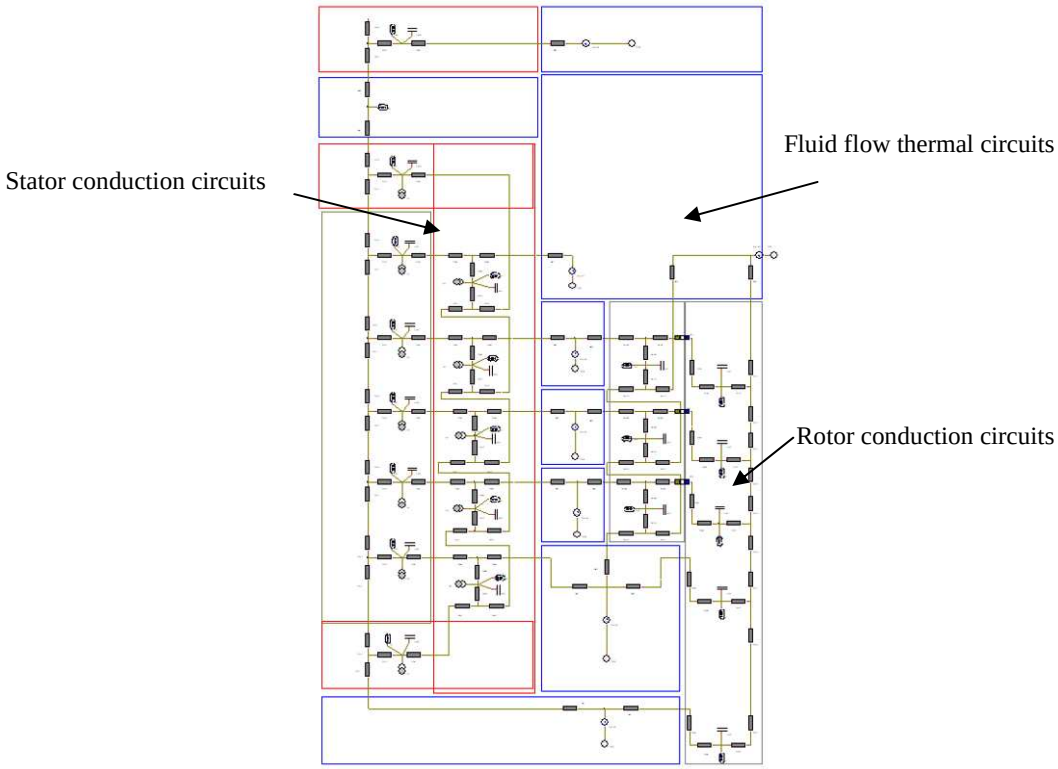

Fig. 5-2. 2D generic thermal circuit of axial flux permanent magnet generator.

5.2.1. The Generic Conduction Thermal Circuit

To analyse the process of conductive heat transfer in an electrical machine, the standard machine geometry was chosen and divided into basic elements. Each basic element was identified, in general, by an annulus. It was assumed that the heat flow in the radial and axial directions of the annulus were independent, allowing the use of one-dimensional equations to model the conduction heat transfer. Furthermore, the mean temperatures in both of these directions were assumed to be the same, allowing the networks to be developed by superimposing the two one-dimensional conductive heat transfer equations, resulting in the two dimensional model shown in Fig. 5-3.

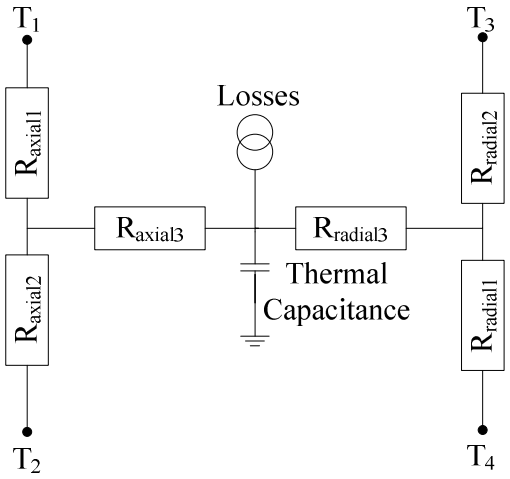

Fig. 5-3. Two dimensional thermal circuit of an annulus.

The conduction thermal resistances used in the generic thermal network circuit were represented as functions of the geometries of the machines, see equations (3.7-3.12) in Chapter 3. These equations were derived directly from the heat storage and Fourier 1-D heat transfer equations of the annulus.

The heat storage of an annulus, shown in Fig. 5-4, can be expressed as:

$$H_s = \rho \cdot V \cdot c_p \cdot T_m \tag{5.1}$$

Where, ρ = material density, kg/m^3

V = Annulus volume, m^3

c_p = Specific heat capacity at constant pressuare, J/kgK

T_m = mean temperature of the annulus, K

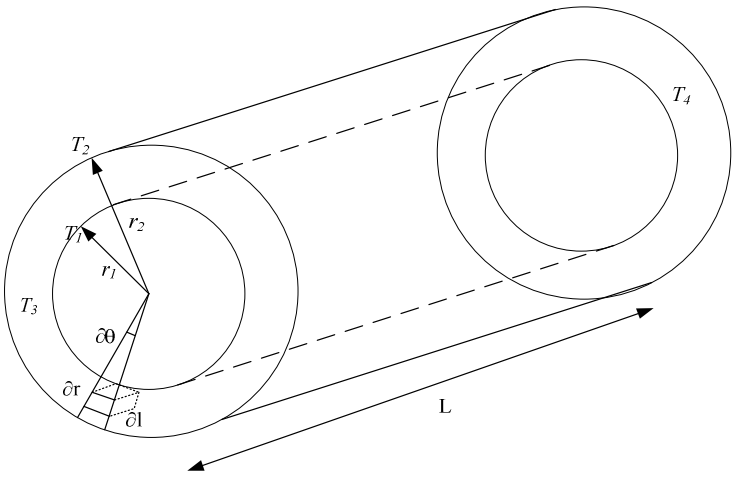

Fig. 5-4. Two-dimensional annulus element

Since,

$$V = \pi\left(r_2^{\,2} - r_1^{\,2}\right)\cdot L \tag{5.2}$$

The heat storage equation (5.1) can be re-written as:

$$H_s = \rho\cdot\pi\left(r_2^{\,2} - r_1^{\,2}\right)\cdot L\cdot c_p\cdot T_m \tag{5.3}$$

Where, L = Length of the annulus

Defining a small elemental volume in the annulus co-ordinates, v_e, (see Fig. 5-4,) small enough to be considered that the volume temperature is uniform, then the elemental heat stored, H_{se}, is given by:

$$v_e = r\cdot\partial\theta\cdot\partial r\cdot\partial l \tag{5.4}$$

$$H_{se} = \rho\cdot c_p\cdot T\cdot r\cdot\partial\theta\cdot\partial l\cdot\partial r \tag{5.5}$$

The volume integral of equation (5.5) can be equated to the total heat stored given by equation (5.3)

$$\rho\cdot\pi\left(r_2^{\,2} - r_1^{\,2}\right)\cdot L\cdot c_p\cdot T_m = \int_0^r\int_0^l\int_0^{2\pi}\rho\cdot c_p\cdot T\cdot r\cdot\partial\theta\cdot\partial l\cdot\partial r \tag{5.6}$$

Therefore, by arranging equation (5.6), the radial mean temperature can be defined by,

$$T_m = \frac{2}{\left(r_2^{\,2} - r_1^{\,2}\right)}\int_{r1}^{r2} T_r\cdot r\cdot\partial r \tag{5.7}$$

Where, T_r = radial temperature profile

Similarly, the axial mean temperature is given by,

$$T_m = \frac{1}{L}\int_0^L T_l\cdot\partial l \tag{5.8}$$

Where, T_l = axial temperature profile

Radial thermal resistances

The one dimensional conductive heat transfer equation which describes the radial temperature distribution is given by,

$$\frac{\partial^2 T}{\partial r^2} + \frac{1}{r}\frac{\partial T}{\partial r} + \frac{g}{k_r} = 0 \tag{5.9}$$

Where, g = heat generated per unit volume (W/m^3)

k_r = thermal conductivity in the radial direction (W/mK)

The general solution of equation (5.9) is

$$T_r = a \cdot \ln r + \frac{g \cdot r^2}{4k} + b \tag{5.10}$$

Where, a, b = arbitrary constants

By substituting in the boundary conditions, $T_r = T_1$ at $r = r_1$ and $T_r = T_2$ at $r = r_2$ into equation (5.10) and subtracting from each other, the arbitrary constant a can be evaluated as:

$$a = \frac{1}{\ln\left(\frac{r_2}{r_1}\right)}\left[T_2 - T_1 + \frac{g \cdot \left(r_2^{\,2} - r_1^{\,2}\right)}{4k_r}\right] \tag{5.11}$$

Substituting equation (5.10) and equation (5.11) into equation (5.7),

$$T_m = T_2\left[\frac{r_2^{\,2}}{r_2^{\,2} - r_1^{\,2}} - \frac{1}{2\ln\frac{r_2}{r_1}}\right] + T_1\left[\frac{1}{2\ln\frac{r_2}{r_1}} - \frac{r_1^{\,2}}{r_2^{\,2} - r_1^{\,2}}\right] + \frac{g \cdot \left(r_1^{\,2} + r_2^{\,2}\right)}{8k_r} - \frac{g \cdot \left(r_2^{\,2} - r_1^{\,2}\right)}{8k_r \cdot \ln\frac{r_2}{r_1}} \tag{5.12}$$

Presuming the internal heat generation, g, is zero for this case, the radial conductive heat transfer can be modelled by a two resistor network as shown in Fig. 5-5(a). The mean temperature, T_m, in the two-resistor network can be expressed in terms of the boundary temperatures and thermal resistances, as:

$$T_m = T_1 \frac{R_{radial\,2}}{R_{radial\,1} + R_{radial\,2}} + T_2 \frac{R_{radial\,1}}{R_{radial\,1} + R_{radial\,2}} \tag{5.13}$$

Comparing the coefficients of T_1 and T_2 in equation (5.12) and equation (5.13), the radial thermal resistances, $R_{radial1}$ and $R_{radial2}$ are given as:

$$R_{radial1} = \frac{1}{4\pi \cdot k_r \cdot L}\left[\frac{2r_2^{\,2}\ln\frac{r_2}{r_1}}{r_2^{\,2}-r_1^{\,2}}-1\right] \tag{5.14}$$

$$R_{radial2} = \frac{1}{4\pi \cdot k_r \cdot L}\left[1-\frac{2r_1^{\,2}\ln\frac{r_2}{r_1}}{r_2^{\,2}-r_1^{\,2}}\right] \tag{5.15}$$

For the general case where the internal heat generation, g, is not equal to zero, an additional compensation resistance, $R_{radial3}$, is added at the central node of the two resistor network in Fig. 5-5(a), to give the thermal equivalent circuit of Fig. 5-5(b). In the thermal circuit, by assuming both T_1 and T_2 equal to zero, T_m can be expressed as:

$$T_m = g \cdot \left(R_{radial3} + \frac{R_{radial1} \cdot R_{radial2}}{R_{radial1} + R_{radial2}}\right) \tag{5.16}$$

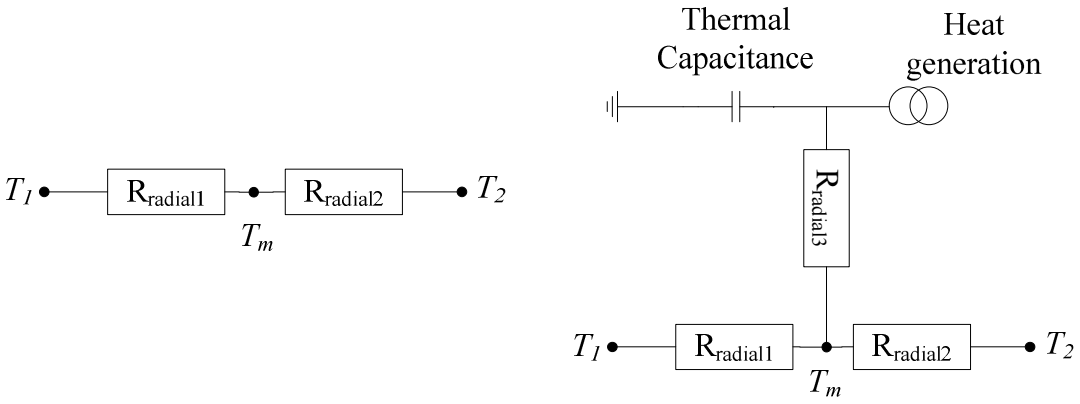

Fig. 5-5. Radial conductive two resistor (a) and three resistor (b) thermal network circuits.

Applying the same boundary conditions into equation (5.12), T_m can be represented as:

$$T_m = \frac{g \cdot \left(r_1^{\,2} + r_2^{\,2}\right)}{8k_r} - \frac{g \cdot \left(r_2^{\,2} - r_1^{\,2}\right)}{8k_r \cdot \ln\frac{r_2}{r_1}} \tag{5.17}$$

Hence, comparing and equating both equation (5.16) and equation (5.17), the additional compensation resistance, $R_{radial3}$, can be expressed as:

$$R_{radial3} = \frac{-1}{8\pi \cdot k_r \cdot L\left(r_2^{\,2} - r_1^{\,2}\right)}\left[r_2^{\,2} + r_1^{\,2} - \frac{4 r_1^{\,2} r_2^{\,2} \ln \frac{r_2}{r_1}}{r_2^{\,2} - r_1^{\,2}} \right] \tag{5.18}$$

As $R_{radial3}$ is negative, the new mean temperature T_m is lower than the original central temperature in the two resistor network.

Axial thermal resistance

In the axial direction, the conductive heat flow in the annulus element is described by:

$$\frac{\partial^2 T}{\partial l^2} + \frac{g}{k_a} = 0 \tag{5.19}$$

Where, k_a = axial thermal conductivity of the annulus

Equation (5.19) is a parabolic differential equation, which has general solution as shown as below:

$$T_l = \frac{-g \cdot l}{2k_a} + A \cdot l + B \tag{5.20}$$

A and *B* are arbitrary constants and they can be evaluated by substituting known boundary conditions: $T_1 = T_3$ at $l = 0$ and $T_l = T_4$ at $l = L$, into (5.20). Hence,

$$A = \frac{1}{L}\left[T_4 - T_3 + \frac{g \cdot L^2}{2k_a} \right] \tag{5.21}$$

$$B = T_3 \tag{5.22}$$

By substituting (5.20) with the known arbitrary constants into (5.8) (which was derived from the heat storage equation), the general equation of the axial mean temperature is denoted as:

$$T_m = \frac{T_3 + T_4}{2} + \frac{g \cdot L}{12k_a} \tag{5.23}$$

Assume that the annulus is symmetric on the central axial plane. This implies that T_3 and T_4 are identical for this particular case. Hence, axial heat flow can be represented by uni-resistor model shown in Fig. 5-6(a), and $R_{axial'}$ can be described as:

$$R_{axial'} = \frac{T_3 - T_m}{G} \tag{5.24}$$

Where,

G is the total heat flux in axial direction

$$G = g \cdot \pi \cdot \left(r_2^{\,2} - r_1^{\,1}\right) \cdot L \tag{5.25}$$

By substituting equation (5.23) into equation (5.24), $R_{axial'}$ can be evaluated.

$$R_{axial'} = \frac{L}{12 \cdot \pi \cdot k_a \cdot \left(r_2^{\,2} - r_1^{\,2}\right)} \tag{5.26}$$

However, the uni-resistor model is only applicable for symmetrical annulus elements. For asymmetrical annulus elements, a three-resistor model is required; see Fig. 5-6(b).

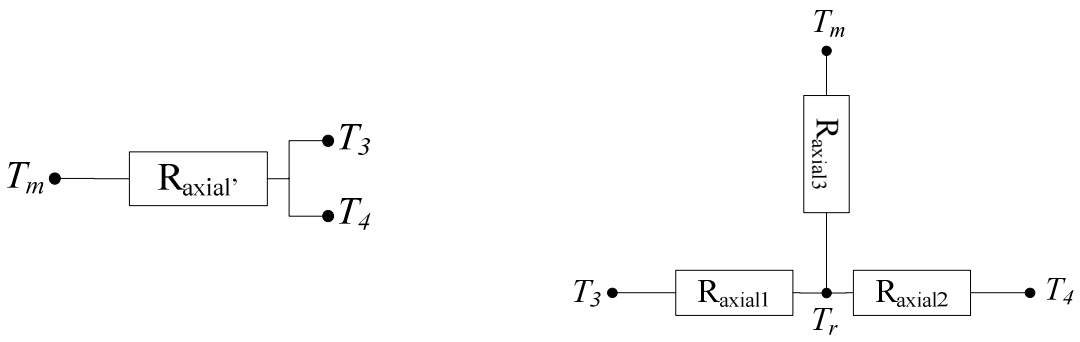

(a) (b)

Fig. 5-6. Axial thermal model of symmetrical (a) and asymmetrical (b) annulus element.

Since the annulus has a constant cross-sectional area, the axial thermal resistances, R_{axial1} and R_{axial2} are equal and can be deduced simply from the thermal resistance equation:

$$R_{axial1} = \frac{\frac{L}{2}}{k_a A} = \frac{L}{2 \cdot k_a \cdot \pi\left(r_2^{\,2} - r_1^{\,2}\right)} = R_{axial2} \tag{5.26}$$

The third axial thermal resistance, R_{axial3}, can be derived by assuming the symmetric boundary conditions on the asymmetrical thermal network model shown in Fig. 5-6(b), where T_3 is assumed to be equal to T_4, and hence the symmetric axial resistance can be re-written as:

$$R_{axial'} = R_{axial3} + \frac{R_{axial1}}{2} \tag{5.27}$$

$$R_{axial3} = \frac{-L}{6 \cdot \pi \cdot k_a \left(r_2^{\,2} - r_1^{\,2}\right)} \tag{5.28}$$

If it is assumed that the mean temperatures in the radial and axial direction are the same, then these axial resistances, R_{axial1}, R_{axial2}, and R_{axial3} can be added to the radial thermal circuit (shown in Fig. 5-5(b)), to give the two dimensional thermal equivalent circuit, shown in Fig. 5-3.

All these axial and radial thermal resistances were derived in the dimensionless form. Hence, these can be easily adapted to any size of annulus elements based on the electrical machine design.

5.2.2. Generic Convection Thermal Circuit

The generic convection thermal circuits are designed to model the fluid-solid heat transfers in the system for various types of flow conditions, for example, flow over a flat surface, or rotating surface, flow in a bending pipe, flow impingement on a flat plate etc. Like the convection thermal circuit which was discussed in the previous chapters, the generic convection thermal circuit consists of an inlet temperature source and a generic convection thermal resistance. Furthermore, to interact with the

conduction circuit, the other end of the generic fluid convection circuit is connected to the wall surface of the solid elements adjacent to it, see Fig. 5-7.

The accuracy of the generic convection thermal circuit depends on the convection thermal resistance specified in the circuit. The generic convection thermal resistances which are derived from the heat transfer coefficient, can be adjusted while the nature of the flow changes. On the other hand, it indicates that the physical flow pattern in the air control volume can be simply represented by the convectional thermal resistance. Therefore, by controlling the thermal resistance, the generic convection thermal circuit can be adapted to model different types of flow, with various boundary conditions.

Nevertheless, the convection heat transfer coefficients on the wall surfaces in the electrical machine are unknown. Furthermore, the heat transfer coefficients may vary with the machine geometry and the machine operating conditions, for example, rotational speed, different working fluid etc. Parametric studies of convection heat transfer coefficient with various electrical machine geometric parameters were conducted by Airoldi [54] to establish empirical formulae that can be applied to the generic convection thermal circuit. In that study, the author used CFD packages to model a range of machines with different feature sizes (for example, radius, size of air clearance and depth of the magnet grove) and operating conditions (for example, rotational speed) to evaluate the convection heat transfer coefficients on the wall surfaces in the machine. Based on all these test cases, empirical formulae of the convection heat transfer coefficient were deduced as a function of machine geometries and operating conditions, equation (5.29). Further details about the surface heat transfer parametric studies can be obtained from [54].

$$Nu = fn(r, c, dm, \omega) \tag{5.29}$$

Where, Nu = Nusselt number

r = Radii

c = Air clearance

dm = Depth of the magnet groove

ω = Rotational speed

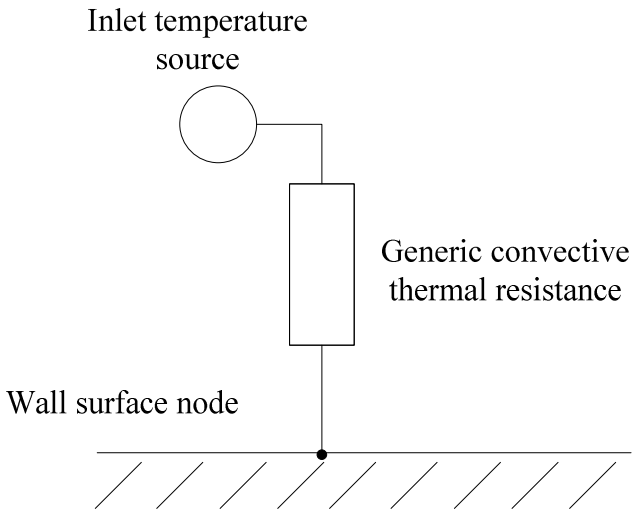

Fig. 5-7. The generic convection thermal circuit of single air control volume.

All the developed empirical formulae were pre-programmed into the generic convection thermal circuit. Therefore, the generic convection thermal circuit directly refers to the user inputs for the machine specifications and operating conditions, to model the convection heat transfer in the machine. No extra CFD simulation or experimentation is required. The generic convection thermal circuit of each air control volume in the system is interconnected by the Temperature Passing Algorithm: The inlet temperature in the convection thermal circuit is taken from the outlet temperature of the air control volume prior to the current one, and the process is updated for every time step during the modelling. Further information about the Temperature Passing Algorithm can be found in Chapter 3.

5.2.3. Heat Sources: Losses

The heat generated in the windings within the electrical machines transfers to the cooling air or the surroundings via several heat flow paths. In the generic thermal equivalent circuit model, the heat losses in the machine are determined as functions of measurable quantities, such as the generator output current, voltage, rotational speed etc. The heat loss in electrical machines is the combination of resistive and inductive losses: The resistive loss consists of Joule losses in the winding; the inductive losses

are the eddy current and hysteresis losses. Most of the stator cores used in the commercial electrical machines are laminated, to reduce the both the eddy current and hysteresis losses. For example if a block of stainless steel is laminated into N laminations, the inductive losses are reduced to $1/N^2$ times [138]. Therefore, in most commercial electrical machines, the heat loss is mainly governed by the Joule losses in the stator windings.

Joule loss, also refers to as the "I squared R" loss, increases with the square of the current through the windings and it is directly proportional to the electrical resistance. The output currents of the generators are easily available or can be easily measured, to be specified in the thermal network model. As for the electrical resistances of the stator windings, it depends on further geometrical information, such as the winding diameter, winding number of turns, conductor resistivity and length per turn. It is defined in equation (5.30). Furthermore, the resistivity of the winding conductor also differs as the conductor temperature changes; for a given current, the total losses can vary up to 50% between cold and hot machines [129]. Hence, to model the machine temperatures and heat losses in electrical machines accurately, the heat sources in the thermal circuit are updated for every time step based on the winding temperatures, by using the equations (5.30) and (5.31).

$$P_{JouleLoss} = I^2 \cdot \rho \frac{4 \cdot n \cdot L}{\pi \cdot d^2} \tag{5.30}$$

$$\rho = \rho_{25}\left[1 + \alpha(T - 25)\right] \tag{5.31}$$

Where,

I	=	current, A
n	=	number of turns
L	=	Length of winding per turn, m
d	=	Diameter, m
ρ	=	Resistivity of the conductor, Ωm
ρ_{25}	=	Resistivity of the conductor at 25°C, Ωm
α	=	Conductor temperature constant, °C $^{-1}$
T	=	Conductor temperature, °C

The continuous movement of the magnetic particles in the ferromagnetic stator core, as they align themselves with the change of magnetic field due to the rotating permanent magnets on the rotor disk, produces molecular friction. The heat generated by the molecular friction is known as the hysteresis loss. Based on the consideration of a variety of iron types, and over a considerable range of flux density, Carter [138] observed that the hysteresis loss in the stator core is proportional to the peak magnetic flux density power of γ, B_{max}^{γ} , and hence he suggested that:

$$P_{hysteresis} = f \cdot \lambda \cdot B_{\max}^{\gamma} \tag{5.32}$$

Where, f = rotational frequency

λ, γ = material constants

B_{max} = Peak magnetic flux density

In equation (5.32), the constants λ and γ vary according to the material; γ lies near to 1.6 and λ is about 3000, for cast iron.

The changing of the magnetic field direction in the ferromagnetic materials induces circulating flows of electrons, or current within the body of the stator core. This circulating current, also referred as the eddy current, generates heat and warms the stator core. The loss due to eddy currents in the stator core depends on the geometry of the stator cross-section and the amplitude and waveform of the magnetic flux density. For a metal block of thickness *2b*, width *d*, length *l* and resistivity ρ, carrying a uniform flux density of peak value B_{max} and frequency *f*, the induced eddy current loss is:

$$P_{eddy} = \frac{2\pi \cdot l \cdot b^3 \cdot d \cdot B_{\max}^{\ 2} f}{3\rho} \tag{5.33}$$

Eddy currents can be minimized by lamination. If the block is divided into N laminations, the eddy current loss is reduced to:

$$P_{eddy,n} = \frac{2\pi \cdot l \cdot b^3 \cdot d \cdot B_{\max}^{\ 2} f}{N^2 \cdot 3\rho} \tag{5.34}$$

Equation (5.34) can be modified to model the eddy currents in the annulus stator core, by assuming the annulus as a rectangular block (Fig. 5.8) with thickness (r_{out}-r_{in}), width d, and length $\pi(r_{out}+r_{in})/2$. The new eddy current loss in the stator is illustrated in equation (5.35).

$$P_{eddy,stator} = \frac{\pi^2 \cdot (r_{out} + r_{in}) \cdot (r_{out} + r_{in})^3 \cdot d \cdot B_{\max}{}^2 f}{N^2 \cdot 3\rho} \tag{5.35}$$

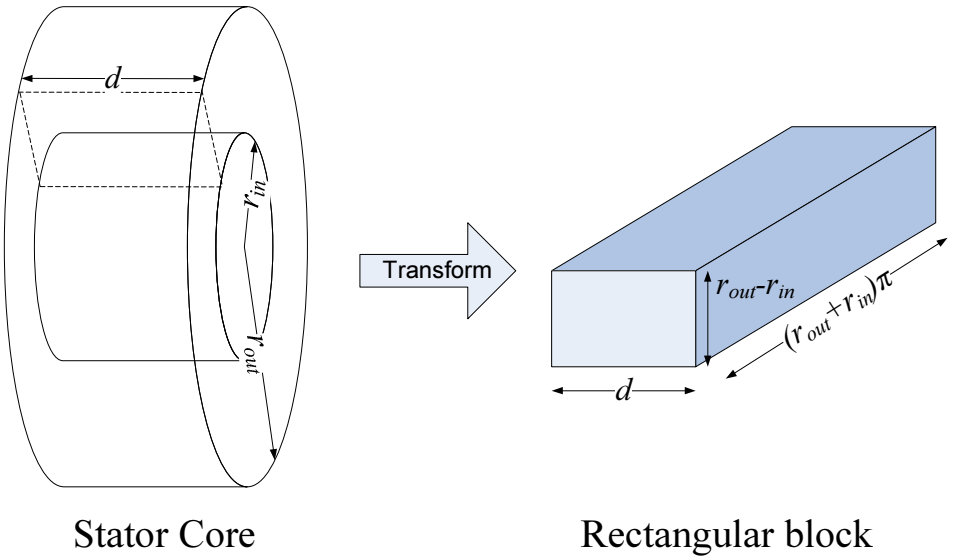

Fig. 5-8. Annulus to rectangular block transformation for eddy current prediction.

5.2.4. Thermal Contact Resistance

When two materials are placed in contact with each other, due to the apparent surface irregularities, the contact between two materials is made only at a few discrete points. Hence the two materials are separated by large air gaps. As a consequence, the heat conduction through the surface joints takes place partly through the actual contact points and partly through the gas gap. The imperfect nature of surface contact results in additional thermal resistance, which manifests itself as a temperature drop at the interface [139].

For conductance in the solid, Mikic [140] suggested that for conforming rough surfaces, the solid spot contact coefficient is:

$$h_{contact,solid} = \frac{2.26 \cdot k_1 \cdot k_2 \cdot |\tan\theta|}{(k_1 + k_2) \cdot \delta} \left(\frac{P}{H}\right)^{0.94} \quad (5.36)$$

Where, δ = Surface profile height, m

$tan\theta$ = The profile slope

k_1, k_2 = thermal conductivity of two contact substances, W/mk

P = Contact pressure, Pa

H = Fluid flow pressure, Pa

On the other hand, the gas gap contact coefficient is calculated from, Kennard [141]:

$$h_{contact,gas} = \frac{k_g}{\delta_{eff}} \quad (5.37)$$

Where, δ_{eff} = Effective mean thickness

k_g = Gas thermal conductivity

Both the derived equations (5.36) and (5.37), are used in the generic thermal circuit to model the temperature drop in between the solid contacts in the generator. Nevertheless, some of the parameters required in these contact coefficient predictions are unknown or not easily available from the material manufacturers. Therefore, to simplify the contact coefficient prediction, Table 5-1 and 5-2 lists the common contact coefficients that can be applied into the generic thermal circuit.

Table 5-1: Solid spot contact coefficient

Solids in contact	P = 0.1MPa		P = 1 MPa	
Contact	*(P/H)*	$h_{contact,solid}$ (W/m^{2}K)	*(P/H)*	$h_{contact,solid}$ (W/m^{2}K)
Aluminum/Aluminum	7x10^{-5}	3616	7x10^{-4}	31500
Aluminum/S.Steel	7x10^{-5}	551	7x10^{-4}	4800
S.Steel/S.Steel	2.6x10^{-5}	117	2.6x10^{-4}	1025

Table 5-2: Gas gap contact coefficient

Gas	h_g (W/m^{2}K)

	P/H = $7x10^{-5}$	P/H = $2.6x10^{-5}$	P/H = $7x10^{-4}$	P/H = $2.6x10^{-4}$
CO_2	6890	6350	7970	7440
Air	9400	8690	10800	10110
Helium Gas	31900	30360	34800	33460

The total thermal contact resistance can be viewed as two parallel resistances: that due to the solid contact spot and that due to the gas gap, as shown in equation (5.38). The contact area is typically small, and especially for rough surfaces, hence the major contribution to the resistance is made by the gaps.

$$\frac{1}{R_{contact}} = \frac{1}{\frac{2.26 \cdot k_1 \cdot k_2 \cdot \left|\tan\theta\right|}{\left(k_1 + k_2\right) \cdot \delta}\left(\frac{P}{H}\right)^{0.94} \cdot A} + \frac{1}{\frac{k_g}{\delta_{eff}} \cdot A} \tag{5.38}$$

5.3. The User Interface of the Generic Lumped Parameter Thermal Circuit

A sophisticated user friendly interface was designed to simplify the manipulation of the generic lumped parameter thermal circuit for axial flux machines. The interface was constructed in an Excel spreadsheet and it consists of seven macro scripts and seven forms. The details of the macro scripts and forms can be obtained from Excel spreadsheet attached in Appendix B. The interface provides a platform for the machine specifications and boundary conditions allocation. From the inputs obtained from the users, the Excel spreadsheet converts the machine specifications into thermal resistances and capacitances by the equations developed in Section 5.2. An automation macro script was developed and used to activate *Portunus* and to feed the generic thermal network circuit, with the corresponding thermal resistances and capacitances. After the solutions have reached converged values, the simulation results are extracted and post-processed automatically, with the used of anoather post-processing macro script.

5.3.1. Machine List

The machine specifications of the axial flux machines are allotted in the Excel spreadsheet in sets. The machine specification set can be created and saved by users from spreadsheets, making the thermal circuit setting-up process easier and more effective. Each machine set created can be saved with its corresponding machine name and reloaded for simulations with different boundary conditions. Similarly, the specifications of the machine can be edited to perform a rapid simulation. Fig. 5-9 (a) shows the user interface of the generic LPM thermal circuit and the machine specification sets are governed and managed by the macro form shown in Fig. 5-9 (b). The machine list form is activated after the "machine" button is pressed on the main interface. It allows the user to create, edit and delete machine specification sets. Fig. 5-10(a) and (b) show the forms for creating and editing machine specification sets respectively. Alternatively, the machine specification sets created can be exported, or imported to/from other machine specification formats, used in the machine design and manufacture industries.

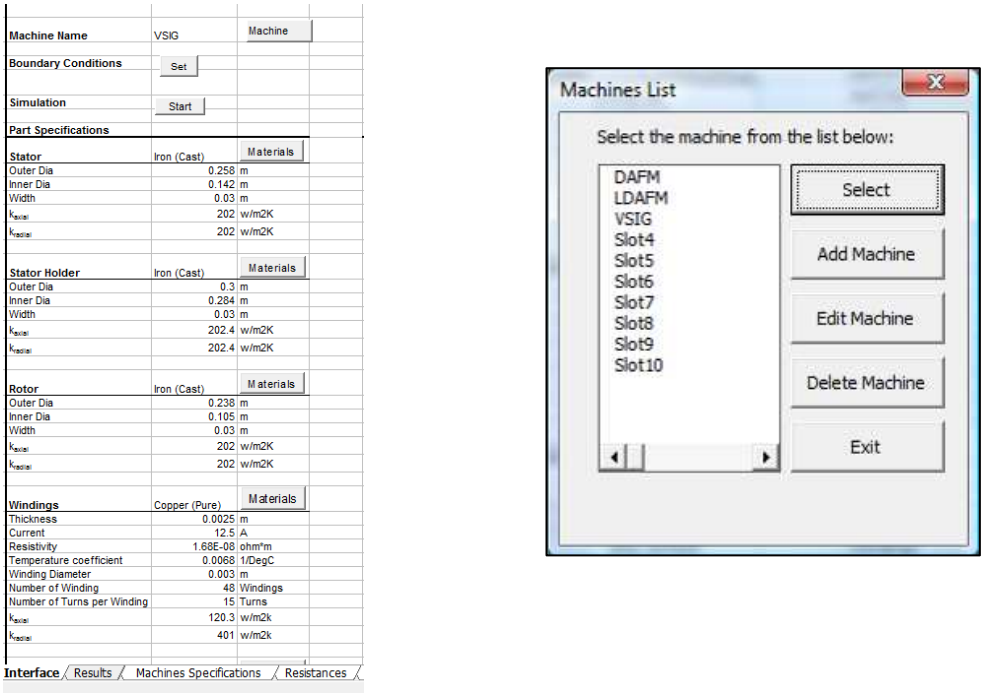

(a) (b)

Fig. 5-9. The interface of the 2-D generic LPM thermal circuit (a) and the machine list form (b)

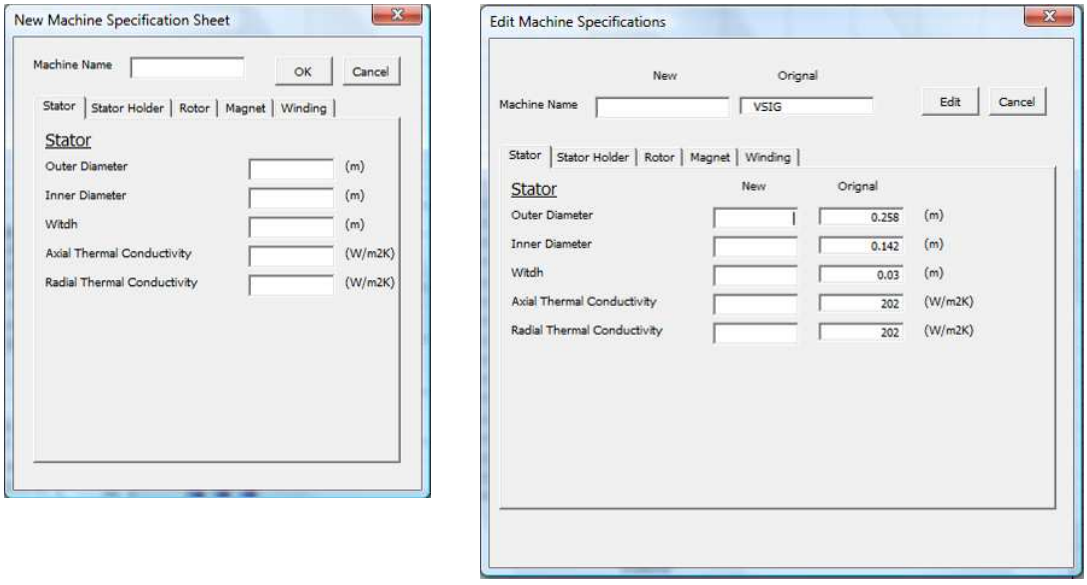

(a) (b)

Fig. 5-10. New machine specification form (a) and machine editing form (b)

5.3.2. Part Specifications

The topology of the axial flux machine used in this research follows the design of the commercial 4kW VSIG air cooled machine manufactured by *Cummins Generator Technologies*. The model generator consists of five major parts, which are the stator holder, stator, rotor disks, magnets and coupling boss. These parts and their corresponding parameters are summarized in Fig. 5-11 and Fig. 5-12.

Several adaptations were made to enable the axial flux machine to be modelled with the 2-D generic LPM thermal circuit. Firstly, the stator windings are simplified into rectangular blocks attached on the peripheral surfaces of the stator core; whereas the depth of these rectangular blocks is equal to the average depth of the windings (Fig. 5-12). The thermal conductivities (in the axial and radial directions) are evaluated by the CLM winding modelling method discussed in Chapter 4.

Also, the 2-D generic LPM thermal circuit neglects the heat flow in the circumferential direction and the convective heat transfer in the inter-magnet grooves is omitted. Therefore, the magnets affixed on the rotor discs are simplified into a

single annulus, with inner and outer radii equal to the magnets (Fig. 5-11). However, the simplification is only valid if the inter-magnet grooves are small, in comparison with the width of the magnets. Otherwise, the air flows in the inter-magnet grooves may induce high heat transfer in circumferential direction, causing large discrepancy in the simulation results.

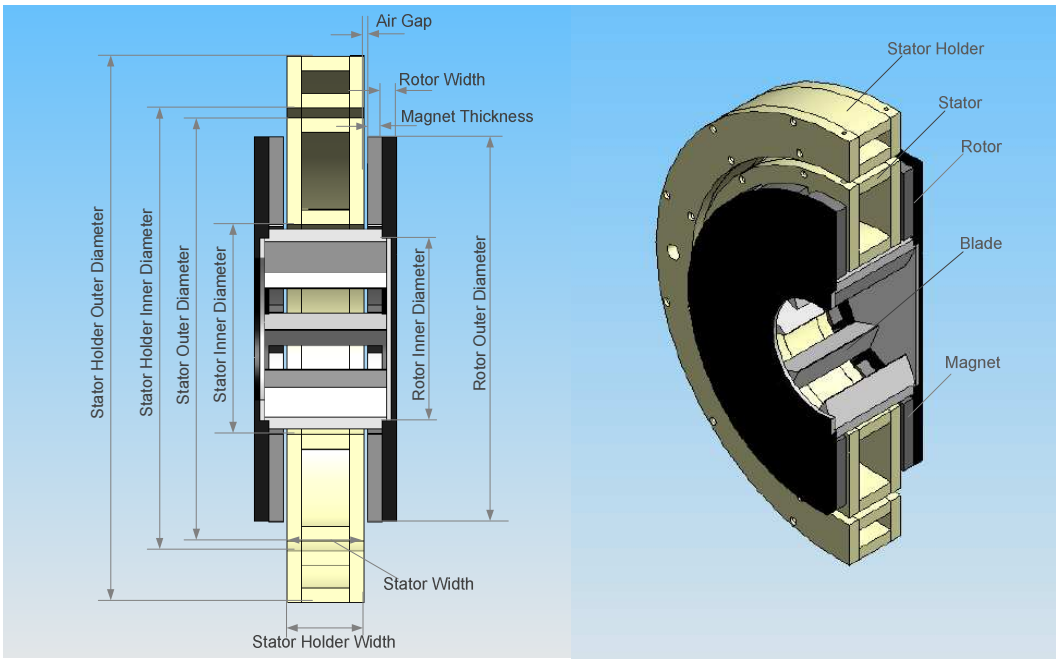

Fig. 5-11. Axial flux permanent magnet generator cross sectional view.

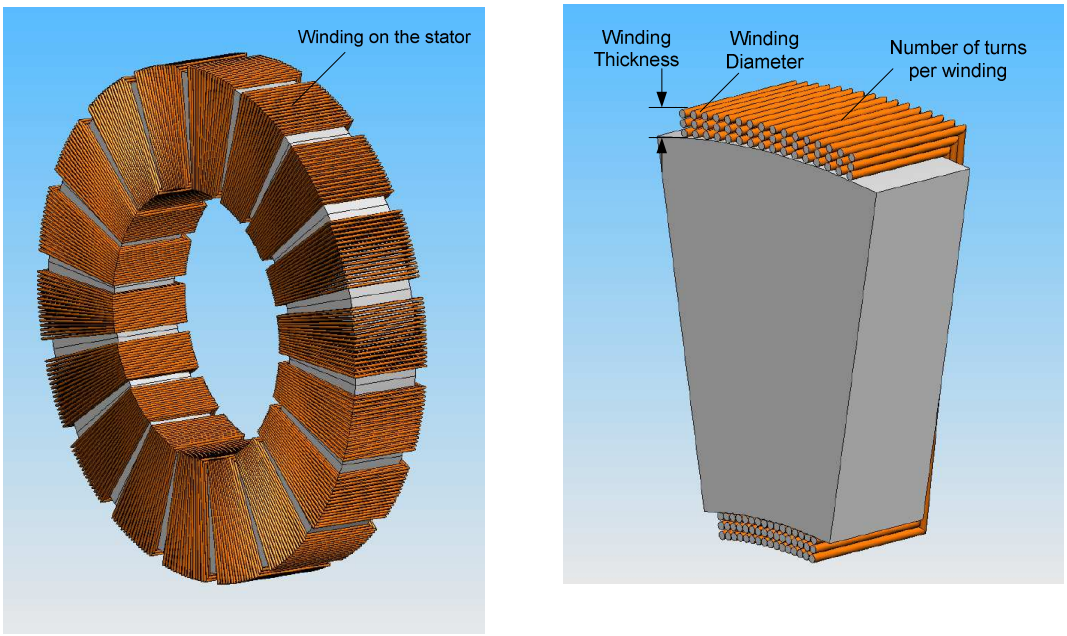

(a) (b)

Fig. 5-12. Windings on the stator (a) and the winding's cross-sectional view (b).

A list of material properties is stored in the spreadsheet to accommodate simulations of various machines configurations with different materials. The list of material properties is shown as below:

Table 5-3: Material properties

Material	Specific heat capacity (J/kgK)	Density (kg/m^3)	Thermal conductivity (W/mK)
Aluminum(Alloy 195)	833	2790	168
Brass (70%Cu, 30%Zn)	385	8522	111
Cooper (Pure)	382	8933	401
Iron (Pure)	447	7870	80
Iron (Cast)	420	7920	52
Iron (Silicon 1%)	460	7769	42
Iron (Silicon 5%)	460	7417	19
Stainless Steel 302	480	8055	15.1
Stainless Steel 304	477	7900	14.9
Stainless Steel 316	468	8238	13.4
Stainless Steel 347	480	7978	14.2
Stainless Steel 410	460	7770	25
Epoxy	1500	1200	0.22
Nomex 410	1300	1400	0.14
Nylon	1600	1100	0.24
Plastic-ABS	1260	1014	0.25
Polycarbonate (PC)	1250	1200	0.29
Polyethylene (PE)	2200	940	0.33
Polyethylene (PP)	1900	905	0.17
PVC	1200	1600	0.16
PTFE (Teflon)	1050	2200	0.25
Polystyrene (PS)	1350	1040	0.10
Rubber (Hard)	2010	1190	0.16
Telfon	1040	2200	0.22

Table 5-4: Material thermal resistivity [142-144]

Material	Resistivity/x 10^{-8} (Ωm)	Temperature Coefficient (K^{-1})
Silver	1.59	0.0038
Copper	1.72	0.0039
Gold	2.44	0.0034
Aluminum	2.82	0.0039
Calcium	3.30	N/A
Tungsten	5.60	0.0045
Nickel	6.99	N/A
Iron	10.0	0.005
Tin	10.9	0.0045
Platinum	11.0	0.00392
Lead	22.0	0.0039
Manganin	48.2	0.000002
Constantan	49.0	0.00001
Mercury	98.0	0.0009
Nichrome	110	0.0004
Carbon	3500	-0.0005

5.3.3. Boundary Conditions and Loading Profile

The machine operating conditions are governed separately by the boundary condition macro list. (Details of the boundary condition macro script can be found in Appendix B.) These operating conditions, including the machine rotational speed, ambient temperature, peak magnetic flux (for eddy current and hysteresis losses), and the current in the windings, operate separately from the machine specifications set. Hence it provides greater flexibility for users to perform a greater range of simulations more efficiently, i.e. the same machine configuration can be tested with different boundary conditions without re-allotting the machine specifications. Fig. 5-13(a) shows the interface of the boundary condition macro script.

The current drawn from the generator varies with the load in the network. For example, a sudden surge of the demand (or load) induces a drop of current in the electrical network and machine or vice-verse. In other words, the change of current in the generator due to the varying load in the network alters the heat generation (or Joule loss) in the electrical machines. Hence, it is necessary implement the time dependent heat sources in the generic thermal circuits.

An electrical loading profile macro script was created to take into account the time dependent load in the generic thermal circuit. In conjunction with the temperature dependent Joule loss, the heat generated from the winding of the axial flux generator can be deduced from:

$$P_{JouleLoss} = I^2(t) \cdot \rho_{25}\left[1+\alpha(T-25)\right] \cdot \frac{4 \cdot n \cdot L}{\pi \cdot d^2} \tag{5.39}$$

Where, I(t) = current profile varies with time

n = number of turns

L = Length of winding per turn, m

d = Diameter, m

ρ = Resistivity of the conductor, Ωm

ρ_{25} = Resistivity of the conductor at 25°C, Ωm

α = Conductor temperature constant, $°C^{-1}$

T = Conductor temperature, °C

An interface was designed to model the electrical load profile as shown in Fig. 5-13(b). The interface consists of two columns, which are separated with commas: The first column indicates the time, whereas the second column indicates the corresponding current at the specified time. For example, the loading profile specified in Fig. 5-13(b) indicates the current is switched on at time 0 and is switch off from time 100s to 200s and from 300s to 400s. The automation macro script was pre-programmed to extract the information from this interface and feed into the generic 2D LPM thermal circuit.

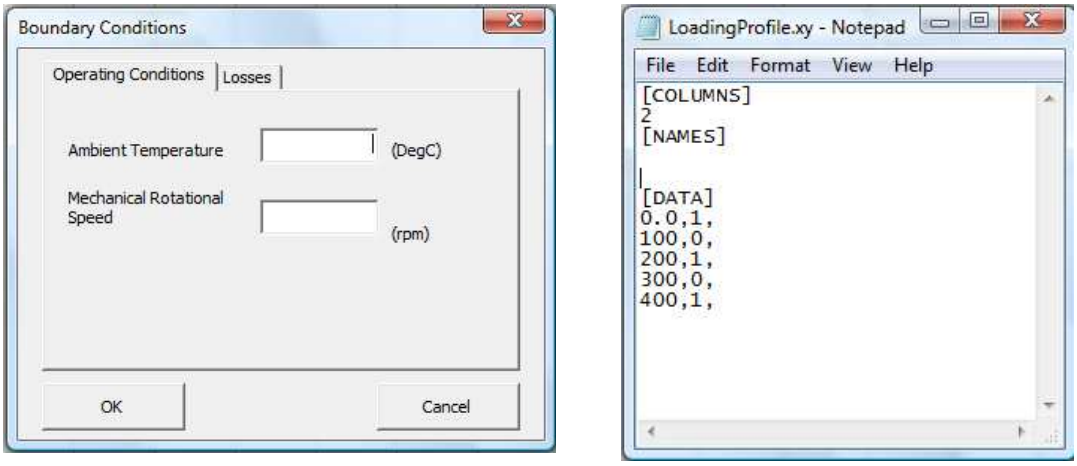

(a) (b)

Fig. 5-13. Machine boundary conditions (a) and loading profile macro script interfaces (b).

5.4. Validation of the 2-D Generic Lumped Parameter Model

This case study describes the use of the 2-D generic lumped parameter model to perform thermal modelling for Cummins Generator Technologies VSIG axial flux machines. Both solid and air temperatures calculated from both the generic lumped parameter model thermal circuit and the CFD model were compared. However, due to the unavailability of experimental results of VSIG machines, the developed 2-D generic lumped parameter model was validated by CFD results. The validations were carried out by investigating the solid and air temperature distributions predicted from 2-D generic LPM and CFD models for different rotational speeds and air gap clearances (or the axial distance between the rotor and stator surface). At the end, the time dependent boundary conditions, such as temperature dependent Joule losses and time dependent heat source, were specified on the developed 2-D generic lumped parameter model. The disparities between the results predicted from the 2-D generic lumped parameter model and CFD models are examined and discussed.

5.4.1. VSIG Axial Flux Generator Specifications.

Currently, CGT's VSIG is commercially available and is in mass production for industrial applications. Due to the confidential agreement with Cummins Generator

Technologies, to protect the competiveness of VSIG in the power generation market, the geometry of the axial flux machine used in this research was based on physical estimation. Table 5-5 summarises the approximated geometrical information of VSIG used for the validation of 2-D generic lumped parameter model thermal circuit.

Table 5-5: Geometry of the axial flux machine used for the generic lumped parameter model validation.

Dimension	Stator	Stator Holder	Rotor	Magnet
Outer Diameter (m)	0.258	0.300	0.238	0.232
Inner Diameter (m)	0.142	0.284	0.105	0.166
Width (m)	0.03	0.030	0.030	0.0035
Axial Thermal Conductivity (W/m^2K)	202	202	202	202
Radial Thermal Conductivity (W/m^2K)	202	202	202	202

Windings	
Axial Thermal Conductivity (W/m^2K)	120.3
Radial thermal conductivity (W/m^2K)	401
Winding Thickness (m)	0.0025
Winding Resistivity (Ωm)	$1.68x10^{-8}$
Current (A)	12.5
Temperature Coefficient ($°C^{-1}$)	0.0068
Number of Winding	48
Number of winding turns	15
Air clearance (m)	0.004

5.4.2. CFD Model of the Simplified AFPM Generator

A 2D-axisymmetric CFD model of the simplified AFPM generator was constructed and simulated in FLUENT. Since there is no direct correlation or empirical equation that can be used to evaluate the heat transfer coefficients and mass flow rate for the VSIG generator, the simulated results obtained from the CFD model were used. In

addition, the comparison between the temperatures predicted from both generic lumped parameter and CFD models is more prudent if both are using the same heat transfer coefficients and mass flow rate.

The computational mesh of the axial flux machine is shown in Fig. 5-14: Both solids and fluid inside the generator were meshed, except for the stator core. In the near wall regions, dense meshes were applied to capture the thermal boundary layers in the immediate vicinity of the wall boundaries. Realizable k-epsilon with enhanced wall treatment model is used to model the turbulence inside the generator. At both the inlet and outlet of the generator, pressure boundary conditions were used: Zero total pressure was specified at the inlet, and at the outlet, zero static pressure was specified. This model solves the flow equations around the rotating parts, including the rotating rotor disk and magnets. Hence, the rotating reference frame model was used. The additional acceleration terms in the flow equations which occur due to the transformation from the stationary to the rotating parts, were solved in the unsteady-state manner. The temperature dependent heat sources were used in both 2-D LPM and CFD models to investigate the effect of temperature dependent Joule losses in the generator windings.

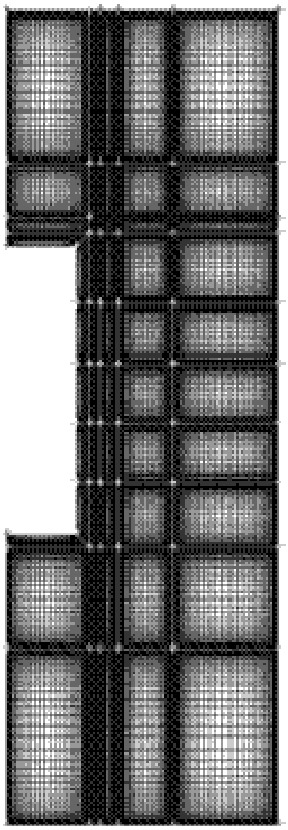

Fig. 5-14. Simplified AFPM generator meshing grid.

5.4.3. Results and Discussions

The AFPM generator solid surfaces and air temperatures were calculated from both the LPM and CFD models. The temperatures predicted from these two models were plotted and compared in Fig. 5-15. Generally, as compared with the temperatures predicted from the CFD model, LPM predicted slightly higher temperatures except on the rotor disk surfaces (RDisks). Additionally, it can be noticed that the temperature discrepancies of these two numerical models were high on the solid surface, as compared with the fluid. The biggest discrepancy occurred in the surface temperature of the stator holder, where the error is around 6%.

The validation was extended by testing the 2-D generic thermal circuit for two different rotational speeds, which were 750 rpm and 3000 rpm, and an additional air clearance size, which was 4 mm. To adapt these machine operating conditions and geometries into the 2-D generic model, a few slight modifications on the machine and

boundary condition forms (Section 5.3) were required. Since the heat flow paths in the generator do not change as these variables alter, the same thermal circuit was used. However, in order to validate the temperatures predicted from the 2-D generic thermal circuit, the CFD models with these particular machine operating conditions and geometry were reconstructed. Unlike the LPM modelling technique, these CFD models were required to be constructed from the begining. New mesh models of the axial flux machines were built and simulated until the average solutions were converged. All the solutions evaluated from three different boundary conditions by the two different modelling techniques are shown in Fig. 5-16, Fig. 5-17 and Fig. 5-18.

The discrepancies between the temperatures predicted from the 2-D generic thermal circuit and the CFD models were quantified by the relative errors in percentage ratio, shown in Fig. 5-15 – 5-18, on the secondary, Y-axes (on the right hand side of the graphs). The relative error is defined as the percentage ratio of the temperature discrepancy between the LPM and CFD and the temperature increase from CFD models (equation (5.40)). The relative error is a better measure for temperature discrepancy, than absolute error because the relative errors, normalise the temperature differences (between 2-D generic thermal circuit and CFD model) with its corresponding inlet temperature. Therefore, the relative error is independent from the inlet temperature specified from the user, i.e. by varying the inlet temperature will not change the relative errors obtained.

$$\text{Relative error} = \frac{(T_{LPM} - T_{in}) - (T_{CFD} - T_{in})}{(T_{CFD} - T_{in})} \times 100\% \tag{5.40}$$

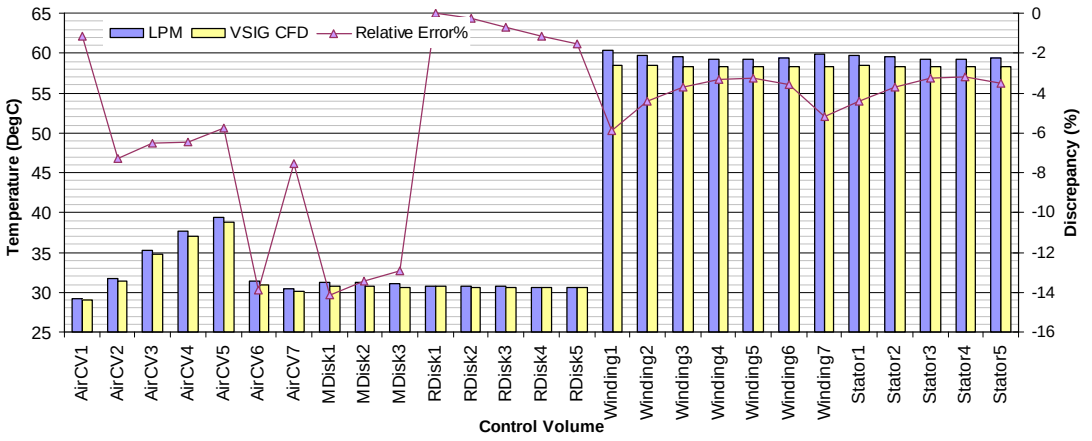

Fig. 5-15. The air control volume s and solid surface temperature calculated from LPM and CFD model respectively at *1500rpm* and *2mm* air clearance.

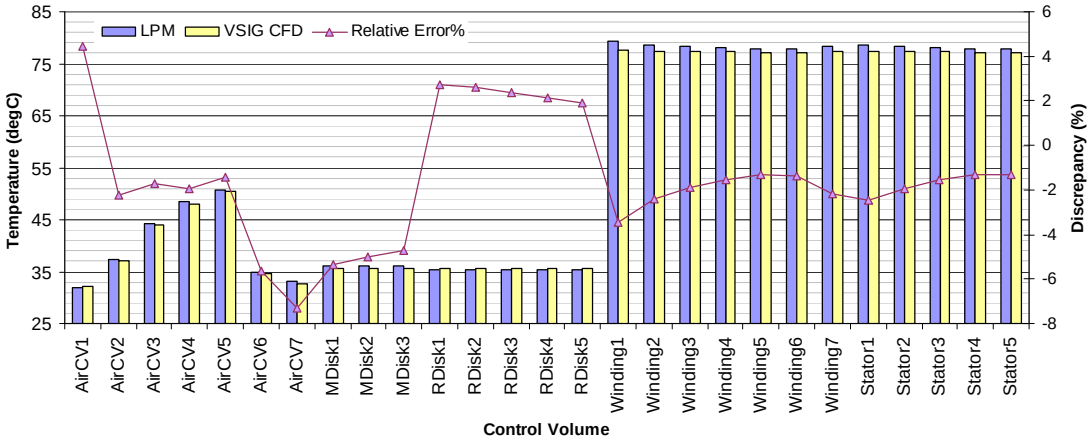

Fig. 5-16. The air control volume s and solid surface temperature calculated from LPM and CFD model respectively at *750rpm* and *2mm* air clearance.

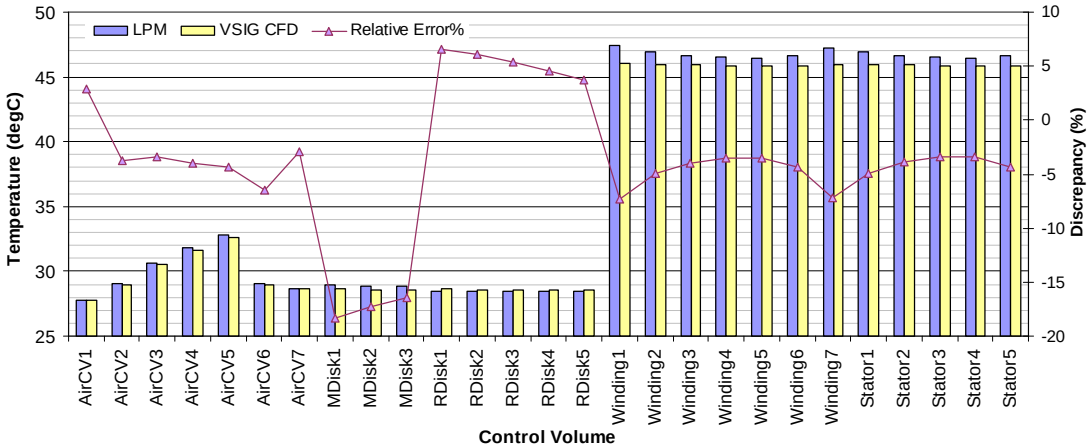

Fig. 5-17. The air control volume s and solid surface temperature calculated from LPM and CFD model respectively at *3000rpm* and *2mm* air clearance.

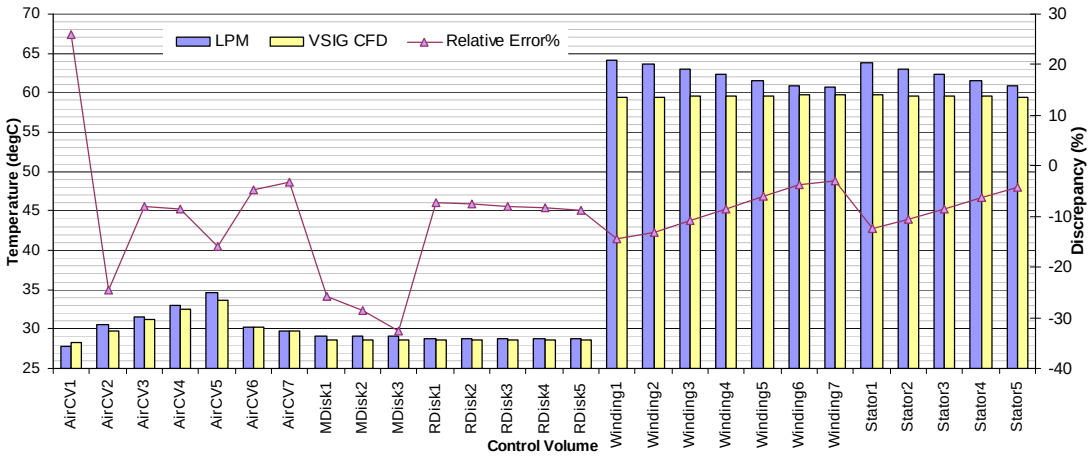

Fig. 5-18. The air control volume s and solid surface temperature calculated from LPM and CFD model respectively at *1500rpm* and *4mm* air clearance.

From these simulations, it can be noticed that the temperature increase of the rotor disk, magnets and the air control volumes were generally smaller when compared with the stator and winding control volumes. For example: the temperature increase of the rotor disk control volumes varied from 5°C to 10°C, whereas for the stator winding, the temperature increase was about 50°C, depending on the operating conditions and the generator geometry. Also, it can be noticed that the temperature increases of the stator winding and the stator core were about the same, as well as for the rotor disk and magnet. This is because the contact resistances between the two solid surfaces were neglected in these simulations. Since the aim of this research is to verify the accuracy of the 2D generic thermal circuit, it is not necessary to include the contact resistances into both the thermal circuit and CFD models.

The stator core and stator winding temperatures predicted by the 2D generic thermal circuit were in good agreement, where the relative errors were within 15%. On the other hand, the temperatures predicted for the rotor disk and magnet were less accurate; the relative errors varying from 2% to 30%, depending on the machine operating conditions and machine geometry. The main reason is that the accuracy of the rotor disk and magnet temperature is strongly affected by the fluid convective circuit used n the generic thermal circuit, whereas for the stator core and windings, the accuracy of the fluid convective circuit has a less significant effect, because they are

mainly determined by the heat sources and the thermal properties on the windings. Temperatures predicted for the stator core and stator windings are more reliable.

Overall, the temperatures predicted from the 2-D generic thermal circuit show a good agreement with the CFD model, especially for low rotational speed and small air clearance models (Fig. 5-16). When the rotational speed increased, the accuracy of the generic thermal circuit deteriorated. For example, the maximum relative error for the 750 rpm model was 8% (in air control volume 7), whereas at 1500 rpm, the maximum relative error was 15% (in the magnet disk control volume 1). However, the accuracy of the generic thermal circuit depreciated less rapidly when the rotational speed increased above 1500 rpm. At 3000 rpm, the maximum relative error was about 18% (in magnet disk control volume 1, see Fig. 5-17).

When the generator air clearance increases from 2 mm to 4 mm, the temperatures of the rotor disk and magnet decrease. On the other hand, the winding and stator temperatures increase (Fig. 5-18). The temperature drops in the rotor disk and magnet were due to the increase of the axial distance between the rotor disk and winding: As the rotor disk is moved further away from the windings, the velocity of the local air in the vicinity of the stator winding decreases. Therefore, the local heat transfer coefficients on the stator wall, which are directly influenced by the local air velocity, reduce. Consequently, less heat is transferred from the winding to the moving air, the winding temperature increases.

Also, it can be observed that the accuracy of the generic thermal circuit deteriorates at higher air clearance. The highest relative discrepancy evaluated from the generic thermal circuit was about 30%, on the magnet disk control volume 3. These illustrate that for high air clearance electrical machine models, higher discretisation level for fluid convective circuits are required.

The 2-D generic thermal circuit validation was continued by examining its transient responses to the time dependent boundary conditions. In this investigation, temperature dependent heat sources (Joule loss) were specified in both CFD and generic thermal circuit models. In addition, the heat sources were switched off after

500 s, and switched back on at 1000 s. The aim of the boundary condition configuration was to examine the machine's cooling responses.

Fig. 5-19 plots the air mass-weighted average temperature of seven air control volumes with respect to time. The stator winding volume-average temperature transient responses are illustrated in Fig. 5-20. Both Fig. 5-19 and Fig. 5-20 show the temperature responses predicted from both CFD and the 2-D generic thermal circuit. The temperature responses of the same (air and solid) control volumes predicted by the CFD and generic thermal circuit models are represented in the same graph with similar colour band for comparison purposes. For example: In Fig. 5-19, the temperature responses of air control volume 1, *AirCV1*, predicted by the CFD and generic thermal circuit were coloured in dark blue and royal blue, respectively; For the solid winding control volume 2, *W2*, the temperature responses were coloured in bright and dull pinks respectively (Fig. 5-20). Both the CFD and thermal circuit models were simulated for 10 hours operating time. Since the temperature responses reach steady states after 1 hour operating time, the temperature responses after 1.6 hours (which is roughly equal to 5000 s) were neglected and omitted from the graphs (Fig. 5-19 and Fig. 5-20).

The steady state results predicted from both CFD and generic thermal circuit models did not perfectly match with each other. The maximum relative error is 14% (Fig. 5-15) and these errors resurface in the transient temperature responses in Fig. 5-19 and Fig. 5-20, in both the heating and cooling curves. As a result, the transient temperature response predicted by the generic thermal circuit model was generally colder while the machine was heating up, and warmer when the machine was cooling down. However, the steady state temperature differences were small: 2 °C for the stator winding, and 0.8°C for the air control volumes, respectively.

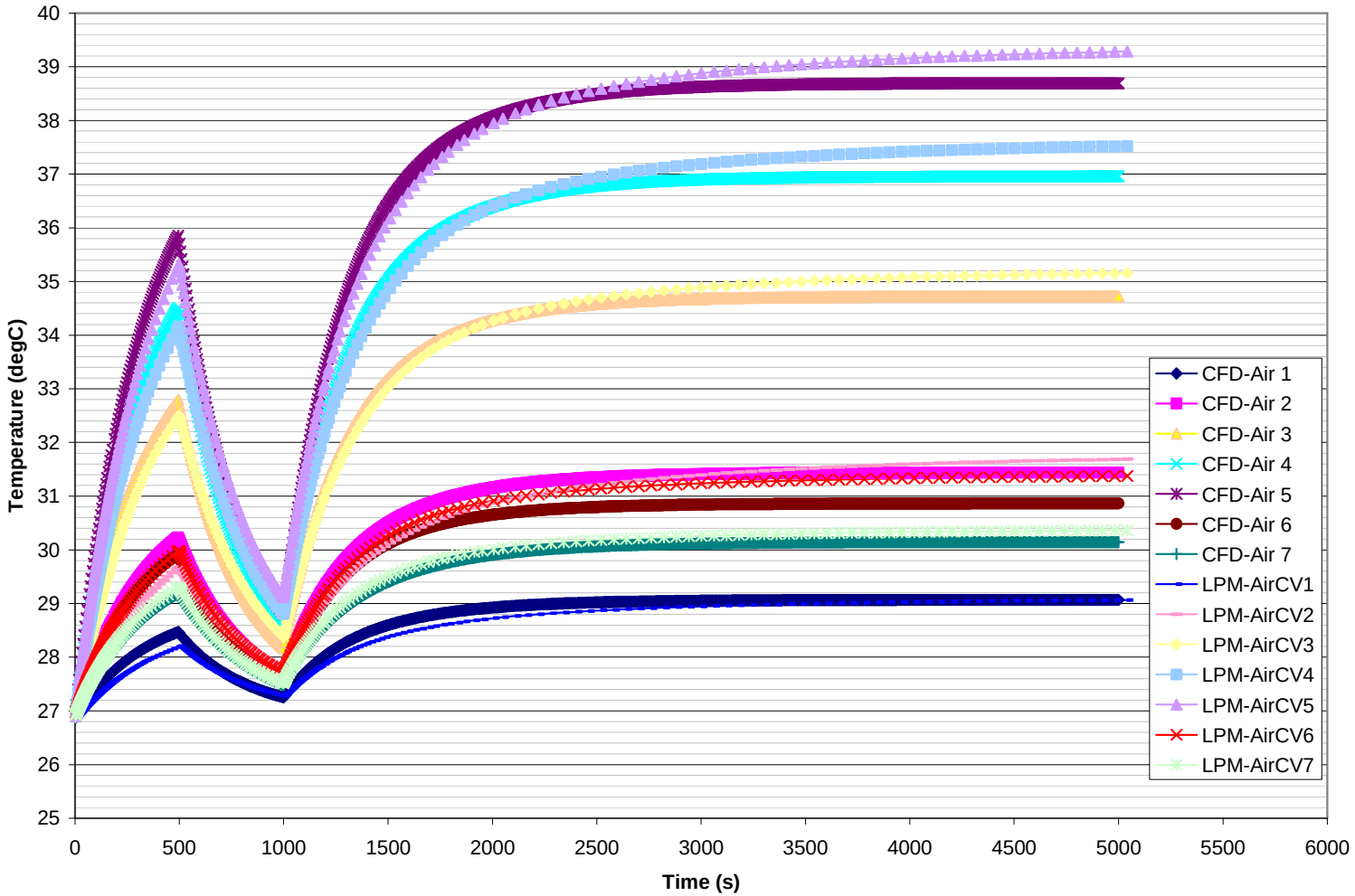

Fig. 5-19. Transient temperature responses of air control volume predicted by both CFD and 2-D generic thermal circuit models.

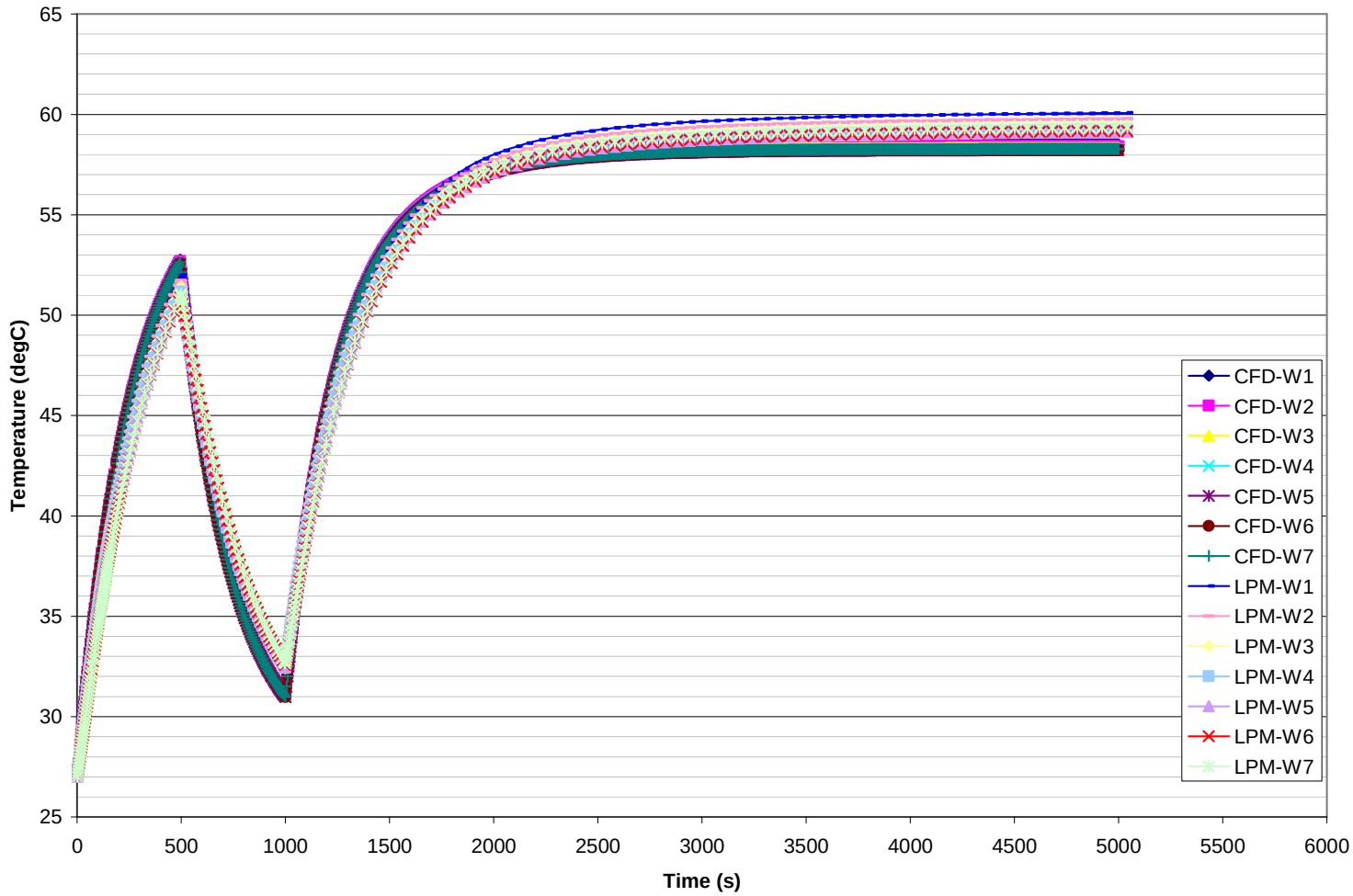

Fig. 5-20. Transient temperature responses of solid winding predicted by both CFD and 2-D generic thermal circuit models.

Except for the slight steady state errors, the transient temperature responses predicted by the 2-D generic thermal circuit shows a good agreement with the CFD models. Further investigations in the accuracy of the transient responses of both the numerical models were conducted, to determine the accuracy of the time constant (the time required to reach 66.6% of the steady state response) of each control volume. The results are shown in Fig. 5-21. The results indicate that the temperature responses predicted by the 2-D generic thermal circuit lagged behind the CFD model, by 20-75 sec, which is about 5% as compared with the CFD time constant. The reason is because the stator core was not modeled in the CFD model. Therefore, an additional mass of the stator core in the generic thermal circuit model was contributing to the 5% time lag for both heating and cooling curves of the machine when compared with the CFD model.

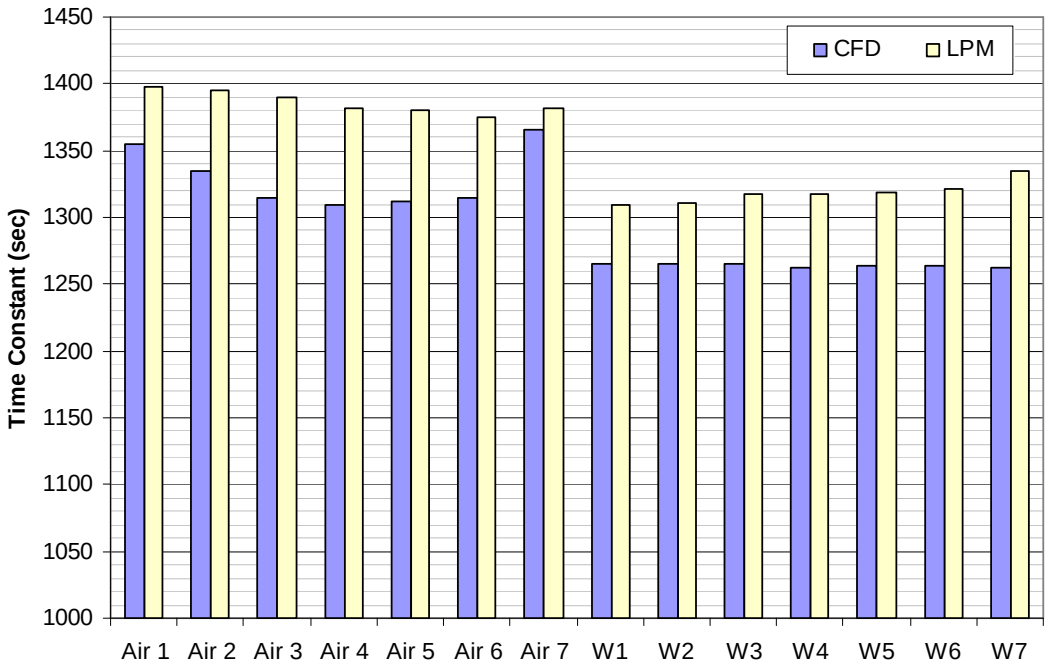

Fig. 5-21. Time constant for each solid and air control volume.

In conclusion, the temperatures predicted by LPM were in good agreement with the temperatures simulated from the commercial CFD package, where the highest relative discrepancy is 30%, or 4 °C maximum absolute temperature difference. The accuracy of the 2D generic thermal circuit was improved at low rotational speeds, and at low air clearance. For transient simulation, the errors inherited from the steady state

simulation persisted. However, the time constant of each control volume was well predicted by the 2D generic model.

5.5. The Construction of the Generic Lumped Parameter Model of Water-cooled, Totally Enclosed Axial Flux Machines

5.5.1. Introduction

Totally enclosed axial flux machines are designed for machine operation in harsh working environments, such as in underwater, and environments with corroding working fluids, gases, pollutants etc. Unlike the open channel axial flux machines, which use the surrounding air to cool the components inside the generator, the totally enclosed machines have metal casings to insolate windings and magnets from dangerous working fluids. For cooling, totally enclosed axial flux machines embrace water cooling systems. External water pumps are commonly used to drive and circulate coolant inside the water jacket, to remove heat generated from the stator winding and stator core. Since water is a thousand times denser than air, most of the heat loss is dissipated via the coolant in the water jacket, instead of via air convection or radiation.

The stator of the totally enclosed machine consists of three major parts, which are the iron core, the aluminum water jacket and the centre water column, see Fig. 5-22. The stator windings that go around the top and bottom of the water jacket, are slotted inside the iron core grooves. The heat losses due to resistive heating in the windings and eddy current and hysteresis losses in the core are conducted by the high thermal conductivity water jacket. While the coolant (water) passes through the water column inside the water jacket, heat is discarded via the coolant by convection to an external heat exchanger or radiator. The convection heat transfer coefficients on the water column walls are high, e.g. 2000-2500 W/m^2K. Due to the high density of water and the high fluid flow speed, the increase of the water temperature is only a fraction of degree, during normal machine operating conditions.

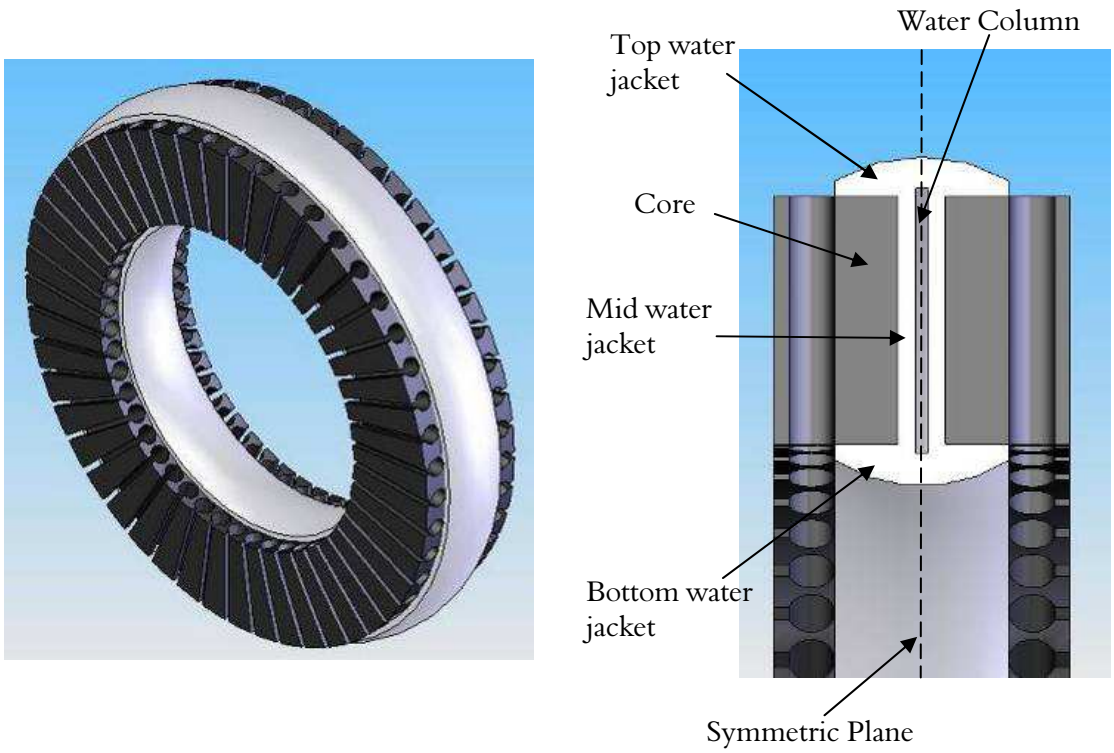

Fig. 5-22. The water-cooled stator of the totally enclosed axial flux generator (a) and cross-sectional view.

5.5.2. The Generic Lumped Parameter Thermal Circuit of Water-cooled Totally Enclosed Axial Flux Machines

The heat losses in the totally enclosed machines are dissipated by means of two main heat flow paths: One is via the coolant in the water jacket in the stator, and the other is via the circulating air in the totally enclosed machine. Based on experiments conducted by Cummins Generator Technologies, 95% of the total heat losses are transmitted through the coolant in the water jacket, whereas the circulated air only accounts for 5% of the total heat dissipation. Therefore, to simplify the thermal equivalent circuit, the local air convection from the stator to the generator casing is represented as a one-off convection thermal resistance.

The stator is divided into thirteen annuli, which are the stator core, top, bottom and middle water jacket, and top, bottom and side windings, see Fig. 5-23. The stator core, middle water jacket and side winding annuli are further discretised into three smaller

control volumes to improve the accuracy of temperature prediction. Each of the annuli of the stator model is represented by the two dimensional thermal circuit described in section 5.2, and inter-connected to match their physical attachment. Between two material contacts, e.g. side windings to side core, water bracket to core etc, thermal contact resistances are introduced to model the temperature drops due to surface asperity. Also, given that the coolant in the water column has high density and the increase of temperature of the coolant is a fraction of a degree, the water column is simplified as one thermal resistance with the coolant inlet temperature as the temperature source. Some totally enclosed axial flux generators are attached to, or adjacent to other electrical or mechanical machines. Hence, additional temperature sources are added to the thermal circuit around the casing, to model the interaction thermal effect between the totally enclosed axial flux generators and the other machines.

In the previous thermal circuit models, the axial flux machines were assumed to be axis-symmetric. Therefore, the windings were simplified as annulus disks and modelled directly by the two dimensional annulus thermal equivalent circuit. However, the stator windings of the totally enclosed axial flux machines are different: Stator windings are packed in bundles and slotted inside the stator core. Since the stator winding bundles are discrete in the circumferential direction, the thermal equivalent circuit of the totally enclosed machine is governed by two separated type of thermal circuits, which are the winding circuit, and the stator core circuit, see Fig. 5-23. The two circuits work interactively in each time step to model the thermal state of the totally enclosed permanent magnet generators.

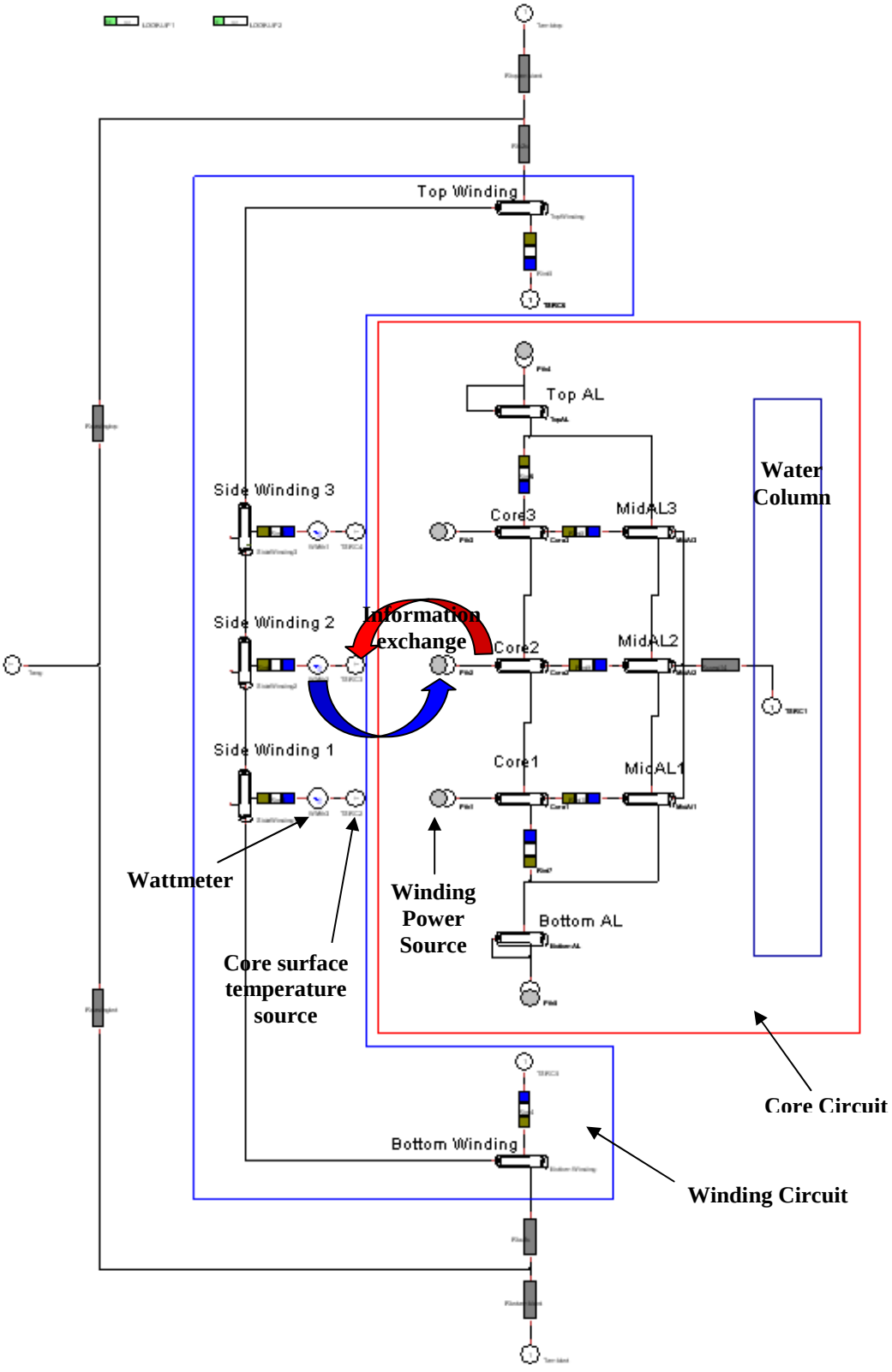

Fig. 5-23. Generic lumped parameter thermal circuit of totally enclose water-cooled axial flux machines.

The winding circuit models the thermal system of one winding bundle. It consists of a contact resistance, a Watt (or Amp) meter, a temperature source and a two-dimensional cylinder thermal circuit. The contact resistance models the gas gap conductance between the two materials in contact, which in this case, it is between the winding bundle and the stator core. Equation (5.41) evaluates the contact resistance of the winding bundle-stator core interface, where the contact area, A_c can be found by equation (5.42), Fig. 5-24.

The temperature sources of the winding circuit are linked to the temperature obtained from the core surface of the stator-core circuit. At each time step, the winding circuit is run based on the core surface temperature obtained from the stator core circuit from the previous time step. The resistive heat passing through the each control volume is recorded and passed to the stator-core circuit in the next time step.

$$R_C = \frac{1}{h_{w-c} \times A_c} \tag{5.41}$$

$$A_c = 2\pi r_c \times \frac{360 - \theta}{360} \times L_w \tag{5.42}$$

Where

$h_{w\text{-}c}$ = Winding bundle and stator core contact coefficient, W/m^{2}K

r_c = Winding slot diameter, m

L_w = Winding Length, m

θ = Contact Angle, °

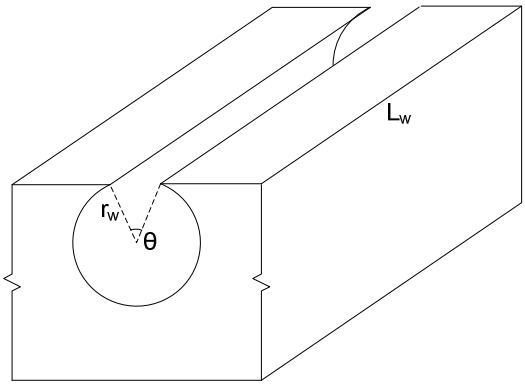

Fig. 5-24. Schematic sketch of the totally enclosed water-cooled slotted core section.

The stator core and water jacket are modeled by the stator core circuit, see Fig. 5-23. In this circuit, the stator core is discretised in to three smaller annuli, whereas the water jacket is split into top, bottom and three middle annuli. All the annuli are modeled by the two-dimensional cylinder thermal circuit. The existence of winding bundles in the stator core circuit is represented by the winding power sources in the stator-core circuit. As the winding circuit only models the thermal path of one winding bundle, the heat power recorded in the Wattmeters of the winding circuit represent the heat losses of one winding bundle. Therefore, the total power used in the winding power sources in the stator-core circuit is evaluated by the multiplication of the total heat recorded in the Wattmeters in the winding circuit and the total number of winding bundles, in the totally enclosed axial flux generator. For example, if the total heat measured in the Wattmeters of the winding circuit is P_w, and the total number of winding bundles is N_w, the winding power sources used in the core circuit are equal to P_w x N_w.

The winding and stator core circuit works interactively during the thermal simulation process: the winding circuit acquires the core surface temperature from the stator core circuit to predict the winding temperature and heat losses due to resistive loss. At the same time, it passes the corresponding total heat measured by the Wattmeters to the stator core circuit, to evaluate the core temperature. The simulation is re-iterated until it reaches a steady state, for each time step.

5.5.3. Transient Boundary Conditions

The generic lumped parameter thermal circuit of the water-cooled totally enclosed axial flux machine adopts the transient solver; hence this implies that the transient temperature solutions can be obtained. Also, based on the generator application, the thermal circuit can be fed by time dependent boundary conditions, such as temperature dependent heat losses, time dependent electrical loading etc.

The winding resistance is temperature dependent: when the winding temperature increases, the electrical resistances and the Joule loss increase. Therefore, in order to acquire better accuracy for the temperature prediction of totally enclosed axial flux machines, the consideration of temperature dependent heat losses in the winding is necessary. In the generic thermal circuit of water-cooled totally enclosed axial flux machines, the resistive heat losses in the winding are represented as power sources. These power sources are pre-programmed accordingly, to evaluate the heat losses in the windings by using the winding temperature predicted from the previous time step. The equations that govern the temperature dependent heat losses are shown in equation (5.30) and equation (5.31). Thus, the generic thermal circuit automatically updates the newly calculated heat resistive power losses in the windings, at every time step, until the system reaches the steady state.

Also, the Joule loss in the axial flux generator depends on the magnitude of the electrical current passing through the stator windings (equation (5.30)). For different machine applications, the Joule loss varies with different electrical loading profiles or patterns. For instance, generators which are directly connected to the grid, the corresponding Joule loss in the winding is proportional to the electrical loading curve. Thus, in order to take account the change of current in the electrical machines in the generic thermal circuit, the heat sources (in the generic thermal circuit) are pre-programmed to acquire the current magnitude, at the different time, from a look-up table specified by the users. The look-up table composes of two columns: The first column states the time interval and second column corresponds to the electrical loading.

Several water-cooled totally enclosed axial flux generators are installed on portable vehicles, where the water pumps of the generators are connected directly to the vehicle engines. When the engine of a vehicle is switched off, the sudden halt of flowing water in the stator water jacket causes the temperature of the generator to soar, due to sudden drop of cooling in the water jacket and the latent heat stored in the engine and the generator. In extreme situations, the temperature of the generator skyrockets above the temperature limits of the generator insulation materials and causes the generator to breakdown or drop in efficiency. Thus, the generic thermal

circuit of the water cooled axial flux generator is modified to take into consideration the sudden stop of the water pump power. In this approach, another look-up table is used in the generic thermal circuit to model the power alteration of the water pump of the generator. Users are allowed to prescribe or amend the power of the water pump in the look-up table, by specifying "1" for water pump power on and "0" for power off at the corresponding time.

5.5.4. Case Study: Generic Thermal Circuit of Water Cooled Totally Enclosed Axial Flux Generators with Transient Conditions

The generic thermal circuit constructed for the totally enclosed, water-cooled axial flux machines was tested with two transient boundary conditions. Two loading curves, which were the square wave and sinus wave loading curves (Fig. 5-25), were used. For the square wave loading curve, the current in the windings varies in steps, from 0 amp to 15 amp, with frequency of 2.77×10^{-4}Hz; whereas for the sinus wave loading curve, the loading frequency is 5.56×10^{-4} Hz, and the amplitude of 7.5 amp at 7.5 amp offset. For both cases, the inlet water temperature was set to 80°C, and the temperature on the casing wall next to the engine was fixed at 100 °C. The ambient temperature specified in the model was 20 °C.

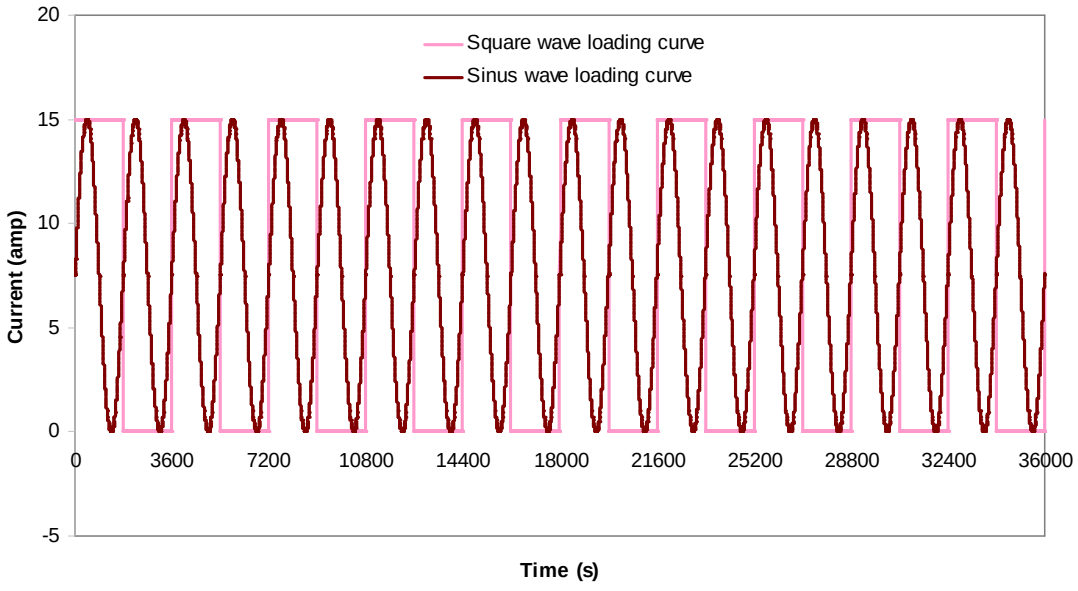

Fig. 5-25. Square and sinus loading curves

Fig. 5-26(a) and (b) show the temperature responses predicted from two different loadings, which are the square and sinus load curves, respectively. The simulated results show that the aluminum water jacket reached the steady state a lot faster than the stator core and windings. This indicates that during the first two hours, the generator was heated by water inside the water jacket (where the water temperature was 80°C). The winding temperature increased when the current passed through the conductors. After two hours, the winding temperature rose above the water jacket inlet temperature and heated up the stator core. The generator system reached a steady state after three hours. It can be noticed that the change in the loading curve caused large temperature fluctuations in the winding temperature. However, the mean final steady state temperatures were not affected by the loading curve profiles.

The rapid temperature change of the aluminum water jacket at the beginning of the operation was due to the temperature source specified in the generic thermal circuit. To simplify the thermal circuit, the water cooling system was represented by a combination of one thermal resistance and temperature source. Therefore, the temperature of the water jacket immediately responded to the temperature of the temperature source after the simulation was started. Nevertheless, the simplification has minimal effect on the final steady state temperatures predicted by the generic thermal circuit.

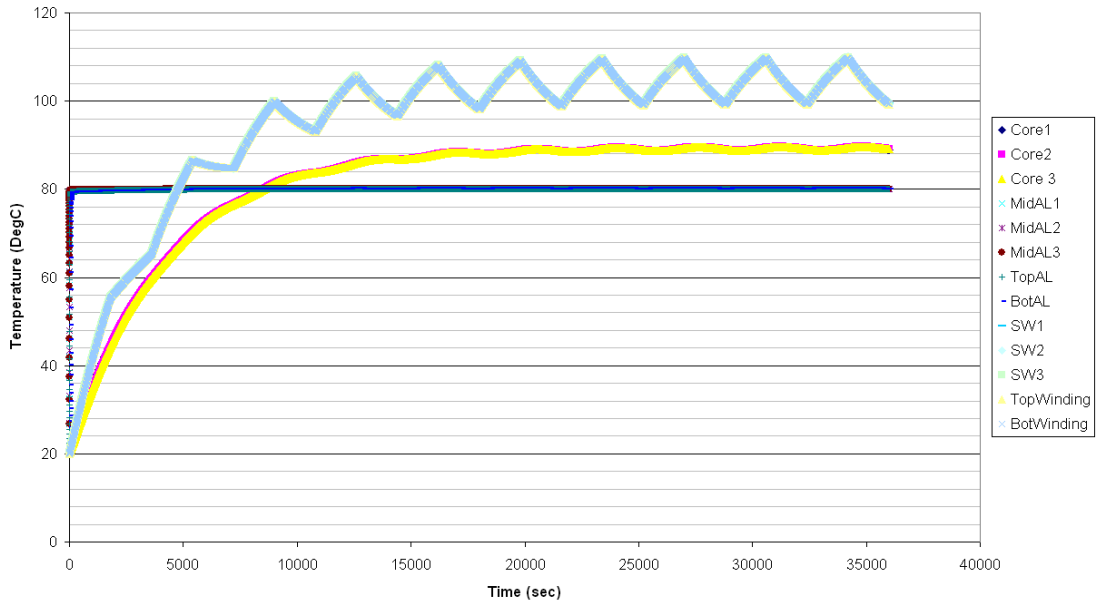

(a)

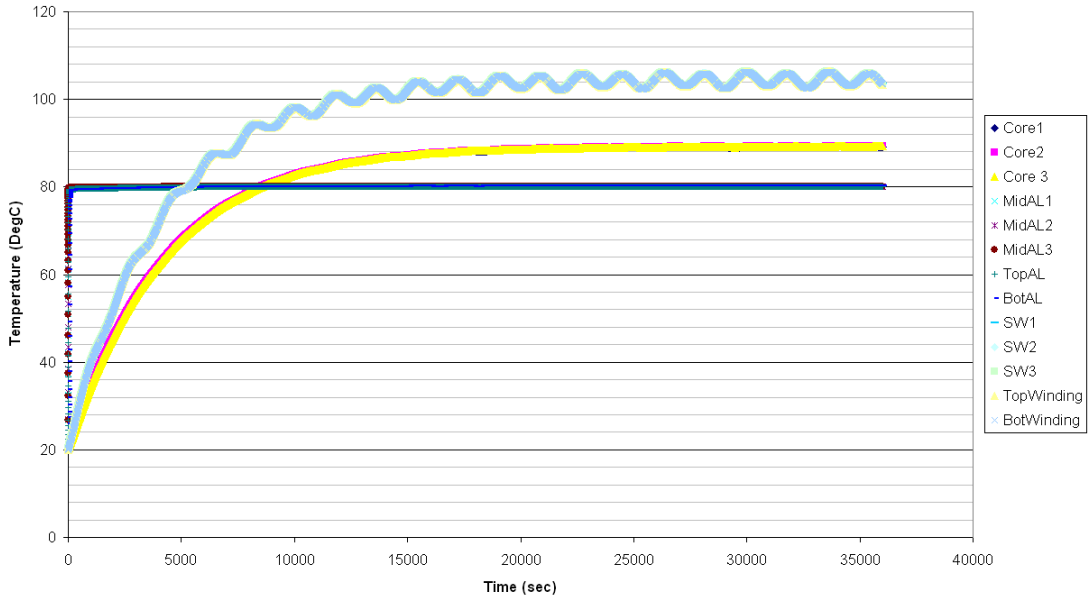

(b)

Fig. 5-26. Temperature responses predicted from the water-cooled totally enclosed axial flux machine with square wave (a) and sinus wave (b) loading curves.

Fig. 5-27(a) and (b) show the generator temperature responses after the generator and water pump were switched off at the fifth hour of the operation, for both loading curves. Once the water pump was switched off, both the stator core and water jacket were heated by the latent heat stored in the windings and by the engine next to the

generator. In these simulations, the generator was set adjacent to an engine of wall temperature equivalent to 100°C. Thus, when both the generator and water pump were switched off, the whole generator reached an equivalent temperature of 90°C.

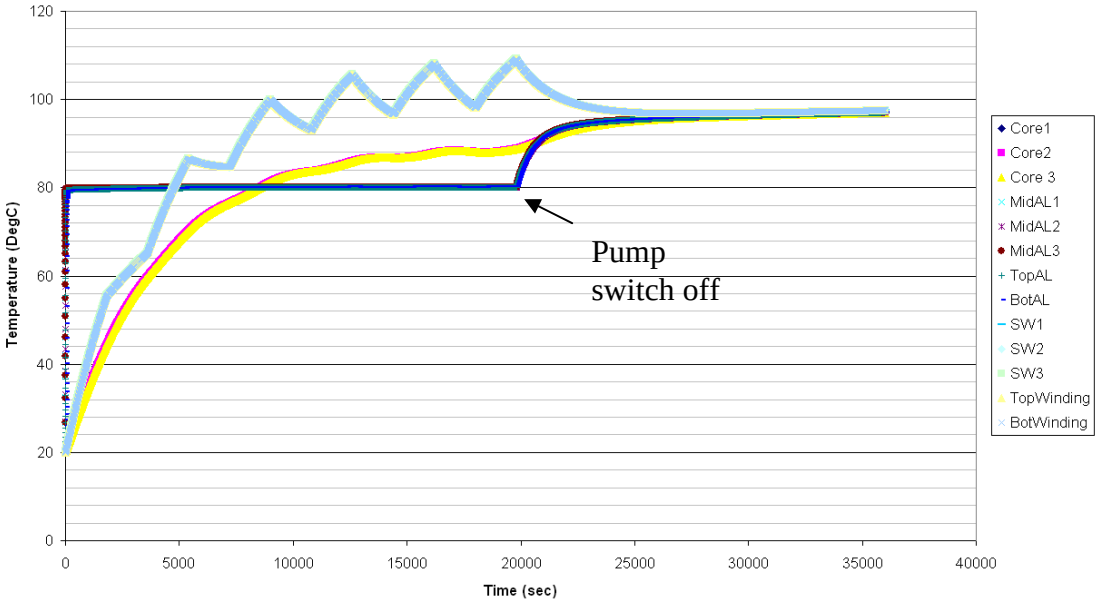

(a)

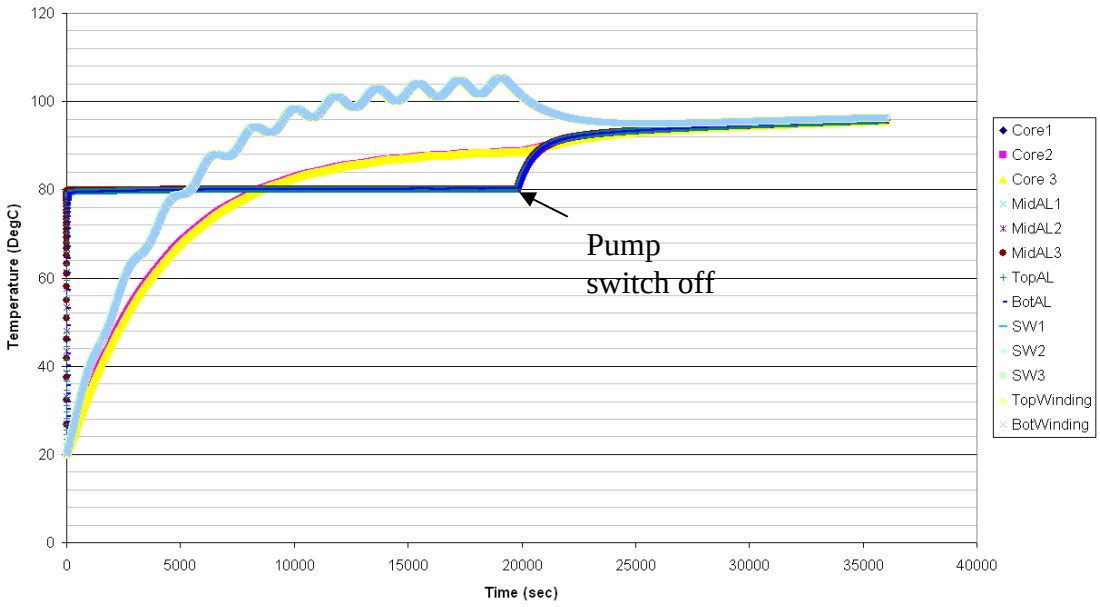

(b)

Fig. 5-27. Temperature responses predicted from the water-cooled totally enclose axial flux machine after the generator and water pump were switched off at the fifth hour of operation, for square wave (a) and sinus wave (b) loading curves.

5.6. Conclusions

Lumped parameter thermal circuits are capable of predicting the thermal state of electrical machines effectively, but the construction of the thermal circuit can be tedious and requires high level of understanding of thermodynamics and heat transfer. Therefore, the idea of the generic lumped parameter thermal circuit has been proposed. The generic thermal circuit consists of the basic conductive and convective sub-circuits. With the thermal resistances and capacitances derived in dimensionless form, the generic thermal circuit can be used to model the thermal states of a collection of electrical machines with wide range of machine sizes, which have broadly similar topology. With small modifications, the generic thermal circuit can be adapted to other types of electrical machines, such as air-cooled axial flux generators, single-sided core-less generators and totally enclosed water-cooled electrical machines.

A sophisticated spreadsheet was designed to further simplify the use of the thermal circuit for the simulation of electrical machines. A user friendly interface was created, in Excel, to input the machine geometries by the user. Also, a set of macro scripts were written to convert the machine specification automatically into its corresponding thermal resistances and capacitances. This information is fed into the generic thermal circuit to perform the thermal analysis. On completion, the results obtained from the generic thermal circuit are transferred back to the Excel spreadsheet for post-processing.

The generic thermal circuit of water-cooled totally enclosed axial flux machines has been proposed. Since the water has higher density than the air, 95% of the heat losses are dissipated via the water jacket to the flowing coolant in these water-cooled machines. Thus, the heat convection to the air was neglected in the thermal circuit of the water-cooled generators. Also, due to the slotted winding design, the generic thermal circuit is split into two sub-circuits, which are the winding circuit and core stator circuit. The two thermal circuits work interactively to predict the temperature responses for transient boundary conditions, such as temperature dependent heat losses, time dependent electrical loading and water pump loading.

In conclusion, both the generic thermal circuit and the sophisticated user interface spreadsheet circumvent the complexity of manually constructing the thermal circuits of the electrical machines. Consequently, the user, who may have little experience of thermal network models, is able to perform rapid engine thermal simulations effectively with the support of these two thermal modelling tools.

Chapter 6

Experimental Validation of the Lumped Parameter thermal modelling technique: Single-sided Slotted Axial Flux Permanent Magnet Generator

6.1. Introduction

The advanced lumped parameter modelling technique has been introduced and discussed. Several case studies have been conducted to verify the results predicted by the lumped parameter thermal network circuit against CFD models. Strong evidence shows that the advance lumped parameter modelling technique is capable of producing good results for temperature and heat flux predictions for simple heat transfer models with sufficient levels of discretisation.

The single-sided slotted axial flux generator has a unique pancake profile and it is widely used for electric vehicle regenerative braking and renewable energy power generation. Fig. 6-1(a) shows the sectional sketch of a 3-kW single-sided slotted axial flux generator. Experimental verifications were carried out on this type of machine to further examine the feasibility and accuracy of the advance lumped parameter modelling technique. The lumped parameter thermal network and the CFD model of the single-sided slotted axial flux permanent magnet generator were constructed. The single-sided slotted axial flux generator rig, which is shown in Fig. 6-1(b) was built to

perform experimental testing, to verify the results simulated from both of the numerical models.

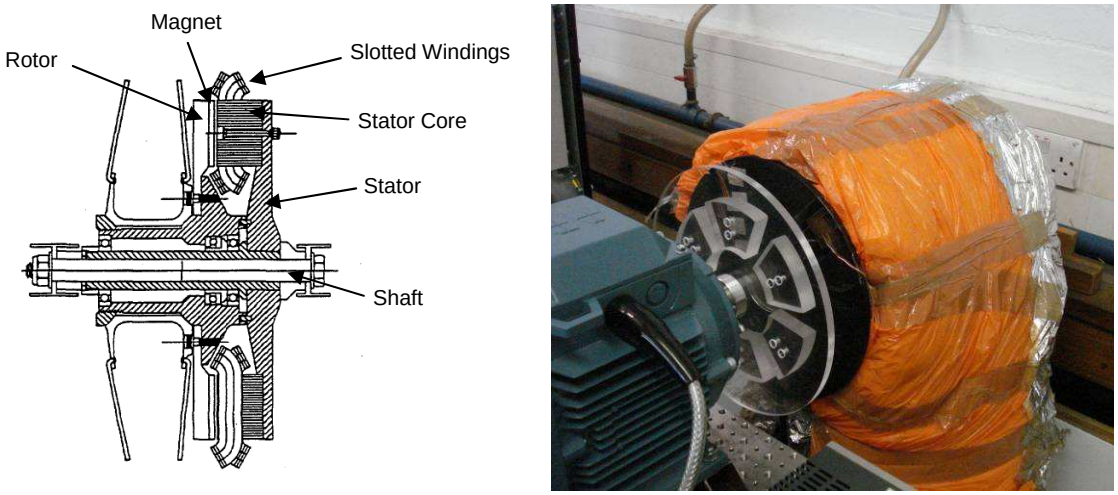

(a) (b)

Fig. 6-1. Single-sided slotted axial flux permanent magnet generator.

6.2. The Construction of the Single-sided Slotted Generator 2-D Lumped Parameter Thermal Circuit

The 2-D lumped parameter thermal circuit of the simplified single-sided slotted generator was constructed, as shown in Fig. 6-2. It consisted of a rotor disk (on the left hand side) and a stator disk (on the right hand side); each of them split into four and three annular control volumes, respectively. These annular control volumes were represented by the annular conductive circuit and they were connected in the same way that they are physically connected in the real machine. The thermal resistances of the conduction thermal circuit were calculated based on the geometry and material properties of each annular control volume.

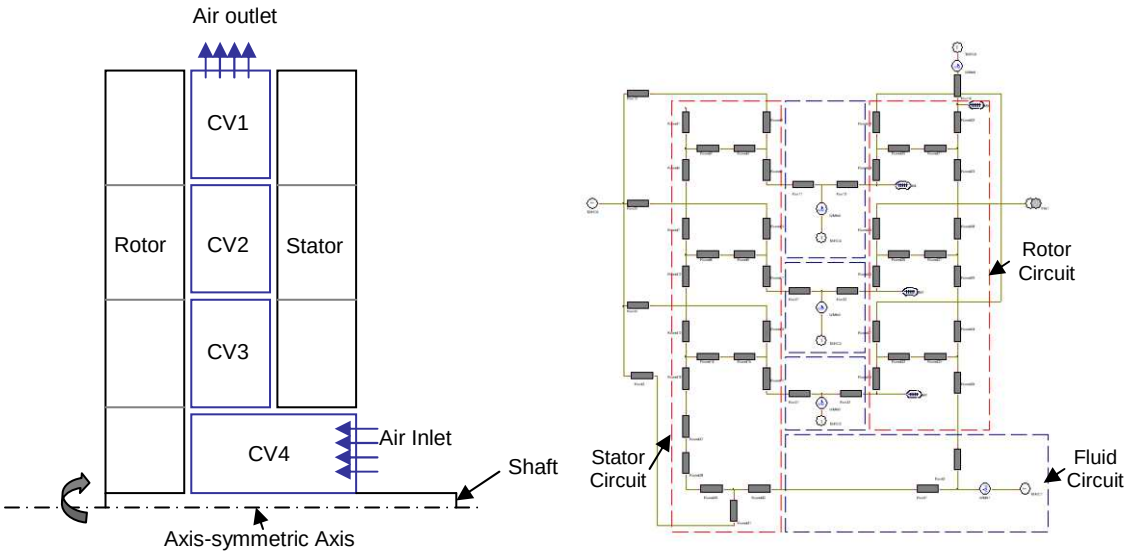

(a) (b)

Fig. 6-2. (a) Simplified single-sided slotted axial flux generator and (b) the corresponding 2-D lumped parameter thermal circuit

The single-sided slotted axial flux machine has thin magnets protruding from the rotor disk surface. Typically, the magnet grooves range between 2 to 4mm. In this analysis, the magnets were assumed to be flush with the rotor disk. The air domain inside the generator was split into four control volumes and each control volume was represented with the fluid convective circuits. The fluid convective circuit was connected to the annular conduction circuits, to allow heat transfer from the air to the solid or vice versa. The temperature dependent Joule loss in the stator windings was modelled by transient heat sources in the 2-D LPM thermal circuit.

6.2.1. Convection Heat Transfer Coefficient

The accuracy of the temperature prediction of the LPM thermal circuit is closely related to the convective heat transfer coefficients used in the model. Nevertheless, accurately determining the convection heat transfer coefficients is difficult due to the complexity of the flow regimes and it involves extensive theoretical and experimental explorations. In this LPM model, the convective heat transfers were evaluated by a

number of existing empirical models [145] based on the flow characteristic in the axial flux machine.

Free rotating dics:

The average heat transfer coefficient on the left hand side of the rotor surface was developed using the formula developed for a combination of laminar and turbulent flow of free rotating plate [146], which is shown as bellow:

$$\bar{h}_f = \frac{k}{r}.N\bar{u}_f \tag{6.1}$$

$$N\bar{u}_f = 0.015 \cdot \mathrm{Re}^{4/5} - 100 \cdot \left(\frac{r_c}{r}\right)^2 \tag{6.2}$$

$$r_c = \left(2.5x10^5 \frac{\nu}{\omega}\right)^{\frac{1}{2}} \tag{6.3}$$

Where,

r_c is the radius at the transition occurs from laminar flow to turbulent flow, m

ν is the fluid kinematic viscosity, m^2/s

ω is the rotational speed, rad/s

r is the disk outer radius, m

Re_ω is the rotational Reynolds number, which is defined as $\mathrm{Re}_\omega = \frac{\omega r^2}{\nu}$

k is the air thermal conductivity, W/mK

By considering the single slotted axial flux generator described in Fig. 6-2(a), which has outer radius, r_c, of 0.15 m, and rotational speed, ω, of 1495 rpm (or 156.5 rad/s), air kinematic viscosity and thermal conductivity of 16.97 x 10^{-6} m^2/s and 0.0271 W/mK respectively, the convection heat transfer coefficient on the rotor side surface, $\bar{h}_f$, calculated from equations (6.1)-(6.3) is 26.83 W/m^2K.

Rotor peripheral edge:

The heat transfer coefficients for the radial peripheral edge of the rotor disk are similar to the rotating cylinder in air. Hence, the average heat transfer coefficient is given as [145]:

$$\bar{h}_p = \frac{k}{D}.N\bar{u}_p \tag{6.4}$$

$$N\bar{u}_p = 0.133 \cdot \mathrm{Re}_D^{2/3} \cdot \mathrm{Pr}^{1/3} \tag{6.5}$$

$$\mathrm{Re}_D = \frac{\omega \cdot D^2}{v} \tag{6.6}$$

Where,

D is the rotor disk diameter, m

Pr is the air Prandtl Number

By applying D = 0.30 m, Pr = 0.711, and a rotational speed of 156.5 rad/s into equations (6.4)-(6.6) the average convection heat transfer coefficient at the peripheral edge of the rotor disc, $\bar{h}_p$, can be determined, which is 94.7W/m^{2}K.

Flow passage between the rotor-stator:

Owen [147] provided an approximate solution for the flow between a rotating and a stationary disks, which relates the stator-side average Nusselt number to the volumetric flow rate by the following equation:

$$\bar{h}_{rs} = \frac{k}{r}.N\bar{u}_{rs} \tag{6.8}$$

$$N\bar{u}_{rs} = \frac{0.333 \cdot Q}{\pi \cdot \upsilon \cdot r} \tag{6.9}$$

Currently no mass flow correlation has been developed for the single slotted axial flux generator. Hence, the mass flow measured from the experiments, 3.61 g/s, was used to calculate the average stator side heat transfer coefficient, $\bar{h}_{rs}$. 22.63 W/m^{2}K was obtained from equations (6.8) and (6.9). Wang [145] suggests that the convection heat

transfer coefficient on the rotating disc can be assumed to be the same as on the stator-side.

6.2.2. Mass Flow Rate Measurement

There is neither a theoretical nor empirical mass flow correlation that has been developed for the single slotted axial flux generator. Hence, the mass flow used in the LPM model was obtained from the experiments. In future work, more sophisticated parametric variation studies of convective heat transfer coefficient and mass flow rate will be performed to develop empirical formulae that relate the heat transfer coefficient and mass flow rate to different flow conditions and geometrical parameters. Therefore, the LPM will be able to provide accurate temperature values inside the AFPM generators independently from either the experiments or CFD models.

6.3. The Single-sided Slotted Generator CFD Model

A 2-D axisymmetric CFD model of the simplified single-sided slotted generator was constructed and simulated in the FLUENT 6.3.26 package. Fig. 6-3 illustrates the mesh grid of the simplified single-sided slotted generator CFD model which consists of 40,000 nodes. The extra air volumes at the inlet and outlet were modeled to eliminate the boundary interference. On a modestly powered desktop computer (1.773GHz Core Duo Intel processor, 1 GB RAM machine), the meshing process and iterative calculation of the CFD model took up to nine hours of computational time. The input data and the boundary conditions that applied in the CFD model are as follows:

- 0.3m outer diameter and 0.01m thick rotor disk.
- 0.3m outer diameter, 0.07m inner diameter and 0.008m thick stator disk.
- 3mm Rotor-stator clearance.
- 15 °C ambient temperature.
- Fine meshes are used in the near wall region to maintain Y^+ below 5.

- Realisable k-epsilon turbulent model with Enhanced Wall Treatment (EWT) is used to model the turbulence in the flow. EWT is a near-wall modelling method used in the turbulent models, to evaluate the fluid velocity field adjacent to the wall boundaries. The details of EWT can be found in [131].
- Zero total pressure and zero static pressure conditions are specified at the inlet and outlet of the simplified AFPM generator respectively.
- The rotor parts are identified to have a rotational speed of 1495 rpm with the use of a rotating reference plane.
- 553W/m^2 heat flux input is specified at the back of the stator to model the winding joule losses. The heat flux specified here is obtained from the experimental results.

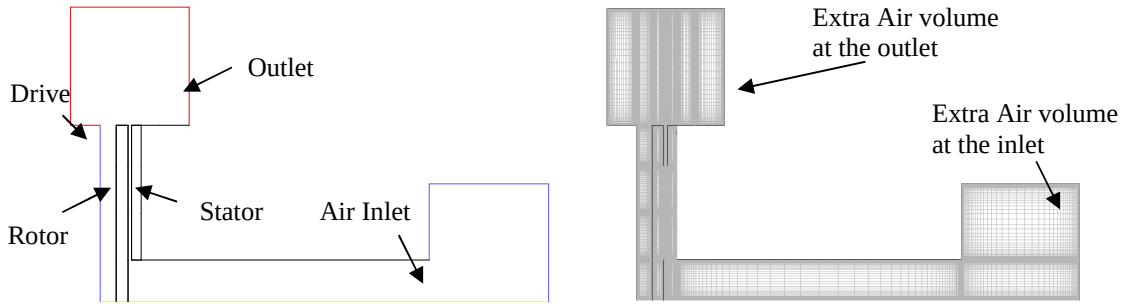

(a) (b)

Fig. 6-3. (a) The schematic plan of the simplified single-sided slotted axial flux generator and (b) corresponding CFD mesh model.

6.4. Experimental Set Up

6.4.1. Test Rig

The single-sided axial flux generator test apparatus is shown in Fig. 6-4(a). The experimental rig was designed to allow thermal and mass flow measurements to be taken with minimal experimental errors. The test apparatus consists of two major parts, which are the rotor and stator disks. The outer diameter of the rotor disk is

150mm and it is made of high thermal inertia 10mm thick Perspex sheet. It is transparent and hence it allows flow visualization experiments to be conducted. The rotor disk is powered by a 3kW 2-pole-50Hz induction motor (Fig. 6-4(b)). The speed of the induction motor is controlled by a 4kW AC vector drive speed ABB inverter.

The stator disk of outer diameter 150mm, inner diameter 70mm, is made of high thermal conductivity 8mm thick Aluminum sheet. An Aluminum tube of inner diameter 30mm and length 150mm is welded to the back of the stator disk. The Aluminum tube serves two main purposes. Firstly, it is used to support the stator disk so that the Aluminum stator disk can be aligned to the rotor. Secondly, it acts as a crude converging nozzle, compressing the air at the inlet to allow accurate mass flow measurements. The stator disk structure is supported by two adjustable stands mounted on the floor. The adjustable stands are designed to allow the stator structure, to shift in both axial and radial directions to attain the desired air gap and height for the different test cases. The details of the test rig geometrical information are illustrated in Fig. 6-4(c).

Six 8 W, 12 V_{dc} silicon heaters were affixed at the back of the stator disk; see Fig. 6-4(b). These heaters were connected in parallel electrically and were powered by an 18 V_{dc} 360 W rated adjustable DC power supply, to replicate the heat generation due to Joule loss in the single-sided axial flux generator. The DC power supply was adjusted below 360W so that it did not exceed the power rating of the silicon heaters.

The experimental errors can be minimised by increasing the temperature on the stator surface. Since the power input from the DC power supply is limited by the silicon heaters, in order to increase the stator front surface temperature, the back of the stator was insulated with several fibre glass insulation blankets (Fig. 6-1(b)), to minimise the heat dissipated from the back of stator and heater pads.

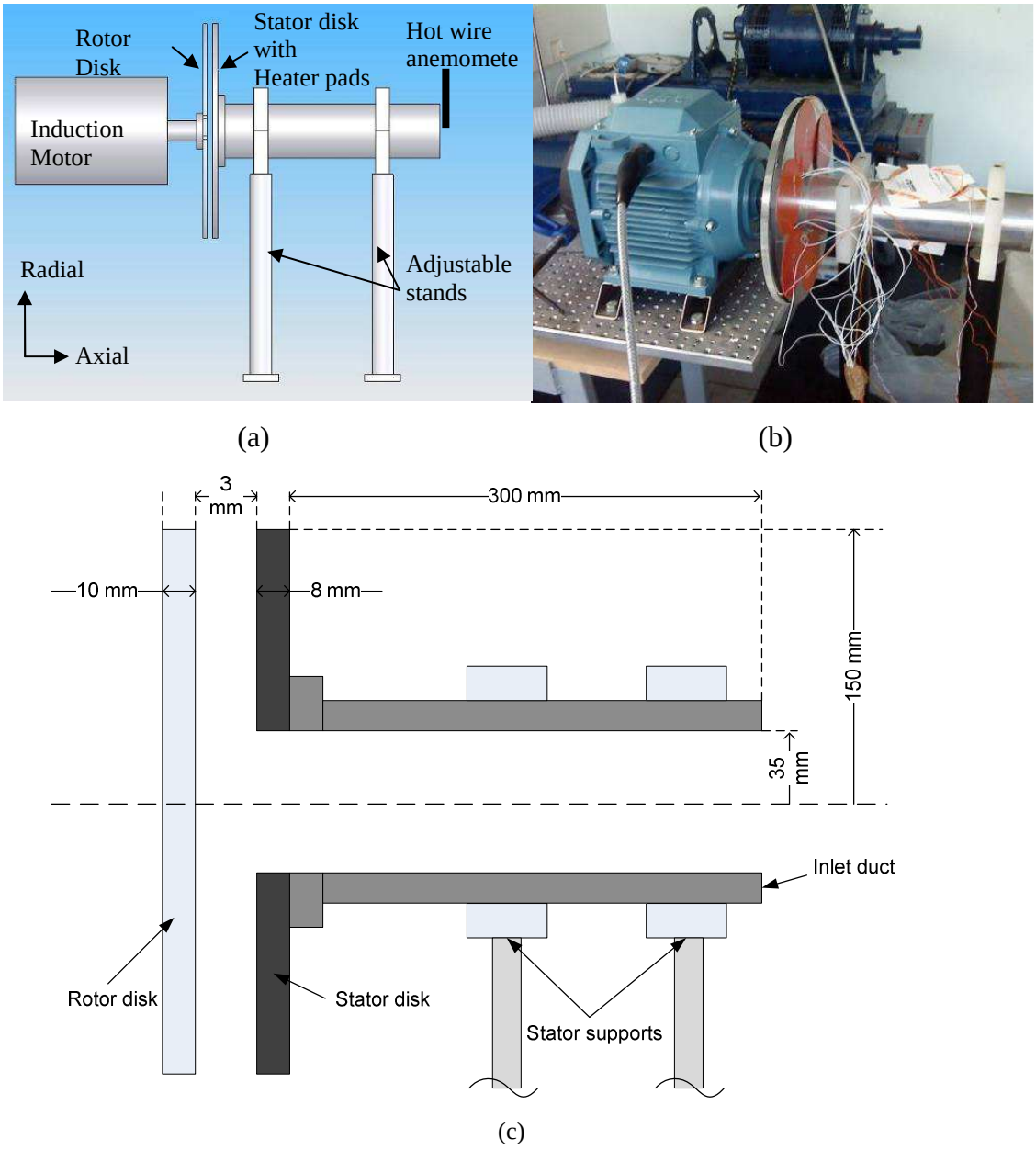

Fig. 6-4. The schematic (a), snapshot (b) and geometrical information (c) of the simplified experimental rig.

6.4.2. Experiment Apparatus

Surface temperature measurements

The temperature of the surface inside the generator was measured using the T-type surface thermocouple. Thermocouples are the most commonly used devices for temperature measurement. However, when measuring the temperature of a substance

using the thermocouple, it can only indicate its own temperature and does not always reflect the actual temperature of the substance. In general, the temperature of the thermocouple is not equal to the temperature of the substance, unless special precautions are taken. It is also vital to identify the sources of spurious EMF in the thermocouple before conducting experiment testing.

One common thermocouple measurement problem is caused by unintentional thermocouple junctions, such as, using other wire types for extending the leads of the thermocouples, or directly connecting the thermocouple to an existing microvolt meter. The former error can be easily corrected by simply using the same type of extension leads, but for the error that occurs in the latter configuration, cold junction compensators (CJC) are required. Fig. 6-5 illustrates the configuration used in this work in which the thermocouples were CJC compensated. This configuration introduces an intermediate metal (usually copper), into the loop and hence two additional thermal junctions are created. Although the law of intermediate metals states that a third metal, inserted between the two dissimilar metals of a thermocouple junction will have no effect provided that the two junctions are at the same temperature, since the thermocouple measures temperature differentially, the temperature at the two thermal joints must be known in order to determine the actual temperature measured at the hot junction. The CJC algorithm compensates the output voltage measured at the two copper ends to determine the exact temperature at the hot junction.

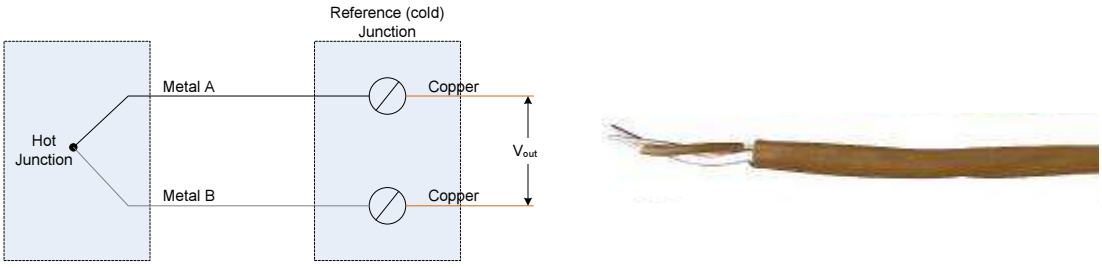

(a) (b)

Fig. 6-5. Thermocouple cold junction compensator (a) and twisted and screened thermocouple (b).

On the other hand, in order to minimize the thermal shunting effect during the temperature measurements, thermocouples with small diameter wires, 32 AWG (0.20mm diameter) were used in the experiments. However, this caused the thermocouples to have very high resistance which made them very sensitive to noise and errors due to the input impedance of the measuring instrument. For a 32 AWG wire, at 80 °C, the electrical resistance is about 15 Ohms/m. However, when it was coupled with the PICO-TC08 data acquisition unit, which has an input resistance of 2 MOhms, the error was only 0.01%, for a 12m length of the 32 AWG wire.

Thermocouples generate a relatively small voltage (in μV) and hence noise is always an issue. The common noises are magnetic field, unearthed surface, static electricity, and utility AC power line (50 or 60Hz) noise. However, the PICO-TC08 data logger, which was used in the experiments, rejects any common mode noise. The noise in the low voltage signal can be minimised by twisting the wires together to help ensure both wires pick up the same noise signal. Additionally, the PICO TC-08 data logger uses an integrating analogue to digital converter which helps average out any remaining noise. In extremely noisy environments, such as near the induction motor, screened extension cables were used (Fig. 6-5(b)).

The surface temperature was measured by OMEGA® SA1-T type surface thermocouples. On the top side of the thermocouple, a fibreglass reinforced polymer insulation layer was affixed to minimise the effect of the fluid temperature on the thermocouples; on the bottom side, high temperature resistance acrylic double-sided tape is used to attach the thermocouples on top of the measured surface (Fig. 6-6). As a result, the temperature reading obtained directly from the thermocouple was the temperature of the top surface of the acrylic double-sided tape. In addition, acrylic has very low thermal conductivity hence the temperature drop across the double-sided tape is significant. To obtain the temperature of the solid surface, a correction factor was introduced, which was derived from the heat conduction equation, as shown in equations (6.10) & (6.11):

$$T_{surface} - T_{measured} = \frac{q \times L}{k} \tag{6.10}$$

$$T_{surface} = \frac{q \times L}{k} + T_{measured} \tag{6.11}$$

Where $T_{surface}$ is the temperature on the solid surface

$T_{measured}$ is the temperature obtained from the thermocouple

q is the heat flux

L is the thickness of Acrylic

k is the thermal conductivity of Acrylic

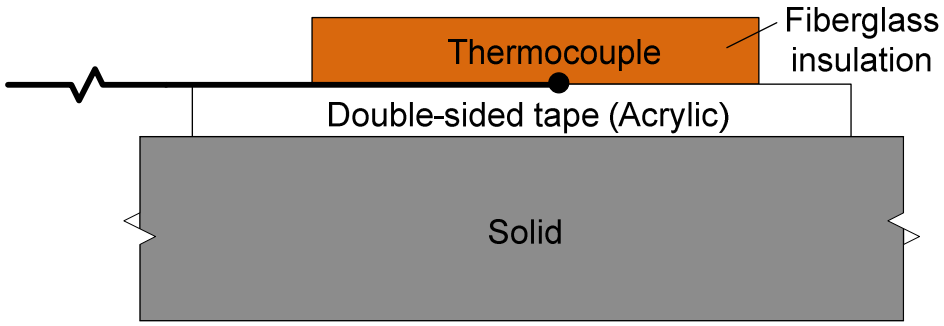

Fig. 6-6. OMEGA®SA1-T type thin film surface thermocouple attached to the solid substance with Acrylic double-sided tape.

Thermocouples have wide temperature ranges, for example, K-type thermocouples have range from -200 °C to 1350 °C; T-type thermocouple measures temperature from -270 °C to 400 °C. However, it is crucial to make sure that the surface temperature is not only within the thermocouple temperature limits, but also that it does not exceed the wire insulation temperature limits. When the substance exceeds the insulation temperature limits, the wire insulation material diffuses into the thermocouple and cause decalibration. Since the operating surface temperature for the experiment testing was 80 °C, the OMEGA®SA1-T type thin film surface thermocouple with the insulation temperature limits of -60 °C to 175 °C was chosen for this application.

Heat Flux Measurement

The stator surface heat flux was measured by using the OMEGA® HFS3 heat flux sensors (Fig. 6-7(a)). The heat flux sensors have very low thermal profile and are designed for precise measurement of heat transfer through any material, on flat or

curved surfaces. The OMEGA® HFS3 is a differential thermocouple sensor; it measures the heat transfer rate by measuring the temperature difference across a thermal barrier. In the centre of the sensor, there is a thin Kapton barrier, for which the thermal characteristic is known. On either side of the Kapton barrier, 50 copper/constantan junction thermopiles are bounded. These copper/constantan junctions are wired in series on the alternate side of the Kapton barrier, where the copper output leads are attached, one to the first junction on the upper surface and one from the last junction lower surface (Fig. 6-7(b)). As a result, the sensor can be directly interfaced to a microvolt meter with no cold-junction compensator required. Table 6-1 lists the thermal properties of the OMEGA® HFS3 heat flux sensor:

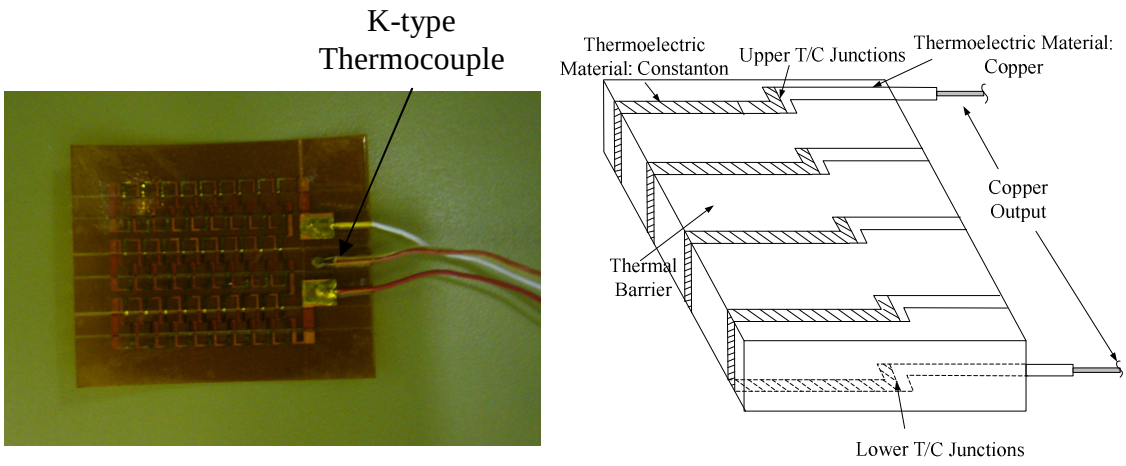

(a) (b)

Fig. 6-7. OMEGA® HFS3 heat flux sensors

Table 6-1: Thermal properties of OMEGA® HFS3 heat flux sensor:

Properties	Quantity	Unit
Thermal Resistance	0.002	$^oC/W/m^2$
Thermal Capacitance	600	$Ws/ ^oC\ m^2$
Response Time	0.6	S
Sensitivity	0.8-1.3 (Vary with sensors)	$\mu V/W/m^2$
Temperature Limit	150	^oC
Heat Flux Limit	100	kW/m^2

The *OMEGA® HFS3* heat flux sensors are self-generating devices requiring no external voltage or current stimulation. Before the heat flux sensors were used, they were calibrated by a simple experimental rig as shown in Fig. 6-8. The simple rig comprises of a 100mm diameter heater mat, an aluminum disk, and glass fiber insulation surrounding it. The heater mat was used to heat the Aluminum disk until it reached its thermal steady state. Firstly, the heat flux sensor was attached on the top surface of the Aluminum disk, the measured EMF on the heat flux sensor was recorded. Subsequently, the same heat flux sensor was attached at the bottom surface of the heat mat. Again, the measured EMF on the bottom surface was recorded. The sum of the two incurred EMFs from the top and bottom surfaces obtained from the heat flux sensor was calibrated to the total power input from the heater power supply. Each calibration process was repeated five times, and the calibration factor varied from 3.5% to 8.7%, depending on the heat flux sensors. The uncertainty of each calibrated heat flux sensor was recorded and was taken into account when they were used to measure the heat transfer coefficients in experiments.

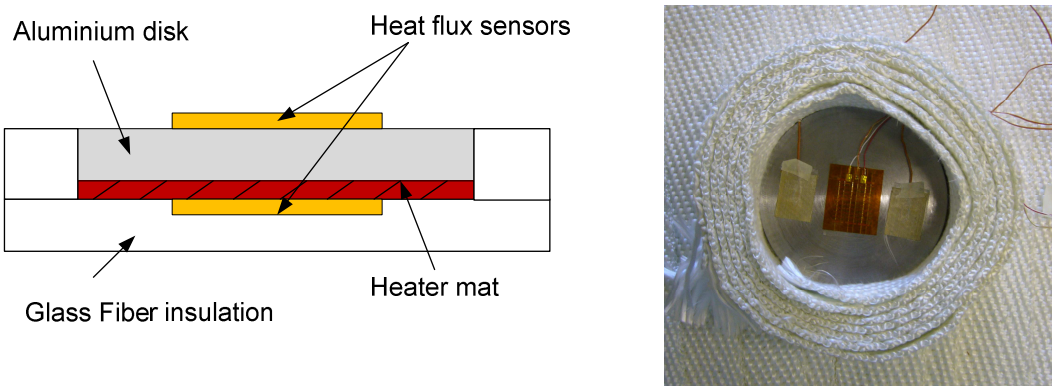

(a) (b)

Fig. 6-8. Schematic (a) and top view (b) of the simple experimental apparatus for heat flux sensor calibration.

The heat flux can be calculated from the sensor self-generated voltage output with the calibration factor as follows:

$$\text{Measured heat flux} = \frac{V_{HF3}}{K_{calibration}} \tag{6.12}$$

Where V_{HFS} is the voltage output generated from the sensor, in μV

$K_{calibration}$ is the calibration factor, in $\mu V/W/m^2$

The OMEGA® HFS3 sensor has an additional K-type thermocouple affixed at the bottom of thermal barrier (Fig. 6-7(a)) to provide additional local surface temperature measurements. Therefore, in total there are four output leads from the OMEGA® HFS3 sensor. Two of the sensor leads are for the heat flux measurement, which are indicated in red (*+ve*) and white (*-ve*) respectively. Since both the heat flux sensor leads are copper, OMEGA® U type connectors were used to eliminate the extra thermocouple joints. The two ends of the U-type connector were slotted into the PICO TC-08 USB data logger micro-volt channels. The other two end leads, which are colour-coded in yellow and brown, were connected to the K-type thermocouple on the heat flux sensor. K-type connectors were used to attach the thermocouple into the PICO TC-08 USB data logger K-type thermocouple channels. In total, three heat flux sensors and four thin film surface thermocouples were used in the experiments. The position of each thermocouple and heat flux sensor is shown in Fig. 6-9 (a) and (b). The thin film surface thermocouple is represented as *TC1 to TC4* in Fig. 6-9(a), and *HF1 and HF2* indicate the positions of the heat flux sensors on the front stator surface. An additional heat flux sensor, *HF3*, was attached at the back of the stator, to evaluate the heat that escapes at the back of the stator disk (Fig. 6-9(b)).

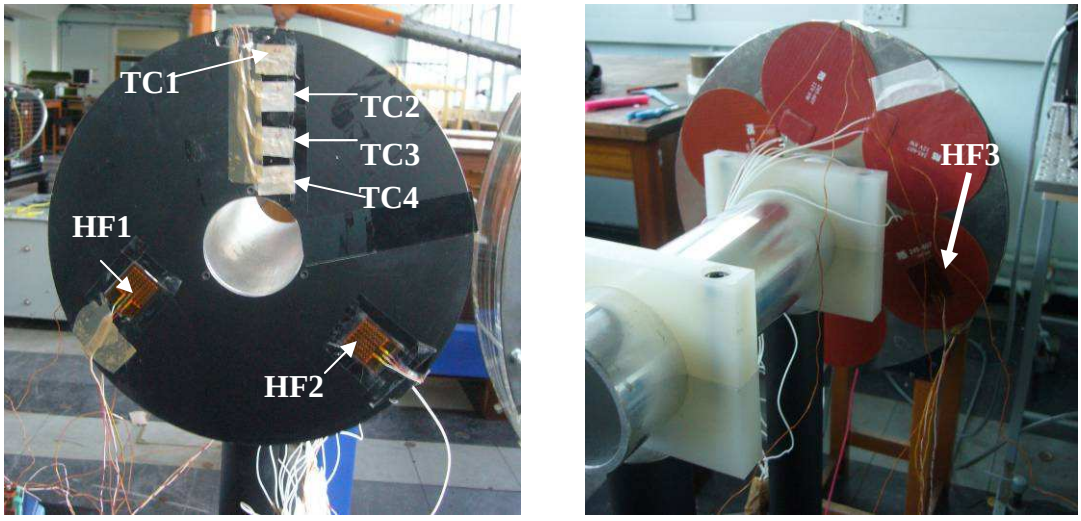

(a) (b)

Fig. 6-9. Thermocouples and heat flux sensors positioning on the stator front (a) and back (b) surface.

Mass flow measurements

A one-dimensional constant temperature hot wire anemometer was used to measure the air mass flow rate at the inlet duct of the simplified single-sided slotted generator. All the flow readings were taken by placing the hot wire perpendicular to the rotational axis, to avoid the reading measured from being affected by the extra swirl velocity component. The hot wire anemometer velocity measurement response time is 200ms. However, in order to obtain accurate velocity measurements, each velocity reading is recorded 5 seconds after the anemometer probe has moved into a new position, to eliminate the experimental errors that may occur in the measuring processes. For a single test, the anemometer was traversed to measure the air velocity at 17 different positions at the inlet end of the aluminum cylinder, as shown in Fig. 6-10 (a). Fig. 6-10(b) shows an example of the velocities measured on X-axis and Y-axis.

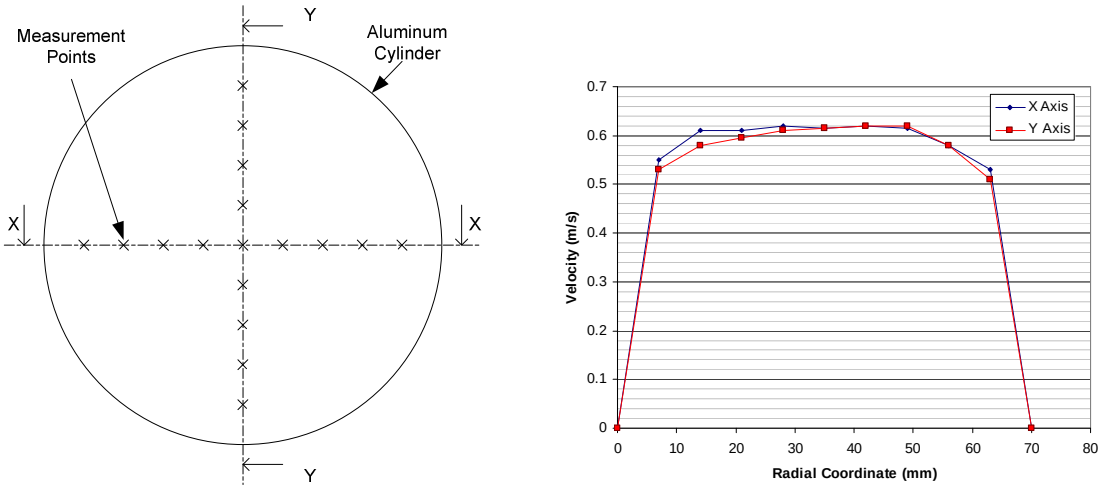

(a) (b)

Fig. 6-10. Velocity measurement positions at the inlet of the aluminum cylinder (a) and corresponding velocity profiles on X- and Y-axes.

Theoretically, the inlet air mass flow rate of the system can be evaluated as equation (6.13), if the X- and Y-axes velocity profiles are known.

$$\dot{m} = \rho \int_0^{\frac{\pi}{2}} \int_{-r}^{r} \frac{v_{X-axis}(r) + v_{Y-axis}(r)}{2} \partial r \partial \theta \tag{6.13}$$

Where r = radius of the aluminum cylinder, m.

$v_{X\text{-}axis}(r)$= Velocity profile on X-axis

$v_{Y\text{-}axis}(r)$= Velocity profile on Y-axis

ρ = air density, kg/m^3

Since the velocity profiles were unknown, the mass flow rate was evaluated numerically by the trapezium rule, as shown as equation (6.14):

$$\dot{m} = \pi\rho \times \frac{r}{5}\left[\frac{V_x(r_1)+V_y(r_1)}{2} + \frac{V_x(r_n)+V_y(r_n)}{2} + 2\times \sum_{k=1}^{k=n-1}\left(\frac{V_x(r_k)+V_y(r_k)}{2}\right)\right] \tag{6.14}$$

Where $V_x(r_k)$ and $V_y(r_k)$ is the velocity measured at n position on X- and Y-axes respectively.

6.5. Experimental Procedure

Prior to the start of the experimentation, the aluminum stator disk was preheated, with the back of the disk insulated by the glass-fiber insulation blankets. The DC power supply to the heater pads at the back of the stator was switched on and the variac was adjusted so that the stator temperature was maintained at 80°C. Simultaneously, the thermocouples and heat flux sensors on the stator front surface were recalibrated to ensure their satisfactory performance during the test. The thermocouples and heat flux sensor calibration table is shown in Table 6-2:

Table 6-2: Thermocouple and heat flux sensor calibration table.

Data Logger	Channel number	Device	Calibration Factor
HAT 33/417	Channel 1	TC1	T-type thermocouple
HAT 33/417	Channel 2	TC2	T-type thermocouple
HAT 33/417	Channel 3	TC3	T-type thermocouple
HAT 33/417	Channel 4	TC4	T-type thermocouple
HAT 33/417	Channel 5	HF1	0.942 μV/Wm^{-2}

HAT 33/417	Channel 6	HF2	0.901 μV/Wm^{-2}
HAT 33/417	Channel 7	HF3	0.969 μV/Wm^{-2}

From the CFD simulation results presented by Airoldi [54], it can be noticed that big separation between the stator and rotor disks induces complex flows into the system, i.e. reverse and circulative flows. These possibilities may result in noisy and unsteady signals obtained from the heat flux sensors and thermocouples, which complicates the experimental procedures. Hence, the air clearance between the stator and rotor disks was fixed to 3 mm in these experiments, to ensure that reliable readings are obtained for CFD validation. The rotational speed of the induction motor was regulated to 1495 rpm by the drive inverter and the rotor disk was spun for 3 hours, to ensure the system had reached thermal equilibrium. The thermocouple and heat flux sensors were connected to a high precision 20 bit 8 channels PICO TC-08 USB thermocouple data logger. The stator surface temperature and heat fluxes were monitored and recorded continuously at 1 reading per second using the *PicoLog* commercial software. The data collection was stopped after both the surface temperature and heat flux had reached the asymptotic steady state. Each test was repeated 3 times to ensure the repeatability of the data.

The air mass flow rate in to the single-sided axial flux generator test rig was evaluated by measuring the average air flow velocity at the inlet of the stator duct. The hot wire anemometer was supported at the inlet of the stator duct, see Fig. 6-4(a) to measure the air average inlet velocity. The anemometer was articulated to measure air velocity at 20 different positions at the inlet after the system had reached the asymptotic steady state. The measured air velocities were converted to air mass flow by equation (6.14).

Although the rear of the stator was thermally insulated by fibre glass matting, there is still a fraction of the heat produced by the heater mat that escapes by the back of the stator. Therefore, the total heat input to the front of the stator disk, $P_{front,}$ is reduced by the heat flow from the back of the heater pad, P_{back}, as described by in equation (6.15).

$$P_{front} = P_{electrical\ input} - P_{back} \quad (6.15)$$

The uniform heat fluxes specified in the two models were calculated by dividing the total heat input to the front of stator, P_{front}, obtained from equation (6.15), by the total area of the stator front surface. The uniform heat flux boundary condition assumption was verified by measuring the heat fluxes at two different positions on the stator front surface. Heat flux sensors, HF1 and HF2 were used and the position of these sensors is shown in Fig. 6-9(a). The measured surface heat fluxes from these two heat flux sensors are shown and compared in the following section.

6.6. Results and Discussions

Both CFD simulation and experimental measurements were conducted to verify the temperatures predicted from the 2-D lumped parameter model of the single-sided slotted axial flux machine. Figs. 6-11 and 6-12 show the temperature and velocity contours, respectively, of the simplified single-sided slotted axial flux machine obtained from the 2-D CFD model at 1495 rpm.

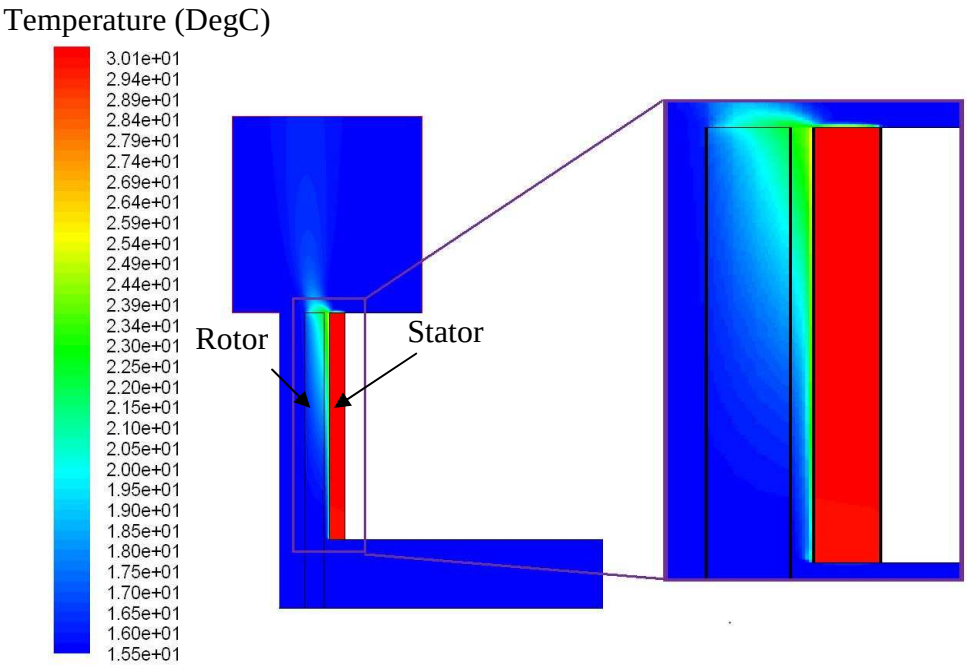

(a)

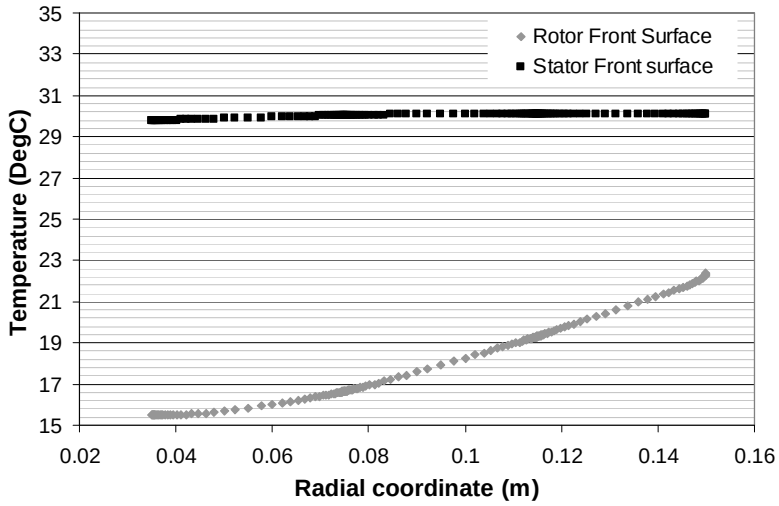

(b)

Fig. 6-11. Temperature contours (a) and stator and rotor surface temperature plots (b) inside the of the single-sided slotted axial machine test rig predicted by the CFD model.

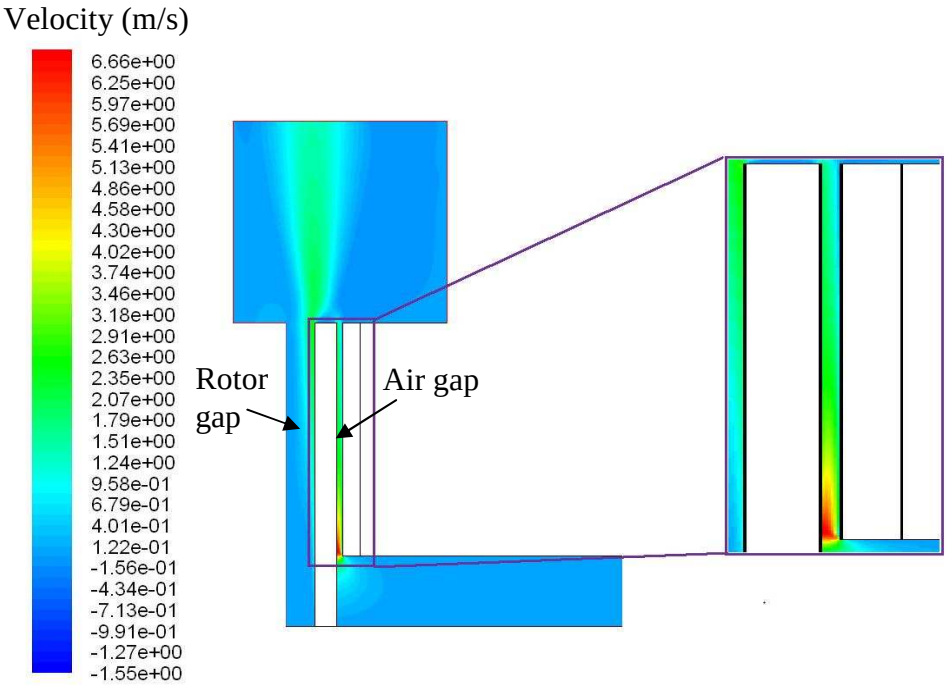

(a)

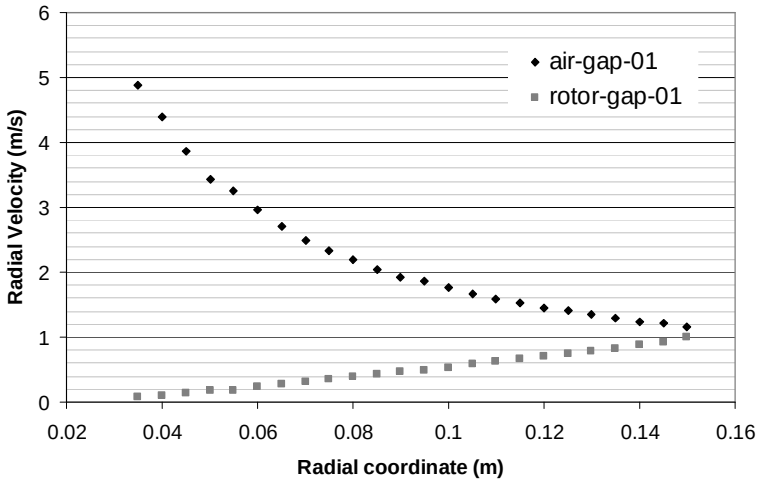

(b)

Fig. 6-12. Velocity contours (a) and the Radial velocity plots in the air and rotor gaps (b) of the single-sided slotted axial machine test rig predicted by the CFD model.

6.6.1. Computational Fluid Dynamic Results and Discussions

As expected, the air temperature had increased as it passed through the single rotor-stator system (see Fig. 6-11 (a)). In this CFD model, the inlet air temperature was specified as 15.0 °C. When the rotor was rotating, it drew the air from the surroundings by the centrifugal force. The air was heated as it passed over the warm stator surface on the right hand side. At the outlet, the air temperature has increased by 8.2 °C, from 15 °C to 23.2 °C.

Fig. 6-11(b) plots the surface temperatures of the stator and rotor disks which are directly adjacent to the air clearance. It can be noticed that the stator surface temperature did not increase but remained unchanged along the radial direction. Therefore, it demonstrates that the heat generated from the stator heater mats was slowly taken away by the moving air adjacent to them. Also, since Aluminum has high thermal conductivity, the temperature of the stator disk is uniform. On the other hand, the rotor surface temperature increased rapidly with distance from the rotational axis. This is because the moving air heated the rotor disk as it travelled along the air

gap clearance. But since the rotor disk was made of low thermal conductivity Perspex material, a high temperature gradient was generated on the rotor surface.

To understand the fluid flow inside the generator, the radial velocity contours of the generator rig are shown in Fig. 6-12(a). As illustrated in Fig. 6-12(a), there are two gaps in the rig, which are rotor gap and air gap. Rotor gap is defined as the gap in between the rotor disk and machine; Air gap is defined as the gap in between stator and rotor disk. In the air gap, it can be seen from the simulated results that the radial velocity was highest at the entrance of the stator. Before entering the air gap, the air was drawn through the inlet duct before turning through 90°. The abrupt shrinking of the cross-sectional at the gap entrance caused the high air radial velocity shown in Fig. 6-12(a). However, as the air flow path cross-sectional area in the air gap increased with radius, the radial velocity reduced correspondingly (Fig. 6-12(b)).

The air flow in the rotor gap demonstrates the reverse trend. Here, the air radial velocity in the rotor gap is the smallest at the innermost radial coordinate and is the highest at the outer periphery. It can be notice in the graph shown Fig. 6-12(b). At high radius, the centrifugal force is high due to the high air tangential velocity developed on the rotor disk. The centrifugal force hence pushes the air flows faster in radial direction. The simulation results show that in the air gap, the centrifugal force has lesser effect on the air radial velocity than in the rotor gap. One of the main reasons is that the stator plate is proximate to rotor plate in the air gap. Hence the centrifugal force in the air gap is less than in the rotor gap and has less effect on the air radial flow velocity.

6.6.2. Experimental Results and Discussions

The measured temperatures at four different radii along the stator surface were recorded after the rotor-stator system had reached the steady state. The measured temperatures are plotted in Fig. 6-13 and are compared with the temperatures predicted from CFD and two 2-D lumped parameter models. The two 2-D lumped

parameter models, shown in Fig. 6-13, applied the same 2-D thermal circuit described in section 6.2, but one of the thermal circuits employed the convection heat transfer coefficients evaluated from the empirical equations developed by [145, 147], whilst the other thermal circuit used the convection heat transfer coefficients obtained directly from the CFD model.

Table 6-3 shows the heat fluxes measured from the heat flux sensors attached on the front and back sides of the stator disk. The results show that the local heat fluxes measured on the stator surface were reasonably close. Therefore, the uniform heat flux boundary conditions were applied confidently on the stator front surface in the CFD and lumped parameter models, for the thermal modelling of the test rig.

Table 6-3: Local heat fluxes measured on the stator front and back surfaces

	HF1 (Front)	*HF2* (Front)	*HF3* (Back)
Heat flux (W/m^2)	554.56	553.23	364.04

The temperatures measured (from the experiments) and predicted (from the CFD & LPM models) were lower as compared with the winding temperatures in commercial electrical machines. Typically, commercial electrical machines usually operate at stator surface temperatures of 80-120 ºC, but the surface temperatures measured or predicted from the experiments and CFD & LPM models respectively were in the range from 30 ºC to 35 ºC. This is due to the low rated power of heater mat used in the experiment. The rated power of each of the heat mats was 8 Watt and six heater mats were used in total. The total heat input was 48 Watt. In comparison the winding losses of the commercial electrical machines, range in between 90-200 watt, and consequently the temperatures measured from the experiments and predicted from the CFD were low.

Fig. 6-13 shows a large disparity between the temperatures predicted from the 2D thermal circuit which used the empirical convection heat transfer coefficients and temperatures measured from the experiments. The maximum relative error was 45.8%, which was equivalent to 5.5°C in absolute temperature rise. The high

discrepancy is mainly due to the empirical equations suggested by [145-147] which failed to predict the corresponding heat transfer coefficients on the rotor and stator surfaces.

To further improve the 2D LPM, instead of using the convection heat transfer coefficient predicted by the empirical equations, the local convection heat transfer coefficients extracted from the CFD model were used. These local convection heat transfer coefficients were calculated based on the local working fluid (or air) bulk temperature, the surface temperature and surface heat flux. The local air bulk temperature was calculated by taking the volumetric average air temperature of the fluid control volumes. With the local heat transfer coefficients obtained from the CFD model, the temperatures predicted from the 2D thermal circuit show a relatively good agreement with the temperatures measured from the experiments. The maximum relative error has improved to 25%, which corresponds to 3°C in absolute temperature rise. The temperatures matched with the temperatures predicted from the CFD model.

It may be concluded that the 2D lumped parameter circuit is sensitive to the convective resistances, as opposed to the conductive resistances. For most of the air cooled axial machine, the magnitude of the convective resistance is about two orders of magnitude greater than the conductive resistance. For example the convective resistance at T4 is 3.35 K/W but the radial conductive resistance on the rotor disk is only 0.022 K/W. This highlights the necessity of developing a more sophisticated parametric variation study of convective heat transfer coefficients and mass flow rates for axial flux machines to complete the LPM model.

Unlike the CFD modelling technique, to obtain the local heat transfer coefficients experimentally is very difficult, because it is impossible to determine the local air bulk temperature accurately by using the thermocouples in the narrow stator-rotor gaps. Therefore, the global heat transfer coefficients were measured from the experiments, by using the inlet air temperature (instead of using the local air bulk temperatures) as the reference temperature. The measured heat transfer coefficients are shown in Fig. 6-14. On the other hand, a new set of heat transfer coefficients was obtained from the CFD model, by changing the reference temperature from the air

bulk temperature to the inlet air temperature. These CFD results were compared with the experimental global heat transfer coefficients, as well as with the empirical heat transfer coefficients evaluated from [145-147], in Fig. 6-14. It is shown that the CFD is better in predicting the global convective heat transfer coefficient than the empirical heat transfer coefficients derived by [145-147].

Overall, the temperatures predicted from the 2-D thermal circuit and CFD model deviates slightly to the experimental ones. This is because both the CFD model and 2-D thermal circuits did not take into account the extra heat transfer from the stator inlet pipe. All the heat generated from the heat mats only travelled through the stator surface. No heat is travelled through the stator inlet pipe. However, it is not the case for the test rig. After the experiments, the temperature of the stator pipe has increased 4-5 °C. These indicate that in the experiment, a fraction of heat generated from the heat mats has flowed to the stator and pre-heated the inlet air. Therefore, the temperature measured on the stator surface is less than the computation ones.

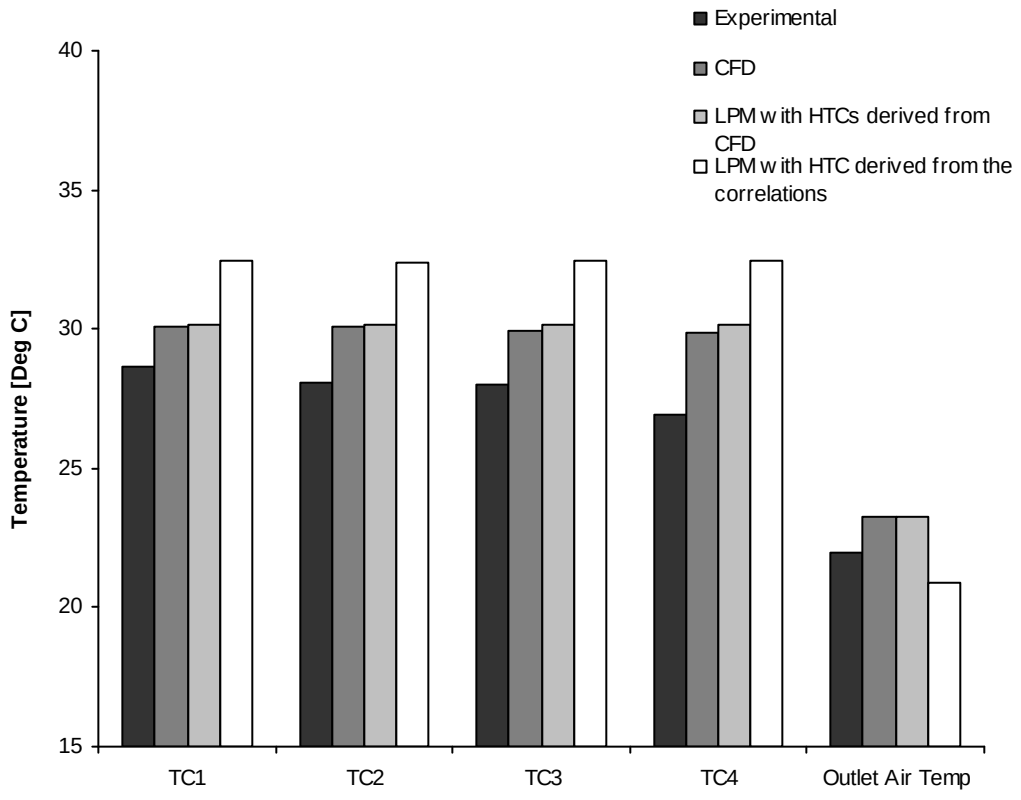

Fig. 6-13. The temperatures measured and predicted from experimental rig and numerical models (CFD and 2-D LPM) respectively.

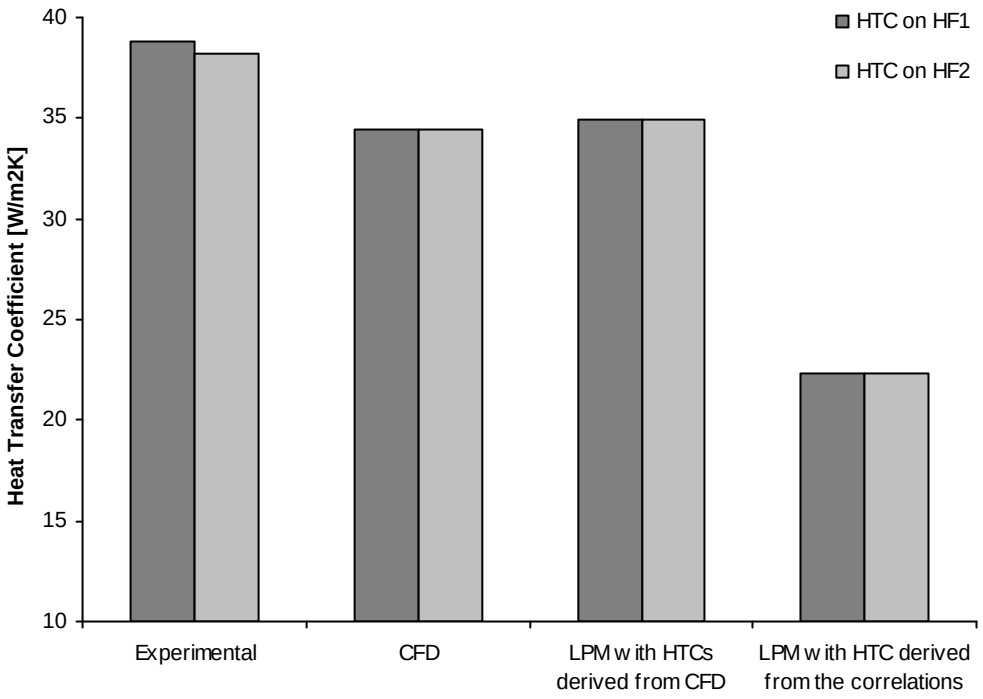

Fig. 6-14. The global heat transfer coefficients measured and predicted from experimental rig and numerical models (CFD and 2-D LPM) respectively.

The surface heat transfer coefficient discrepancy of the between the CFD model and the experiments was due to the inaccurate air mass flow rate predicted in the CFD model. Table 6-4 summarises the air mass flow rate measured from the experiments and evaluated from the CFD model. The surface heat transfer coefficient is higher when the air mass flow rate is higher. Hence, it can be noticed that the mass flow rate predicted by the CFD model was about 11% lower than the mass flow rate measured from the experiments. These results in the heat transfer coefficient predicted by the CFD model being 10.5% lower than the experimental ones.

Table 6-4: Mass flow rates comparison.

	Experiments	CFD model
Mass flow rate (g/s)	4.03	3.61

The local temperatures and heat transfer coefficients predicted from the 2-D LPM thermal circuit show good agreements with the CFD models (Fig. 6-12 and Fig. 6-13). They demonstrate that both the annular conductive circuit and fluid convective circuit

used in the 2-D LPM work well in predicting the conduction and convection heat transfers in the stator-rotor system.

6.7. Experimentation on the Rotor Disk with Magnets.

Experiments were conducted to investigate the compatibility of the 2D LPM thermal circuit on the 3D heat flow modelling. Six Perspex arc sectors were affixed to the existing rotor disk to model the existence of magnets on the single-sided axial flux generator. The existence of the Perspex arc sectors transforms the existing test rig to the 3D heat flow model, where the heat travels in the axial, radial and circumferential directions. The results obtained from the experiments were compared with the temperatures predicted from the 2-D LPM thermal circuit. Based on the simulated and experimental results, several modifications were suggested to adopt the 2-D LPM thermal circuit into the 3-D heat flow modelling.

6.7.1. Experimental Procedures

The original Perspex rotor disk was modified and fitted with six 45° Perspex arc sectors (magnet) of 12mm thick, with 15° inter-sector gap (Fig 6-15(a)). The same stator disk configuration from the previous test was used (Fig 6-9 (a) and (b)). The air clearance, which is defined as distance between the stator and the Perspex arc sector front surfaces, was set to 2mm in the experiments. Fig. 6-15(b) shows the new test rig configuration.

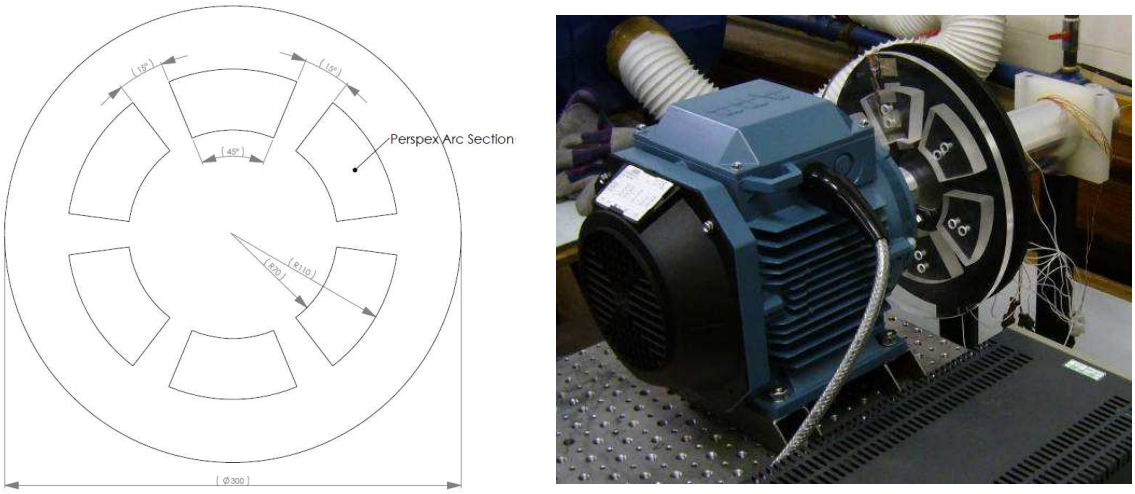

(a) (b)

Fig. 6-15. Rotor with six Perspex arc sectors (a) and the modified single-sided axial flux generator test rig (b).

Prior the commencement of the experiments, the power supply of the heat mats was switched on for 2 hours to warm the stator disk. The heat flux sensors and thermocouples were attached on the stator surfaces and their calibration factors were checked to ensure the satisfactory performance of the heat flux and temperature measurements.

The induction motor was switched on after the preheated stator disk had reached the steady state. The rotational speed was controlled at 1495 rpm by the drive inverter. Both data loggers and computer were switched on simultaneously with the induction motor, recording the signals generated from the heat flux sensors and the thermocouple. The recording process was continued for 2 hours until the system had reached its asymptotic steady state again. The air mass flow rate and ambient air temperature were measured at the end of the experiment by using the TSI ® anemometer. Table 6-5 shows the experimental record sheet used for the testing. The first column shows the temperature of the stator surface before the rotor disk was spun, and the second column records the stator surface temperature after the system had reached the asymptotic steady state. The final state stator surface heat transfer coefficients are recorded in the third column of Table 6-5. The experiment was repeated three times for 2 mm air clearance, to minimise the experimental errors.

Table 6-5: Experiment record sheet

Test 1	Temperature Reading (°C)		Heat transfer coefficient
Date: 17/03/09	Initial	Final	(W/m^2K)
T4 (°C)	71.26	30.92	-
T3 (°C)	72.29	31.71	-
T2 (°C)	73.00	31.16	99.87
T1 (°C)	71.43	29.78	-
Tambient (°C)	24.39	23.77	-
Heat Flux (W/m^2)	413.33	768.22	-
Mass flow rate	0.0235		-

6.7.2. CFD Simulations

The 3-D CFD model of the single-sided axial flux machine with magnets was constructed using pre-processing software, Gambit, (Fig 6-16 (a)). To reduce the size of the model, only one-sixth of the machine was modeled: a 60° periodic boundary condition was applied at both of the edges, to simulate flow and heat transfer inside the full machine. In total, the one-sixth of the generator model consists of 2 million cells. Fine boundary meshes, (Fig 6-16(b)), were applied on the fluid cells near to the solid surfaces to capture the near wall effects. The Y^+ was kept below 5 in the model to ensure good simulation results.

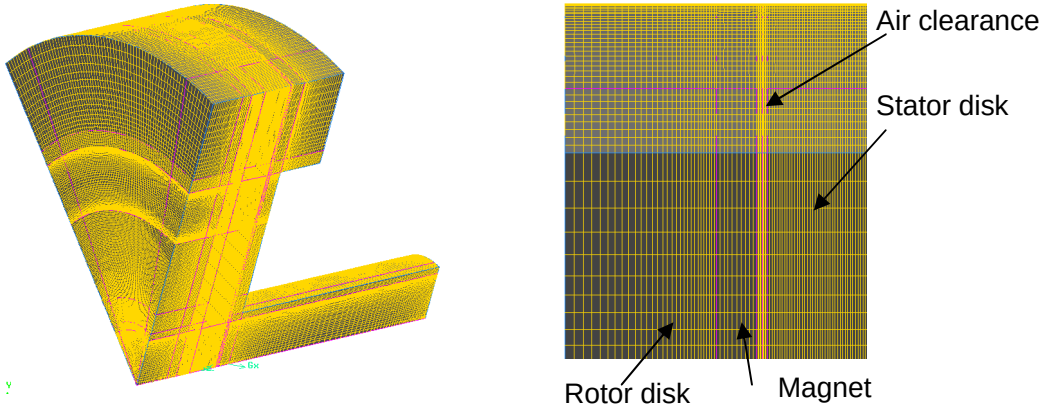

(a) (b)

Fig. 6-16. The 3-D CFD model of the single sided axial flux machine with magnets (a) and the boundary layers mesh on the fluid near the solid surfaces (b).

Fluent modelling which involves in both stationary and moving zones requires the use of a moving cell zone boundary condition, which for this case, is the Multiple Reference Frames (MRF) [148] model. MRF is a steady state approximation for rotating and moving systems: it is capable of providing reasonably accurate time-averaged solutions for flows where the interactions of stationary and moving zones are weak, which is the case for single-sided axial flux machines. The boundary conditions specified in the CFD model are:

- 2mm Rotor-stator clearance.
- 15 °C ambient temperature.
- Realisable k-epsilon turbulent model with EWT was used to model the turbulence in the flow.
- Zero total pressure and zero static pressure conditions were specified at the inlet and outlet of the simplified AFPM generator respectively.
- The rotor parts were specified to 1495 rpm, with the use of multiple rotating reference frames (MRF) model.
- 768 W/m^2 heat flux input was specified at the back of the stator to model the winding Joule loss. The heat flux used was obtained from the experimental results.

6.7.3. Lumped Parameter Model of the Rotor-Stator System with Magnets

In the new rotor-stator system, with additional Perspex arc sectors attached on the rotor disk, the heat flows in three directions, which are the radial, axial and circumferential directions. Therefore, a 3D lumped parameter thermal circuit (which takes into account the three-direction heat flow paths) is required to model the system. Nevertheless, the construction of the 3D lumped parameter thermal circuit is complex and tedious. In this investigation, instead of developing a new 3D lumped parameter thermal circuit for the rotor-stator system, the same 2D lumped parameter thermal circuit described in section 6.2 was used. For the 2D lumped parameter thermal circuit, the six magnets on the rotor disk (Fig. 6-17(a)) were simplified into a single annulus (Fig. 6-17(b)).

Consequently, the stator surface temperatures predicted from the 2-D thermal circuit were compared with the temperatures predicted from the 3D CFD model and the temperatures measured from the experiments, to investigate the compatibility of the 2D thermal circuit in three dimensional heat flow modelling.

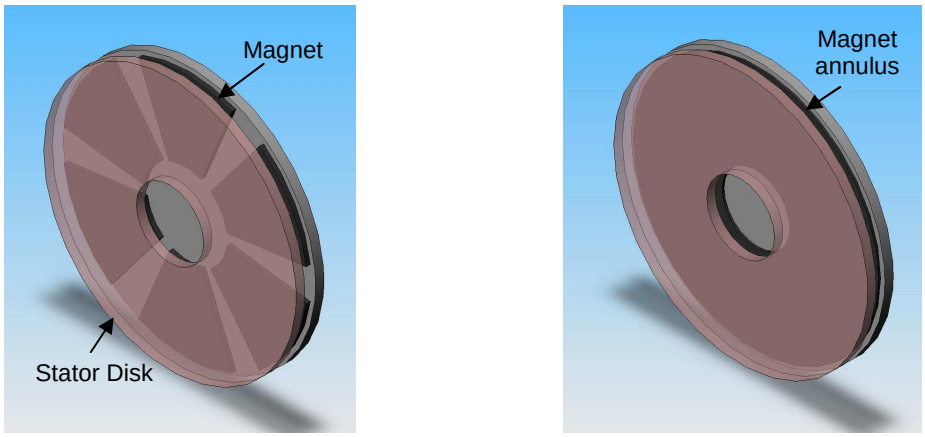

(a) (b)

Fig. 6-17. 3-D rotor-stator with magnets system (a) and its 2-D simplification (b).

The convective thermal resistances and air mass flow rate used in the 2D thermal circuit were evaluated from the 3D CFD model. However, the heat transfer coefficients on the stator and rotor walls vary in the circumferential direction. This is due to the effect of the magnets on the stator-rotor system. In the 2D thermal equivalent circuits, the convective thermal resistances used were circumferentially averaged. Similarly, the temperatures evaluated from the 3D CFD model were also circumferentially averaged.

6.7.4. Results and Discussions

The stator surface temperatures predicted from the 3D CFD model and the 2D lumped parameter models were compared with the surface temperature measured from the experiments (Fig. 6-18). The stator surface temperatures at different radial coordinates, varying from 0.035m to 0.15m are plotted. The experimental results, shown in Fig. 6-18, have an experimental error of ±0.1°C, which is a limitation imposed by the selected thermocouples.

Firstly, the temperatures predicted from the 3D CFD model and the experiments were compared. Fig. 6-18 shows that the temperatures predicted by the 3D CFD model match well with the temperatures measured from the experiments. The maximum absolute discrepancy, at the innermost radial coordinate, is 0.6±0.2°C, which corresponds to 10.3% in the relative scale, at the inlet temperature of 24°C.

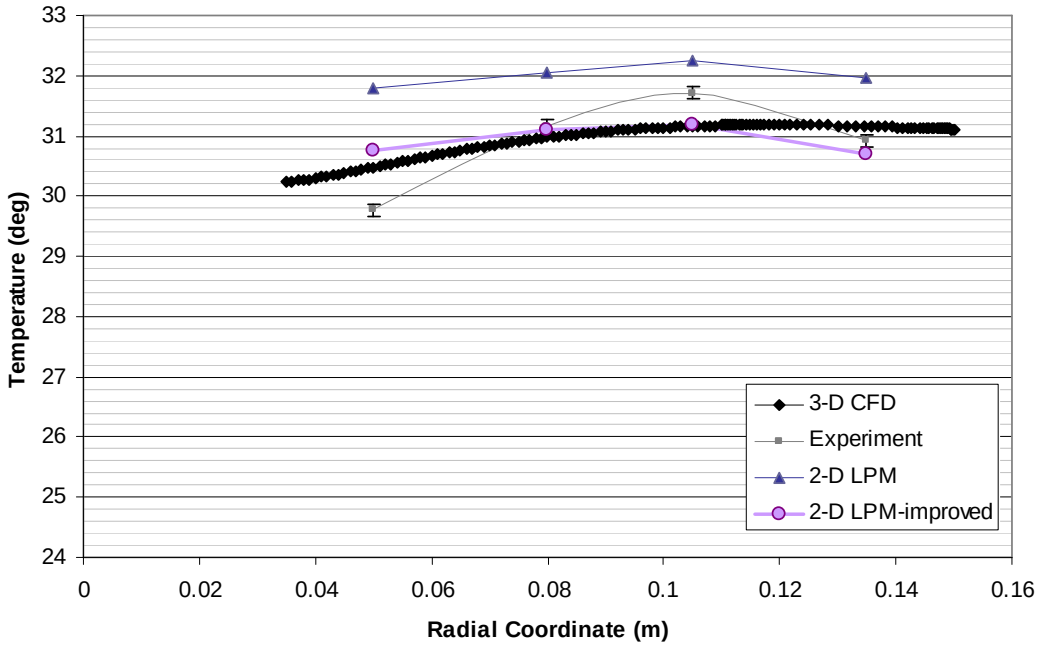

Fig.6-18. Temperature distributions on the stator of the single-sided axial flux machine obtained from both the CFD and experiments.

The air flow path-lines are illustrated in Fig. 6-19. In Fig. 6-19, the stator disk of the test rig is omitted to demonstrate the complex air flow between the stator and rotor disks. The color contour illustrates the magnitude of the air radial flow velocity. The air radial velocity increases gradually from the center of the disk until the inner peripheral edge of the magnets. The present of the magnets reduces the cross-sectional area of the air gap, hence, the air radial velocity surges in the inter-magnet grooves. More over, the present of the magnets also direct the most of the air to via the inter-magnets grooves; a small fraction of air flows in the gap between the magnet and stator surfaces, see Fig. 6-19. On the other hand, reverse flows are also observed at the outer peripheral edge of the rotor disk.

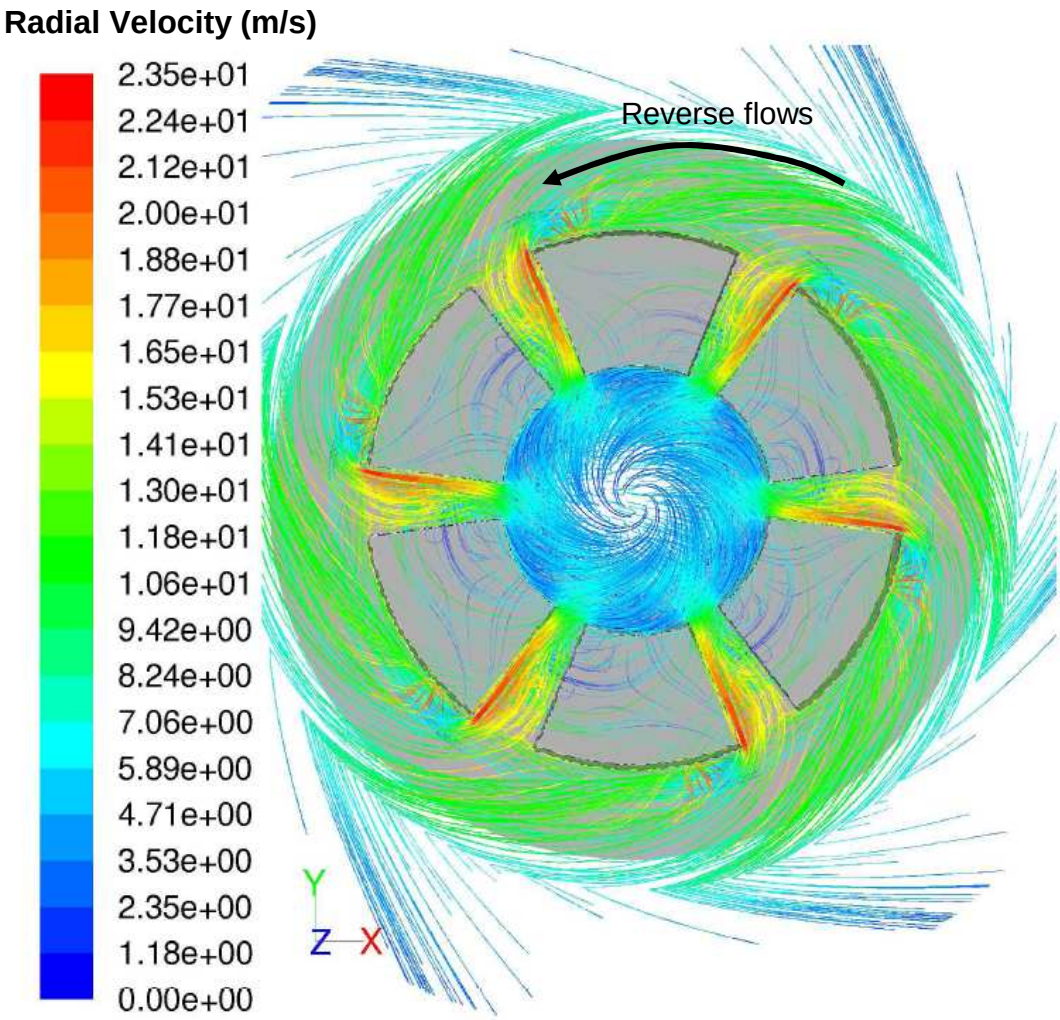

Fig.6-19. Air flow path-line in the air gap. The stator disk is hidden to illustrate the complex flow path in the air gap.

Similarly, the convection heat transfer coefficient on the stator surface predicted by CFD is shown in Fig. 6-20(a). The surface convection heat transfer predicted corresponds to the air velocity shown in Fig. 6-19. High surface heat transfer coefficient is located at proximity of the magnet inner peripheral edges and inter-magnets grooves; low surface heat transfer is observed on the magnet surface. Also, the reverse flow induces high convection heat transfer coefficient at the rotor disk outer peripheral.

Fig. 6.20(b) plots the convection heat transfer coefficients at the centre line of the stator disk predicted by the CFD model and the experimental convection heat transfer

coefficient measured from the test rig. Due to the size of the heat flux sensors and the limitation of the data logger, heat transfer coefficient at only one radial coordinate was measured. Both the heat transfer coefficients were evaluated by setting the air inlet temperature as the reference temperature to allow for direct comparison. The heat transfer experiments were repeated five times, and the experimental error of the measured heat transfer coefficient was 3.34%. The results shown in Fig. 6-20(b) suggest that the 3D CFD model under-predicts the stator surface convection heat transfer coefficients, by 10.04%. But, it is believed that the slight difference of the 3D CFD model in predicting the convective heat transfer coefficients accounts for the stator surface temperature discrepancies shown in Fig. 6-18.

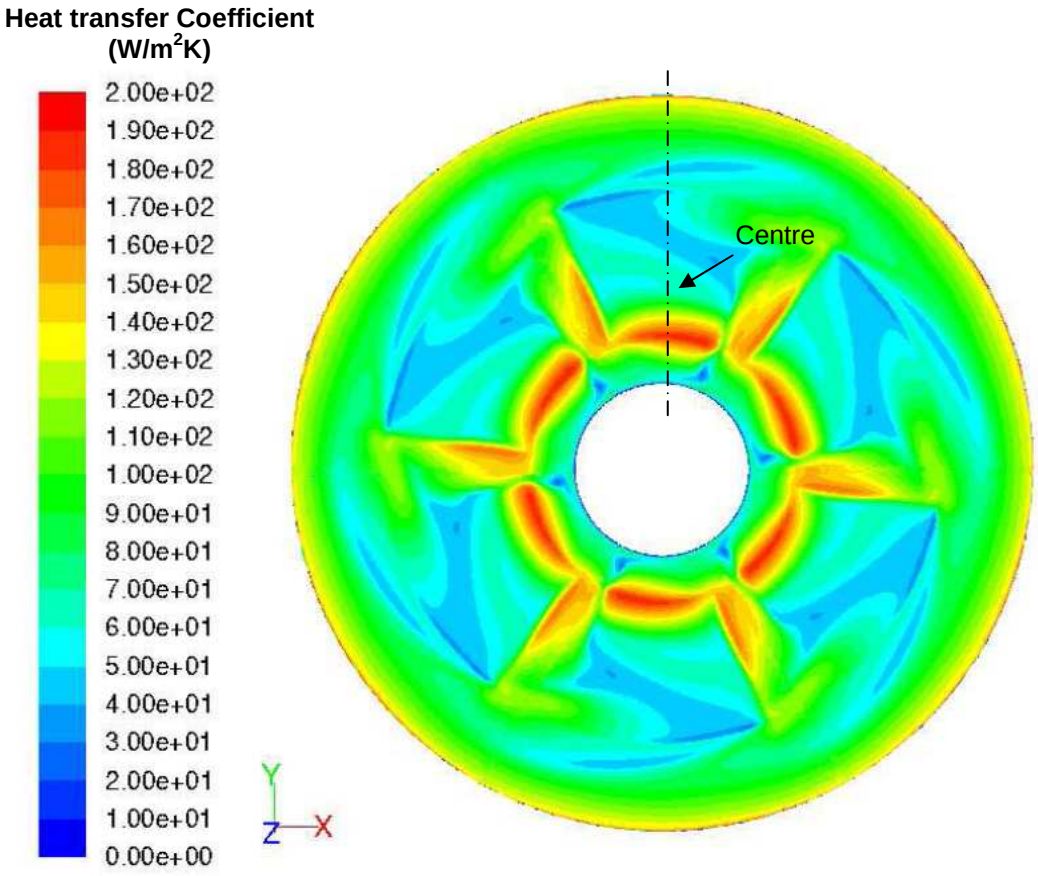

(a)

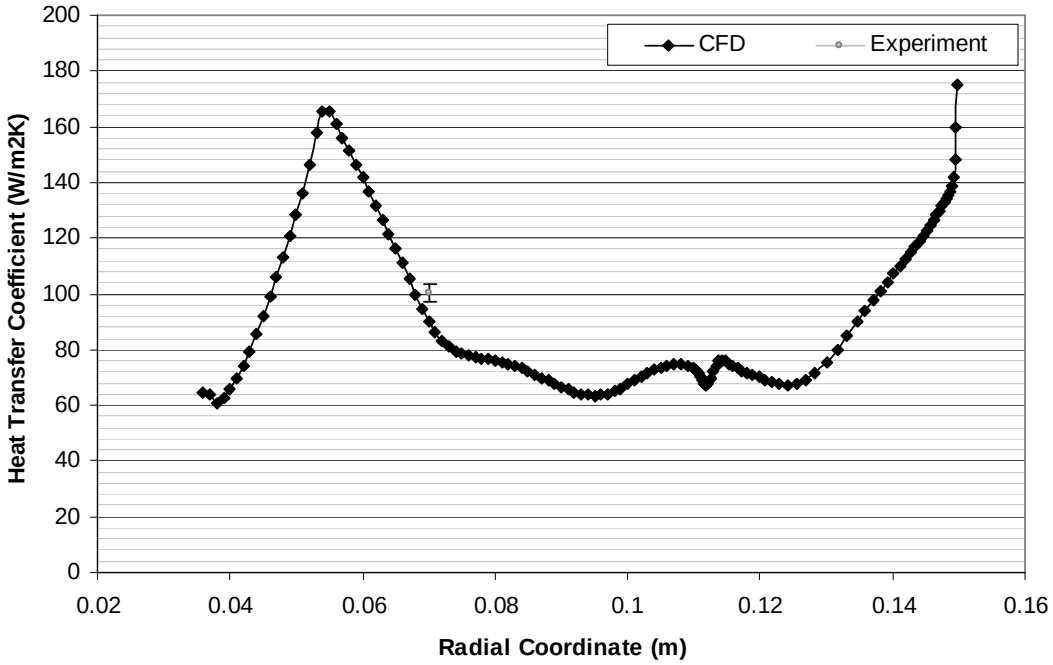

(b)

Fig.6-20. Stator surface heat transfer coefficient predicted by CFD (a) and temperature distributions on the stator of the single-sided axial flux machine obtained from both the CFD and experiments (b).

The 2D lumped parameter thermal circuit over-predicted the stator surface temperature by 2°C, which is equivalent to a relative error of 42.2%, when compared with the experimental data. Likewise, when comparing the 2D lumped parameter thermal circuit results with the temperature predicted by the 3D CFD model, the maximum discrepancy is 1.5°C, for which the equivalent relative error is 25.5%. Since the 2D lumped parameter thermal circuit applied the air mass flow rate and convection heat transfer coefficients extracted from the 3D CFD model, low discrepancy was expected. However, high temperature discrepancies were found. This is mainly due to the exclusion of heat flow path in the circumferential direction in the 2D lumped parameter thermal model.

As discussed in the previous section, the 2D lumped parameter thermal circuit only accounts for the heat flow in the radial and axial directions in the rotor-stator system. When the magnets were added into the rotor-stator system, the air flow in the inter-magnet grooves absorbed extra heat from the magnet circumferentially. The exclusion

of the extra heat flow in circumferential direction therefore results the higher temperature prediction on the stator surface.

Furthermore, simplifying the magnets on the rotor disk into a single annulus (Fig. 6-17), reduces the total solid-to-fluid contact area, by neglecting the side area of the magnets. By simplifying the six Perspex section arcs of 12mm thick into a single annulus, the reduction of the solid-to-fluid contact area on the rotor disk from 2.83×10^{-2} m^2 to 2.26×10^{-2} m^2, which corresponds to 25.4% contact area reduction. The reduction of the solid-to-fluid contact surface area contributed to the significant discrepancy of temperature prediction in the 2D lumped parameter thermal circuit. Nevertheless, the 2-D lumped thermal circuit can be improved by adjusting the solid-to-fluid contact area in the convective thermal resistances, to take into account the extra (circumferential) heat flow from the side of the magnets to the inter-magnet grooves. By adding the extra six pairs of magnet side areas into the existing annulus area (Fig. 6-21), the new convective resistances were evaluated. In Fig. 6-18, the stator surface temperatures predicted by the improved (area-corrected) 2D lumped parameter thermal circuit is plotted. It can be seen that, by adjusting the corresponding solid-to-fluid surface area, the accuracy of the 2D lumped parameter thermal circuit has improved. The maximum absolute temperature discrepancy when compared with the 3D CFD model was 0.5°C, which corresponds to 6.9% relative error.

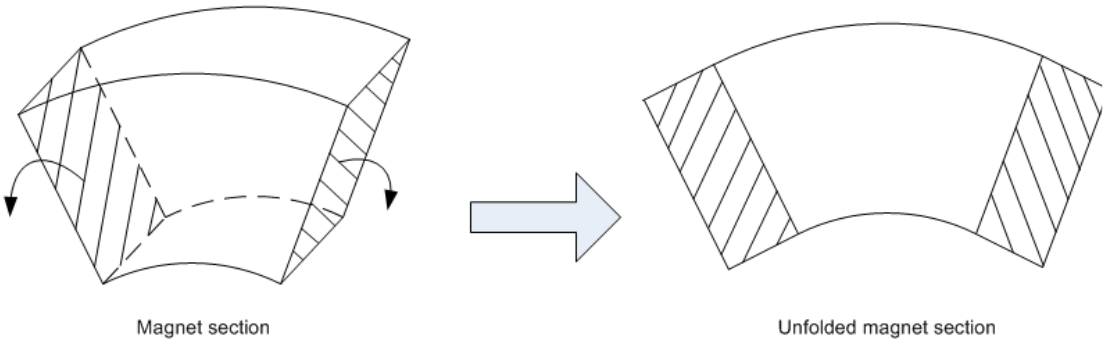

Fig. 6-21. Magnet side sections are unfolded in the 2-D lumped parameter thermal circuit to improve the accuracy of temperature prediction.

Although, by adjusting the corresponding solid-to-fluid surface area has significantly improved the accuracy of the 2D lumped parameter thermal circuit, the discrepancy when compared with the experimental data was still high. For example, the relative error at the innermost stator surface was 17.2%. As shown in Fig. 6-19, the convection heat transfer predicted from the 3D CFD model was 14.3% higher. Therefore, it is concluded that the low accuracy of the 2D lumped parameter thermal circuit (when compared with experimental data) was due to the convection heat transfer coefficients used in the circuit, which were extracted from the 3D CFD model.

6.8. Conclusions

These results have led to the conclusion that the accuracy of the 2D lumped parameter thermal circuit is heavily dependent on the convection heat transfer coefficients that are used in the circuit. In the 2D test case (stator-rotor system), the stator temperatures predicted by the 2D lumped parameter match the temperatures predicted by the CFD model. Likewise, for the 3D model, in which extra magnets were affixed on to the rotor disk, the prediction of the 2D lumped thermal circuit was improved, when taking into account of the extra solid-to-fluid surface area on the sides of the magnets for new convective thermal resistance evaluation. It was clearly shown that the improved 2D lumped parameter model is capable of modelling three-dimensional heat flow systems with the two-dimensional thermal circuits.

Chapter 7

Experimental Validation of CFD Modelling Method: Large Scale Low Speed Test Rig

7.1. Introduction

In the development of lumped parameter thermal circuit for axial flux machines, it is important to obtain reliable local heat transfer coefficients (HTC) for each component inside the machine. This is because the accuracies of the thermal equivalent circuits are heavily dependent on these HTCs. In the case studies discussed in the previous chapters, all the local HTCs in the lumped parameter models were extracted from the CFD solutions. Thus, in order to develop a lumped parameter thermal equivalent circuit that is capable of working independently from the CFD models, it is necessary to develop a set of empirical relationships between the local HTC and the size and topology of different AFPM machines through parametric studies.

HTC parametric studies can be achieved either by conducting experiments, or by CFD modelling. However, the construction of a flexible test rig that is capable of evaluating a range of different sizes and topologies of the axial flux machine is uneconomical and time consuming. Thus, the CFD modeling technique was used, as an alternative. Several commercial available CFD solvers and models are available. Each of these CFD solvers is designed to model different kinds of flow condition and

has certain computational limitations. Additionally, these CFD modelling techniques are mostly mesh dependent. Therefore, it is necessary to carry out experimental studies to validate the CFD models before they are used to perform the HTC parametric studies.

The design of the large scale test rig for measurement of the heat transfer coefficient measurement is discussed in this chapter. Dimensional analysis was performed to ensure that the flow characteristic inside the large scale test rig would be similar to the Durham 1.5kW 1500rpm AFPM generator. Experiments were designed and conducted on both open channel and totally enclosed machine designs. The heat transfer coefficients and temperatures obtained from these experiments were compared with CFD models and discussed.

7.2. Test rig Topology and Dimensional Analysis

The basic configuration of the Durham 1.5kW, 1500rpm, AFPM generator is shown schematically in Fig. 7-1(a). The axial flux generator consists of a pair rotating disks, a centre boss, six permanent magnet pairs, an annulus stator core, a stator holder and an optional casing. The two rotor disks have neodymium-iron-boron (NdFeB) permanent magnets positioned circumferentially around in an N-S-N-S-N-S arrangement and, when assembled, the magnets on each rotor disk are aligned with N facing S, creating a strong magnetic field in the axial direction. When the generator rotates, the magnetic fluxes cut through the conductor on the stator windings, and generates electricity.

The two rotor disks are held together by the centre boss (Fig. 7-1(b)). When the rotor disks rotate, the centre boss acts like the impeller in a centrifugal pump, converting the power from the shaft to kinetic energy in the fluid. Subsequently, the fluid is accelerated radially outward from the centre boss, creating a low pressure at the centre of the boss that continuously draws more cooling fluid axially from the surroundings into the generator. The design of the centre boss is critical for the cooling in the machines.

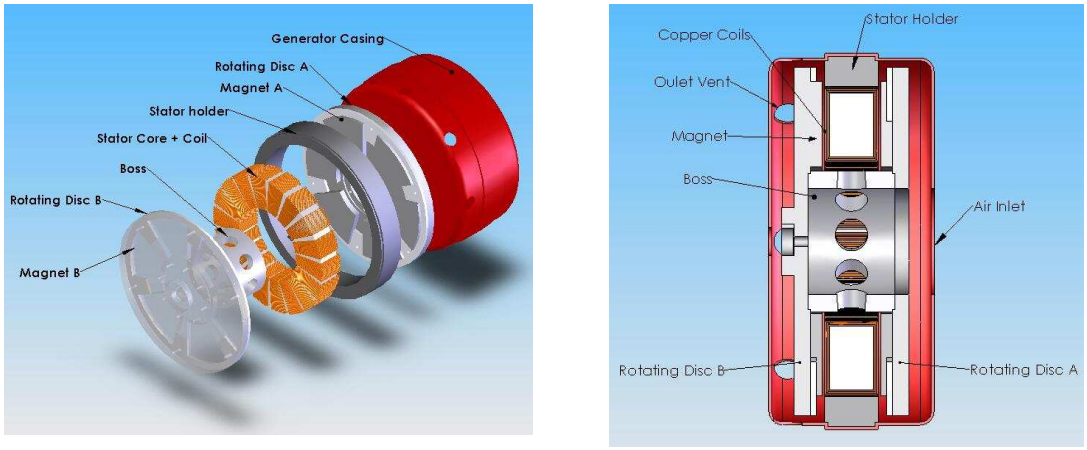

(a) (b)

Fig. 7-1. Schematic representation of the axial flux permanent magnet generator.

Increasing the running clearance between the stator and rotor disks raises the amount of air drawn into the generator, and hence improves the machine cooling. However, at the same time, when the running clearance is increased, the electromagnetic efficiency of the generator deteriorates. Therefore, to maximize the electrical yield and efficiency of the generator, the running clearance is kept to the minimum for most commercial axial flux machines. Depending on the manufacturing tolerance and the machine size, the running clearance of commercial machines varies from 2mm-8mm. Several high power, low running clearance machine designs adopt water jacket cooling system stator design to dissipate excessive heat generated in the core and windings.

When conducting experiments, direct heat transfer coefficient measurements on the stator and rotor discs surfaces of these commercial axial flux generators are difficult, as the internal surfaces and flow paths are narrow and inaccessible. Furthermore, the presence of the thin film thermocouples and heat flux sensors (where the sensors thickness are around 1-2mm) inside these narrow internal gaps generate significant air flow disturbances, affecting the flow patterns and the local heat transfer coefficients. Therefore, to minimise disturbances due to the measuring equipment, it was decided to construct a test model four times larger than the original Durham 1.5kW 1500rpm axial flux permanent magnet generator. The rotational speed was scaled down by the factor of sixteen, to maintain the same Reynold's number. The large scale test rig also

allows higher resolution measurements to be made and it is safer to conduct the experiments, as the generator rotational speed was reduced.

Dimensional analysis was performed to determine the appropriate geometrical parameter groups and to ensure that appropriate scaling between the model and the original Durham 1.5kW 1500rpm axial flux permanent magnet generator. The dimensions of the Durham AFPM generator are summarized in Table 7-1. These parameters are converted into dimensionless parameters (Table 7-2) by adopting the axial distance between the stator and magnet, H_{airgap}, (which is also known as the air gap clearance,) as the reference (or characteristic) length. For example, the outer radius, magnet inner radius, coil thickness dimensionless forms are defined as equation (7.1), equation (7.2) and equation (7.3) respectively.

$$R^* = \frac{R}{H_{airgap}} \tag{7.1}$$

$$R^*_{maginner} = \frac{R_{maginner}}{H_{airgap}} \tag{7.2}$$

$$d_{coil}{}^* = \frac{d_{coil}}{H_{airgap}} \tag{7.3}$$

Some of the geometric parameters have subtle effects on the flow characteristics inside the generator. Computational analyses were conducted, using the commercial CFD package, *Fluent*, to investigate these flow independent geometrical parameters. By identifying these independent parameters beforehand, it is possible to simplify the rig's design and hence reduce the manufacturing cost. For example, the rotor disk thickness was found to have no significant effect on the air flow inside the generator. Hence it is appropriate to use a rotor disk that is thinner than the dimensionally correct thickness. Thus, it reduces the material cost and manufacturing and handling cost. At the same time, it also improves the rig's safety. Table 7-2 shows the dimensionless parameters which are critical for the flow characteristic in the generators and Table 7.3 shows the exact dimension of the large scale test rig.

Table 7-1: Original Dimensions

$H_{air\ gap}$	=	0.0020	(m)
R	=	0.1230	(m)
$R_{mag\ inner}$	=	0.0530	(m)
$R_{mag\ outer}$	=	0.1130	(m)
Rin	=	0.0375	(m)
Rout	=	0.0200	(m)
Rcasing	=	0.1330	(m)
Rshinner	=	0.1150	(m)
Rshout	=	0.1420	(m)
$R_{core\ inner}$	=	0.0600	(m)
$R_{core\ outer}$	=	0.1050	(m)
Rbh	=	0.0115	(m)
Lout	=	0.0452	(m)
Hcoil	=	0.0370	(m)
Hboss	=	0.0576	(m)
Hsh	=	0.0310	(m)
Hcasing	=	0.1176	(m)
d_{boss}	=	0.0250	(m)
d_{mag}	=	0.0080	(m)
d_{coil}	=	0.0030	(m)
θmag	=	60	(deg)
N_{outlet}	=	8	
N_{mp}	=	6	
Rcm	=	3	
ω	=	1500	(rpm)

Table 7-2: Dimensionless Variables

R*	=	61.50
$R^*_{mag\ inner}$	=	26.50
$R^*_{mag\ outer}$	=	56.50
R_{in}*	=	18.75
R_{out}*	=	10.00
R_{casing}*	=	66.50
$R_{shinner}$*	=	57.50
R_{shout}*	=	71.00
$R_{core\ inner}$*	=	30.00
$R_{core\ outer}$*	=	52.50
R_{bh}*	=	5.75
L_{out}*	=	22.60
H_{coil}*	=	18.50
H_{boss}*	=	28.80
H_{sh}*	=	15.50
H_{casing}*	=	58.80
d_{boss}*	=	12.50
d_{mag}*	=	4.00
d_{coil}*	=	1.50
Re_{ω}	=	1263.00

Table 7-3: Test Rig Dimensions

$H_{air\ gap}$	=	0.0081	(m)
R	=	0.5000	(m)
$R_{mag\ inner}$	=	0.2154	(m)
$R_{mag\ outer}$	=	0.4593	(m)
Rin	=	0.1524	(m)
Rout	=	0.0813	(m)
Rcasing	=	0.5406	(m)
Rshinner	=	0.4675	(m)
Rshout	=	0.5772	(m)
$R_{core\ inner}$	=	0.2439	(m)
$R_{core\ outer}$	=	0.4268	(m)
Rbh	=	0.0467	(m)
Lout	=	0.1837	(m)
Hcoil	=	0.1504	(m)
Hboss	=	0.2341	(m)
Hsh	=	0.1260	(m)
Hcasing	=	0.4780	(m)
d_{boss}	=	0.1016	(m)
d_{mag}	=	0.0325	(m)
d_{coil}	=	0.0122	(m)
θmag	=	60	(deg)
N_{outlet}	=	8	
N_{mp}	=	6	
Rcm	=	3	
n	=	93	(rpm)

Other than the geometric parameters mentioned in Table 7-1, the rotational Renolds number also has strong effect on the flow. According to equation (7.4), by multiplying the axial distance between the stator and magnet, H_{airgap}, by the factor of four, the rotational speed has to scale down to the factor of sixteen, from 1500rpm to 93 rpm.

$$\mathrm{Re}_{\omega} = \frac{\rho \omega R H_{airgap}}{\mu} \tag{7.4}$$

Fig. 7-2(a) shows the configuration of the large scale test rig. The outer diameter of the generator is 1136mm and the maximum axial dimension is 336mm. The configuration of the scaled-up test rig is similar to the Durham AFPM generator, apart from the design of the boss and the number of the magnets. In most commercial axial flux generator designs, the connecting boss adopts an eight-prism supporting structure design (see, Fig. 7-2(b)), to increase the radial velocity in the air gap clearance, and to enhance the cooling of the generators. Also, some commercial axial generators operate at rotational speeds from 500 rpm to 900 rpm, which are much lower than the Durham 1500 rpm rig. For low speed axial flux machines, in order to generate 3-phase electricity at 50 Hz, the number of magnet pairs (and stator windings) on the rotor disk (and stator core respectively) has to be increased. As the result, to match with the commercial axial flux generator designs, the scaled-up test rig employs an eight-prism supporting structure connecting boss and sixteen magnet pairs configuration (Fig. 7-2(b)). Details of the dimensions of each of the generator component are shown in drawings attached in Appendix C.

The large scale test rig was manufactured in Perspex, including the stator, stator holder, magnets and rotor discs. The total weight of the test rig is about 150 kg, excluding the weight of the supporting units and the power and drive equipments. Since Perspex is seven times lighter than Steel and three times lighter than Aluminum, the use of Perspex for the scaled-up test rig leads to a lighter design. Consequently, smaller and lighter supporting units are required, such as smaller diameter shafts for the rotor disks and stator holder and a smaller bearing unit etc. It also reduces the cost of some of the power drive and measuring equipment. For example, smaller slip rig size and lower rated power induction motor can be used. Overall, the use of Perspex

for the scaled-up test rig has reduced the overall construction cost by a factor of four, as compared with aluminum, and a factor of ten as compared with steel.

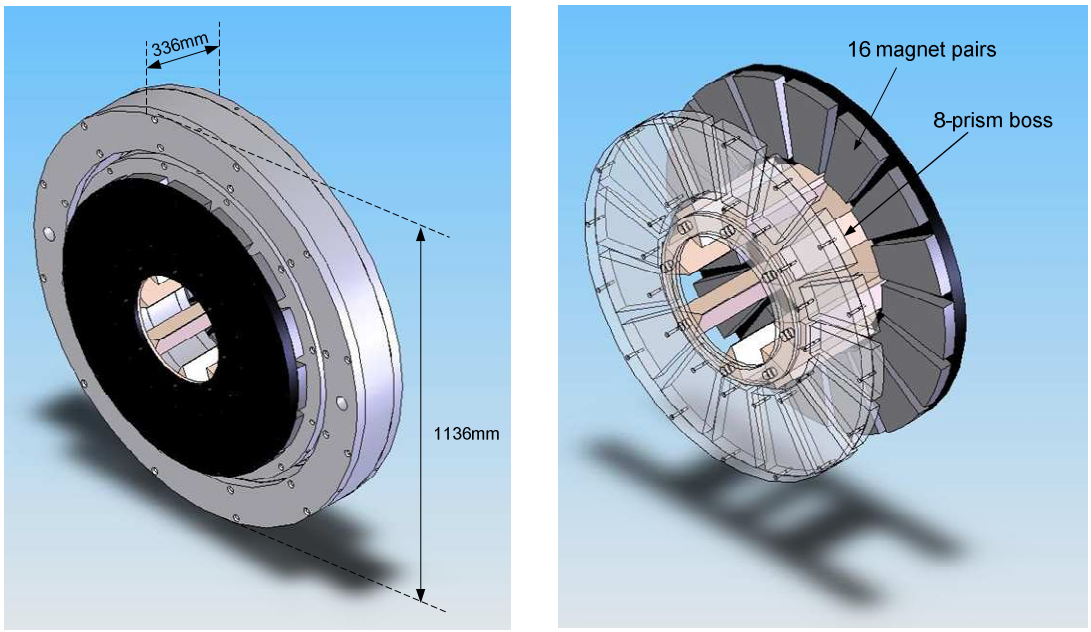

(a) (b)

Fig. 7-2. The scaled-up test rig (a) and the new boss and magnet pairs design (b).

Perspex has low thermal conductivity and high specific heat capacity. Unlike the high thermal conductivity and low specific heat capacity alternative materials, such as Steel and Aluminum, Perspex has less boundary effect on the measuring sensors and it is less sensitive to subtle changes of the ambient boundary conditions [79]. It is thermally more stable as compared with Steel and Aluminum. Consequently, the temperature and heat flux measurements taken on the Perspex surfaces have less noise and are independent of the ambient condition [149]. Furthermore, Perspex is an optically accessible material. This offers the potential for flow visualization experiments to be carried out.

The limited selection of Perspex block sizes and manufacturing processes make the fabrication of Perspex parts which are thicker than 30mm extremely costly. Therefore, some of the large test rig parts, such as the stator core and the stator holder, which have thickness larger than 30 mm, were split into a number of thinner annuli (Fig. 7-3(a) and (b)). In addition, the stator core and stator holder assemblies were designed

to be hollow, to further reduce their weight and hence the cost of the material and the test rig supporting units.

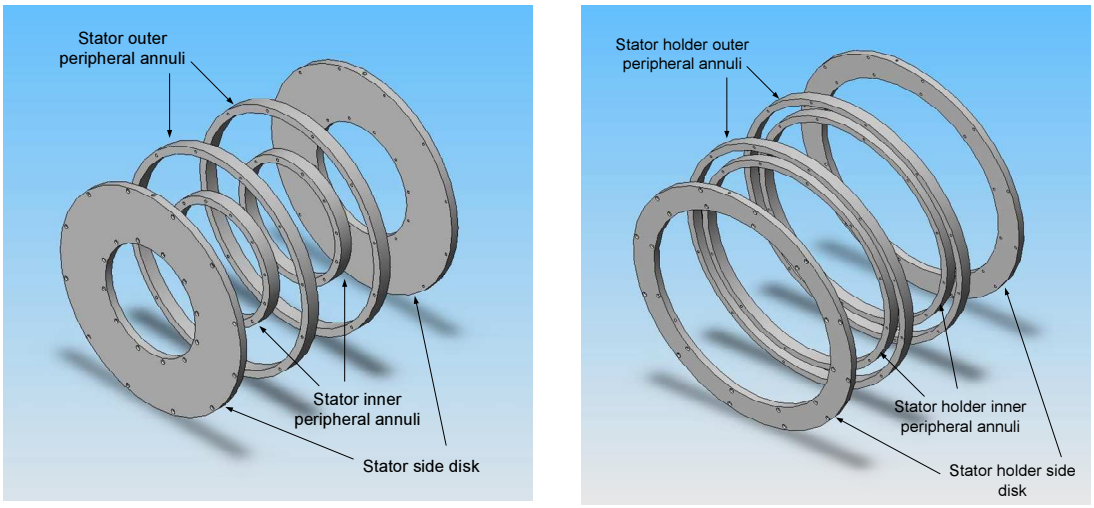

(a) (b)

Fig. 7-3. Stator (a) and stator holder (b) exploded views.

7.3. Experiment Setup

Experiments were designed to measure the surface temperatures and convection heat transfer coefficients of the stator and rotor disks of the large scale test rig. A schematic plan of the experimental setup is shown in Fig. 7-4. The stator assembly is supported on a metal workbench, by two 1.5 inch diameter steel shafts (Fig. 7-5(a)). One end of the shafts is secured on the metal workbench; and the opposite ends are welded to a crescent-shaped steel plate which pinches on the stator holder. The rotor disks are held in together by the eight-prism structural boss, as shown in Fig. 7-2(b). The front rotor disk is hollow-centred, allowing air to flow from the surroundings for machine cooling. The back rotor disk is attached to a 1.5 inch diameter steel shaft, via an aluminum flange (Fig. 7-5(a)). The rotor shaft is held by two, 1.5 inch inner diameter *NSK* pillow-block bearing units on the metal workbench. The rotor shaft is coupled to the ABB 5.5kW induction motor directly by a spider shaft coupling (Fig. 7-5(b)).

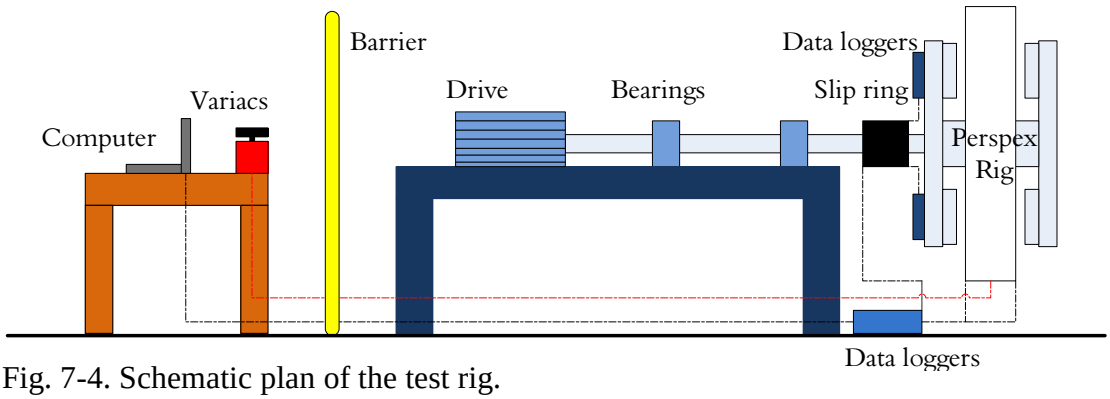

Fig. 7-4. Schematic plan of the test rig.

For testing the totally enclosed machine design, a detachable, cylindrical Perspex casing was manufactured (Fig. 7-5(c)). The Perspex casing can be attached on the stator supports and transforms the existing large scale test rig in to a totally enclosed system. Totally enclosed axial flux generators are fully concealed and the working fluid inside the generator is isolated from the external working environment. Experiments were designed to investigate the heat flow path and the change of convection heat transfer coefficient in this configuration as compared with open-channel axial flux generators.

The rotor disks were driven by an ABB 5. 5 kW 50 Hz 380-420 V 11.5 A star-configuration induction motor (model number of *3G AA132001ADA*) (Fig. 7-5(d)). The drive was modulated by an ABB 5.5kW 380-480V, 11.9A 3-phrase inverter, (model number of *ACS550-01-012A-4*) (Fig. 7-5(e)). The inverter was regulated to 150 rpm to prevent the test rig from over speeding, which could overstress the rotor shaft. The stator core was heated by three pairs of silicone heater mats. These heater mats were specially tailored to fit on to the stator core inner, outer and side faces (Fig. 7-5(f) & 7-5(g)). The rectangular strip inner and outer peripheral heater mat pairs were rated at 500 W and 900 W 240 V_{dc} respectively, and the annular side heater mat pairs were rated at 2000 W 240 V_{dc}. The heat output of these heater mats was controlled by two 10 Amp and one 20 Amp enclosed variac autotransformers (Fig. 7-5(e)). The power input and output of the heater mats was monitored by two power analysers via a 42-terminal patch box. A schematic plan of the power circuit and the patch box configurations is shown in Fig. 7-6 and Fig. 7-7 respectively. Safety barriers were installed, 3m from the test rig to protect the experimenters.

(a) Stator and rotor supporting units

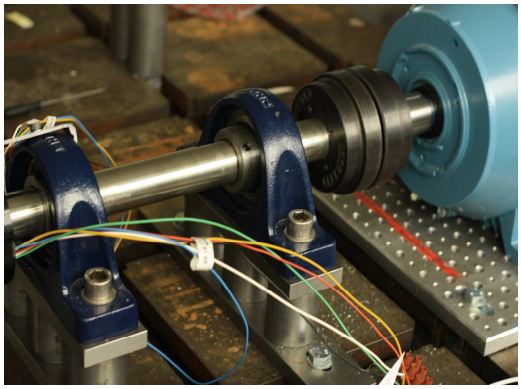

(b) Bearings and HRC shaft coupling

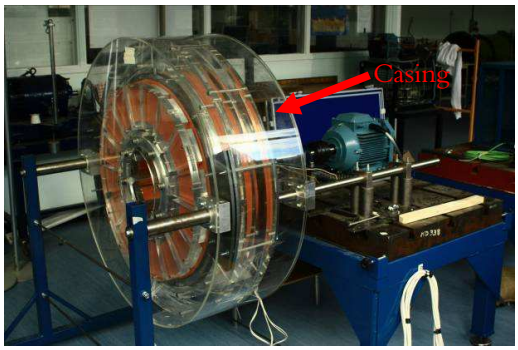

(c) Casing and its supporting units

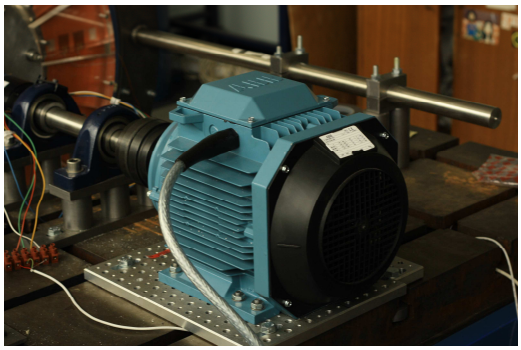

(d) ABB 5.5kW Induction motor

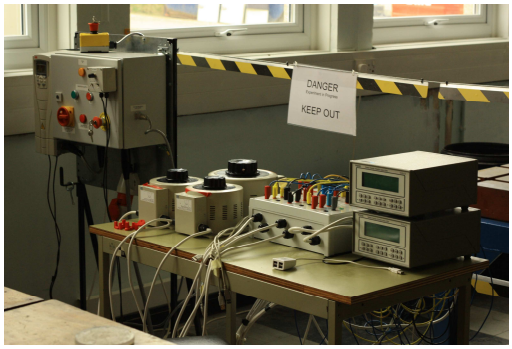

(e) Control and measuring equipments

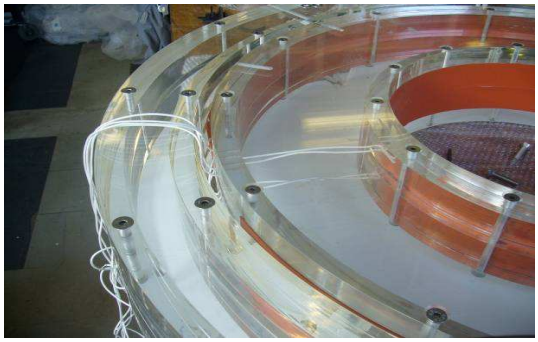

(f) Heater mats on peripheral faces

(g) Heater mats on side faces

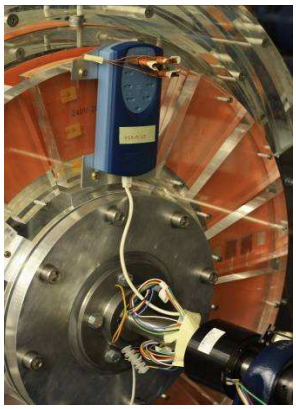

(h) Slip ring and data logger

Fig. 7-5. The scaled-up Perspex rig and the measuring and control equipments.

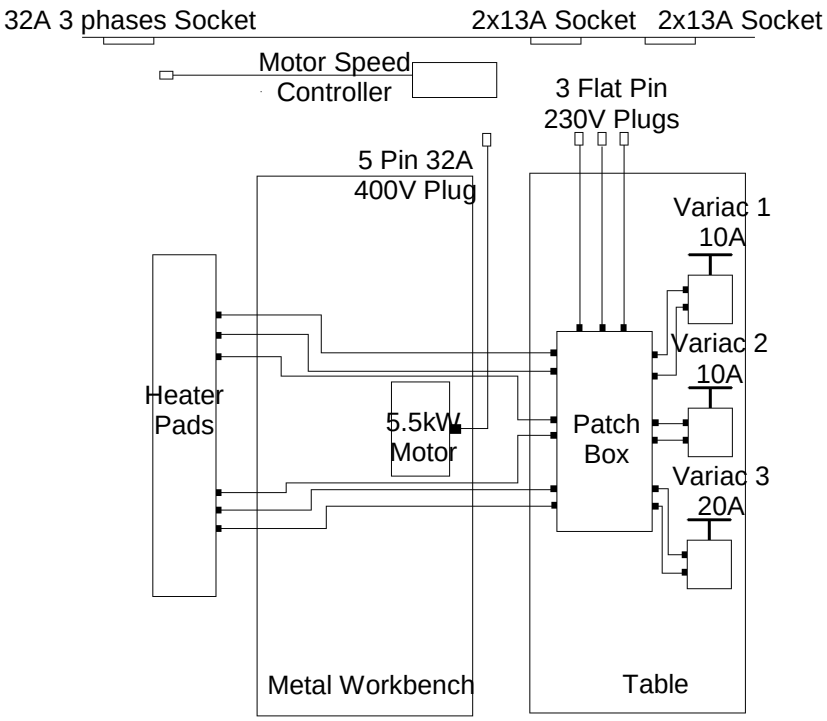

Fig. 7-6. Schematic plan of the power circuits for the heater mats and induction motor.

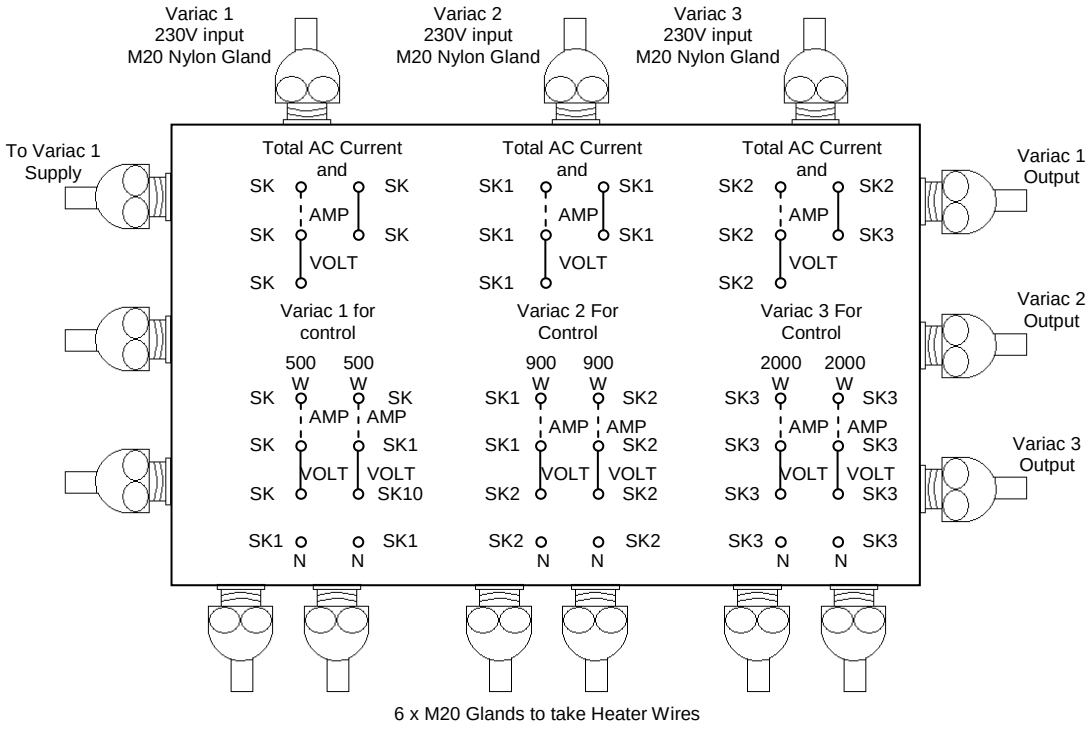

Fig. 7-7: The 42-terminal patch box configuration

The convection heat transfer coefficients on the stator and rotor surfaces were measured by using both the *OMEGA® HFS3* heat flux sensor and *OMEGA®SA1* T-type thin film surface thermocouples. The technical details of the heat flux sensor and the T-type thin film surface thermocouple can be found in section 6.4.2. On the stator core, six heat flux sensors and eight thermocouples were used, whereas on the rotor disks, two heat flux sensors and five thermocouples were attached. These sensors were affixed directly on the silicone heat mats and rotor disk surface by *TESA* tackified acrylic double-sided adhesive tape. The *TESA* double-sided tape has high adhesive strength at high temperature (The adhesive strength is 12.8 N/cm at 80 °C on PVC surfaces). Additionally, it is extremely thin (205 μm), re-useable and peelable. Therefore, it is ideal for high temperature heat transfer experimentation, especially attaching the heat flux sensors in between the narrow gaps in the test rig. The position of each heat flux sensor and thermocouple on the stator core and rotor surfaces is illustrated in Fig. 7-8.

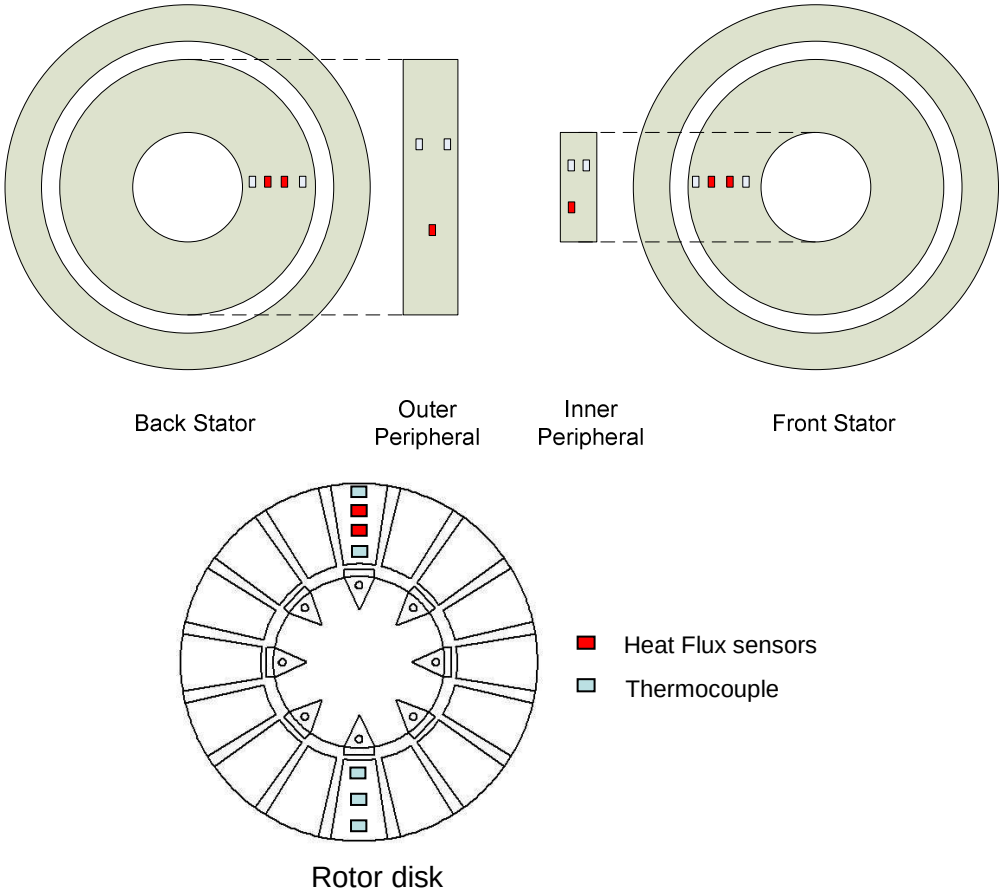

Fig. 7-8. Heat flux sensors and thermocouple positions on the stator core and rotor disk.

The direct connection between the heat flux sensors and thermocouples and the data logger is impossible on the rotor surfaces. Hence, a 1.5 inch through bore rotary slip ring was assembled on the rotor shaft, to transmit the signals generated from the sensors on the rotating surfaces to the personal computer (Fig. 7-5(h)). Nevertheless, the signal produced from the thermocouples and heat flux sensors are relatively weak, having a magnitude of just a few μVs, as compared with the noise signal caused by the mechanical rotary contacts of the slip ring, which is about $0.1mV$. As a result, the high noise level of the slip ring masks the signals produced from the rotating sensors if direct connections are used. Also, connecting the thermocouples and heat flux sensors directly on the slip rings creates extra redundant thermal joints (the junctions of two different metals meet) which further compromise the acquired data quality.

Therefore, to eliminate these potential experimental errors on the rotating surfaces by using the slip ring, two *PICO* data loggers were attached at the back of the rotor disk, amplifying the generated signals, before they were transmitted to the personal computer for data logging (Fig. 7-5(h)). So, instead of transmitting the μVs signals across the slip ring, the signals were amplified to range between ±5 V. This new configuration also circumvents the extra thermal joints in the signal circuits, which significantly improves the accuracy of the measurements, obtained from the data loggers.

7.4. Pre-experiment Equipment Investigation I: Silicone Heater Mats

The silicone heater mats used in the experimentation to heat the stator core are made of rapid heating etched resistance foil tracks. These foil tracks are laminated and protected between thin sheets of silicone (Fig. 7-9). Additional fibre glass insulation layers are laminated at the back of the heater mats, to reduce the heat dissipation from the back surface. In the experiments, the silicone heater mats were appended to the stator outer surfaces, where the back surfaces were affixed on the stator core surfaces by *Hi-Bond VST* acrylic foam double sided tape. This double sided tape has high

temperature resistance and it can resist temperature up to 120 °C for long term applications. The front surfaces of the silicone mats were exposed to the air, mimicking the stator windings of the real axial flux generators.

It is computationally costly to model the heater mat inner structure exactly in the CFD models. Hence, they were represented as constant heat flux boundaries conditions in the CFD models. Although the heater mats were designed for precise even heating, the etched resistance foil tracks, the silicone layers on the front surface, and the double-sided tape (which is used on the heater mat back surface) have significant effect on boundary conditions on the front surface. Therefore, a *FLIR A20* infrared camera was used to visualise the temperature distribution on the front surface of the stator-side silicone heater mat.

Since the infrared camera is not capable of penetrating through the Perspex rotor disk, to measure the temperature of the heater mat on the stator core, these experiments were conducted without the front rotor disk (Fig. 7-10). Initially, the side heater mat was powered for 2 hours. When the heater mat front surface temperature reached a steady state, the induction motor was switched on. The 8-prism structure connecting boss was spun and cooled the heater mats on the stator. After 3 hours, both the heater mats and induction motor were switched off. The infrared camera was set to take thermal images of the side heater mat just before the induction motor was switched on and just after the induction motor was switched off. The temperature profiles and thermal images are shown in Fig. 7-11 (a) and Fig. 7-12(a) respectively.

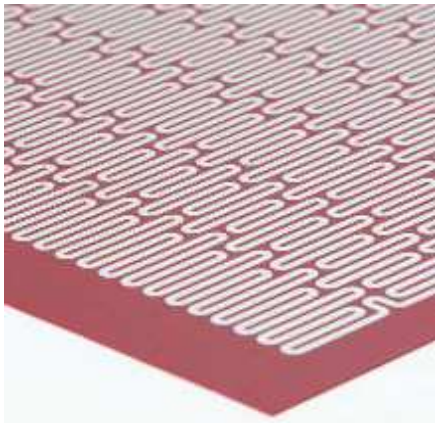

Fig. 7-9. Silicone heater mats: Etched resistance foil tracks

Fig. 7-10. Test rig without front rotor disk.

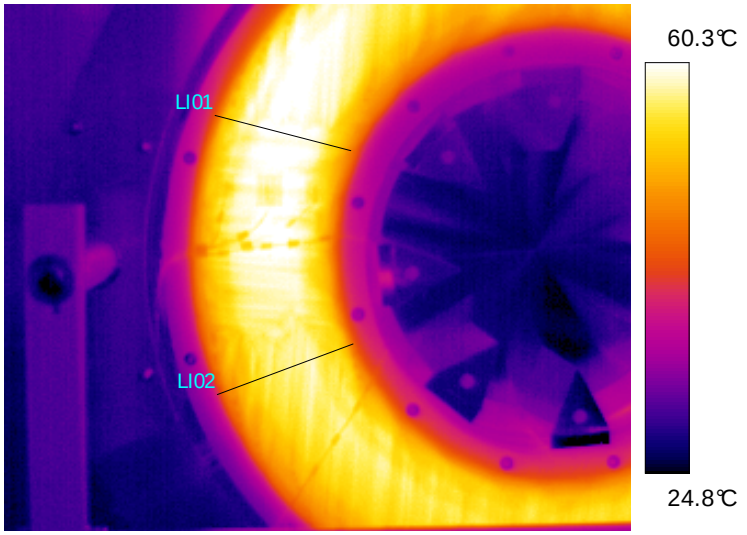

(a)

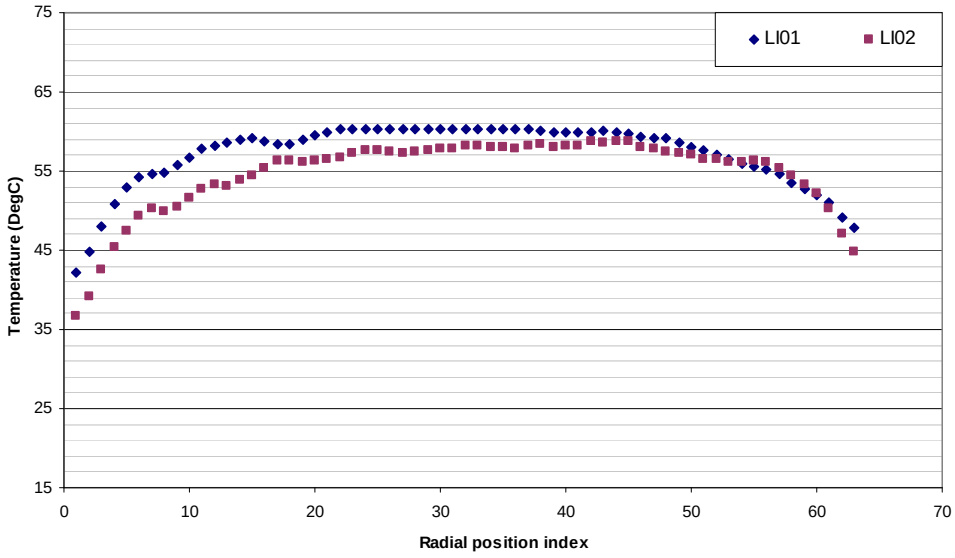

(b)

Fig. 7-11. Infrared thermal image (a) and temperature profiles (b) of the heater mats before the induction motor was switched on.

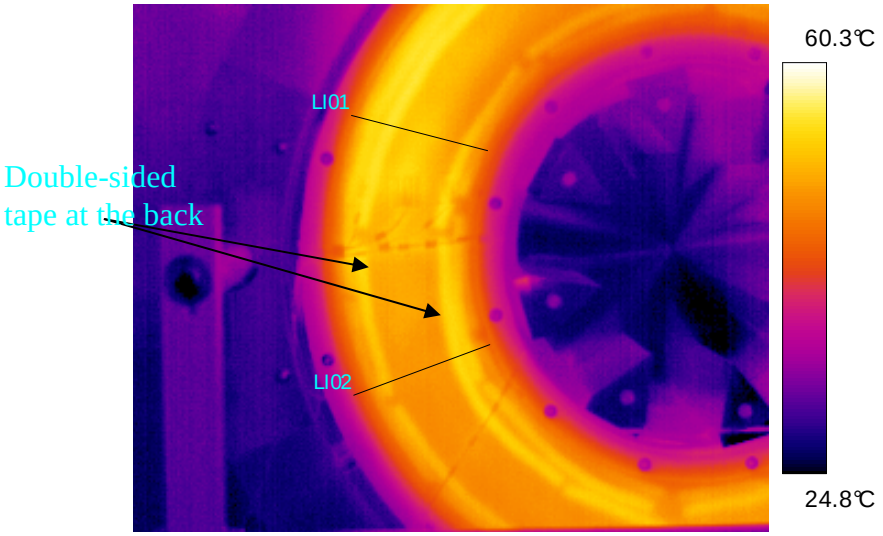

(a)

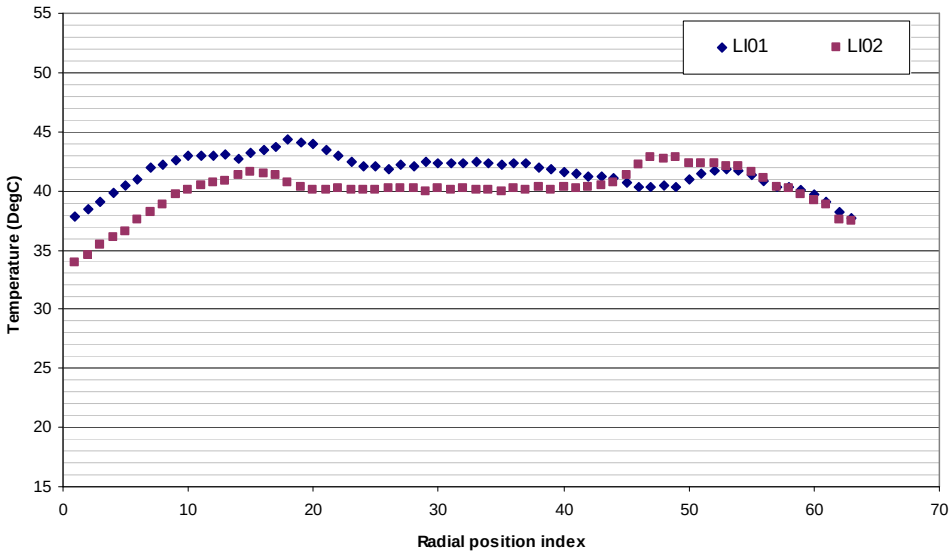

(b)

Fig. 7-12. Infrared thermal image (a) and temperature profiles (b) of the heater mats 3 hours after the induction motor was switched on.

From Fig. 7-11(a), the shadow of the silicone rubber mesh (vertical and horizontal fine lines) can be observed on the heater mat surface in the thermal image. These fine lines faded away 3 hours after the induction motor was switched on, but the high temperature area caused by the presence of the double-side tape at the back of the heater mats appeared. This can be observed in the thermal image shown in Fig. 7-12(a).

Fig. 7-11(b) and Fig. 7-12(b) show the temperature radial profiles on the lines *LI01* and *LI02* of the heater mat surface before the induction motor was switched on and after the induction motor was switched off, respectively. The results show that surface temperature on the front heater mat varies from 10-20 °C. Discrepancies between temperature radial profiles at different positions (at *LI01 and LI02* for instance) are also found on the heater mat surface, where the maximum discrepancy is 5 °C. This may be due to the effect of natural convection or the uneven heating surface. Also, it can be seen that the temperature of the heater mat is lowered when the induction motor was switched on. The temperature dropped approximately by 10 °C, by forced convection caused by the spinning 8-prism boss.

In conclusion, the silicone heater mats which have lower thermal conductivities, result in uneven surface temperature. The results show that both the silicone rubber lamination (on the front surface) and the double-sided tape at the back of the rubber mat have significant effects on the thermal boundary of the heater mat. Consequently, discrepancies between the temperatures measured from the experiments and obtained from the CFD model are expected, due to the inconsistency of the thermal boundary conditions applied in the CFD model. However, since heat transfer coefficient is independent of the surface thermal boundary conditions, the experimental rig is still applicable to validate the heat transfer coefficients predicted from the CFD models.

7.5. Pre-experiment Equipment Investigation II: Slip Rings

1.5 inch through bore slip rings were used to transmit the signals generated from the heat flux sensors and thermocouples on the spinning rotor disks, to the stationary data logging system. To eliminate experimental errors which may occur from the noise of the slip rings, the signals generated from the sensors were amplified by the *PICO* data loggers, before transmitting through the slip ring. These data loggers were positioned at the back of the rotor, rotating together with rotor disks during the experiments.

A simple experiment was conducted to identify signal distortion by using the slip ring for transmitting the amplified thermocouple signals from the *PICO* data logger. Two

identical thermocouples were attached on to Aluminum plate front surface (Fig. 7-13(a)). The first thermocouple was connected to the computer directly via a PICO data logger. For the second thermocouple, the signal was amplified by a PICO data logger, and transmitted to the computer via a 1.5 inch through bore slip ring. The slip ring was mounted on a shaft, powered by a 12 V_{dc} oscillating motor (Fig. 7-13(a)).

At the bottom surface of the aluminum plate, an 8 W 12 V_{dc} silicone heater mat was attached (Fig. 7-13(a)), powered by an adjustable 18 V 20 Amp rated DC power supply. The DC power supply was adjusted to 12 V and 1.25 Amp and connected to power the silicone heater mat. Prior to switching on the DC power supply to energise the heater mat, the data loggers were activated and the motor was set to oscillate the shaft through ±180° at 0.83 Hz. The surface temperature of the Aluminum test plate was recorded while it was heated for a period of four minutes. Fig. 7-13(b) shows the temperatures measured from two different thermocouples on the Aluminum test plate.

The result shows that the temperatures measured by the two connection configurations (with and without slip ring) coincide exactly with each other. It confirms that the connecting configuration, where the data logger is connected to the thermocouples prior to the slip rings, is not adversely affected by the slip rings themselves. Hence, this configuration can be embraced for the large scale test rig, to measure temperature and heat flux on the rotor surfaces.

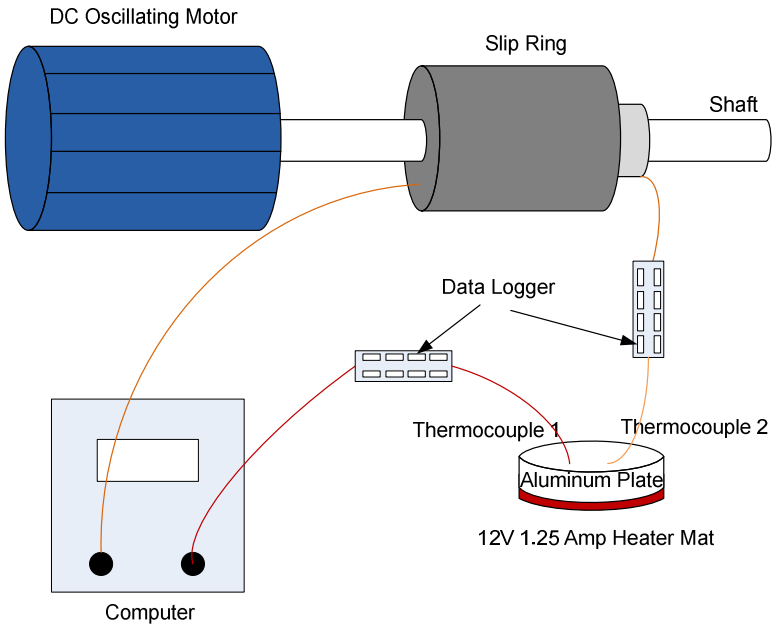

(a)

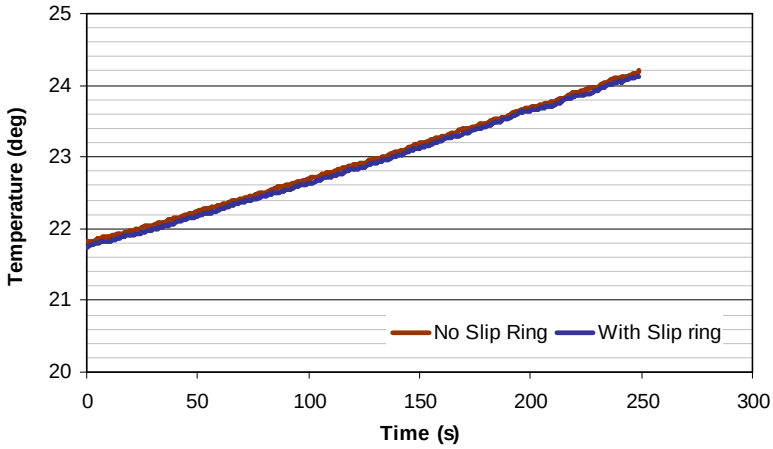

(b)

Fig. 7-13. Slip ring test aluminum test plate configuration (a) and its corresponding surface temperature results (b).

7.6. Convection Heat Transfer Coefficient Measurements

Several experiments were designed and carried out to measure the surface convection heat transfer coefficients in the large scale Perspex test rig. The results obtained were then compared with the numerical surface heat transfer coefficients calculated from the CFD models. Additional experiments were conducted with different heat inputs and rotational speeds, to investigate the dependency of the convection heat transfer

coefficients at different heat flux levels and the effect of natural convection. Finally, the test rig was converted into a totally enclosed system, to determine the effect of the enclosure on the surface heat transfer coefficients.

7.6.1. Experiment Validation of CFD Modelling Technique

The stator core was initially heated by the silicone heater mats for three hours, until it had reached its thermal steady state. The power outputs of the heater mat were controlled by three separate variacs, which are Variac 1 (10 Amp rated), Variac 2 (10 Amp rated), and Variac 3 (20 Amp rated). The mechanical dials of the three variacs were pre-set to a nominal 80 Volts and remained unchanged during the experiments. Additional voltmeters and ammeters were used to monitor the precise output voltage of the variacs.

Table 7-4 shows an example of the power input and output measure from the variacs. The inconsistencies between the input and output powers, for example: Variac 1 input power and output are 113.77W and 107.76 W respectively, were due to the mechanical and heat losses in the variacs. Furthermore, since the electrical resistances of the heater mats change as the temperature rises or drops, these voltage and current measurements were recorded only at the end of the experiments.

Table 7-4: Variac power inputs and outputs

	Variac 1		Variac 2		Variac 3	
Measurement	Input	Output	Input	Output	Input	Output
Voltage (V)	239.5	78.97	239.5	53.64	239.3	67.31
Current (Amp)	0.478	1.366	0.415	1.686	1.364	4.466
Power (W)	113.77	107.76	98.78	90.28	324.7	300.62

After the stator core was pre-heated for three hours, the drive inverter and induction motor were switched on. From the dimensional analysis conducted in section 7.2, the required rotational speed for the large scale Perspex test rig was 93 rpm (or 9.74rad/s), in order to maintain the same (rotational) Reynolds's number as the small scale, high

speed Durham 1.5 kW axial flux generator. The inverter was set to 3.1 Hz (see equation 7.5), to maintain 93 rpm on the 4-pole induction motor.

$$\omega = \frac{60 \times f}{n} \qquad (7.5)$$

$$f = \frac{2 \times 93 rpm}{60} = 3.1 Hz$$

Where ω = rotational speed in RPM

f = inverter frequency in Hz

n = Number of pole-pair

The data loggers and computer were run simultaneously when the induction motor was switched on. The signals generated and received from the thermocouples and heat flux sensors were logged into the computer at one second intervals, for four hours, until the rig had reached the thermal steady state again.

The CFD model of the large scale test rig was constructed and tested by Airoldi [54]. The corresponding stator local surface heat transfer coefficients obtained from the CFD models, by considering the air inlet temperature as the reference temperature, are plotted in Fig. 7-14 and 7-15. For the stator back and front surfaces, the local surface heat transfer coefficients are plotted at the radial distances from generator centre axis, from 250 mm to 410 mm (Fig. 7-14). This corresponds to the radial coordinates from the inner to the outer radii of the annulus heater mats. In Fig. 7-15, the coordinates represent the axial distance from the stator back surface of the stator inner and outer peripheral surfaces respectively. The local surface heat transfer coefficients were plotted from axial coordinate 137 mm to 237 mm, which corresponds to the positions in between the front to back sides of the stator core.

Similarly, the stator local surface heat transfer coefficients measured from the experiments are demonstrated in Fig. 7-14 and 7-15, compared with the results obtained from the CFD models. Overall, the results show that the CFD models under-predict the local heat transfer coefficients on the stator, by 2-8 W/m^{2}K, corresponding to relative discrepancies of 7%-61%, on the stator surfaces. The highest relative

discrepancy occurs on the stator outer peripheral surface. This is because the main air flow in the machine does not flow through the stator outer peripheral gap, where the heat transfer is mainly dominated by natural convection. Since the CFD model used in this study neglected the air buoyancy modelling, it might account for the high relative discrepancy on the stator outer peripheral surface.

The experimental uncertainties of the heat flux sensor measurement were discussed in section 6.4.2. The same analysis was used in this experiment since the similar heat flux sensors were used. The evaluated heat transfer coefficient uncertainty for each of the heat flux sensor is shown in Table 7-5, and illustrated in Fig. 7-14 and Fig. 7-15.

Table 7-5: Heat transfer coefficient uncertainty of each heat flux sensor

	Back 1	Back 2	Front 1	Front 2	Inner Peripheral	Outer Peripheral
Uncertainty	±3.753%	±8.738%	±7.891%	±7.751%	±5.053%	±4.278%

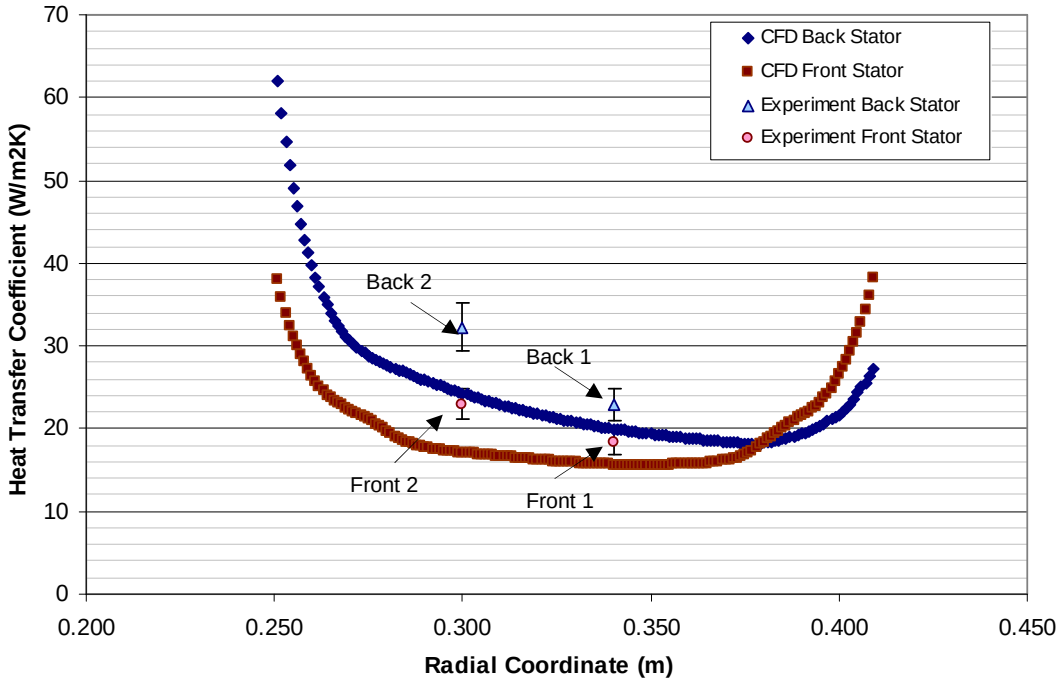

Fig. 7-14. Surface heat transfer coefficients measured (from the experiments) and evaluated (from CFD models) on stator core back and front surfaces.

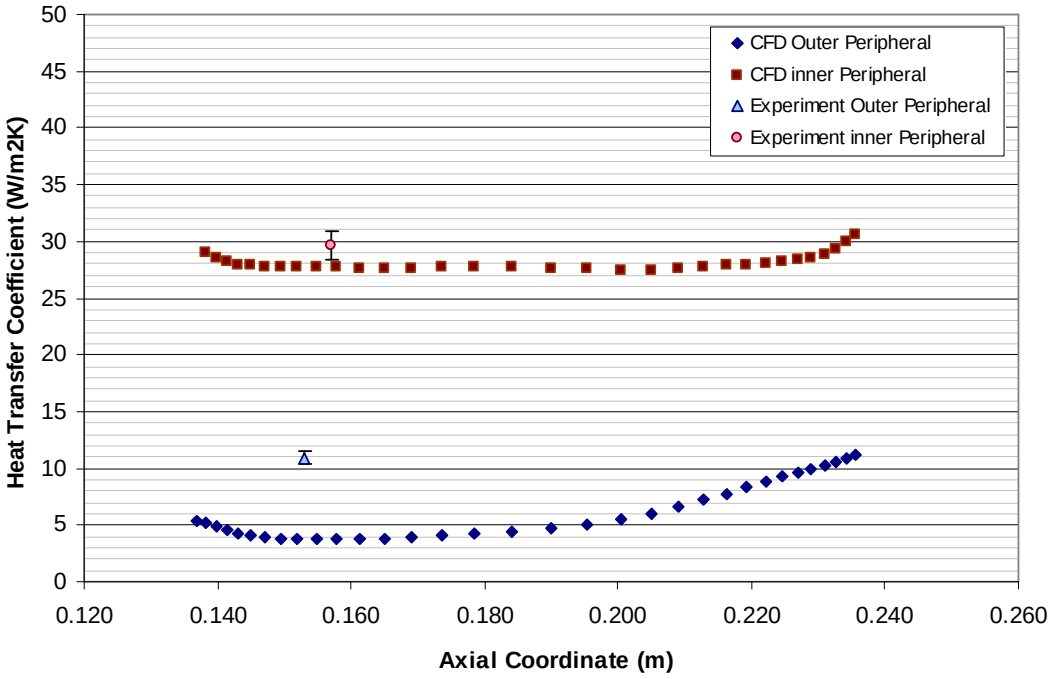

Fig. 7-15. Surface heat transfer coefficients measured (from the experiments) and evaluated (from CFD models) on stator core outer and inner peripheral surfaces.

7.6.2. Heat Transfer Coefficient Versus Rotational Speed: Investigation of Natural Convection

Similar experiments were conducted at different rotational speeds, which were at 0 rpm, 45 rpm and 120 rpm. The local surface heat transfer coefficients measured on different stator surfaces are illustrated in Fig. 7-16, for those rotor speeds. The corresponding linear regression lines of each set of heat transfer coefficient are included in the Fig. 7-16, as well as the equivalent linear regression value, R^2. It can be seen that all the linearly approximated regression lines have high R^2 values (close to 1.0). Therefore, it is clear that all the local heat transfer coefficients on the stator surfaces are linearly dependent on the rotor rotational speed.

Also, the inlet air mass flow rates at different rotational speeds were measured, using the TSI hot-wire anemometer. Fig. 7-17 shows the air inlet mass flow rate at different rotor rotational speeds. Again, the air inlet mass flow rate shows a strong linear

dependency on the rotor rotational speed, with the linear R^2 value of 0.9999 (Fig. 7-17).

It is well documented that the surface convection heat transfer coefficient is dependent on the fluid velocity boundary layer adjacent to it [150]. Since the air mass flow rate increases linearly with the rotor rotational speed, the local heat transfer coefficients follow the same trend. The stator outer periphery heat transfer coefficients show the weakest dependency with respect to rotor rotational speed. The gradient of the graph for stator outer peripheral edge is 0.037 W/m2K/rpm. The stator outer periphery lies in the gap between the stator core and stator holder (Fig. 7-8). Since the fluid velocity here has only a weak connection with the main air flow rate, the surface heat transfer coefficient remains almost unchanged when the rotor rotational speed increases.

At 0 rpm, the rotor disk is stationary and the local heat transfer coefficient on the stator surfaces varies in the range from 8-12 W/m^{2}K. This may be compared to the heat transfer coefficients measured on the stator surface at 93 rpm, which range from 14 W/m^{2}K to 45 W/m^{2}K at 93rpm. These highlight the importance of considering natural (or free) convection cooling in the large scale test rig CFD modelling.

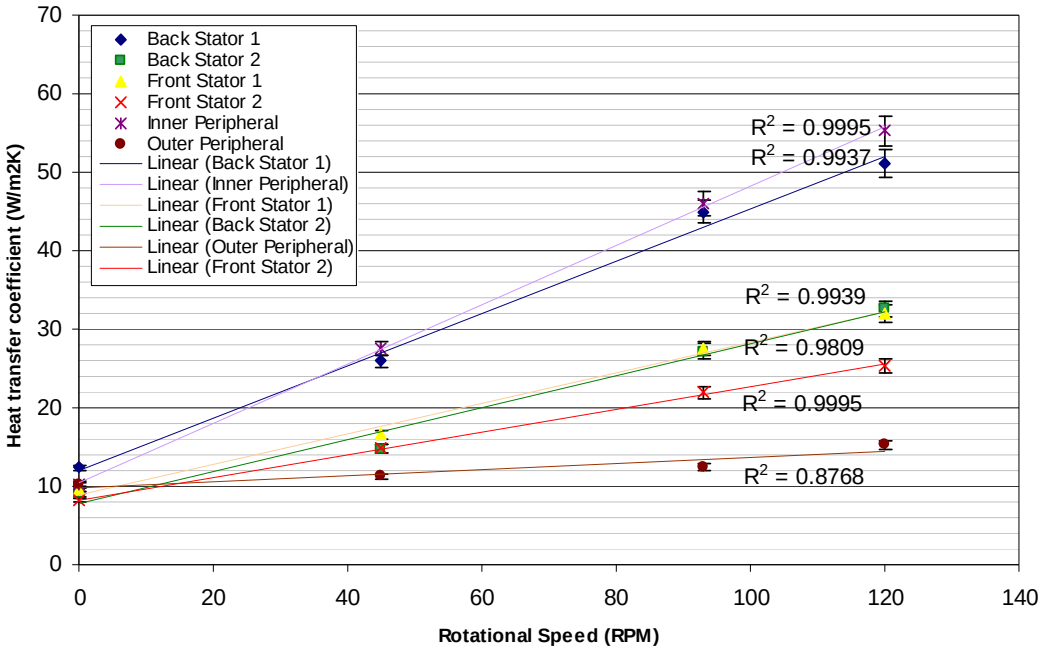

Fig. 7-16. Local heat transfer coefficients measured from the experiments, on different stator surface at various rotational speeds.

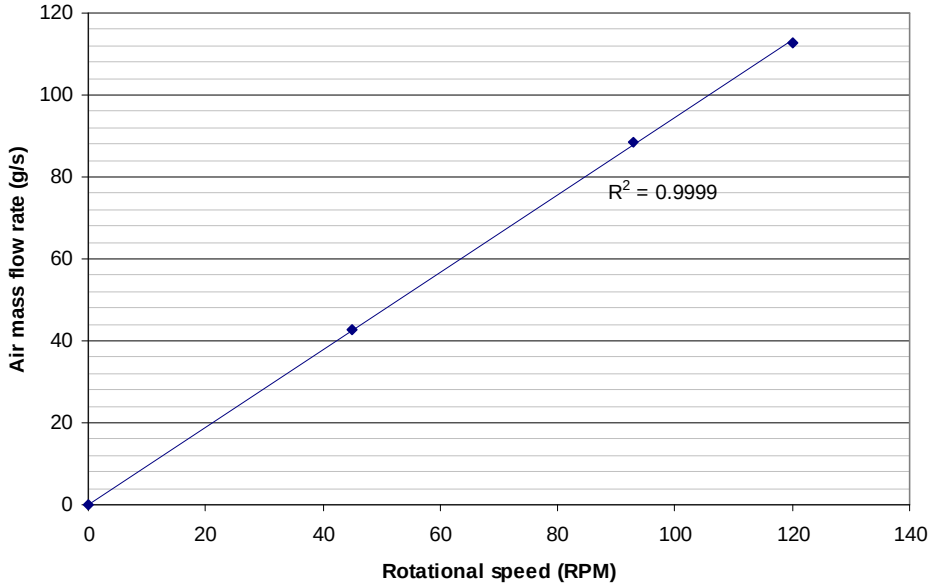

Fig. 7-17. Inlet air mass flow rate measured from experiments, at various rotational speed.

The fluid motion on the surface due to natural convection is caused by the buoyancy force within the fluid. The buoyancy force is due to the combined presence of the fluid density gradient and the gravitational force: Hot air rises and cold air sinks. However, in the CFD models produced by Airoldi [54], the air density gradient was neglected and the extra natural convection cooling effect in the large scale test rig was not taken into consideration. Hence, the CFD surface heat transfer coefficients shown in Fig. 7-14 and 7-15 only account for the forced convection heat transfer, and they did not agree with the experimental results, which comprise of both forced and natural convection effects.

In mixed convection flows, where the natural and forced convection effects co-exist, it is inappropriate to neglect either process. Churchill [151] suggested that the effect of buoyancy on heat transfer in a forced flow is influenced by the direction of the buoyancy force relative to that of the flow. For assisting flow, where the buoyancy force and air flow are in the same direction, the mixed convection heat transfer coefficient results for internal flows can be superimposed from the heat transfer

coefficients from both forced and natural convections, with the exponent *n*, as shown in equation (7.6).

$$Nu_{mixed-assisting}{}^{n} \equiv Nu_{forced}{}^{n} + Nu_{natural}{}^{n} \tag{7.6}$$

For opposing flows, the mixed convection heat transfer coefficient is expressed as equation (7.7).

$$Nu_{mixed-opposing}{}^{n} \equiv Nu_{forced}{}^{n} - Nu_{natural}{}^{n} \tag{7.7}$$

Where $Nu_{mixed\text{-}assisting}$ = Mixed Nusselt number for buoyancy-induced and forced motions having the same direction.

$Nu_{mixe\text{-}opposinge}$ = Mixed Nusselt number for buoyancy-induced and forced motions having the opposite directions.

Nu_{forced} = Forced convection Nusselt number

$Nu_{natural}$ = Natural convection Nusselt number

n = Correlation parameter based on different flow patterns

The exponent *n* has been rationalised for flows around immersed bodies [152] and in channels [153] by Churchill. Churchill examined the various sets of experimental and theoretical values for isothermal and uniformly heated, vertical plates and concluded that $n = 3$ is a good approximation. Theoretical support for $n = 3$ was also provided by Ruckenstein[154]. Nevertheless, the exponent numbers depend on the flow patterns, the thermal boundary conditions and the definition of the heat transfer coefficients for Nusselt's number. Most of the available literature relates to the case of a uniform flat plate (for both vertical and horizontal plate), with isothermal or uniform heat flux boundary conditions and the heat transfer coefficients were defined by taking the free stream temperature as the reference temperature. Hence it is not suitable to use the derived *n* exponent for the application of the large scale test rig.

Consequently, experiments were conducted to investigate the effect of natural convection in the large scale test rig. Extra heat flux sensors were attached on the both sides of the stator front surface: three heat flux sensors on both the right and left sides of the stator core (Fig. 7-18). Since the rotor disks were rotated in a clock-wise

direction, on the left hand side of the stator core, the buoyancy force acts to enhance the rate of heat transfer associated with the forced convection; on the right hand side, the air buoyancy force acts to decrease the rate. Therefore, by evaluating the corresponding local heat transfer coefficients on both sides of the stator surface, the effect of the natural convection on the surface of the stator can be realized. The exponent *n* can be evaluated, by subtracting equation (7.6) to equation (7.7), which leads to equation (7.8). Equation (7.8) can be solved by Newton-Raphson method.

$$Nu_{mixed-assisting}{}^{n} - Nu_{mixed-opposing}{}^{n} = 2 \times Nu_{natural}{}^{n} \tag{7.8}$$

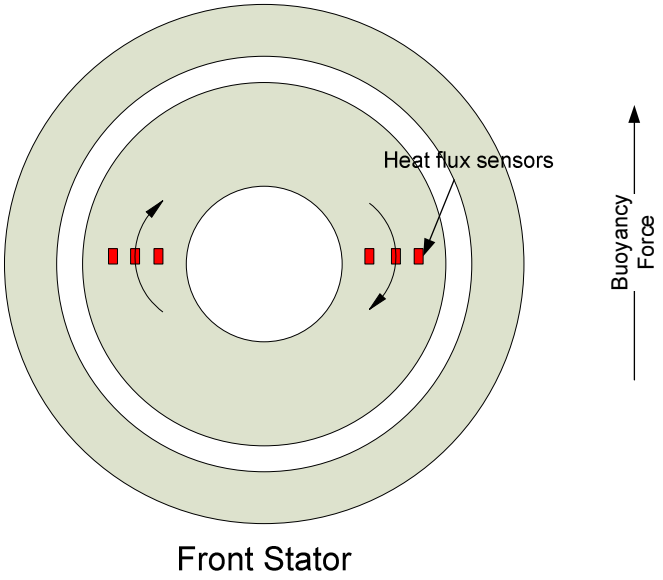

Fig. 7-18. New heat flux sensor positions for natural convection investigation.

Since natural convection on a heated surface is temperature dependent, i.e. the natural convection heat transfer coefficients on the high temperature surfaces are higher and lower on the low temperature surfaces. Hence, the power inputs of the silicon heater mats were carefully controlled and monitored to maintain the surface temperature at 80 °C, which was the same temperature when the rotor disks were rotating at 93 rpm.

The measured heat transfer coefficients on the left and right hand sides of the stator are illustrated in Table 7-6. The first two rows of Table 7-6 show the mixed convection heat transfer coefficients measured on the left and right hand sides of the front stator, respectively. The natural (or free) convection heat transfer coefficients

measured when the rotor disks were stationary are summarised in the third row of Table 7-6. By substituting the measured heat transfer coefficients from the assisting flow, opposing flow and natural convection into equation (7.8), the *n* exponents can be calculated. The fourth row of Table 7-6 illustrated the *n* exponents calculated at different radial coordinates. Finally, by applying the calculated *n* exponent into equation (7.7), with the corresponding mixed and natural convection heat transfer coefficients, the heat transfer coefficients due to forced convection only were evaluated and shown in the last row of Table 7-6.

Table 7-6: Heat transfer coefficients due to mixed convection, natural convection and forced convection.

	Radial Coordinate (mm)		
	290	330	370
HTC- Right (W/m^2K): Opposing flow	19.1641	16.1314	18.0431
HTC- Left (W/m^2K): Assisting flow	24.5049	17.7960	21.9919
HTC- Natural Convection (W/m^2K)	6.4731	8.6178	13.5264
n exponent*	1.4335	2.8856	3.0531
HTC-Forced convection only	21.9084	17.0021	20.2153

* *n* exponents are calculated by Newton-Raphson's method with equation (7.8)

As mentioned previously, the heat transfer coefficients predicted from the CFD model did not take into account the effect of natural convection since the air density was assumed to be constant. Therefore, to compare the experimental results with the CFD model, the experimental heat transfer coefficients were adjusted by subtracting the natural convection effect (equation (7.9)).

$$Nu_{forced}^{\ n} = Nu_{mixed-assisting}^{\ n} - Nu_{natural}^{\ n} \tag{7.9}$$

However, the *n* exponent in equation (7.9) varies for different flow conditions. For the stator front and back surfaces, the *n* exponents shown in Table 7-6 were used but for the inner and outer peripheral surface of the stator, since they have the same configuration as the flat plate model, the *n* exponent suggested by Churchill [152] and Ruckenstein [154] was adopted. The experimental heat transfer coefficients due to

forced convection only are plotted and compared with the CFD results in Fig. 7-19 and Fig. 7-20. The uncertainty of the measured heat transfer coefficient due to forced convection at each position on the stator surfaces is summerised in Table 7-7. As compared with the uncertainty estimated in previous experiments (Table 7-5), the uncertainty of these experimental results is higher. This is because the heat transfer coefficients due to forced convection only were evaluated from equation 7.9, which consists of two parameters: $Nu_{mixed\text{-}assisting}$ and $Nu_{natural}$. These parameters were obtained experimentally, with a corresponding measurement uncertainty. Therefore, the uncertainty of the heat transfer coefficient due to forced convection only is the sum of the measurement uncertainties of both $Nu_{mixed\text{-}assisting}$ and $Nu_{natural}$.

Table 7-7: Experimental uncertainty of the heat transfer coefficient due to forced convection only at different positions.

	Back1	Back2	Front1	Front2	Front3	Inner Peri.	Outer Peri.
Uncertainty	±7.5	±17.5	±15.8	±15.5	±12.4	±10.2	±8.6

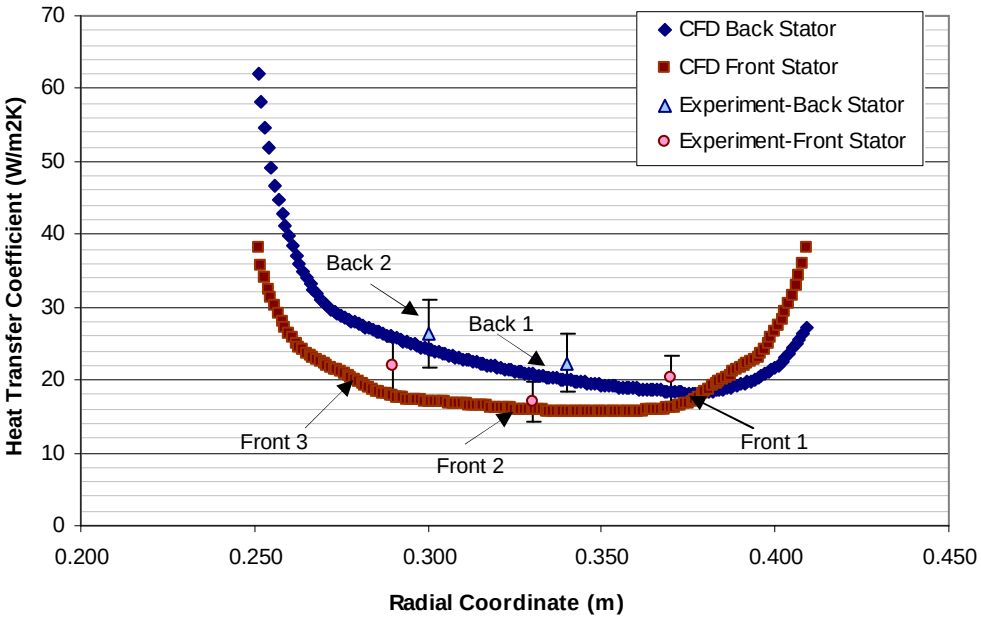

Fig. 7-19. Surface heat transfer coefficients (forced convection only) deduced (from the experiments) and evaluated (from CFD models) on the stator core front and back surfaces.

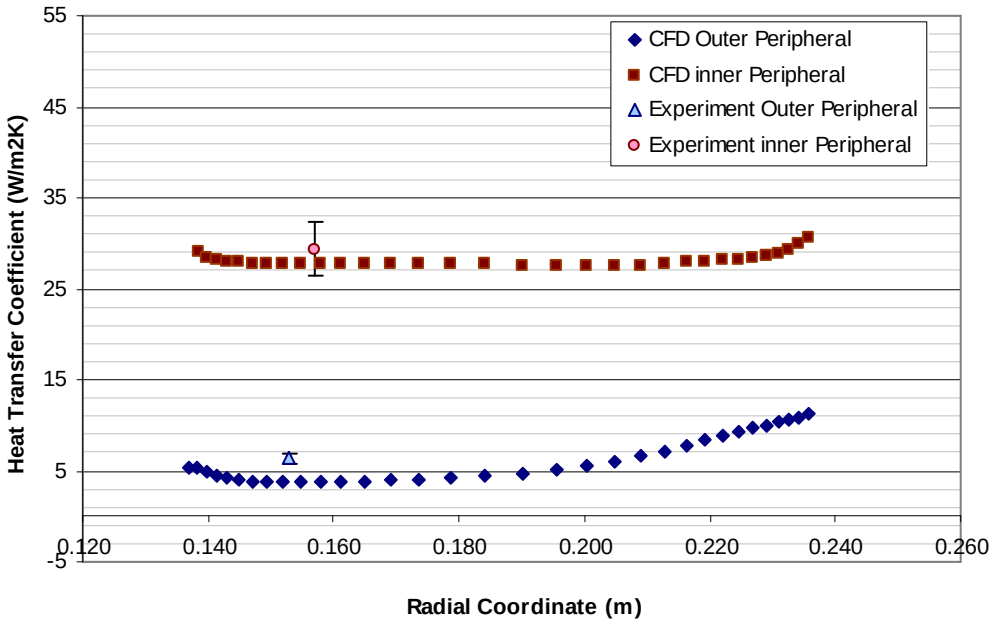

Fig. 7-20. Surface heat transfer coefficients (forced convection only) measured (from the experiments) and deduced (from CFD models) on the stator core outer and inner peripheral surfaces.

These results illustrate that the surface heat transfer coefficients due to forced convection only which were predicted by the CFD model, show a good agreement with the experimental results. The absolute discrepancies are reduced from 2.1-8.0 W/m^2K, to 1.1-4.5 W/m^2K, which correspond to the relative discrepancies have improved from 6.8%-65.8% to 5.4%-41.5%. The highest relative discrepancy occurs on the stator outer peripheral surface. Since the stator outer surface has relatively low heat transfer coefficient, a small difference in the absolute heat transfer coefficient, may incur high relative discrepancy.

7.6.3. Convection Heat Transfer Coefficient-Heat Flux Dependency Study

Theoretically, the convection heat transfer coefficient on a solid surface depends on the fluid properties (such as density, viscosity, thermal conductivity, and specific heat), the geometry of the surfaces and the flow Reynolds number. The functional dependence of the average Nusselt number can be defined as [150, 155]:

$$\overline{Nu} = \frac{\bar{h}L}{k_f} = f(\mathrm{Re}, \mathrm{Pr}) \tag{7.10}$$

Where,

$\bar{h}$ = average convection heat transfer coefficient, (W/m^{2}K)

k_f = fluid thermal conductivity, (W/mK)

Pr = Prandtl number

No evidence was shown in equation (7.10), that the surface convection heat transfer coefficients are dependent of the surface heat flux. Also, the CFD models constructed by Airoldi [54] assumed that the surface convection heat transfer coefficients are independent of the surface heat flux. To validate the equation (7.10) and the assumption made in the CFD validation experiments, a series of experiments were conducted to investigate the heat flux dependency of convection heat transfer coefficients.

The same experimental setup as described in section 7.3 was used to conduct the heat flux dependency study. In this case study, three additional heat inputs were tested, by altering the variac transformers from the original 80 Volts to 40 Volts, 60 Volts and 100 Volts, respectively. The rotor disks were kept rotating at 93rpm throughout the investigation. The effect of heater mat power input on the surface heat transfer coefficients is shown in Fig. 7-21.

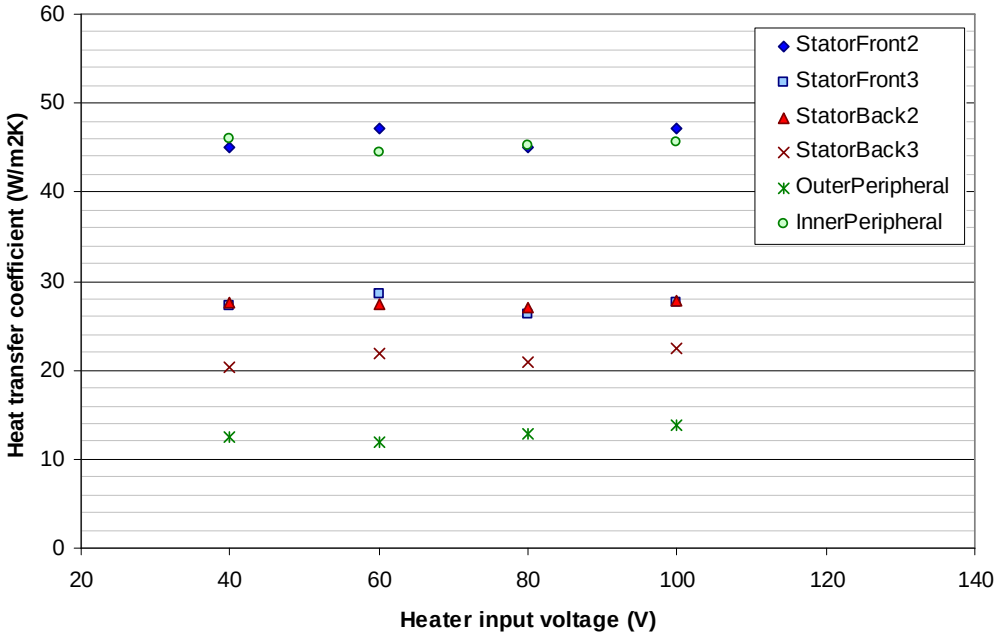

Fig. 7-21. Surface heat transfer coefficients on the stator surface at different power input to the heater mats.

The experimental results support the hypothesis that the surface convection heat transfer is independent of the magnitude of heat flux. When the heater mat power input was increased from 40 Volt to 100 Volt, the change of the convection heat transfer coefficient on the stator core surfaces was negligible (Fig. 7-21). The experimental results show that at higher level of heat inputs on the heater mats at similar flow condition, the solid surface temperatures increase but they are compensated by the high heat generated from the heater mats, to maintain the same surface convection heat transfer coefficient. Similar trends were found on CFD models when higher magnitudes of heat flux were used.

7.6.4. The Totally Enclosed Permanent Magnet Generator

In this study, the large scale test rig was enclosed by a Perspex casing (Fig. 7-5(c)), to evaluate the surface heat transfer coefficients of an equivalent totally enclosed machine design, and to compare them with heat transfer coefficients obtained from the open channel machine. In totally enclosed axial flux generators, the air inside the casing circulates inside the machines, transferring the heat generated from the heater

mats on the stator core to the external casing, and then across the casing to the ambient external conditions.

The heat flux sensors and thermocouple were attached to the test rig with the same layout shown in Fig. 7-8. Additional thermocouples were used to monitor the air temperature inside the casing and the heat transfer coefficients on the test rig were evaluated by using the measured air temperature as the reference temperature. The experimental rig was pre-heated by three pairs of the silicon heater mats for five hours, until it had reached its thermal steady state. Prior to switching on the inverter unit and the induction motor, the surface temperatures and local heat fluxes were recorded by the *PICO* data loggers, into a personal computer. The rotor disks were spun for six hours, until the test rig had reached a new thermal steady state. The power inputs into the heater mats were kept unchanged throughout the experiment.

The stator surface heat transfer coefficients of the totally enclosed generator design are illustrated in Fig. 7-22. The local surface heat transfer coefficients are lower when the test rig is totally enclosed by the Perspex casing. In this configuration, the air passes through the heated stator, and re-circulates back to the stator-rotor gaps from the front rotor disk. Due to the constraint of the external casing and the air flow path, the air velocity in the air gap is lower than the open-channel axial flux machines. As the results, the surface heat transfer coefficients measured were generally lower for the totally enclosed generators.

However, the heat transfer coefficient on the outer peripheral surface remains the same for both totally enclosed and open channel generators. From the air flow paths in the generator predicted by the CFD model, the major air flow in the stator-rotor gap does not flow through the outer peripheral surfaces. As the result, the surface heat transfer on the stator outer peripheral is mainly due to natural convection, which is independent on the air flow pattern in the generator.

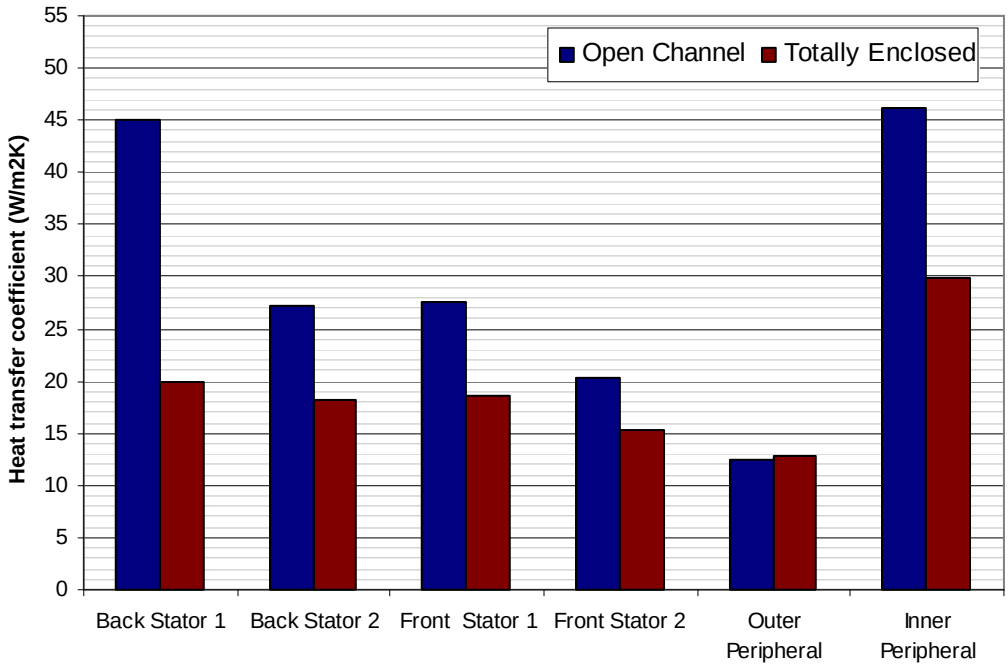

Fig. 7-22. Comparisons of the stator surfaces heat transfer coefficients of totally enclosed and open channel generator design.

7.7. Conclusions

An axial flux permanent magnet generator experimental rig and instrumentation were designed and built to validate the surface heat transfer coefficients predicted by CFD models. However, without taking into consideration of the extra cooling effect from natural convection, the CFD model under-predicts the surface heat transfer coefficients on the machine stator, compared with the experimental results. Further experiments were conducted, to acquire the heat transfer coefficient relationship between mixed convection, forced convection and natural convection. By modifying the experimental data to remove the effect of natural convection, the surface heat transfer coefficients due to forced convection only are in good agreement with surface heat transfer coefficients predicted by the CFD model, within the margins of experimental measurement error.

To investigate the surface convection heat transfer coefficient-heat flux dependency, the test rig was tested with different levels of heat input from the heater mats. The experimental results show that the surface convection heat transfer coefficients have

no relation to the heat flux output from the stator surface. For higher levels of heat input from the heater mats at the same flow condition, the increase of solid surface temperature compensates for the extra heat generated from the heater mats, to maintain the same surface convection heat transfer coefficients. The same results were obtained from the CFD simulations. Therefore, the results consolidate the assumption that the surface heat transfer coefficient is only dependent on the fluid properties and fluid flow conditions and it is independent on the magnitude of the surface heat fluxes.

Finally, the existing test rig was modified into a totally enclosed axial flux machine configuration, by attaching a Perspex cylinder casing around it. The stator surface heat transfer coefficients were measured and compared with measurements taken from the open channel axial flux machine. The results show that the surface heat transfer coefficients surge when the axial flux machine was encased in the Perspex casing. In the future, these experimental results can be used, to validate other thermal modelling methods including CFD and lumped parameter modelling for totally enclosed axial flux machines.

Chapter 8

Conclusions and Recommendations

A new thermal modelling tool for axial flux permanent magnet (AFPM) generators has been developed. The new modelling technique integrates both the lumped parameter method and the generic thermal equivalent circuit, to model the conduction and convection heat transfer in the radial and axial directions, in both open and totally enclosed axial flux permanent magnet generators. This chapter summarises all the findings and conclusions obtained from developing and validating the new thermal modelling method, which have been described in the previous seven chapters. Recommendations for future work and experimental practices are also included.

The feasible alternative to CFD modelling of the thermal state of electrical machines is the application of the advanced lumped parameter modelling technique. This technique divides the electrical machine into lumped components and represents them into thermal equivalent circuits by collections of thermal impedances and capacitances. The solid components of the electrical machines were discretised into annular control volumes, and the heat conduction between the solid components was modeled by the annulus conductive circuit. The moving fluid inside the machines was discretised into air control volumes and the convective thermal circuits were used to model the convection heat transfer between the moving fluid and the solid surface of the electrical machines.

Two convective thermal circuit algorithms were investigated, which were the Temperature Passing Method (TPM), and the Heat Pick-up Method (HPM). TPM was

developed by the author, based on the energy conservation equations, whereas HPM was the convection heat transfer modelling method introduced by previous researchers by imposing the heat fractions in the thermal circuit. Several case studies were carried out to examine the accuracies of these two convective thermal circuit algorithms with steady and transient boundary conditions, by comparing the results obtained from CFD models. The investigations show that the HPM algorithm gives better results for steady state boundary conditions, whereas the TPM algorithm is better in performing transient state thermal modelling.

During the electric machine daily operation cycle, resistive loss in the stator winding is the major heat source and temperature hot spots normally occur in the machine windings due to the low thermal conductivity of the winding filling/insulation. Hence, it is paramount to model the thermal properties of the stator winding of the machines accurately, to prevent their degradation or breakdown. The thesis describes two techniques for predicting the radial thermal resistances of the stator windings, which correspond to the Simple Concentric Model (SCM) and the Concentric-annular Layer Model (CLM). Both techniques circumvent the necessity of conducting experiments, and evaluate the radial thermal resistance based on winding parameters, such as the thermal conductivities of the conductor and winding filling, packing ratio, conductor and winding radii.

SCM lumps the conductors and winding filling in the stator winding separately, and calculates the equivalent thermal resistance by imposing simple cylinder and annulus conductive circuits. The thermal resistances predicted by SCM were validated by several numerical models and by the experimental results published by previous researchers and experimenters on five different two-phase materials. Good agreement was obtained between SCM and the other numerical models and experimental data.

During machine operation, the conductors inside the stator winding act as independent heat sources when a current passes through the stator winding. It is important to take into account the position and composition of these heat sources in the stator winding, while evaluating the equivalent radial thermal resistances, because the position and magnitude of the conductors (or heat sources) affect the heat flow paths and

temperature distributions in the winding. CLM was proposed to model the distributed heat sources inside the stator winding. CLM divides the stator windings into alternative annular layers of conductor and winding filling, and each of the conductor and winding filling annular layers is represented by an individual annulus conductive thermal circuit. The equivalent radial thermal resistance of the stator winding is calculated by summing all the annular conductive thermal circuits of the conductor and winding filling. The radial thermal resistances of the stator winding predicted by CLM were validated by pre-constructed CFD models. The results conclude that CLM is more capable of predicting accurate thermal resistances, when the electrical machines are running, or when the current is passing through the stator winding, as compared with SCM and the other numerical models developed by previous researchers. The discrepancy between thermal resistances evaluated from CLM and CFD models was less than 10%.

A 2D generic lumped parameter thermal equivalent circuit of AFPM generators with a fully automated user interface was constructed. CLM was implemented into the thermal equivalent circuit to model the stator windings of the electrical machines. Since the thermal resistances and capacitances used in the generic thermal circuit were programmed in their dimensionless form, the generic thermal circuit can be used to perform thermal modelling for a range of axial flux machines which share similar topologies. A 2D-axisymmetric, single-sided, AFPM generator CFD model was constructed and simulated with both steady and transient boundary conditions in FLUENT, to validate the results simulated from the developed 2D generic lumped parameter thermal equivalent circuit. The research shows that the temperatures predicted from the 2D generic thermal circuit were in good agreement with the CFD models, especially at low rotational speeds and low air gap clearances. At 1500rpm, with a 2 mm air gap clearance, the maximum relative discrepancy was 15%. When the rotational speed was reduced to 750rpm, the relative discrepancy fell to 8%. The relative discrepancy increased to 30% when the air gap clearance was doubled (4 mm). It was suspected that the accuracy of the 2D generic thermal circuit is strongly influenced by the convection heat transfer coefficients used in the circuit. Further discretisation of the generic thermal circuit was recommended to improve the temperature prediction of the AFPM machine when using the 2D generic thermal

circuit. In transient thermal modelling, the errors inherited from the steady state simulations persisted. By specifying the solid thermal and mass properties accurately to evaluate the thermal capacitances in the 2D generic thermal circuit, the time constant of each solid component was well predicted, in response to several different transient boundary conditions.

Subsequently, the 2D generic thermal circuit was used to perform thermal modelling of a single-sided axial flux generator with magnets affixed on the rotor surfaces. Unlike the previous 2D-axisymmetric AFPM generator, when the magnets were included, the heat flow in the circumferential direction was substantial, relative to the heat flows in the radial and axial directions. Experimental work was carried out to investigate the reliability of the 2D generic thermal circuit for 3D heat flow thermal systems. The investigation illustrated that, by taking into account the extra solid-fluid surface area on the sides of the magnets to re-evaluate the convective thermal resistances, the temperatures predicted by the 2D generic thermal circuit matched well the temperatures obtained from the experiments. Therefore, it is concluded that, by introducing suitable correction factors on the convective thermal resistances, the 2D generic thermal circuits are capable of carrying out thermal modelling for three-dimensional heat flow systems.

In general, the convection heat transfer mechanism plays an important role in the overall heat transfer of electrical machines, especially for air-cooled axial flux machines. Previous research showed that the accuracy of the temperature predicted by the 2D generic thermal circuit strongly influences the convection heat transfer coefficients between the generator solid surfaces and the moving fluid. Therefore, it is paramount to conduct sophisticated parametric variation studies, to develop empirical formulae that relate the convective heat transfer coefficient and mass flow rate to the electrical machine's geometrical parameters.

The parametric studies can be achieved either by carrying out a series of experiments, or by using the CFD modelling technique. Since the construction of a flexible test rig that is capable of performing experiments on a range of different sizes and topologies of the axial flux machine is very costly and time consuming, the CFD modelling

technique was used by Airoldi [53], to carry out parametric studies of convection heat transfer coefficient on the axial flux generator stator surfaces. A large scale low speed test rig was designed to validate the CFD modelling technique used by Airoldi and to perform convection heat transfer parametric studies for axial flux generators. The experimental results show that natural convection plays an important role, especially for large scale low speed axial flux generators. The CFD model, which did not take into account the fluid buoyancy in its calculations, under-predicted the surface heat transfer coefficients on the machine stator. Further experiments were performed, to determine the relationship between mixed convection, forced convection and natural convection. By subtracting the measured natural convection from experimental results, the experimental surface heat transfer was in good agreement with results predicted by CFD model, within the experimental measurement error margins.

The modelling in CFD of the non-uniform heating surface on the silicon heater mats used in the experiments is complex and difficult. To simplify CFD models, uniform surface heat flux boundary conditions were used. Since the silicon heat mats have a non-uniform heating surface, the experimental validation of the CFD is only valid if the convection heat transfer coefficients are independent of the magnitudes of surface heat flux. Experiments were designed and conducted to investigate the dependency of heat transfer coefficients upon the heat flux on the stator wall. The results confirm that the surface heat transfer coefficient has a weak influence on the heat flux.

In conclusion, a new thermal modelling tool for AFPM generators was developed and validated with both CFD and experimental results. Thermal modelling of typical AFPM generators is reduced from days into seconds, by introducing the 2D generic thermal circuit. However, the new thermal modelling method is limited by the availability of accurate convection heat transfer coefficients on the solid surfaces of the AFPM generators. Several recommendations are suggested for future development of the 2D generic thermal circuit for AFPM generators as follows:

- Convection heat transfer coefficient parametric studies on all the solid surfaces in AFPM generators are required. However, the CFD modelling method may be applied with confidence to perform the parametric studies, to circumvent costly and time consuming experimental methods.

- It is useful to carry out the experiments on the large scale test rig with better calibrated heat flux sensors on the stator and rotor surfaces, especially on the stator side and peripheral surfaces, to support validations conducted in this research.
- Experiments on a real AFPM generator such as the Durham 1500rpm axial flux machine, are required to further validate the reliability of the 2D generic thermal circuit, especially with regard to the eddy and hysteresis losses, surface contact resistances and stator winding thermal resistances.
- CFD modelling and experimental studies are required to validate the generic thermal circuit of water-cooled totally enclosed axial flux machines.
- The 2D generic thermal circuit can be improved by considering radiation heat transfer thermal circuits. It is also worth exploring the possibility of transforming the 2D generic thermal circuit to a fully 3D generic thermal circuit, which can be used to model three-dimensional heat flow systems more accurately, without the need for correction factors.

References

[1] J. R. Bumby, R. Martin, Axial-flux permanent-magnet air-cored generator for small-scale wind turbines, IEE Proceedings- Electrical Power Applications, Vol. 152, No. 5, pp 1065-1075, September 2005.

[2] P. Aumann, H. Barnewitz, H. Schwarten, K. Becker, R. Heinrich, B. Roll, M. Galle, N. Kroll, Th. Gerhold, D. Schwamborn and M. Franke, MEGAFLO: Parallel complete aircraft CFD, Parallel Computing, Vol 27, pp 415-440, 2001.

[3] M. S. Fisher, M. Mani and D. Stookesberry, Parallel processing with the Wind CFD code at Boeing, Vol 27, issue 4, pp441-456, March 2001.

[4] B. Vincenzo, M. Oronzio, N. Sergio, R. Mario, Numerical investigation of transient thermal and fluidynamic fields in an executive aircraft cabin, Applied Thermal Engineering, Vol 29, pp 3418-3425, 2009.

[5] N. Kroll, Th. Gerhold, S. Melber, R. Heinrich, Th. Schwarz, B. Schonig, Parallel large scale computation for aerodynamic aircraft design with the German CFD system MEGAFLOW, Parallel Computational Fluid Dynamics, pp 227-236, 2002.

[6] M. Takagi, Application of computers to automobile aerodynamics, Journal of Wind Engineering and Industrial Aerodynamics, Vol 33, Issues 1-2, March 1990, pp 419-428.

[7] H. K. Kim, C. J Kim, A numerical analysis for the cooling module related to automobile air-conditioning system, Applied Thermal Engineering, Vol 28, Issuses 14-15, Oct 2008, pp 1896-1905.

[8] R.J. Corin, L. He, and R.G. Dominy, A CFD investigation into the transient aerodynamic forces on overtaking road vehicle models, Journal of Wind Engineering and Industrial Aerodynamics, Vol 96, Issues 8-9, Sep 2008, pp 1390-1411.

[9] Y. Ferng, H. Chang, CFD investigating the impacts of changing operating conditions on the thermal hydraulic characteristics in a steam generator, Applied Thermal Engineering, Vol 28, Issues 5-6, April 2008, pp 414-422.

[10] Yehia A. Eldrainy, Khalid M. Saqr, Hossam S. Aly, Mohammad Nazri Mohd Jaafar, CFD insight of the flwo dynamics in a novel swirler for gas turbine combustors, International Communications in Heat and Mass transfer, vol 36, Issue 9, Nov 2009, pp 936-941.

[11] C.A. Baxevanou, P.K. Chaviaropoulos, S.G. Voutsinas, N.S. Vlachos, Evaluation study of a Navier-strokes CFD aeroelastic model of wind turbine airfoils in classical flutter, Journal of Wind Engineering and Industrial Aerodynamics, Vol 96, issues 8-9, Sep 2008, pp 1425-1443.

[12] I-Sun Park, Chae Hoon Sohn, Sungcheol Lee, Hwagyu Song and Jangkeun Oh, Flow-induced noise in a suction nozzle with a centrifugal fan of a vacuum cleaner and its reduction, Applied Acoustics, June 2009.

[13] P.S. Mirade, J.D. Daudin, F. Ducept, G. Trystram, J. Clément, Characterization and CFD modelling of air temperature and velocity profiles in an industrial biscuit baking tunnel oven, food research international, volume 37, issue 10, 2004, pages 1031-1039.

[14] Matthias Heitsch, Risto Huhtanen, Zsolt Téchy, Chris Fry, Pál Kostka, Jarto Niemi, Berthold Schramm, CFD evaluation of hydrogen risk mitigation measure in a VVER-440/213 containment, Nuclear Engineering and Design, Vol 240, issue 2, Feb 2010, pp 285-296.

[15] Y.M. Ferng, Predicting local distribution of erosion-corrosion wear sites for the piping in the nuclear power plant using CFD models, Annals of Nuclear Energy, Vol. 35, issue 2, Feb 2008, pp 304-313.

[16] Akashi Mochida, Shuzo Murakami, Toshio Ojima, Sangjin Kim, Ryozo Ooka, Hirokatsu Sugiyama, CFD analysis of mesoscale climate in the Greater Tokyo area, Journal of Wind Engineering and Industrial Aerodynamics, Vol 67-68, April-June 1997, pp 459-477.

[17] Shuzo Murakami, Environmental design of outdoor climate based on CFD, Fluid Dynamics Research, Vol. 38, issues 2-3, Feb-Mar 2006, pp 108-126.

[18] Asmund Huser, Thor Foyn, Martin Skottene, A CFD based approach to the correlation of maximum explosion overpressure to process plant parameters, Journal of Loss Prevention in the Process Industries, Vol. 22, issue 3, May 2009, pp 324-331.

[19] D. Makarov, F. Verbecke, V. Molkov, O. Roe, M. Skotenne, A. Kotchourko, A. Lelyakin, J. Yanez, O. Hansen, P. Middha, S. Ledin, D. Baraldi, M. Heitsch, A. Efimenko, A. Gavrikov, In inter-comparison exercise on CFD model capabilities to predict a hydrogen explosion in a simulated vehivle refueling environment, International Journal of Hydrogen Energy, Volume 34, Issue 6, March 2009, Pages 2800-2814.

[20] Lin Ma, Philip J. Ashworth, James L, Best, Lionel Elliott, Derel B. Ingham, Leslie J. Whitcombe, Computational fluid dynamics and physical modelling of an upland urban river, Journal of Geomorphology, Vol 44, 2002, pp 371-391.

[21] A.K.M. Chu, R.C.W. Kwok, K.N. Yu, Study of pollution dispersion in urban areas using CFD and Geographic information system (GIS), Environmetal Modelling & Software, Vol. 20, issue 3, March 2005, pp 273-277.

[22] Jean-Baptiste Apoung Kamga, Olivier Pironneau, Numeical zoom for multiscale problems with an application to nuclear waste disposal, Journal of Computational Physics, Vol. 224, issue 1, May 2007, pp 403-413.

[23] CFD-online, http://www.cfd-online.com/Wiki/Best_practice_guidelines_for_turbomachinery_CFD

[24] Ansys Canada, Best Practice Guide for Turbomachinery, Ansys CFX release 10.0, 2005

[25] Fluent Inc., Fluent 6.3 User's guide, Sep 2006

[26] William L. Oberkampf, Timonth G. Trucano, Verification and validation in computational fluid dynamics, Progress in Aerospace sciences, Vol. 38, 2002, pp209-272.

[27] Fred Stern, Robert V. Wilson, Hugh W. Coleman, Eric G. Paterson, Verification and validation of CFD simulations, Iowa Institute of Hydraulic Research and Propulsion Research Centre, Sep 1999.

[28] H. M. Prasser, Novel experimental measuring techniques required to provide data for CFD validation, Nuclear Engineering and Design, Vol. 238, Issue 3, March 2008, pp 744-770.

[29] M.V. Casey, Validation of turbulence models for turbomachinery flows- A review, Engineering turbulence modelling and experiments 5, Sep 2002, pp 43-57.

[30] Liao C. M., Chen C. L., Thermal Analysis of High Performance Motors, The Sixth Intersociety Conference on Thermal and Thermomechanical Phenomena in Electronic Systems, 1998, ITHERM '98, pp 424-433, May 1998.

[31] Pickering S. J., Lampard D., Shanel M., Modelling Ventilation and Cooling of the Rotors of Salient Pole Machines, IEEE International Electric Machines and Drives Conference (IEMDC) 2001, pp 806-808, June 2001.

[32] Liao C. M., Chen C. L., Katcher T., Thermal Management of AC Induction Motors Using Computational Fluid Dynamic Modelling, International Conference IEMD '99 Electric Machines and Drives, pp 189-191, May 1999.

[33] Scowby S. T., Dobson R. T., Kamper M. J., Thermal modeling of an axial flux permanent magnet machine, Applied Thermal Engineering 24 (2004), pp 193-207.

[34] Mellor P. H., Robert D., Turner D. R., Lumped parameter thermal model for electrical machines of TEFC design", Electric Power Application, IEE Proceeding B, Sep 1991, Vol. 138, Issue 5, pp 205-218.

[35] Bousbaine A., McCormickm M., Low W. F., In-Situ Determination of Thermal Coefficient for Electrical Machines, IEEE Trans. Energy Conversion, 10(3), 1995, De Montfort University, Leicester, U.K.

[36] Okoro I. O., Steady and Transient States Thermal Analysis of a 7.5-kW Squirrel-Cage Induction Machine at Rated-Load Operation, IEEE TRANSACTIONS ON ENERGY CONVERSION, VOL. 20, NO. 4, DECEMBER 2005.

[37] Liu Z. J., Howe D., Mellor P. H., Jenkins M. K., Thermal Analysis of permanent Magnet Machines, Electrical Machines and Drives, 1993, Sixth International Conference on, Sep 1993, pp 359-364.

[38] Janne Nerg, Marko Rilla, Juha Pyrhonen, Thermal analysis of radial flux electrical machines with a high power density, IEEE Transactions on industrial electronics, Vol. 55, NO.8 Oct 2008.

[39] Vilar Z. W., Patterson D., Dougal R. A., Thermal Analysis of a Single Sided Axial Flux Permanent Magnet Motor, Industrial Electronics Society, 2005. IECON 2005, pp 5.

[40] Bogliettia A., Cavagnino A., Staton D. A., TEFC Induction Motors Thermal Models: A Parameter Sensitivity Analysis, IEEE Transactions on Industry Applications, Volume 41, Issue 3, May-June 2005 Page(s): 756 – 763

[41] Staton D.A., Boglietti A., Cavagnino A., Solving the More Difficult Aspects of Electric Motor Thermal Analysis in Small and Medium Size Industrial Induction Motors, IEEE Transactions on Energy Conversion, Volume 20, Issue 3, Sept. 2005 Page(s): 620 – 628

[42] Boglietti A., Cavagnino A., Staton D. A., TEFC Induction Motors Thermal Models: A Parameter Sensitivity Analysis, IEEE Transactions on Industry Applications, Volume 41, Issue 3, May-June 2005 Page(s): 756 – 763

[43] Boglietti A., Cavagnino A., Staton D. A., Popescu M., Cossar C., Mcglip M. I., End space heat transfer coefficient determination for different Induction Motor enclosure types, Industry Applications Conference, 2008. Edmonton, October 2008

[44] Motor design LTD, http://www.motor-design.com/motorcad.php

[45] Belicova E. and Hrabovcova V., Analysis of An Axial Flux Permanent Magnet Machine (AFPM) Based on Coupling of Two Separated Simulation Models (Electrical and Thermal Ones), Journal of Electrical Engineering, Vol. 58, No.1, 2007, 3-9.

[46] Lim C. H., Brown N., Bumby J. R., Dominy R. G., Ingram G. I., Mahkamov K., Shanel M., 2-D Lumped-Parameter Thermal Modelling of Axial Flux Permanent Magnet Generators. IEEE International Conference on Electrical Machines 08.

[47] P.H.Mellor, D.Robers, D.R. Turner, Lumped parameter thermal model for electrical machines of TEFC design, IEE Proceedings-B, Vol.138, No. 5, September 1991.

[48] Axcell B. P., C. Thainpong C., Convection to rotating disk with rough surfaces in the presence of an axial flow, Experimental Thermal and Fluid Science 25 (2001) pp3-11.

[49] Kreith F., Convection heat transfer in rotating system, Advanced Heat transfer 5(1968) 129-251.

[50] Debuchy R., Dyment A., Muhi H., Micheau P., Radial inflow between a rotating and a stationary disc, European Journal of Mechanics B- Fluids 17 (6) (1998) pp 791-810.

[51] Schiestel R., Elena L., Rezoug T., Numerical modelling of turbulent flow and heat transfers in rotating cavities, Numerical Heat Transfer A- Applications 24 (1993) pp45-65.

[52] Djaoui M., Dyment A., Debuchy R., Heat transfer in a rotor-stator system with radial flow, European Journal of Mechanics B- Fluid 20 (2001), pp 371-298.

[53] Owen J. M., An approximation solution for flow between a rotating and stationary disk, ASME J. Turbomach, Vol. 111, no. 4, pp 323-332, 1989.

[54] Airoldi G., Numerical Investigation of Air Flow and Heat Transfer in Axial Flux Permanent Magnet Electrical Machine, P.h.D. Thesis, Durham University School of Engineering and Computing Sciences, March 2010.

[55] Kamel Rekab, Muzaffar Shaikh, Statistical Design of Experiments with Engineering Applications, CRC, April 2005.

[56] Douglas C. Montgomery, Design and Analysis of Experiments, Wiley 6th Edition, Dec 2004.

[57] J.C. Maxwell, A Treatise on Electrical and Magnetism, 3rd edn., Vol I and II, Chapter 9, Vol. I, article 314, Dover, New York (1954).

[58] J.M. Foster, C. B. Smith and R. I. Vachon, On predicting thermal conductivity of a binary mixture of solids, J. Spacecraft Rockets 3(2), 287-288 (1966).

[59] L.S. Kowalczyk, Thermal conductivity and its variability with temperature and pressure, Trans. Am. Soc. Mech. Eng 77, 1021-1035 (1955).

[60] J.K. Krumhansl, Thermal conductivity of solids, Theory and Fundamental Research in Heat transfer, edited by J.A. Clarm, pp. 105-106. MacMillan, New York 1963.

[61] C. Orr, Jr. And J.M. Dalla Valle, Heat transfer properties of liquid-solid suspensions, Chem. Eng. Prog. Symp. Ser 50(9), 29-45 (1954).

[62] J.B. Jerrferson, O.W. Witze; and W.L. Sibitt, Thermal conductivity of graphite-water suspensions, Ind. Eng. Chem. 50, 1589 (1958).

[63] R.H. Wang and J.G. Knudsen, Thermal conductivity of liquid-liquid emulsions, Ind. Eng. Chem. 50, 1667-1670, (1958).

[64] W.D. Kingery, Thermal conductivity: XIV, conductivity of multi-component systems, J. Am. Ceram. Soc. 42(12), 617-627 (1959)

[65] C.Orr, J.R. and A.McAllister, An investigation of two-phase thermal conductivity, Final Report Contact DA-01-009-ORD-704, Engineering Experiment Station, Georgia Institute of Technology, (1961).

[66] Sakae Yagi and Daizo Kunii, Studies on effective thermal conductivities in packed beds, A.I.Ch.E. Jl3(3), 373-381 (1957).

[67] C.B. Smith and J.M. Foster, Conduction of solid mixtures, Heat Transfer Report, Department of Mechanical Engineering, Auburn University (1964).

[68] V.A. Nieberlein, B.Steverding, Theraml conductivity of epoxy-aluminium powder mixtures, Journal of Material Science, Vol 12, (1977).

[69] G.T-N. Tsao, Thermal conductivity of two-phase materials, Ind. Engng. Chem. 53(5), 395-397 (1961).

[70] S.C. Cheng, R.I. Vachon, A technique for predicting the thermal conductivity of suspensions, emulsions and porous materials, Int. J. Heat Mass Transfer, Vol. 13, pp. 537-546. (1970).

[71] A.Bousbane, Thermal Modelling of Induction Motors Based on Accurate Loss Density Distribution, Electric Machines and Power Systems, Vol 27, pg 311-324, 1999.General Electric, 1969, Heat transfer and fluid flow data book.

[72] General Electric, 1969, Heat transfer and fluid flow data book.

[73] P. R. N. Childs, J. R, Greenwood, C. A. Long, Heat flux measurement techniques, Proceeding Institution of Mechanical Engineers, 1999, Vol. 213, Part C, pp 655-677.

[74] W. Rohsenow, J. Hartnett, Y. Cho, Handbook of Heat Transfer, McGraw-Hill Professional, 1998.

[75] R.C. Martinelli, E.H. Morrin, L.M.K. Boelter, An ivestigation of aircraft heaters, V- theory and use of heat meters for the measurement of rates of heat transfer which are independent of time. NACA, 1942

[76] F.W. Hartwig, C.A. Bartsch, H. McDonald, Miniaturised heat meter for steady state aerodynamic heat transfer measurements, Journal of Aeronautical Science, 1957, pp 239.

[77] N. S. Flanders, Heat flow sensors on walls – What can we learn? In Building Applications of heat flux transducers, ASTM STP 885, 1985, pp 140-159.

[78] M. G. Dunn, J. Kim, and W. J. Rae, Investigation of the heat-island effect for heat flux measurements in short duration facilities, Transaction of the ASME Journal of Turbomachinery, 1997, Vol 119, issue 4, pp 753-760.

[79] ULF Danielsson, Convective heat transfer measured directly with a heat flux sensor, Journal of Application Physiology, 1990, Vol. 68, issue 3, pp. 1275-1281.

[80] D. R. H. Gillespie, Z. Wang, P. T. Ireland, S. T. Kohler, Full surface local heat transfer coefficient measurements in a model of an integrally cast impingement cooling geometry, Transaction of the ASME Journal of Turbomachinery, 1998, Vol. 120, pp.92-99.

[81] S. O'Donovan Tadhg, B. Murray Darina, Jet impingement heat transfer – Part I: Mean and root mean square heat transfer and velocity distributions, International Journal of Heat and Mass Transfer, Vol. 50, 2007, pp. 3291-3301.

[82] R. Gardon, An instrument for direct measurement of intense thermal radiation, Review of Scientific Instruments, 1953, Vol. 24 (5), pp. 366-370.

[83] R. Gardon, A transducer for the measurement of heat-flow rate, Journal heat transfer, 1960, pp. 396-398.

[84] C. H. Kuo, A. K. Kulkarni, Analysis of heat flux measurement by circular foil gages in a mixed convection/radiation environment, Journal of Heat Transfer, 1991, 113, pp, 1037-1040.

[85] T. Rule, J. Kim, Heat transfer behaviour on small horizontal heaters during pool boiling of FC-72, ASME Journal of Heat Transfer, 1999, 121, pp. 386.

[86] T. V. Radhakrishnan, A. K. Verma, C. Balaji, S.P. Venkateshan, An experimental and numerical investigation of mixed convection from a heat generating element in a ventilated cavity, Experimental Thermal and Fluid Science, 2007, 32, pp. 502-520.

[87] D. A. Howey, A. S. Holmes, K. R. Pullen, Radially resolved measurement of stator heat transfer in a rotor-stator disc system, International Journal of Heat and Mass Transfer, 2010, 53, pp. 491-501

[88] R. J. Goldstein, Optical measurement of temperature, Measurement Techniques in Heat transfer, AGARD 130, 1970.

[89] ASTM, Standard test method for E457-96 measuring heat transfer rate using thermal capacitance calorimeter, 1997, American Society for Testing and Materials.

[90] I. Owen, A transient technique for measuring the rates of heat and mass transfer to a body in a humid air flow, International Journal of Mechanical Engineering Education, 19, pp. 171-181.

[91] F. F. J. Schrijer, Transient heat transfer measurements in a short duration hypersonic facility on a blunted cone-flare using QIRT, Master thesis of Delft University of Technology, Department of Aerospace Engineering, 2003.

[92] D. R. H. Gillespie, Z. Wang, P. T. Ireland, S. T. Kohler, Full surface local heat transfer coefficient measurements in a model of an integrally cast impingement cooling geometry, Transaction of the ASME Journal of Turbomachinery, 1998, 120, pp. 92-99.

[93] Z. Wang, P. T. Ireland, T. V. Jones, R. Davenport, A colour image processing system for transient liquid crystal heat transfer experiments, Transaction of the ASME Journal of Turbomachinery, 1996, Vol. 118, pp. 421-427.

[94] A. R. A. Talib, A. J. Neely, P. T. Ireland, A. J. Mullender, A novel liquid crystal image processing technique using multiple gas temperature steps to determine heat transfer coefficient distribution and adiabatic wall temperature, Transaction of the ASME Journal of Turbomachinery, 2004, Vol. 126, pp. 587-596.

[95] J. E. Doorly, Procedures for determining surface heat flux using thin film gauges on a coated metal model in a transient test facility, Transaction of ASME Journal of Turbomachinery, 1988, 110, pp, 242-250.

[96] D. L. Schultz, T. V. Jones, Heat transfer measurements in short duration hypersonic facilities, AGARD-AG-165, 1973.

[97] T. V. Jones, Z. Wang, and P. T. Ireland, Liquid crystals in Aerodynamic and heat transfer testing, Proceeding of Optical Methods and Data Processing in Heat and Fluid Flow, IMechE, London 1992.

[98] R. Davenport, Innovative use of thermochromic liquid crystals for turbine blade internal cooling passage flow visualisation and heat transfer measurements, Proceeding European Propulsion Forum, Modern Techniques and Developments in Engine and Component Testing, Bath, Royal Aeronautical Society, 1989.

[99] P. T. Ireland, T. V. Jones, The measurement of heat coefficients in blade cooling geometries, AGARD Conference Proceeding, 1985, pp. 390.

[100] P. T. Ireland, T. V. Jones , Liquid crystal measurements of heat transfer and surface shear stress, Measurement Science and Technology, 2000, 11, pp. 969-986.

[101] Z. Wang, The application of Thermochromic Liquid Crystal to detailed turbine blade cooling measurements, D. Phil Thesis, Department of Engineering Science, University of Oxford, UK, 1991.

[102] C. Camci, K. Kim, and S.A. Hippensteele, A new hue capturing technique for quantitative interpretation of liquid crystal images used in convective heat transfer studies, Transaction ASME Journal of Turbomachinery, 1992, 114, pp. 765-775.

[103] N. Akino, T. Kunigi, M. Ueda, X. Kurosawa, Liquid crystal thermometry based on automatic colour evaluation and application to measure turbulent heat transfer, Transport Phenomena and Turbulent flows, Hemisphere, Washing ton DC, 1988, pp. 807-820.

[104] J. P. C. W. Ling, P. T. Ireland, L. Turner, A technique for processing transient heat transfer, liquid crystal experiments in presence of lateral conduction, Transaction of ASME Journal of Turbomachinery, 2004, 126, pp. 247-258.

[105] O. C. Den, and C. J. Hoogendoorn, Local convective heat transfer coefficients for jet impingement on a plate: Experiments using a liquid crystal technique, Proc. of the 5th Int. Heat Transfer Conference, Talyor and Francis, London, 1974, pp. 293-295.

[106] T.E. Cooper, R. J. Field, and J.F. Meyer, Liquid crystal thermograph and its applications of the study of convective heat transfer, ASME J.Heat Transfer, 1975, 97, pp. 420-450.

[107] J.W. Baughn, A.E. Hechanova, and X. Yan, An Experimental study of entrainment effects on the heat transfer form a flat surface to a heated circular impingement jet, Transaction of ASME Journal of Heat Transfer, 1991, 113, pp. 1023-1025.

[108] M.G. Lucas, P.T. Ireland, Z. Wang, T. V. Jones, W. K. Pearce, Fundamental studies of impingement cooling thermal boundary conditions, AGARD, Turkey, 1992, Paper 14.

[109] J. E. Sargison, S. M. Guo, M. L. Oldfield, A. J. A. Rawlinson, A converging slot-hole film-cooling geometry part 1: Low-speed flat plate heat transfer and loss, ASME paper 2001-GT-0126.

[110] S. Harmand, B. Watel and B. Desmet, Local convective heat exchanges from a rotor facing a stator, International Journal of Thermal Science, 2000, Vol 39, pp 404-413, 2000.

[111] M. Mori, L. Novak, M. Sekavcnik, Measurements on rotating blasdes using IR thermography, Experimental Thermal and Fluid Science, 2007, 32, 387-396.

[112] J.W. Baughn, P. T. Ireland, T. V. Jones, N. Saniei, A comparison of the transient and heated-coating methods for the measurement of local heat transfer coefficient on a pin fin, Journal of Heat Transfer, 1989, Vol. 111, pp. 877-881.

[113] R. E. Critoph, M. K. Holland, M. Fisher, Comparison of steady state and transient methods for measurement of local heat transfer in plate fin-tube heat exchanger using liquid crystal thermography with radiant heating, International Journal of Heat and Mass Tansfer, Vol 42, pp. 1-12, 1999.

[114] R. J. Butler, and J. W. Baughn, The effect of the thermal boundary condition on transient method heat transfer measurements on a flat plate with a laminar boundary layer, Journal of Heat Transfer, 1996, Vol 118, pp. 831-835.

[115] E. R. G. Eckert, Analogies to heat transfer process, Measurement in Heat Transfer, E. R. G. Eckert and R. J. Goldstein, Eds., Hemisphere, New York 1976, pp. 397-423.

[116] E. R. G. Eckert, R. M. Drake, Analysis of Heat and Mass Transfer, McGraw-Hill, New York 1972, pp. 373-386, 728-734.

[117] F. Kreith, J. H. Taylor, J. P. Chong, Heat and Mass Transfer from a Rotating Disk, Journal of Heat Transfer, 1959, 81, pp. 95-105.

[118] H. Koyama, S. Ohsawa, A. Nakayama, Mass Transfer from a Rotating Inclined Plate, Journal of Heat Transfer, 1981, 103, pp. 204-211.

[119] E. M. Sparrow, A. Chaboki, Heat Transfer Coefficients for a Cup-like Cavity Rotating About Its Own Axis, International Journal of Heat Mass Transfer, 1982, 25, pp. 1333-1341.

[120] E. M. Sparrow, C. S. Preston, Heat Transfer form Rotating Annular Fins, International Journal of Heat Mass Transfer, 1986, 29, pp. 831-839.

[121] E. M. Sparrow, S. S. Kang, L. M. Hossfeld, Heat and Mass Transfer Adjacent to the Free End of a Rotating Cylinder, International Journal Heat Mass Transfer, 1987, 30, pp. 807-809.

[122] Y. N. Lee, W. J. Minkowycz, Heat Transfer Characteristics of the Annulus of Two-Coaxial Cylinder with One Cylinder Rotating, International Journal Heat Mass Transfer, 1989, 32, 711-722.

[123] A. P. Kudchadker, S. A. Kudchadker, R. C. Wilhoit, Naphthalene, API Monograph Ser. 707, American Petroleum Institute, Washington D. C., 1978.

[124] J. A. Dean, Handbook of Organic Chemistry, McGraw-Hill, 1987, 1-308-1-309.

[125] J. S. Lewis, A Heat/Mass Transfer Analogy Applied to Fully Developed Turbulent Flow in an Annulus, Journal of Mechanical Engineering Science, 1971, 13, pp. 177-180.

[126] T.H. Von Karman, The Analogy Between Fluid Friction and Heat Transfer, Transaction ASME 1939, 61, 705-710.

[127] B. S. Petukhov, Heat Transfer and Friction in Turbulent Pipe Flow with Variable Physical Properties, Advanced Heat Transfer 1970, 6, pp. 503-564.

[128] R. J. Goldstein, H. H. Cho, A Review of Mass Transfer Measurements Using Naphthalene Sublimation, Experimental Thermal and Fluid Science, 1995, 10, pp. 416-434.

[129] D. Robert, The application of an induction motor thermal model to motor protection and other functions, PhD Thesis, University of Liverpool, 1986.

[130] C. Mejuto, M. Mueller, M. Shanel, A. Mebarki, M. Reekie, D. Staton, Improved Synchronous Machine Thermal Modelling, International Conference on Electrical Machines (ICEM) 2008.

[131] Fluent 6.3 User's Guide, Fluent Inc, Sep 2006.

[132] A.E. Powers, Conductivity in aggregates, A.E.C. Research and Development Report, KAPL-2145 (1961)

[133] R.L. Hamilton, Thermal conductivity of two-phase materials, Dissertation, University of Oklahoma (1960)

[134] R.L. Hamilton and O.L. Crosser, Thermal conductivity of heterogeneous two-component systems, Ind. Eng. Chem. 1(3), ppg 187-191, 1962

[135] C. H. Lees, On the thermal conductivity of single and mixed solid and liquids and their variation with temperature, Proc. R. Soc. A191, 339-440 (1898)

[136] F.A. Johnson, Thermal conductivity of aqueous thoria suspensions, Atomic Research Establishment, Harwell, Berkshire, AERE R/R 2578 (1958)

[137] L. R. Barrett, Heat transfer in refractory insulating materials: I, Texture and insulating power, Trans. Br. Cerm. Soc. 48, 235-262 (1949)

[138] G. W. Carter, The Electromagnetic Field in its engineering aspects, Longmans Green and Co, 1954

[139] Madhusudana, C.V. and Fletcher. L.S., AIAA Journal, 24, pp510-523(1986)

[140] B.B. Mikic, Thermal contact conductance: Theoretical Considerations, Vol 17, pp205-214, (1974)

[141] E.M. Kennard, Kinectic Theory of Gases, McGraw-Hill pp311-324 (1936)

[142] Serway, Raymond A., Principles of Physics (2nd ed.), Fort Worth, Texas, 1998, pp. 602.

[143] Griffiths, David, Introduction to Electrodynamics (3rd ed.), Upper Saddle River, New Jersey, 1991.

[144] Giancoli, Douglas C, Physics: Principles with Applications (4th ed.), London, Prentice Hall, 1995.

[145] Wang R. J., Kamper M. J., Dobson R. T., Development of a Thermofluid Model for Axial Field Permanent-Magnet Machines, Vol. 20, No. 1, March 2005.

[146] Wong W. Y., Heat Transfer for Engineers. White Plains, N.Y. Longman, 1977

[147] Owen J. M., An approximation solution for flow between a rotating and stationary disk, ASME J. Turbomach, Vol. 111, no. 4, pp 323-332, 1989.

[148] J. Y. Luo, R. I. Issa, and A. D. Gosman. “Prediction of Impeller-Induced Flows in Mixing Vessels Using Multiple Frames of Reference. “ In *IChemE Symposium Series*, number 136, pages 549-556, 1994.

[149] N. Arai, A. Matsunami, S. W. Churchill, A Review of measurements of heat flux density applicable to the field of combustion, Experimental thermal and fluid science 1996, Vol 12, pg 452-460

[150] F. P. Incropera, D. P. DeWit, T. L. Bergman, A. S. Lavine; Fundamentals of Heat and Mass Transfer, 6th Edition, 2007; section 6.5.

[151] S. W. Churchill, A Comprehensive Correlating Equation for Laminar, Assisting, Forced and Free Convection, AIChe J., Vol. 10, pp. 10-16, 1977.

[152] S. W. Churchill, Combined free and forced convection around immersed bodies, Heat exchanger Design handbook, section 2.5.9, Begall House, New York, 2002.

[153] S. W. Churchill, Combined free and forced convection in channels, Heat exchanger Design handbook, section 2.5.10, Begall House, New York, 2002.

[154] E. Ruckenstein, Interpolating equations between two limiting cases for the heat transfer coefficient, AIChE J., Vol. 24, pp. 940-941, 1978.

[155] G. Rogers, Y. Mayhew, Engineering Thermodynamics Work and Heat Transfer, 4th Edition, Prentice Hall, pp. 552-553, 1992.

Appendix A

```
Private Sub CLM_Click()
   Set interface = Worksheets("Interface")
   Set res = Worksheets("Resistances")
   rc = interface.Cells(21, 2) / 2
   rsc = interface.Cells(31, 2) / 2
   rw = interface.Cells(11, 2) / 2
   kc = interface.Cells(23, 2)
   kcf = interface.Cells(27, 2)
   kwf = interface.Cells(34, 2)
   ac = interface.Cells(37, 2)
   assc = interface.Cells(39, 2)
   n = 5000
   k = 1
   l = 1
   p1 = 1
   it = p1 * 3.14 * rc ^ 2

   r1 = rc / (ac ^ 0.5)

   dt1 = it * Log(r1 / rc) / (3.14 * 2 * kcf * l)

**********Centre Circle Thermal Equivalent conductivity calculation**********
  Do While k <= n

      rin = r1 + (k - 1) * (rsc - r1) / n
      rout = rin + (rsc - r1) / n
      req = (rin ^ 2 + ac * (rout ^ 2 - rin ^ 2)) ^ 0.5

      rr1 = (2 * req ^ 2 * Log(req / rin) / (req ^ 2 - rin ^ 2) - 1) / (4 * 3.14 * kc * l)
      rr2 = (1 - 2 * rin ^ 2 * Log(req / rin) / (req ^ 2 - rin ^ 2)) / (4 * 3.14 * kc * l)
      rr3 = (req ^ 2 + rin ^ 2 - 4 * req ^ 2 * rin ^ 2 * Log(req / rin) / (req ^ 2 - rin ^ 2)) /
            (8 * 3.14 * kc * l * (req ^ 2 - rin ^ 2))
      rf = Log(rout / req) / (2 * 3.13 * kcf * l)

      i1 = it
      i2 = 3.14 * (req ^ 2 - rin ^ 2) * p1

      deltat = i1 * (rr1 + rr2 + rf) + i2 * (rr2 + rf)

      it = i1 + i2

      ttotal = ttotal + deltat


      k = k + 1
```

```
    Loop
    keqsc = 1 / (4 * 3.14 * kcf * l * (ttotal + dt1) / (3.14 * rsc ^ 2 * ac * p1))

    interface.Cells(42, 2).Value = keqsc

'###################Annular layer thermal conductivity calculation#############


    r1 = rsc / (assc ^ 0.5)

    it = p1 * 3.14 * ac * rsc ^ 2

    dt1 = it * Log(r1 / rc) / (3.14 * 2 * kwf * l)

    k = 1

    Do While k <= n

        rin = r1 + (k - 1) * (rw - r1) / n
        rout = rin + (rw - r1) / n
        req = (rin ^ 2 + assc * (rout ^ 2 - rin ^ 2)) ^ 0.5

        rr1 = (2 * req ^ 2 * Log(req / rin) / (req ^ 2 - rin ^ 2) - 1) / (4 * 3.14 * keqsc * l)
        rr2 = (1 - 2 * rin ^ 2 * Log(req / rin) / (req ^ 2 - rin ^ 2)) / (4 * 3.14 * keqsc * l)
         rr3 = (req ^ 2 + rin ^ 2 - 4 * req ^ 2 * rin ^ 2 * Log(req / rin) / (req ^ 2 - rin ^ 2))
                / (8 * 3.14 * keqsc * l * (req ^ 2 - rin ^ 2))
        rf = Log(rout / req) / (2 * 3.13 * kwf * l)

        i1 = it
        i2 = 3.14 * (req ^ 2 - rin ^ 2) * p1 * ac

        deltat = i1 * (rr1 + rr2 + rf) + i2 * (rr2 + rf)

        it = i1 + i2

        ttotal = ttotal + deltat

        k = k + 1

    Loop

    interface.Cells(42, 2).Value = 1 / (4 * 3.14 * kwf * l * (ttotal + dt1) / (3.14 * rw ^ 2
* ac * assc * p1))



End Sub
```

Appendix B

Appendix C

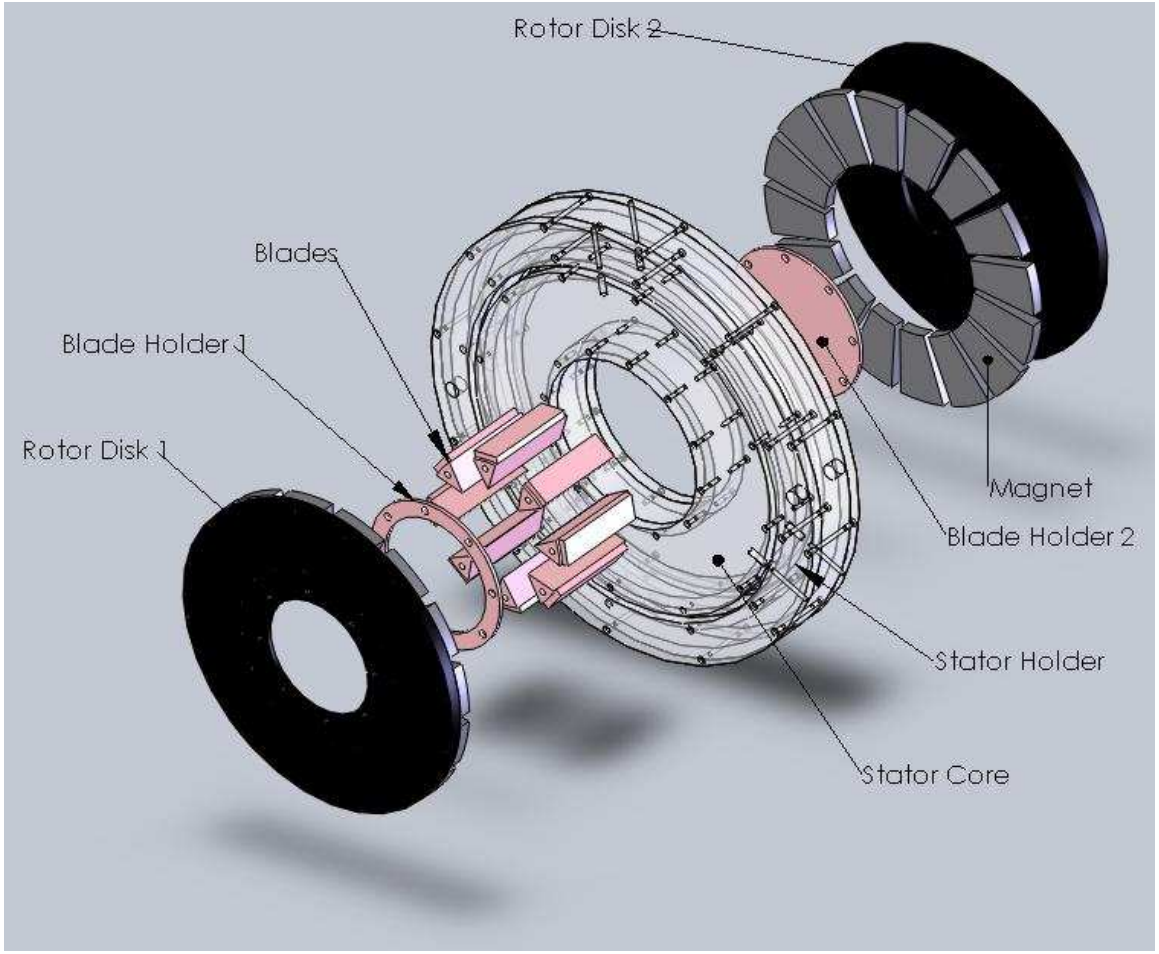
Rotor Disk 2
Blades
Blade Holder 1
Rotor Disk 1
Magnet
Blade Holder 2
Stator Holder
Stator Core

Rotor Disk 1

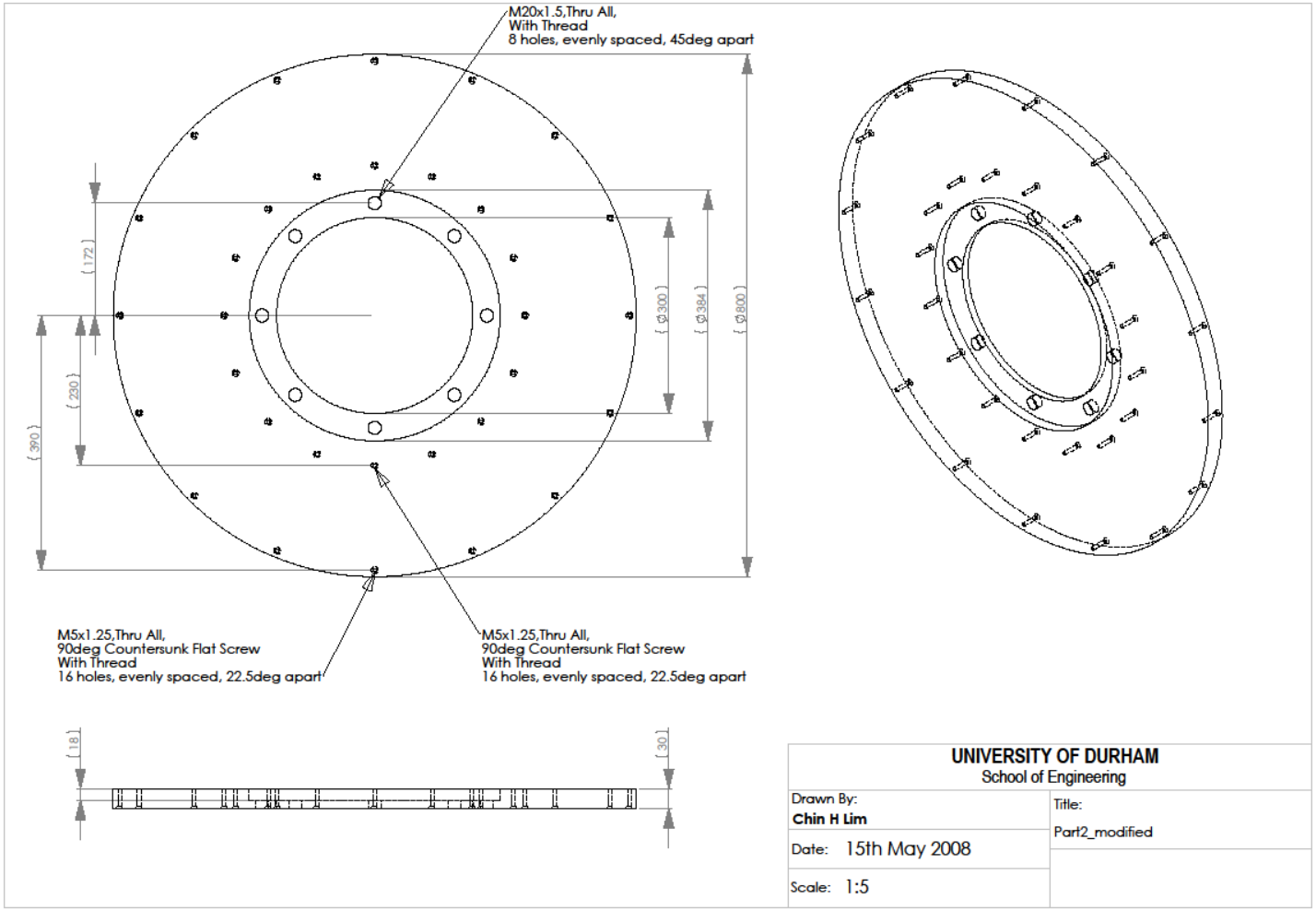
M20x1.5,Thru All,
With Thread
8 holes, evenly spaced, 45deg apart
(172)
(230)
(390)
(Ø300)
(Ø384)
(Ø800)
M5x1.25,Thru All,
90deg Countersunk Flat Screw
With Thread
16 holes, evenly spaced, 22.5deg apart
M5x1.25,Thru All,
90deg Countersunk Flat Screw
With Thread
16 holes, evenly spaced, 22.5deg apart
(18)
(30)
UNIVERSITY OF DURHAM
School of Engineering
Drawn By:
Chin H Lim
Date: 15th May 2008
Scale: 1:5
Title:
Part2_modified

Blade Holder 1

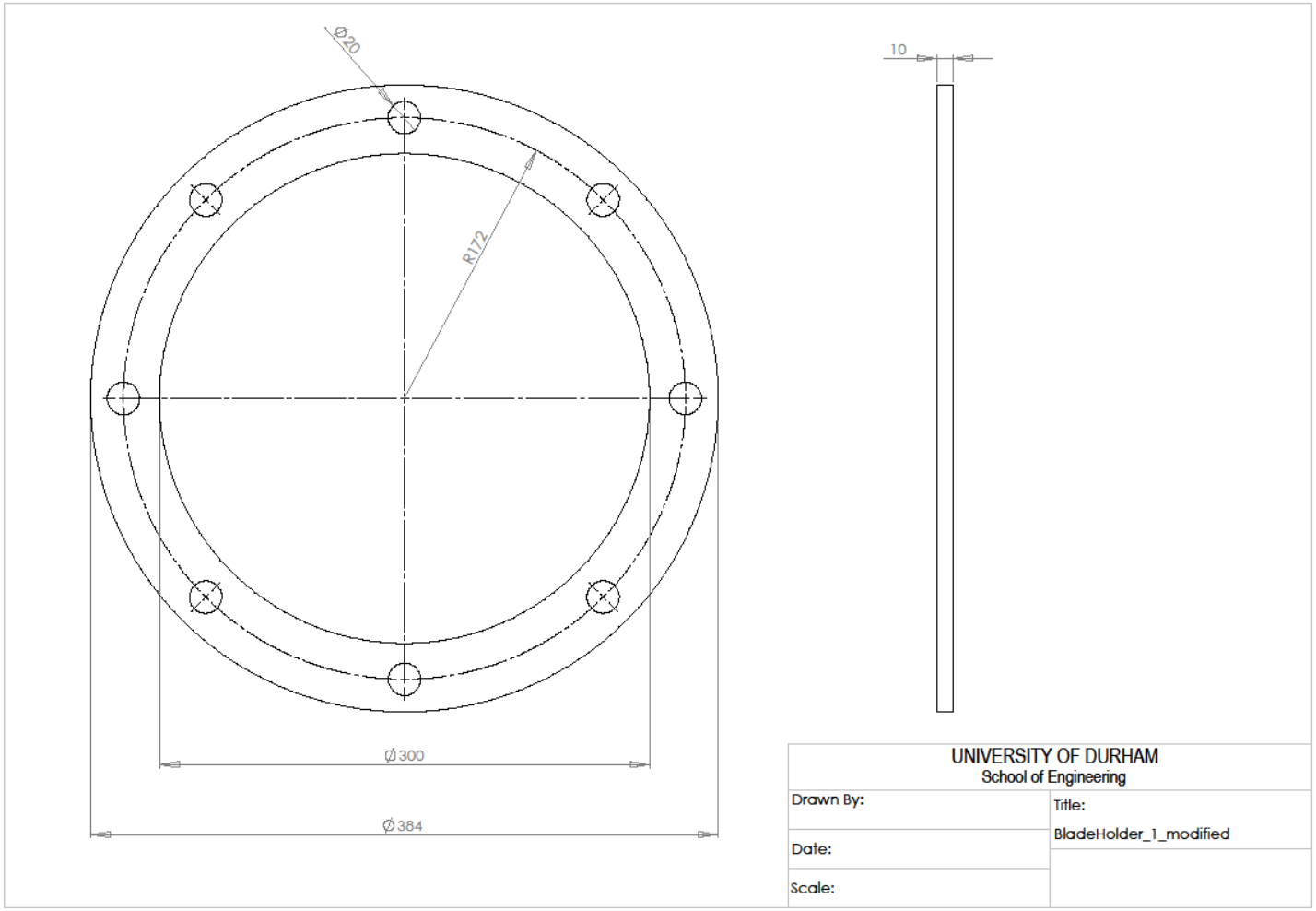

Blades

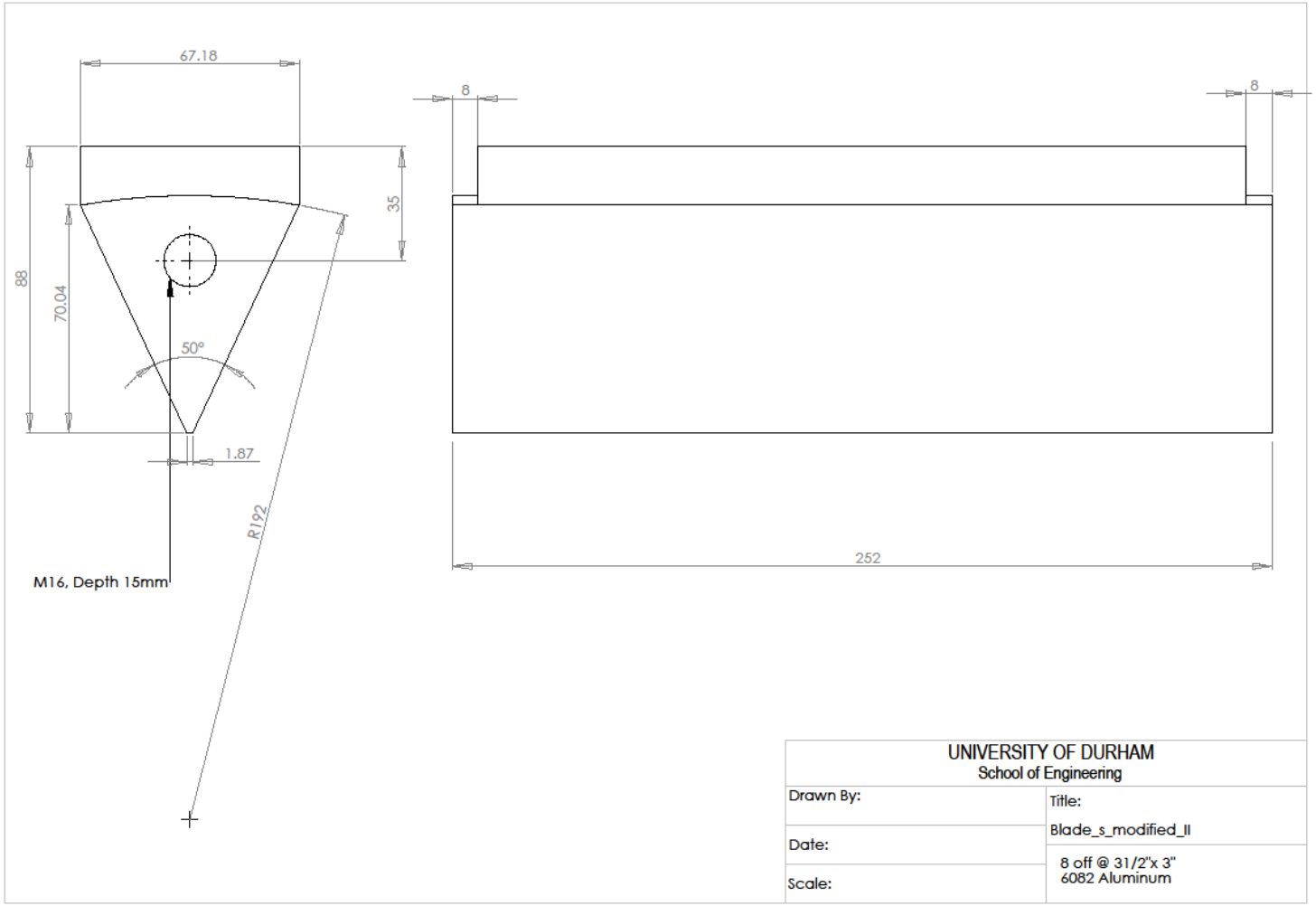
67.18
8
8
35
88
70.04
50°
1.87
R192
M16, Depth 15mm
252
UNIVERSITY OF DURHAM
School of Engineering
Drawn By:
Title:
Blade_s_modified_II
Date:
Scale:
8 off @ 31/2"x 3"
6082 Aluminum

Stator Core

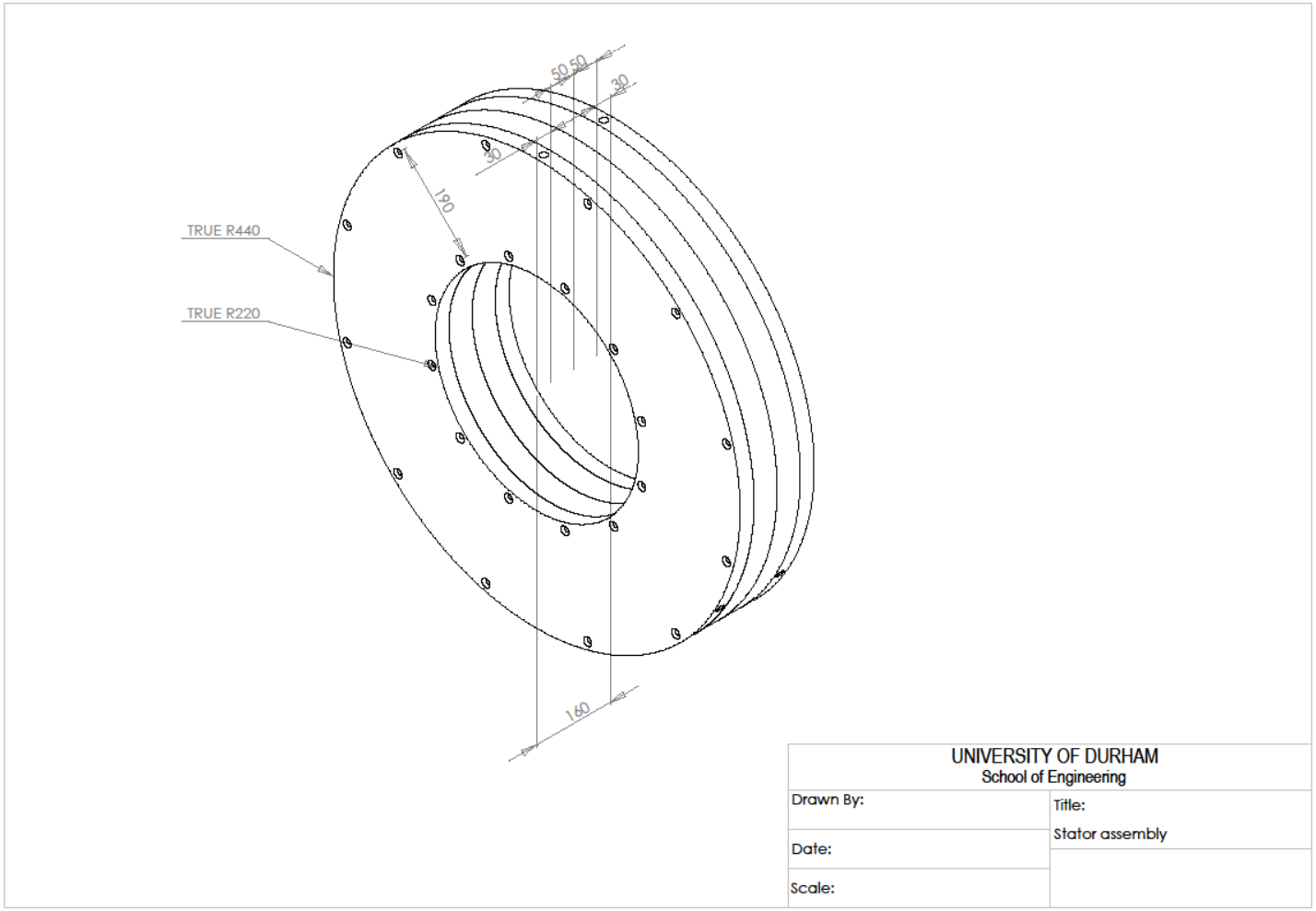
50
50
30
30
190
TRUE R440
TRUE R220
160
UNIVERSITY OF DURHAM
School of Engineering
Drawn By:
Title:
Stator assembly
Date:
Scale:

Stator Holder

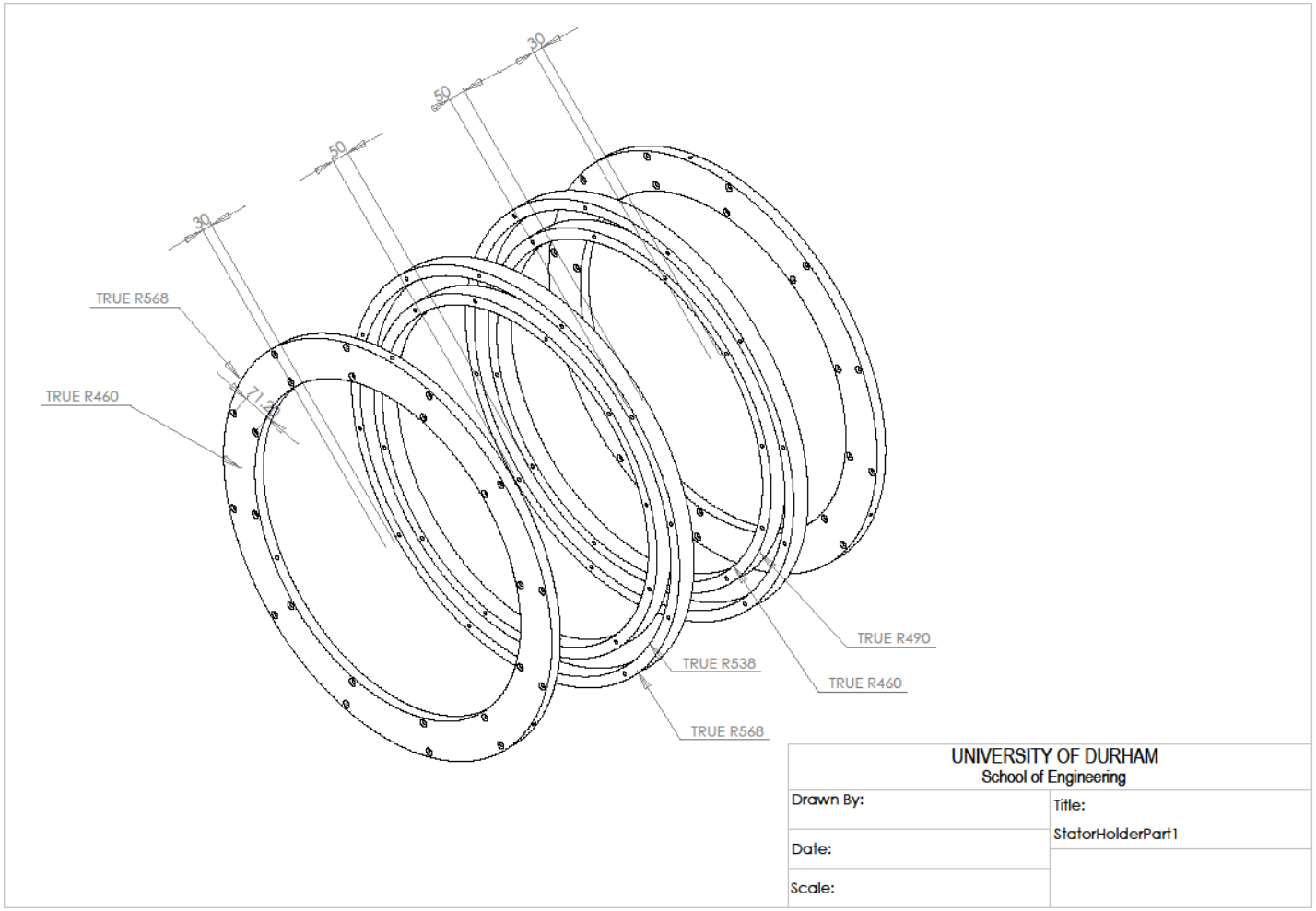

Blade Holder 2

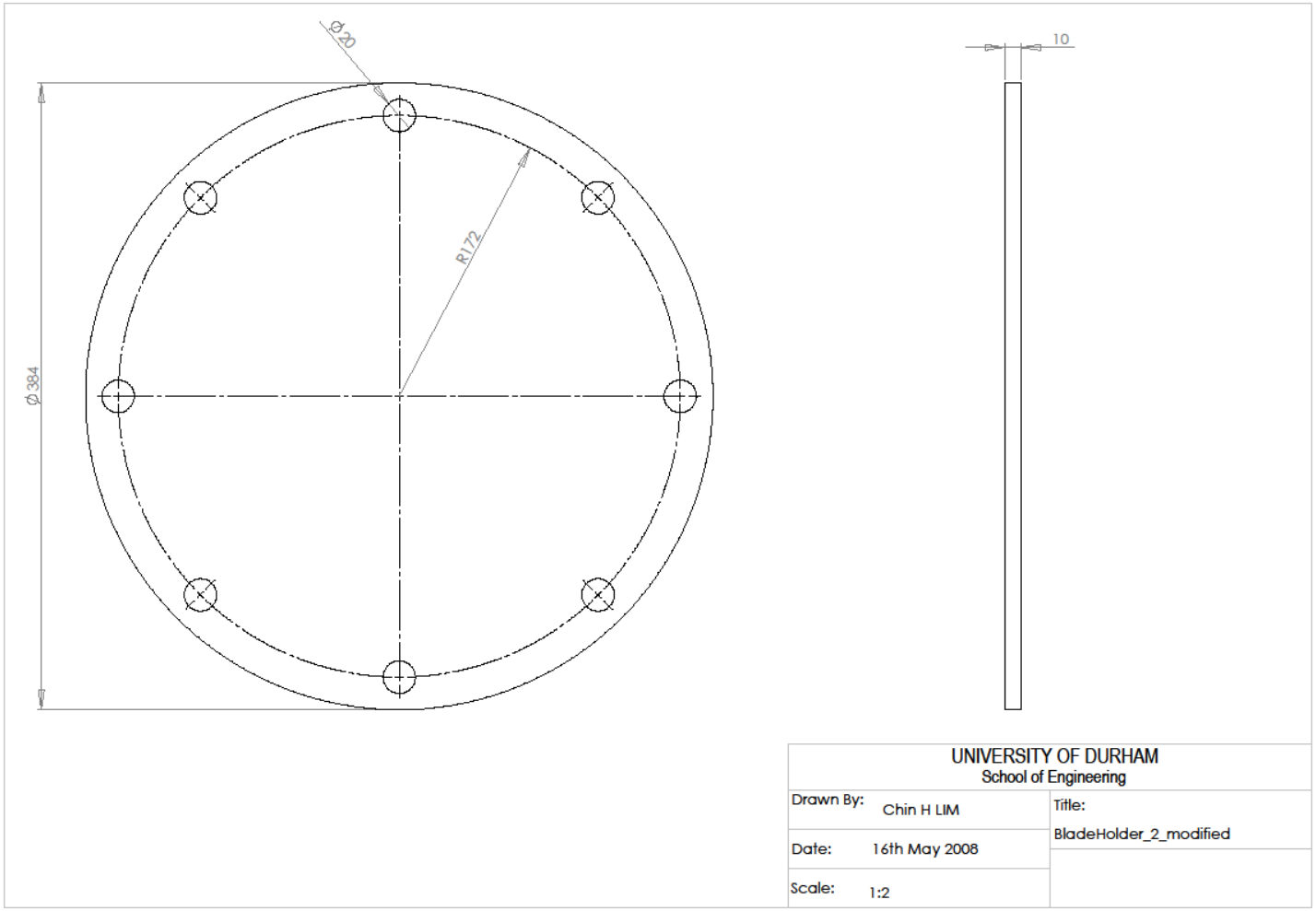

Magnet

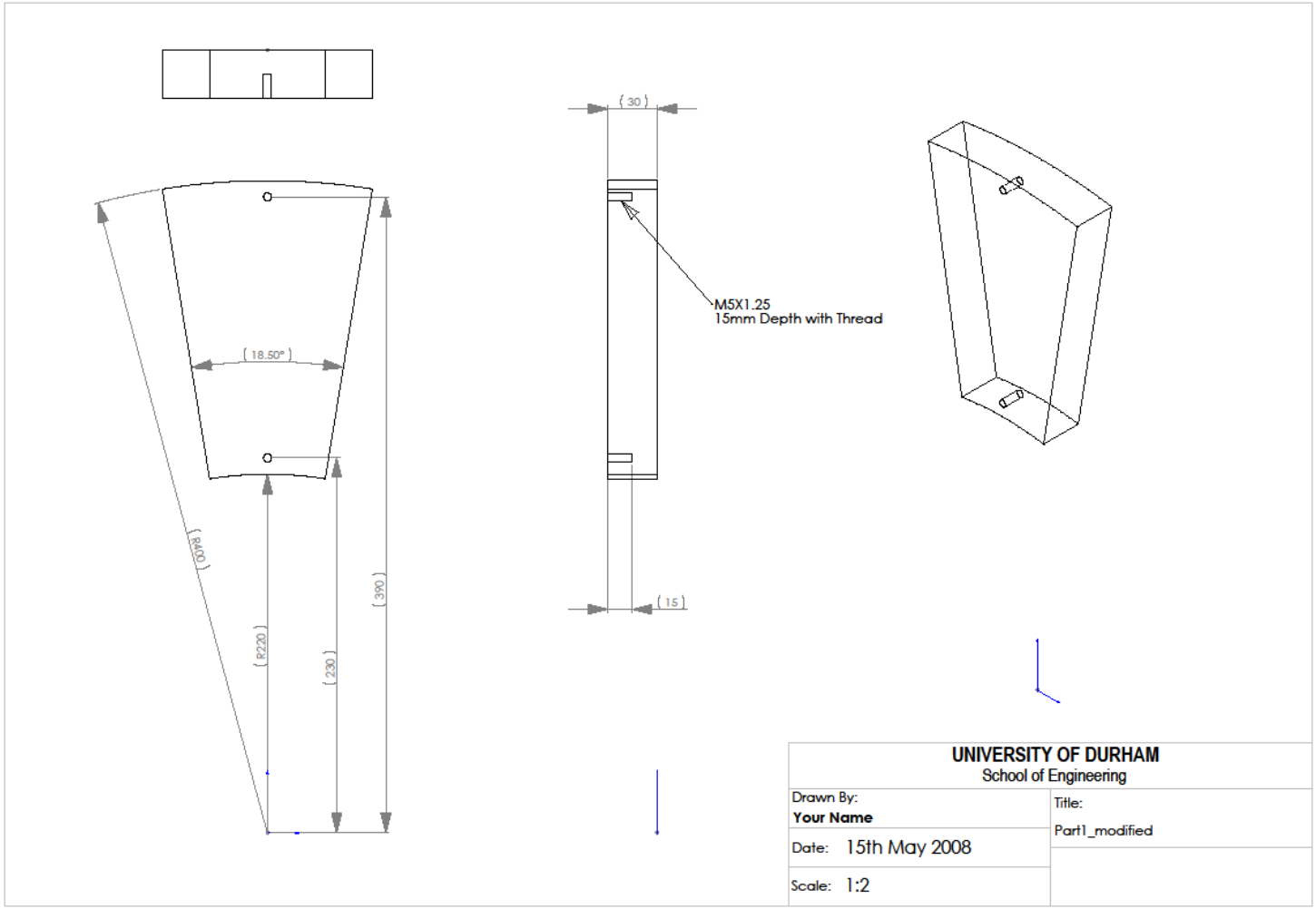
(30)
M5X1.25
15mm Depth with Thread
(18.50°)
(R400)
(390)
(R220)
(230)
(15)
UNIVERSITY OF DURHAM
School of Engineering
Drawn By:
Your Name
Title:
Part1_modified
Date: 15th May 2008
Scale: 1:2

Rotor disk 2

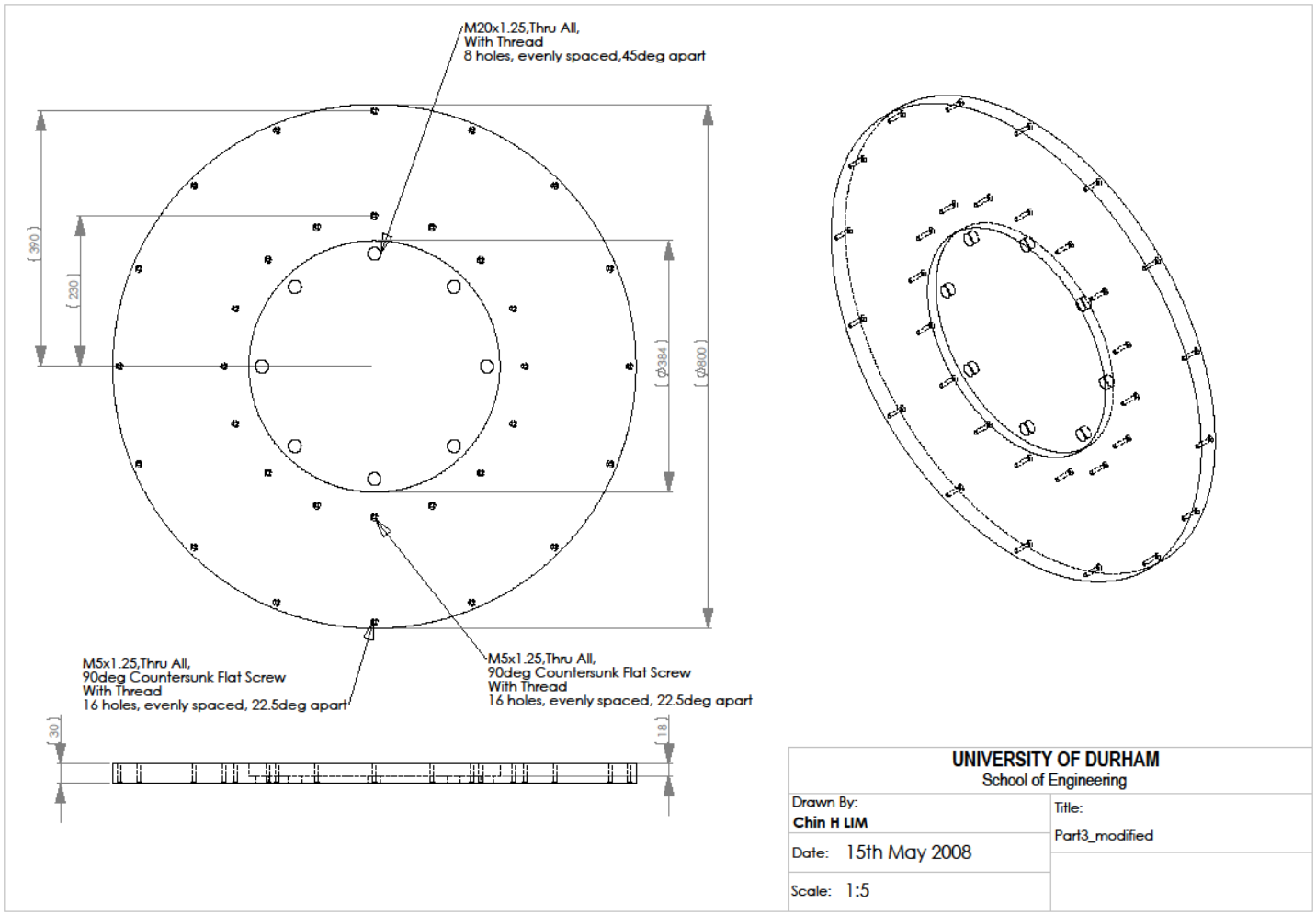
M20x1.25,Thru All,
With Thread
8 holes, evenly spaced,45deg apart
390
230
Ø384
Ø800
M5x1.25,Thru All,
90deg Countersunk Flat Screw
With Thread
16 holes, evenly spaced, 22.5deg apart
M5x1.25,Thru All,
90deg Countersunk Flat Screw
With Thread
16 holes, evenly spaced, 22.5deg apart
30
18
UNIVERSITY OF DURHAM
School of Engineering
Drawn By:
Chin H LIM
Title:
Part3_modified
Date: 15th May 2008
Scale: 1:5